DEVELOPMENT OF AN ON-DEMAND BEAM PULSING SYSTEM FOR PIXE-ANALYSIS OF THICK TARGETS

by

Mohammed Ahamed S. Armaghani, B.Sc. M.Sc.

A thesis submitted for
the degree of
Doctor of Philosophy
to
The University of Aston in Birmingham
Department of Mathematics and Physics

May 1985

I dedicate this thesis

to my beloved wife and family

THE UNIVERSITY OF ASTON IN BIRMINGHAM
DEPARTMENT OF PHYSICS

DEVELOPMENT OF AN ON-DEMAND BEAM PULSING SYSTEM FOR PIXE-ANALYSIS OF THICK TARGETS

by

MOHAMMED A. S. ARMAGHANI

Submitted for
the degree of
Doctor of Philosophy
May 1985

Summary

This work concerns the development of a proton induced X-ray emission (PIXE) analysis system and a multi-sample scattering chamber facility.

The characteristics of the beam pulsing system and its counting rate capabilities were evaluated by observing the ion-induced X-ray emission from pure thick copper targets, with and without beam pulsing operation. The characteristic X-rays were detected with a high resolution Si(Li) detector coupled to a multi-channel analyser.

The removal of the pile-up continuum by the use of the on-demand beam pulsing is clearly demonstrated in this work. This new on-demand pulsing system with its counting rate capability of 25, 18 and 10 kPPS corresponding to 2, 4 and 8 μsec main amplifier time constant respectively enables thick targets to be analysed more readily.

Reproducibility tests of the on-demand beam pulsing system operation were checked by repeated measurements of the system throughput curves, with and without beam pulsing. The reproducibility of the analysis performed using this system was also checked by repeated measurements of the intensity ratios from a number of standard binary alloys during the experimental work.

A computer programme has been developed to evaluate the calculations of the X-ray yields from thick targets bombarded by protons, taking into account the secondary X-ray yeild production due to characteristic X-ray fluorescence from an element energetically higher than the absorption edge energy of the other element present in the target. This effect was studied on metallic binary alloys such as Fe/Ni and Cr/Fe.

The quantitative analysis of Fe/Ni and Cr/Fe alloy samples to determine their elemental composition taking into account the enhancement has been demonstrated in this work. Furthermore, the usefulness of the Rutherford backscattering (R.B.S.) technique to obtain the depth profiles of the elements in the upper micron of the sample is discussed.

Keywords

PIXE, PROTON INDUCED X-RAYS, THICK TARGET ANALYSIS
THICK BINARY ALLOYS ANALYSIS

ACKNOWLEDGEMENTS

I would like to take this opportunity to express my sincere gratitude to my supervisor, Dr. D. Crumpton, for his patient advice and encouragement throughout this work and also to my advisor, Dr. P. N. Cooper, for his helpful guidance and encouragement. My thanks are also due to Dr. N. W. Grimes, the Head of Department of Mathematics and Physics and staff members of Physics Section.

My appreciation to Dr. L. G. Earwaker and to the entire Dynamitron staff at Birmingham University for their time and assistance. A special thanks to Mr. J. Phull and Dr. R. Sokhi of the PIXE group for their informal and invaluable discussions and for their continued friendship.

My thanks to Mrs. H. M. Turner and to Donna Usher for their help in typing and editing the manuscript of this thesis.

I wish to express my sincere thanks to my wife, Nasreen, for the sacrifices made throughout this work and for her unending support, and to my daughter, Aveen, a constant source of pleasure and encouragement for the future.

I pay special thanks to my mother for standing by and offering her help and encouragement for so many years.

Finally, I would like to thank the Ministry of High Education and Scientific Research in Iraq for their verbal and financial support.

TABLE OF CONTENTS

LIST OF FIGURES

CHAPTER 1

INTRODUCTION

Heavy charged particle induced X-ray emission analysis has been known for at least two decades. For example, in 1962 Van Loef et al. presented experimental results on the production of characteristic X-rays by protons with energies between 100 and 250 keV. The X-ray spectra were detected in a Xe-filled proportional counter. However, due to the counting equipment characteristic, the resolution was limited. In 1964, Birks et al. studied proton excitation of characteristic X-rays for X-ray spectrochemical analysis and reported that proton excitation could have considerable advantages over electron excitation because of the reduction of background interference. In 1970, proton induced X-ray emission analysis (PIXE) was reported by Johansson using 1.5 MeV protons as the excitation source employing high resolution semi-conductor lithium drifted silicon Si(Li) detectors for the characteristic X-ray detection.

The high resolution of the Si(Li) detectors allows X-ray lines from adjacent elements of the periodic table ($Z > 15$) to be resolved and up to thirty elements can be detected simultaneously, Folkmann (1975) and Raith et al. (1977). Thus, the combination of X-ray production by protons of a few MeV and X-ray detection by a Si(Li) detector yields a powerful, non-destructive and

simultaneous multi-elemental analysis method for all elements from Z=15.

This analytical technique is based on bombarding the targets to be analysed with protons from an MeV accelerator. When the protons penetrate the target the inner shell electrons of the atoms present in the sample are ejected. The energies of the X-rays emitted when the vacancies are filled by electrons from higher atomic levels are characteristic of the element and of the particular transition. The number of X-rays of a certain energy is proportional to the number of atoms of the corresponding element in the sample

In recent years, this technique has been developed further by many workers including Johansson (1977, 1981) and it is now regarded as a reliable technique for trace element analysis.

Studies have been reported by many authors including Cahill (1975, 1981), Campbell et al. (1981) and Burnett and Mitchum (1981) which deal primarily with analysis of thin targets, demonstrating the many applications of PIXE analysis. Targets commonly presented for elemental analysis, however, are often thick compared with the range of the incident particles which is typically only a few μm for the 2 MeV protons. Several authors, including Reuter et al. (1975), Ahlberg (1977), Huda (1979)

and Richter and Wätjen (1981) have studied the complex situtations relating to thick targets.

The applications of PIXE, its capabilities and its limitations have been reviewed and extensively discussed by many authors including Walter et al. (1974), Folkmann (1975), Deconninck et al. (1975), Johansson et al. (1976) and Khan and Crumpton (1981).

The purpose of this work has been to investigate, and where possible improve the analytical capability of the PIXE technique applied to thick targets.

Previously, little attention has been given to the analysis of thick targets due to the problems associated with the count rate limitation of the PIXE detection system. Thick targets normally lead to high X-ray counting rates which can cause severe problems in analysing a spectrum due to pulse pile-up effects. The prime feature of pulse pile-up is the pile-up continuum which extends from just above the characteristic X-ray peaks to the pile-up peaks. These peaks represent an energy equivalent of twice the original peak energy. This continuum weakens the statistical precision and the detection limit for elemental analysis in this energy region.

One of the methods previously used to eliminate the

pulse pile-up effect is the commercial pulse pile-up rejector, Khan (1975). However, although adequate at relatively low counting rates, it runs into difficulties of a practical nature as the counting rate is increased above 1 kHz.

Consequently, this study concentrates on the modification of the PIXE system at Aston in order to overcome count rate limitations associated with thick targets and lead to an improvement in the analytical capability for thick target analysis.

The concept of on-demand beam pulsing has been exploited in the present study. This approach was proposed by Jaklevic et al. (1972) and subsequently evaluated by Cahill (1975) and recently by Malmqvist et al. (1982).

In the initial stages of this work emphasis was placed on the development, modification and installation of a new PIXE beam line incorporating the on-demand beam pulsing system and on a new target chamber. The characteristics of the beam pulsing system and its counting rate capability were studied.

A computer programme has also been developed to evaluate the X-ray yields from thick targets bombarded by protons based on the procedure similar to that outlined by

Willis et al. (1977). Improvements were made to the basic calculations, taking into account the X-ray yield enhancement due to matrix effects. In particular, binary alloys have been studied. Experimentally, these binary alloys were analysed, and the intensities of the elements of interest were determined after integrating the appropriate peaks in an accumulated X-ray spectrum, using on-line computer facilities. The experimental results agreed favourably with the calculated intensities.

The theoretical aspects for analysis by proton induced X-ray emission, including the fundamentals of X-ray emission and the background production process, are presented in Chapter 2. In addition, the particle and the X-ray interaction processes with matter are discussed.

Chapter 3 deals with thick versus thin target analysis. It includes the computer programme written to calculate the K X-ray yield from thick metal targets bombarded by protons and the programme extended to include the X-ray yield enhancement due to matrix effects. It indicates the choice of data base employed in these calculations, and shows that the outcome of the calculations concerning the magnitude of the enhancement factor are in good agreement with the illustrative calculations of Reuter et al. (1975). The sensitivity of the calculations to the choice of data base has also been investigated.

The development of the on-demand beam pulsing system, the experimental set up of the new beam line and its detection system are described in Chapter 4.

Chapter 5 discusses the properties of the on-demand beam pulsing system, the precision and reproducibility of the system.

The success of the experiments and calculations, and the relative simplicity of PIXE analysis makes it desirable not only for trace element analysis, but also for general analysis of thick samples to determine their main elemental composition.

The feasibility of this is demonstrated in Chapter 6 using thick binary alloys of Fe/Ni and Cr/Fe targets at different concentrations of Fe and Cr. It further discusses the use of the Rutherford back scattering (R.B.S.) technique along with the PIXE technique and shows its usefulness when the first layer of the sample has to be analysed or the thickness of the first micron of the sample has to be measured.

Finally, conclusions and suggestions for further analysis using the present system are discussed in Chapter 7.

CHAPTER 2

MECHANISM OF CHARGED PARTICLE INDUCED X-RAY EMISSION

2.1 INTRODUCTION

This chapter discusses the main principles of ion induced X-rays. Radiative and non-radiative transitions are reviewed. Although only K X-ray emission is studied in this work, Coster-Kronig transitions which occur in shells higher than the K-shell are discussed for completeness. Atomic inner-shell vacancy production by charged particles is discussed in this chapter together with their different theoretical approaches. Also the background radiation associated with proton induced X-ray spectra and the energy loss of charge particles in matter are reviewed together with the absorption of X-rays in matter. These topics are discussed in this chapter as they represent the physical background and the basic principles on which charged particle induced X-ray emission analysis is based.

2.2 EXCITATION AND IONIZATION INDUCED BY CHARGED PARTICLES

Energetic charge particles such as electrons, protons, alphas and heavier ions may be used to induce inner shell vacancies in the atoms of a bombarded target.

The inner shell electrons are either raised to a higher energy level, excitation, or are completely removed from the atom, ionization, as a result of the Coulomb interaction of the accelerated charge particles with the atomic electron. Following the creation of inner shell vacancies the atoms de-excite and the vacancies are filled by transitions of electrons from higher energy atomic orbitals.

The difference in binding energies between the two shells can be given off as a characteristic X-ray photon. A competing process to X-ray emission is Auger electron emission where the difference in binding energies between the two shells is transferred to an outer electron which is then emitted.

For low atomic number elements, Auger emission is more probable than X-ray emission. For high atomic number elements characteristic X-ray emission becomes the dominant de-excitation process.

2.2.1 X-ray Emission

The energy of the emitted characteristic X-ray photons E_X is given by:

$$E_X = h\nu = E_F - E_O \qquad (2.1)$$

where E_F and E_O are respectively the energies of the final and initial states of the electron undergoing a transition, h is Plank's constant and ν the frequency of the emitted radiation. The energy of the photon is characteristic of the element and the shells or sub-shells of the atom between which the transition takes place. Transitions to the K-shell result in emission of X-ray lines which are termed the K-series. Transitions terminating on the L-shell are the L-series and so on. X-rays emitted as a result of L-K and M-K transitions are known as $K\alpha$ and $K\beta$ lines respectively. A complete energy diagram, showing the origin of the X-ray spectral lines and all possible transitions for elements up to Z=92, reproduced from Valkovic(1975), is shown schematically in Figure (2.1).

The transition of electrons between different quantum states is guided jointly by selection rules and the Pauli exclusion principle, Bertin (1978). The selection rules which govern transitions between states are:

$$\Delta L = \mp 1 \qquad (2.2)$$

$$\Delta J = 0 \text{ or } \mp 1 \qquad (2.3)$$

Δn may take any value where n, L and J are the principle, orbital and total angular momentum quantum numbers respectively.

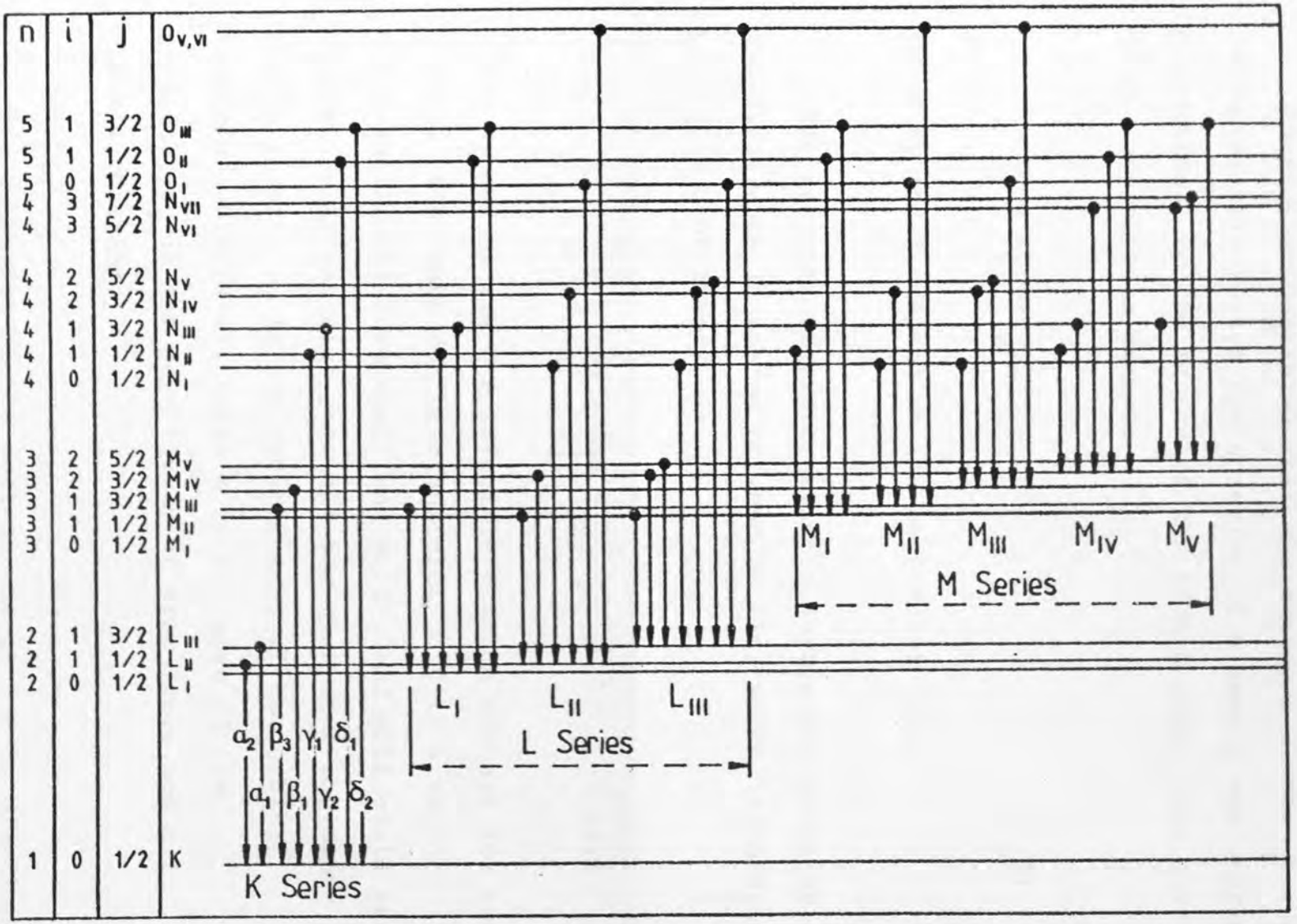

Figure (2.1) Energy level diagram for X-ray emission and their possible transition (Volkovic (1975))

Moseley demonstrated that the energy E of the characteristic X-rays for a series of elements was nearly proportional to the square of the atomic number and given by the approximate formula

$$E_X = K_1(Z-K_2)^2 \qquad (2.4)$$

where K_1 and K_2 depend on the particular line.

The energies of characteristic X-rays are given by the difference in energy between shells, which, according to simple Bohr theory, is:

$$E_X = \frac{m_r e^4}{8\varepsilon_o^2 h^2} \left(\frac{1}{n_1^2} - \frac{1}{n_2^2}\right) Z_{eff}^2 \qquad (2.5)$$

where n_1 and n_2 are the principle quantum numbers for two shells. Electrons making transition to fill a vacancy in the K-shell will have $n_1=1$, and $n_2>2$, and will yield the highest X-ray energies possible for that atom (governed by the $\frac{1}{n^2}$ term). m_r is the reduced mass of the orbital electron (=m.M/(M+m), where M is the mass of the nucleus). ε_o is the permitivity of free space and h is Plank's constant.

The screening of the nuclear charge due to electrons in the inner shell is accounted for in equation (2.5) by using the effective atomic number Z_{eff} (=$Z-K_2$), where K_2 is

a nuclear screening constant. Equation (2.5) is in general agreement with Moseley's law.

2.2.2 Auger Effect

An alternative to X-ray emission is the emission of an Auger electron after the creation of a vacancy in one of the atomic inner shells. This process leads to an atom in a doubly ionized state. Physically, the perturbation causing the transition arises from electromagnetic interaction between neighbouring electrons. The electromagnetic interaction consists of (a) the Coulomb interaction, and (b) magnetic interaction. For a radiationless transition involving the interaction of two atomic electrons, the non-relativistic perturbation theory, such as that employed by Wentzel (1927), adequately explains the transition probability. As a result of Coulomb interaction an outer shell electron is ejected. This process is known as the Auger effect, and the ejected electron an Auger electron. The Auger electron emerges with an energy equal to the energy difference between the excess energy of the initial electron and the binding energy of the Auger electron.

Burhop and Asaad (1972) and Chattarji (1976) have reviewed the mechanism of the Auger process. The energy difference causes emission of a photon or an Auger electron; the sum of the probability of emission of a

photon and of an Auger electron is unity. For energy differences below about 2000eV, the probability of Auger emission is near unity. As a result, the light elements (atomic number <14) de-excite almost exclusively by Auger emission, but Auger electron are emitted by all elements since electronic holes in the outer core levels can have de-excitation energies of less than 2000eV, Holloway (1980).

The energy spectra of the electrons produced in this process can be used to obtain analytical information. Low energy Auger electrons (< 1keV) can escape from only the first few atomic layers of a surface because they are strongly absorbed even by a monolayer of atoms. This property gives Auger electron spectroscopy its high surface sensitivity.

The ability to resolve one element from another with Auger electron spectroscopy is very good, whilst its major weakness lies in its lack of sensitivity to trace elements, Morgan (1983).

The sensitivity of the Auger technique is determined by the transition probability of the Auger transitions involved, the incident beam current and energy, and by the collection efficiency of the analyser, Davis et al., (1976).

The use of Auger electrons for surface analysis is now of major importance, and was first suggested by Lander (1953). Carlson (1975) discusses the use of Auger electrons in the study of spectra of gases and in the elemental analysis of the surfaces of solids. Recent developments in Auger electron spectroscopy (AES) have been mainly in the areas of quantitative analysis and instrumentation. The instrumentation used in AES has been extensively reviewed by Roy and Carette (1977) and Mogami, et al. (1982). The principles, practice, capabilities and application of AES for surface analysis have recently been reviewed by Holloway (1980) and Grant (1982).

The detection of Auger electrons under 1-2MeV ion bombardment has been investigated by Macdonald et al. (1983) as a surface analytical probe of particular utility for low and middle Z elements. The major difficulty in such an application is not the yield of ion-induced Auger electrons, but rather detection of these Auger electrons in the presence of the background contributed by other processes which give rise to electrons of similar energies.

A comparison of Si Auger spectra induced by electron, proton and $^{4}He^{+}$ ions have been disucssed by Macdonald et al. (1983) and Schmidt et al. (1983). They all concluded that the spectra look very similar, and it seems unlikely

that the ion-induced technique will be a serious competitor to electron-induced Auger analysis except perhaps to calibrate the latter method when quantitative results are required.

2.2.3 Coster-Kronig Transition

In shells other than the K-shell, there exists the possibility of nonradiative transitions (Coster-Kronig transitions) which are based on the transition of electrons from one subshell to another within a given shell.

The transitions between the subshells of an atomic shell having the same principle quantum number makes it possible for a primary vacancy created in one of the subshells to shift to a higher subshell before the vacancy is filled by another transition, for example the L_1, $L_{2,3}$, $M_{4,5}$ transition. Suppose an initial vacancy is in the L_1 subshell, then this is filled by an L_2 or L_3 electron leaving a vacancy in L_2 or L_3 subshell. The energy released by this vacancy shifting is transferred to an electron in M_4 or M_5 subshell via Coulomb interaction. As a result, the electron in M_4 or M_5 subshell will be knocked out, leaving the atom in a state of double ionization, Chattarji (1976). Auger and Coster-Kronig transition probabilities have been calculated using the relativistic perturbation theory for frozen orbitals, for

a number of elements with atomic number $18<Z<96$ by Chen et al. (1979, 1981). Recently, Tan et al. (1982) measured the Coster-Kronig transition probabilities (f_{ij}) of the L_1, L_2 and L_3 subshells of Pb. The measured values of (f_{ij}) are in better agreement with the relativistic calculations of Chen et al. (1981) and Krause (1979) than the earlier non-relativistic calculation by McGuire (1971) and Chen et al. (1971).

2.3 FLUORESCENCE YIELD

The fluorescence yield of an atomic shell is defined as the probability that a vacancy in that shell will be filled through a radiative transition. For the K-shell that means $\omega_K = I_K/N_i$, where the number of primary vacancies are created in N_i atoms and I_K of those atoms emit X-rays.

Correspondingly, the Auger yield, a_K, is defined as the fraction of such vacancies filled through radiationless transition. Thus:

$$\omega_K + a_k = 1 \qquad (2.6)$$

This definition is applicable to the K-shell only. The definition of the fluorescence yields of higher atomic shells is more complicated, due to the existence of Coster-Kronig transitions between subshells. Fink et al.

(1966), in their review article, give consistent definitions of fluorescence yields for the three L subshells. In the present study, observations of K-shell X-rays and the K-shell fluorescence yields have been made. The K-shell radiative transition probabililty (fluorescence yield) is an increasing function of atomic number Z, as shown in Figure (2.2) by Krause (1979).

Several attempts have been made to fit experimentally determined K-shell fluorescence yields to semiempirical formulas. A modified formula proposed by Burhop (1955) to allow for screening and relativistic effect is:

$$[\omega_K/(1-\omega_K)]^{1/4} = B_o+B_1 Z+B_3 Z^3 \qquad (2.7)$$

where the constants B_o, B_1 and B_3 are equal to 0.015 ± 0.01, 0.0327 ± 0.0005 and $-(0.64\pm0.07) \times 10^{-6}$ respectively. This formula was adopted by Bambynek et al. (1972) for their fluorescence yield calculations, because they concluded that the fluorescence yield from equation (2.7) was a statistically better approximation to the most reliable experimental data of McGuire (1970a) and Walters and Bhalla (1971) for, $4<Z<80$, $Z=82$ and $Z=93$. The uncertainty of these fitted values range from 1 to 17% for the elements considered by Bambynek et al. (1972). For the elements of interest in the present study the uncertainties range from 2 to 7%. The paper of Bambynek et al. (1972), also summarises experimental fluorescence

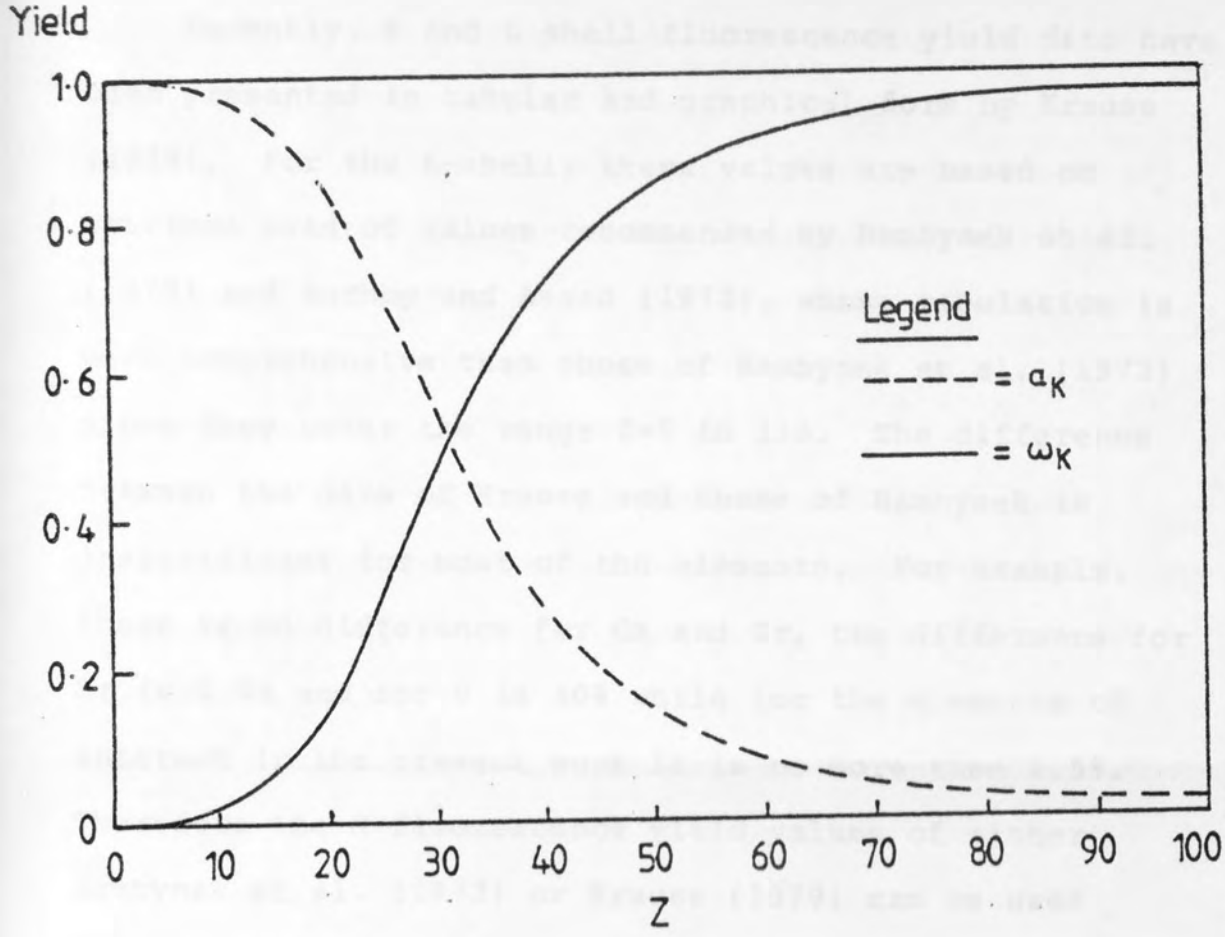

Figure (2.2) K-shell fluorescence and Auger yield vs. Atomic number (Krause (1979))

yield data up to July 1971.

Recently, K and L shell fluorescence yield data have been presented in tabular and graphical form by Krause (1979). For the K-shell, these values are based on previous sets of values recommended by Bambynek et al. (1972) and Burhop and Asaad (1972), whose tabulation is more comprehensive than those of Bambynek et al. (1972) since they cover the range Z=5 to 110. The difference between the data of Krause and those of Bambynek is insignificant for most of the elements. For example, there is no difference for Ca and Zr, the difference for Br is 0.6% and for V is 10% while for the elements of interest in the present work it is no more than 2.5%. Therefore the K-fluorescence yield values of either Bambynek et al. (1972) or Krause (1979) can be used throughout the work.

2.4 K-SHELL IONIZATION CROSS-SECTION

Ionization cross-sections for ion impact are important for an understanding of inner shell vacancy production phenomena, as well as for the assessment of the applicability of proton induced X-ray emission analysis.

During the last decade there has been considerable interest in the production of characteristic X-ray by proton bombardment of materials, see for example Akselsson

and Johansson (1974), Khan et al. (1976, 1977) and Land et al. (1982). The aim of these authors is to establish a comprehensive set of K-shell ionization cross-section data. Such information is required in order to conduct quantitative multi-element microanalysis and to test the validity of different theoretical approaches describing inner shell ionization.

Cross-section information has been determined from experimental measurements of the characteristic X-ray yield from thin or thick pure elements bombarded with protons of energy 1-3MeV. This energy is of particular interest because the rapid increase in cross-sections with energy leads to high sensitivity in proton induced X-ray analysis for a wide range of elements.

The experimental measurements of K-shell X-ray production and ionization cross-sections have been collected together in a compilation by Gardner and Gray (1978) which covers K-shell ionization data from 1973 to 1977. This work is thus a sequel to the 1973 compilation of Rutledge and Watson. With regard to the L-shell ionization by incident protons, the reader is referred to the recent tabulation of Sokhi and Crumpton (1984). These authors have tabulated the total and partial X-ray production and ionization cross-section as well as giving the relevant experimental details. The tabulation covers literature from 1975 to 1982 and is a sequel to the 1976

compilation of Hardt and Watson.

Recent measurements include those of Land et al. (1982) who measured the total K-shell production and ionization cross-section for 0.3 to 2.4MeV protons in Ti, Cr, Co, Ni, Cu and Zn. The uncertainty in their measurements was estimated to be about 5%. The total cross-section data were compared with other recent data obtained by Laegsgaard et al. (1980), Lopes et al. (1980) and Benka and Geretschläger (1980). Comparisons were also made with the theoretical predictions. Overall agreement between data of recent authors is typically ±10%.

Basically, three theoretical approaches describing inner shell ionization by charged particles have been developed.

These are the Plane Wave Born Approximation (PWBA), of Merzbacher and Lewis (1958), the Semi-Classical Approximation (SCA) of Bang et al. (1959) and the Classical Binary Encounter Approximation (BEA) of Garcia (1970a,b).

These approaches all make the assumption that the production of an inner shell vacancy occurs as a result of an interaction of the nucleus of the charged particle with the bound electron.

The PWBA describes both the projectile and the atom quantum mechanically, and the incident and the inelastically scattered particles are depicted as plane waves. The Coulomb interaction between the bound electron and the incident proton is responsible for vacancy production.

However, in the BEA a classical collision is assumed to occur between the projectile and the electron. It is assumed that the atom takes no part in the interaction other than providing the necessary binding energy, which determines the velocity distribution of the electrons. The dominant interaction leading to a transition is a direct exchange of energy between the incident particle and the atomic electron. The derivation and results of the BEA theory have been summarised and discussed fully by Garcia et al. (1973). They have shown that the ionization cross-section σ_i for any shell or subshell derived on the assumption of an hydrogenic velocity distribution of electrons obeys a scaling low which can be expressed in terms of the electron binding energy $U_i(Z)$ and the incident particle energy E_p. Thus, a plot of

$$\frac{U_i^2(Z)\,\sigma_{I_i}}{Z_1} \quad \text{vs} \quad \frac{E_p}{\lambda U_i(Z)}$$

represents a universal curve, where λ is the mass of the projectile in electron mass units and Z_1 is the projectile charge.

The SCA theory for atomic Coulomb excitation by heavy charged particles has been discussed by Bang et al. (1959), the theory is based on an approximate treatment of the Coulomb deflection effects in terms of an impact parameter formulation. Appropriate deflection corrections then can be introduced. These effects become important at low projectile velocity. It should be noted that the PWBA and SCA theories provide a limited scaling unlike the BEA theory which produces a universal curve for all projectile-target combinations. However, Madison and Merzbacher (1975) and Taulbjerg (1976) have shown that the BEA can be obtained from PWBA theory by suitable choice of the representation of the emitted electron. In addition, Taulbjerg (1977) has shown that the total cross-sections obtained from SCA and PWBA are equivalent. The BEA however fails at low impact velocities, especially when it is applied to the ionization of a specific subshell.

Detailed discussion of these models and an extended table from which the cross-sections can be obtained have been published by Basbas et al. (1973) and Rice et al. (1977) for the PWBA; Garcia et al (1973) and Hansen (1973) for the BEA, and Hansteen and Mosebekk (1973) and Hansteen et al. (1975) for the SCA. The cross-section is described in all the theories as increasing with increasing energy of the bombarding particle in the 1-4MeV energy range, as reported by Bearse et al. (1973), Garcia (1970a). The PWBA theory however predicts a maximum when

$$E_p \simeq \frac{M}{m} U_i(Z) \ . \qquad (2.8)$$

Beyond this value of E_p the K-shell cross-section decreases with increasing impact energy. Equation (2.8) implies that this maximum occurs at higher E_p for higher Z.

The qualitative behaviour of the cross-section in terms of the energy and atomic number dependence for $T_m << U_K$ as shown by Merzbacher and Lewis (1958) is given by

$$\sigma_K \propto T_m^4$$

and

$$\sigma_K \propto \frac{1}{U_K^6}$$

where T_m is the maximum energy which an incident proton of energy E_p can transfer in a free collision to an electron at rest, and U_K is the binding energy of the K-shell electron. U_K is proportional to Z_K^2, the effective atomic number.

For a given proton energy, the cross-section for X-ray production is a continuous and smoothly varying function of the atomic number. Hence:

$$\sigma_K \propto \frac{E_p^4}{Z_K^{12}}$$

or

$$\sigma_K \propto \frac{E^4}{U_K^6}$$

therefore

$$\sigma_K \, U_K^2 \propto \left(\frac{E_p}{U_K}\right)^4 .$$

This shows that the product of the K-shell ionization cross-section and the square of the electron binding energy is a function of $\left(\frac{E_p}{U_K}\right)$ and not E_p or U_K alone. Therefore $\sigma_K U_K^2$ is usually plotted as a function of $(E_p/U_K)^4$ and these should define a universal function, BEA of Garcia et al. (1973).

When T_m is of the same order of magnitude as U_K, the cross-section reaches its maximum and then falls off roughly as $1/E_p$.

The recent theoretical approaches of Brandt and Lapicki (1979) and Mukoyama and Sarkadi (1983) have not been restricted to the K-shell cross-section. They have also performed calculations for the three L-subshells. Both of these groups have worked within the PWBA theory and have included corrections for the binding energy (B), Coulomb deflection (C), polarisation (P) and relativisitc effect (R). Brandt and Lapicki (1979) employed the perturbed stationary states approach (PSS). Brandt and Lapicki (1981) added an energy loss correction factor (E)

and the complete theory is usually referred to as the (ECPSSR) theory. Mukoyama and Sarkadi (1983) however, used relativisitc target electron wave functions within the PWBA model but still made similar corrections to those of Brandt and Lapicki. Their theory is referred to as the (RPWBA-BC) theory.

Later experimental work on cross-sections refer to protons of energies less than 3 MeV and is summarised and presented by Johansson (1976). However, both the (BEA) and (PWBA) theories have been found to fit experimental data for proton energy greater than 1 MeV reasonably well. Hence, it can be concluded that either of the two theories could be employed for justifying the systematic behaviour of the cross-section.

Recent extensive graphical comparisons have been performed by Paul (1980) for proton- and alpha-induced K-shell ionization cross-sections on various targets, taken from the literature. These are compared to each other and to the refined calculation by Basbas et al. (1978) for PWBA, and by Laegsgaard et al. (1978) for SCA. Paul (1980) concluded that the best overall agreement exists between the experimental data and the corrected PWBA theory by Basbas et al. (1978), except for high target atomic number Z . For medium to large target atomic number Z , the SCA theory corrected for binding, Coulomb repulsion and relativistic effects by Laegsgaard et al.

(1978), gives acceptable agreement with the data.

For convenience, in computer calculations, useful empirical polynomial expressions based on experimental values and theoretical calculations have been presented by Khan et al. (1977), Johansson and Johansson (1976), and Reuter et al. (1975). These expressions enable the cross-sections to be readily evaluated, for a range of energies and atomic numbers.

For a given proton energy, Khan et al. (1977) proposed an empirical equation showing that the K-shell ionization cross-section σ_i is a continuous and smoothly decreasing function of atomic number Z.

$$\ell n\sigma_i(E) = b_o(E)+b_1(E)\ \ell n\ Z+b_2(E)\ (\ell nZ)^2 \quad (2.9a)$$

where b_o, b_1 and b_2 are energy dependent coefficients.

The polynomials of Khan et al. (1977) are based on their experimental measurements of the K X-ray ionization cross-section of several elements between Z=20 and 50 in the proton energy range of 1 to 3 MeV. This equation is valid within the range $1.3<E\leq 3$ MeV and $23<Z<50$. They are also presented as an alternative approach to a single equation for the ionization cross-section obtained by fitting polynomials to the energy dependent coefficients b_o, b_1 and b_2 employed in equation (2.9a) which is given by

$$\ell n\sigma_i = (41.46-37.32E+8.448E^2)-(12.212-21.242E+4.864E^2).$$

$$\ell nZ-(0.0107+2.737E-0.6551E^2).(\ell nZ)^2 \qquad (2.9)$$

This equation requires only the input of atomic number Z and the proton energy E_p. The equation is reported to differ by less than 3% from the Z-dependent equations. The precision of the initial measurements of production cross-section, on which the equation is based, is reported to be less than 6% for the majority of elements studied.

Johansson and Johansson (1976) have fitted a fifth degree polynomial formulated according to the BEA universal form to the thin target data from ten authors. The polynomial is given by:

$$\ell n(\sigma_i U_K^2) = \sum_{n=o}^{5} b_n X^n \qquad (2.10)$$

where the coefficient b_n can be found in Table (2.1), and $X = \ell n(E_p/\lambda U_K)$, λ is the ratio of the proton mass to electron mass, E_p is the proton energy in eV, U_K is the appropriate binding energy in eV, and where the unit of the ionization cross-section σ_i is expressed in $10^{-14}cm^2$. For the K cross-section the one-sigma confidence interval for the theoretical regression curve is reported to be $< 1\%$ for $E_p/\lambda U_K$ values 0.034 to 0.92

and < 5% at the end points.

Alternatively, a seventh order polynomial fitted by Reuter et al. (1975) to the theoretical tabulation of Garcia et al. (1973) can be employed

$$\log_{10}(U_K^2 \sigma_i / Z^2) = \sum_{n=o}^{7} (\log_{10} E/\lambda U_K)^n \, b_n \qquad (2.11)$$

where the coefficients (b_n) are also reproduced in Table (2.1), and U_K is in keV. This polynomial reproduces the tabulated data to better than 1%.

In the present work, the polynomials by Khan et al. (1977), Johansson (1976) and Reuter et al. (1975) have been adopted and comparisons have been made with regard to X-ray yield enhancement due to matrix effects.

2.5 ENERGY LOSS OF CHARGED PARTICLES

A precise knowledge of proton stopping power (dE/dX) is important in PIXE analysis of thick samples. In these samples, the protons lose energy in penetrating the sample until they are finally brought to rest. Since the X-ray production cross-section is a function of proton energy, the X-ray yield varies over the range of the protons. To determine a properly averaged cross-section along the proton path the energy of the proton must be determined at intervals along the path from a knowledge of dE/dX.

Equation Number	Coefficients							
	b_o	b_1	b_2	b_3	b_4	b_5	b_6	b_7
2.14	2.0471	-0.65906 (-2)	-0.47448	0.9919 (-1)	0.46063 (-1)	0.60853 (-2)	-	-
2.15	-19.04	0.3028 (-1)	-1.11	0.3771	0.1923	-0.7459 (-1)	-0.5084 (-1)	-0.5949 (-2)

Table (2.1) Coefficients for the calculation of the K-shell ionization cross-section for equations (2.14) and (2.15).

The situation for thin samples is less complex. Here, the proton passes through the sample without appreciable loss of energy and the X-ray production cross-section remains essentially constant throughout the sample.

The energy loss of charged particles is briefly discussed in this section, and the formulae adopted to evaluate dE/dX in the present work are also discussed.

Heavy charged particles, such as protons and alpha particles, lose energy primarily by excitation and ionization of atoms along their path, and to a lesser extent by elastic collision with nuclei. The energy loss occurs in a large number of small decrements. The maximum energy T_m, that can be transferred by an ionizing particle, mass M, energy E to a free electron, mass m, in a single collision is given by:

$$T_{max} = \frac{4Mm}{(M+m)^2} E \qquad (2.12)$$

which for a heavy charged particle M>>m, reduces to:

$$T_{max} = \frac{4m}{M} E \qquad (2.13)$$

The energy transferred to the electron must come at the expense of the charged particle, and its velocity is

therefore decreased as a result of the encounter. The energetic electron emitted (delta ray) may itself go on to produce secondary ionizations.

If the energy loss of the incident particle in an encounter is very small compared with its own energy, the process is assumed elastic and the deviation of the particle from its straight line path is considered negligible. The primary particle carries on losing its energy in an absorber until it eventually comes to rest. The mean depth of penetration measured along a straight line from the point at which the particle enters an absorbing material to the point at which additional displacement is no longer detectable, Janni (1966), is known as the range of the incident particle . The range may be calculated from a knowledge of the stopping power. Stopping power (the specific energy loss) (-dE/dX) is defined as the amount of energy lost by a particle per unit distance in the stopping material, Enge (1966).

At high energies, (larger than 1 MeV/amu) the classical expression that describes the specific energy loss for a heavy charged particle with charge Ze moving at velocity V is known as the Bethe formula and is written as:

$$-\frac{dE}{dX} = \left(\frac{1}{4\pi\epsilon_o}\right)^2 \frac{4\pi e^4 Z_1^2}{m_o V^2} NZ_2 \left[\ln\left(\frac{2m_o V^2}{I}\right) + \ln\left(\frac{1}{1-\beta^2}\right) - \beta^2 - \frac{C}{Z_2}\right] \qquad (2.14)$$

where $\beta = \frac{V}{C}$, C is the velocity of light, Z_1 is the atomic number of the projectile, Z_2, I and N respectively are the atomic number, mean excitational ionization potential and density mg/cm^3 of the absorber atoms, m_o is the electron rest mass, e is the electronic charge and C/Z_2 are so called shell corrections. The Thomas-Fermi distribution function has usually been used to estimate the parameter I for each element. The simplest result of such an approach is Bloch's rule; viz $I = I_o Z_2$, where I_o = 10 eV.

When the velocity of the charged particle is large in comparison with the orbital electrons in the absorber, equation (2.14) is generally applicable.

For non-relativistic charged particles (V<<C) equation (2.14) becomes:

$$-\frac{dE}{dX} = \left(\frac{1}{4\pi\epsilon_o}\right)^2 \frac{4\pi e^4 Z_1^2}{m_o V^2} N Z_2 \left[\ln \frac{2m_o V^2}{I}\right] \qquad (2.15)$$

where $\frac{dE}{dX}$ in equation (2.15) varies as $\frac{1}{V^2}$ or inversely with particle energy. The logarithmic term in equation (2.15) is found to be a very slowly varying function of the incident energy, and for the same velocity of different charged particles, the only factor that may change outside the logarithmic term in equation (2.15) is Z_1^2. For a good approximation on a given target:

$$-dE/dX \propto \frac{Z_1^2}{V^2} \qquad (2.16)$$

Therefore, the bombarding particles with higher charge will have the largest specific energy loss. In comparing different materials as absorbers, dE/dX depends primarily on the product of NZ_2 in equation (2.15). Therefore, high atomic number (Z_2), and high density (N) materials will result in the greatest linear stopping power.

It has been observed by Lindhard et al. (1963) that the Bethe formula begins to fail at low particle energies (below 30 keV/amu). However a comprehensive theoretical treatment by Lindhard et al. (1963) to predict the stopping power at low energies is available which uses the Thomas-Fermi statistical model of the atom. The energy loss processes are divided up into energy losses through ionization and excitation of the target atoms (the so-called electronic energy losses) and elastic energy losses to the screened nuclei (nuclear stopping). The nuclear stopping power for hydrogen projectiles is very small at energies >10 keV and increases in relative importance with decreasing energy.

Brice (1975), Varelas and Biersack (1970) proposed interpolation formulae of different levels of complexity to bridge the gap between high and low energy theories.

These formulae are presented and discussed by Anderson and Ziegler (1977). Proton energy loss data for the majority of elements have been presented by these authors over the proton range $10 keV < E < 20$ MeV. The data were fitted to a simple analytical function, and the parameters (A_i) are presented in tables for each element. Also, they attempt to interpolate the fitting parameters to elements for which there is no experimental data. The fitted analytical functions of Anderson and Ziegler were based on the recent bibliography and index of the experimental stopping power and range data of Anderson (1977). The difference between experimental and fitted data at energies above 2 MeV are reported to be accurate to 1%.

For energies from 600 - 2000 keV, experimental data scatter more and there is less theoretical guidance concerning the shape of the shell corrections.

For ease of computation the high-precision stopping power of Anderson and Ziegler (1977) have been adopted in the present work. The expressions employed are as follows:

for the proton energy range: 10 - 999 keV

$$S^{-1} = (S_{low})^{-1} + (S_{high})^{-1} \quad \frac{eV.cm^2}{10^{15}atom} \qquad (2.16)$$

where

$$S_{low} = A_2 E_p^{0.45}$$

$$S_{High} = (A_3/E_p)\ \ell n[1+(A_4/E_p) + A_5 E_p]$$

for the proton energy range: 1000 - 100,000 keV

$$\text{stopping power} = (A_6/\beta^2)[\ell n(\frac{A_7 \cdot \beta^2}{1-\beta^2}) - \beta^2 - \sum_{i=0}^{4} A_{i+8}(\ell n E_p)^i]$$

$$\frac{eV.cm^2}{10^{15} atom} \qquad (2.17)$$

where E_p is hydrogen energy/hydrogen mass [keV/a.m.u], and A_i are the polynomial coefficients fitted to the experimental data for each element.

Prior to Anderson and Ziegler (1977), Reuter et al. (1975) fitted polynomials to the electronic stopping power data of Northcliffe and Schilling (1970) for protons which enabled them to calculate the stopping power for $Z > 10$ and $12.5 < E_p < 4000$ keV. The analytical form is given by the relations:

$$S_L = A_1 \sqrt{E_p}$$

$$S_U = (A_2/E_p)\ \ell n\ (1 + A_3/E_p + A_4 E_p)$$

$$S^{-1} = S_U^{-1} + S_L^{-1} \qquad (2.18)$$

where E_p is the proton energy in MeV and S is in keV.cm^2/mg. The total stopping power S is a composite of an upper (S_U) and a lower (S_L) energy region where the division occurs near the region of maximum S, at approximately 100 keV.

Reuter et al. (1975) have obtained the coefficient A_i by minimising the square difference between S and the tabular data of Northcliffe and Schilling (1970), where the other coefficients were obtained by plotting the fitted coefficients via the atomic number and taking the values from a smooth curve through these points. The largest difference between this analytical form and the tabular data of Northcliffe and Schilling (1970), is in the energy range 0 to 4 MeV is 5.7% and the average difference is about 1.5%.

The analytical form of Reuter et al. (1975) has also been used in the present work in order to demonstrate the sensitivity of the present calculation on thick alloy targets to the dE/dX data base employed, (Chapter 3).

In a target matrix consisting of different elements the total stopping power is the weighted addition of the individual elements, i.e. Bragg-Kleemen's rule,

$$S_m(E) = \sum_{i=1}^{n} C_i \, S_i(E) \qquad (2.19)$$

where $S_m(E)$ is the stopping power of the compound target for projectile E, n is the number of elements present in the target, $S_i(E)$ is the stopping power of the ith element, and C_i is the weight fraction of the ith element in the matrix.

Bragg-Kleemen's rule has been tested by Bewers and Flack (1968) who investigated the stopping power of 16 different fluorine compounds with 1 MeV protons, and found that the deviation from Bragg's rule was less than 2%. Feng et al. (1973) also studied the application of the additive rule for binary metal alloys and metal oxides using $^4He^+$ ion with energies of 0.5 - 2.25 MeV. They found that Bragg's rule correctly predicts the energy loss in Au-Al and Au-Ag mixture to within 1% sensitivity of the experiment and to 2% in Au-Cu alloys. The measured relative stopping power in α-Fe_2O_3 and Fe_3O_4 are consistent with the use of Bragg's rule and the available elemental stopping power, however, a 20% discrepancy was obtained in Al_2O_3. A study by Powers et al. (1973) and a survey by Ziegler et al. (1975), for MeV alphas, suggests that departures from additivity up to 20% are to be expected between solid and gaseous forms of an element, such as oxygen, due to molecular effects. Recently, Blondiaux et al. (1979), using the average stopping power method discussed by Ishii et al. (1978), experimentally determined the stopping power ratio of five metals and

their associated oxides using protons and compared the results with the calculated ratios using the data of Anderson and Ziegler (1977) for the stopping power of the metals and gaseous oxygen.

The authors conclude that above the energies considered (average energy $E_m > 2.35$ MeV/U and threshold > 1 MeV/U) deviation from the additive rule for the oxides investigated are negligible and that the data of Anderson and Ziegler (1977) for hydrogen can be used with confidence.

In the present work, it is assumed that the additivity rule holds well enough to be used in the calculations of the stopping power of thick homogeneous targets.

2.6 ABSORPTION OF X-RAYS IN MATTER

A large number of possible interaction mechanisms may occur with passage of electromagnetic radiation through matter. The processes resulting in attenuation are:

(a) scattering, in which the photon is deflected through a certain angle with little or no energy imparted to the atom in question or to any of the electrons associated with it;

(b) absorption, in which there is a direct transfer of the majority of the photon energy to the atom or to one of its electrons.

The scattering of photons and the absorption of energy by the irradiated atoms are two distinct consequences of X-ray interaction. The number of photons I, transmitted through an absorber of thickness t, in terms of normal incident photons I_o, is given by the exponential attenuation of X-rays as:

$$I = I_o \exp(-\mu_m \rho t) \qquad (2.20)$$

where $\mu_m = (\frac{\mu}{\rho})$ is the mass attenuation coefficient measured in terms of cm^2/g and is independent of the density and physical state of the interacting medium, and ρ is the density of the absorber in g/cm^3.

If the sample is made up of a homogeneous mixture of elements, then each element i contributes to the absorption in accordance with its concentration C_i and the mass absorption coefficient μ_m at X-ray energy E is the weighted sum of the absorption coefficients μ_i of the individual elements and is written as:

$$\mu_m(E) = \sum_i C_i \mu_i \quad \text{(Bragg Additivity Rule)} \qquad (2.21)$$

The mass absorption coefficient $\mu_m(E)$ accounts for various

interactions which can occur in the sample and is composed of three major components which depend on X-ray energies, Dyson (1973). These are:

$$\mu_m(E) = \tau(E) + \sigma_{coh}(E) + \sigma_{inc}(E) \qquad (2.22)$$

where $\tau(E)$ is the photoelectric mass absorption coefficient which describes the photoelectric effects. The total coherent and incoherent mass scattering coefficients $\sigma_{coh}(E)$, $\sigma_{inc}(E)$ respectively describe the coherent and incoherent scattering process. $\mu_m(E)$ and their components depend on the energy of the incident photon as shown in Fig. (2.3), for an iron sample. These coefficients depend on the atomic number of the absorbing material as well, in a way determined by the details of the three important iteraction mechanisms: photoelectric effect, coherent and incoherent scattering processes, through which X-rays interact with matter. Within the energy range of interest, less than 30 keV, the photoelectric effect is the most dominant. A detailed discussion of these interactions is presented by Dyson (1981).

The total mass attenuation coefficient may be obtained from the compilation of Hubbell (1969), Storm and Israel (1970) and Veigele (1973).

The compilation of Storm and Israel (1970) lists μ_m

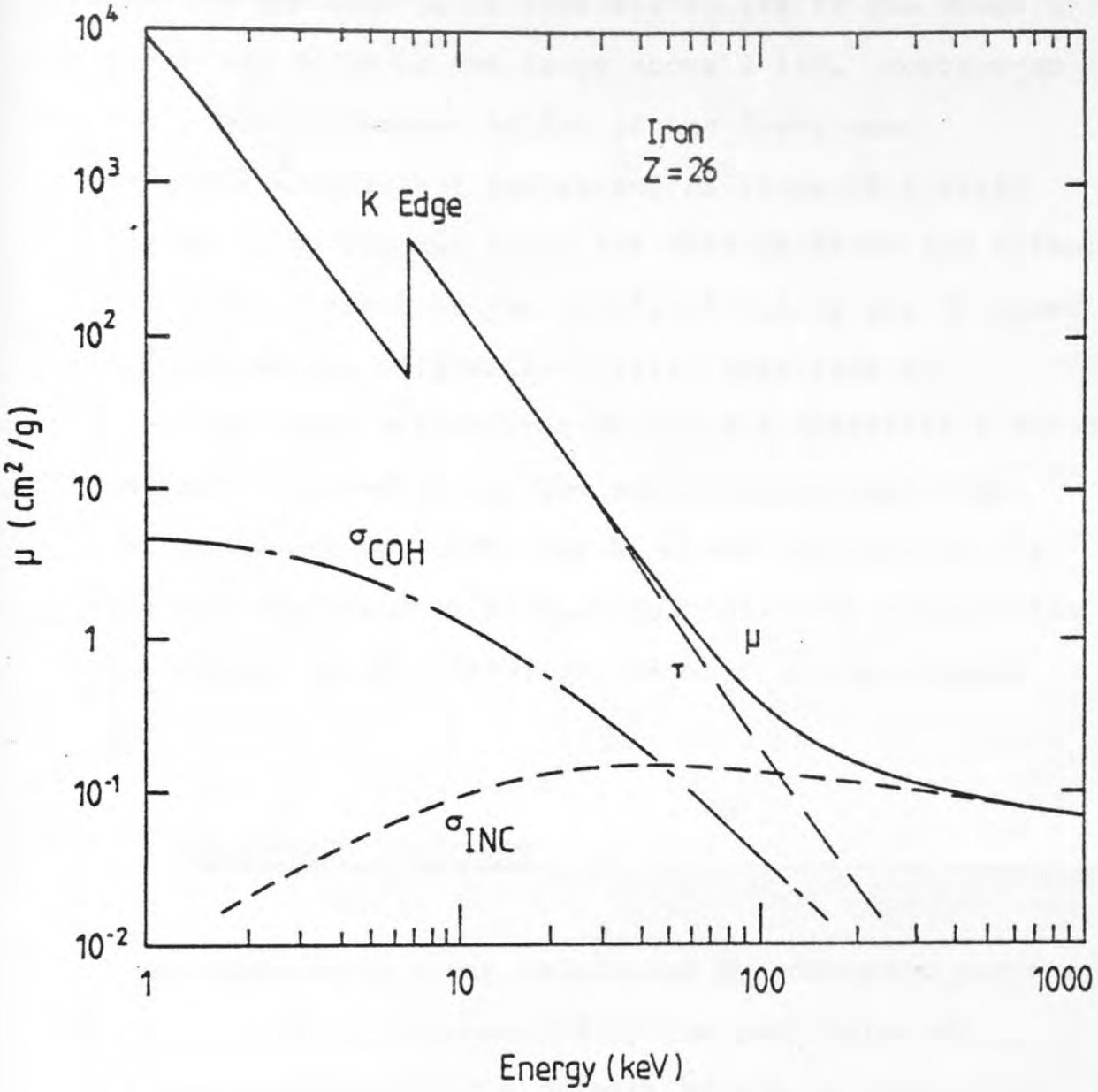

Figure (2.3) Mass attenuation coefficient and its component for pure iron as a function of incident photon energy (McMaster et al. (1969))

for selected X(γ) -rays from 1 keV to 100 MeV. These values are expected to be accurate to 10% in the range 1 to 6 keV and to 3% in the range above 6 keV. Montenegro et al. (1978) presented tables of the X-ray mass attenuation coefficient for Kα and Kβ lines of $17 \leq Z \leq 50$ in $6 \leq Z \leq 33$, , by interpolating the data of Storm and Israel (1970). The fitting of the tabulated values was obtained by a third degree polynomial. Also, they made a comparative study between the absorption coefficient found by the above procedure and the experimental data from Millar and Greening (1974) for N, O, Ne, Ar, Al and the difference was found to be less than 3%. The compilation of Montenegro et al. (1978) can be used in the present work.

2.7 BACKGROUND RADIATION

Characteristic X-ray production by energetic protons will inevitably be accompanied by the production of background radiation. The primary source of this background can be explained by the well known laws of the interaction of charged particles with matter. This background can be attributed to several processes:

(i) the continuous radiation from the secondary electrons ejected from target atoms by the primary ion beam,

(ii) the continuous radiation from the primary ion beam as it slows down in close collision with the target nuclei, and

(iii) Compton scattering of γ-rays from nuclear reactions between projectile and target nuclei.

The continuous radiation, (i) and (ii) above is known as bremsstrahlung. The characteristic X-ray peaks are superimposed on this background, and as a result, the level of bremsstrahlung is a significant source of uncertainty when characteristic X-ray lines are used for analytical purposes. The intensity of the projectile bremsstrahlung is proportional to $(\frac{1}{M})^2$, and thus the use of protons for trace element analysis instead of electrons results in a reduction in the primary ion bremsstrahlung of about 3×10^6 for projectiles of the same velocity, Young et al. (1973).

Thus, the contribution of bremsstrahlung radiation can be minimized but never eliminated and constitutes a fundamental limitation to PIXE sensitivity. The source of these background radiations is discussed in the following subsections.

2.7.1 Secondary Electron Bremsstrahlung

The generation of characteristic X-rays as discussed

in the previous section is accompanied by the emission of energetic inner shell electrons. These ejected electrons lose most of their energy by Coulomb interaction with the target atoms and are finally caught by one of the ionic atoms when their energy is sufficiently reduced. Thus, they give rise to intense bremsstrahlung radiation. Folkmann et al (1974a) have given detailed calculations which confirmed that the intense low energy portion of the X-ray background results from secondary electron bremsstrahlung. The intensity of the bremsstrahlung radiation decreases rapidly above the energy T_m which represents the maximum energy that may be transferred from the proton to a free electron. For proton excitation, T_m is given by equation (2.12), and since $(4m/M)$ in equation (2.12) is approximately (1/460), it follows that proton energies of 1 to 3 MeV give approximately 2 to 6 keV for T_m. For 3 MeV protons T_m is approximately 6 keV, and characteristic X-ray lines from trace elements with energies greater than 6 keV, i.e. manganese, are clear of this continuum background. Characteristic X-ray lines with energies less than 6 keV, however, have to be measured against this bremsstrahlung background. A reduction in proton energy to 1 MeV reduces T_m so that X-rays in the region 2 to 6 keV are clear of this background.

Therefore, the secondary electron contribution to the background could be greatly reduced to meet the

requirement of a particular application.

By reducing the incident proton energy, E_p, the X-ray production cross-section also reduces, and in practice a compromise has to be reached. The optimum requirements for PIXE analysis system have been considered in detail by Saied (1981).

Production of secondary electron bremsstrahlung is a two step process. Electrons are ejected by protons impacting on the target atoms. These electrons are decelerated by the target atoms, and when deflected by their electric field, have a certain probability of emitting bremsstrahlung. This production process offers the possibility of reducing the background by employing extremely thin targets. Folkmann et al. (1974a) have reported an agreement between the theoretical calculation of the cross-section for the production of secondary bremsstrahlung and the experimental observations, for thin targets of carbon and aluminium for proton energies of 2 and 3 MeV. Folkmann (1976) has extended the calculations of Folkmann et al. (1974a) to the case of thick targets and has confirmed that the optimum sensitivities of thick targets (on C and Al) bombarded with protons of 3.0 MeV is not much worse than those for thin targets, measured with a reduced proton energy, i.e. $E_p \simeq 2.0$ MeV. Folkmann et al. (1974a) estimated the intensity of this bremsstrahlung radiation and found that the possibility of the initial

ion ejecting an electron of energy E_e decreases slightly with increasing E_e until $E_e \approx T_m$. The probability for ejection of a secondary electron with $E_e > T_m$ decreases dramatically, approximately as E_e^{-10}, suggesting a rather low background at the high energy end.

Folkmann et al. (1974a) assumed that the angular distribution of the secondary electron bremsstrahlung is approximately isotropic, and not sufficiently pronounced to be exploited for background reduction. Tawara et al. (1976), however, have reported that the angular distribution of the bremsstrahlung is not isotropic but it is generally more intense at 90°. This was confirmed by Ishii et al. (1977) and more recently be Renan (1980).

The angular dependence of the secondary electron bremsstrahlung spectrum for a 1.5 MeV proton beam on a thin Al foil is shown in Figure (2.4), Ishii et al. (1977). In this case, the anisotropy is seen to be typically 40% at 30° and 135° instead of at 90°. Measurement at 4 MeV by these authors indicated that the intensity in the forward direction becomes stronger than that in the backward direction as the proton energy is increased. This is reported to be due to the effect of multiple scattering of electrons which is expected to be small.

Renan (1980) obtained a 30% improvement in

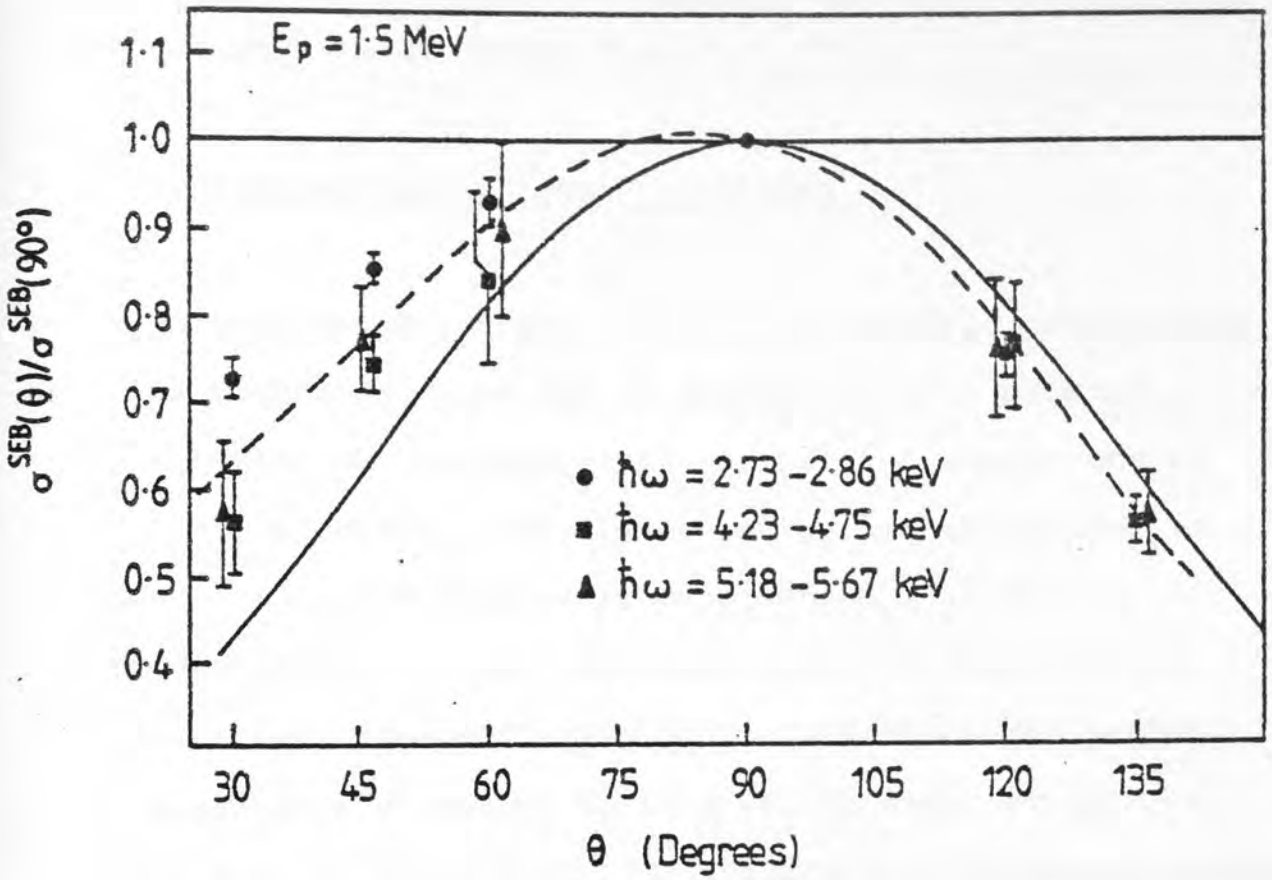

Figure (2.4) Anisotropy of SEB as a function of angle at Ep = 1.5 MeV.
The solid curve shows theoretical prediction without retardation effect and dotted curve represents the theoretical calculation including the retardation effect, fitted to the experimental results.
(Ishii et al. (1977)).

sensitivity by locating the detector at 130° rather than 90°. This was supported by Chu et al. (1981) at 6 MeV protons on a 10 μm Mylar foil.

2.7.2 Bremsstrahlung from Projectiles

Bremsstrahlung from the incident particle contributes to the background also and it appears to be a primary contribution to the background at the high energy end of the X-ray spectrum. The higher energy bremsstrahlung is produced when the projectile experiences a large acceleration in a close encounter with a nucleus of the target atoms. The differential cross-section for proton bremsstrahlung of energy E_r is given by Alder et al. (1956) as:

$$\frac{d\sigma_\gamma^B}{dE_r} = C. \frac{A_1 Z_1^2 Z^2}{E_1 E_r} \left[\frac{Z_1}{A_1} - \frac{Z}{A} \right]^2 + \text{higher multipolarities} \qquad (2.23)$$

where Z_1, A_1 and E_1 are the charge, mass and energy, respectively, of the incident proton, and Z and A are the charge and mass of the target atoms. C is approximately constant.

The term $\left(\frac{Z_1}{A_1} - \frac{Z}{A}\right)^2$ arises from interference between the radiation of the projectile and of the recoiling nucleus. If $Z_1/A_1 = Z/A$, then this bremsstrahlung should

vanish. In these cases, higher multipolarities become important, but according to Folkmann et al.(1974a), are of much less intensity. Many trace elements are present in a carbon matrix and for this matrix, $Z/A = 1/2$. The projectile bremsstrahlung should be considerably reduced if the projectile $Z_1/A_1 = 1/2$, which is true for such ions as $^{4}_{2}He$, $^{12}_{6}C$, $^{16}_{8}O$ and $^{20}_{10}Ne$.

Figure (2.5) reproduced from Folkmann et al. (1974a) illustrates the level of the bremsstrahlung background where the contribution at high energy is due to proton bremsstrahlung.

2.7.3 Compton Scattering of Gamma Rays

Gamma radiation will be produced when the incident protons have sufficient energy to excite the nuclei of the target atoms.

The Compton scattering of these γ-rays by the sample, materials of the target chamber and around the detector itself, is responsible for producing a low energy continuous background in the X-ray energy region, Folkmann et al (1974b). The amount of γ-radiation produced depends on the elemental composition of the target and the experimental arrangement. If some nuclides such as ^{19}F, ^{23}Na and ^{27}Al, which exhibit large resonance reaction cross-sections for γ-emission are present, then

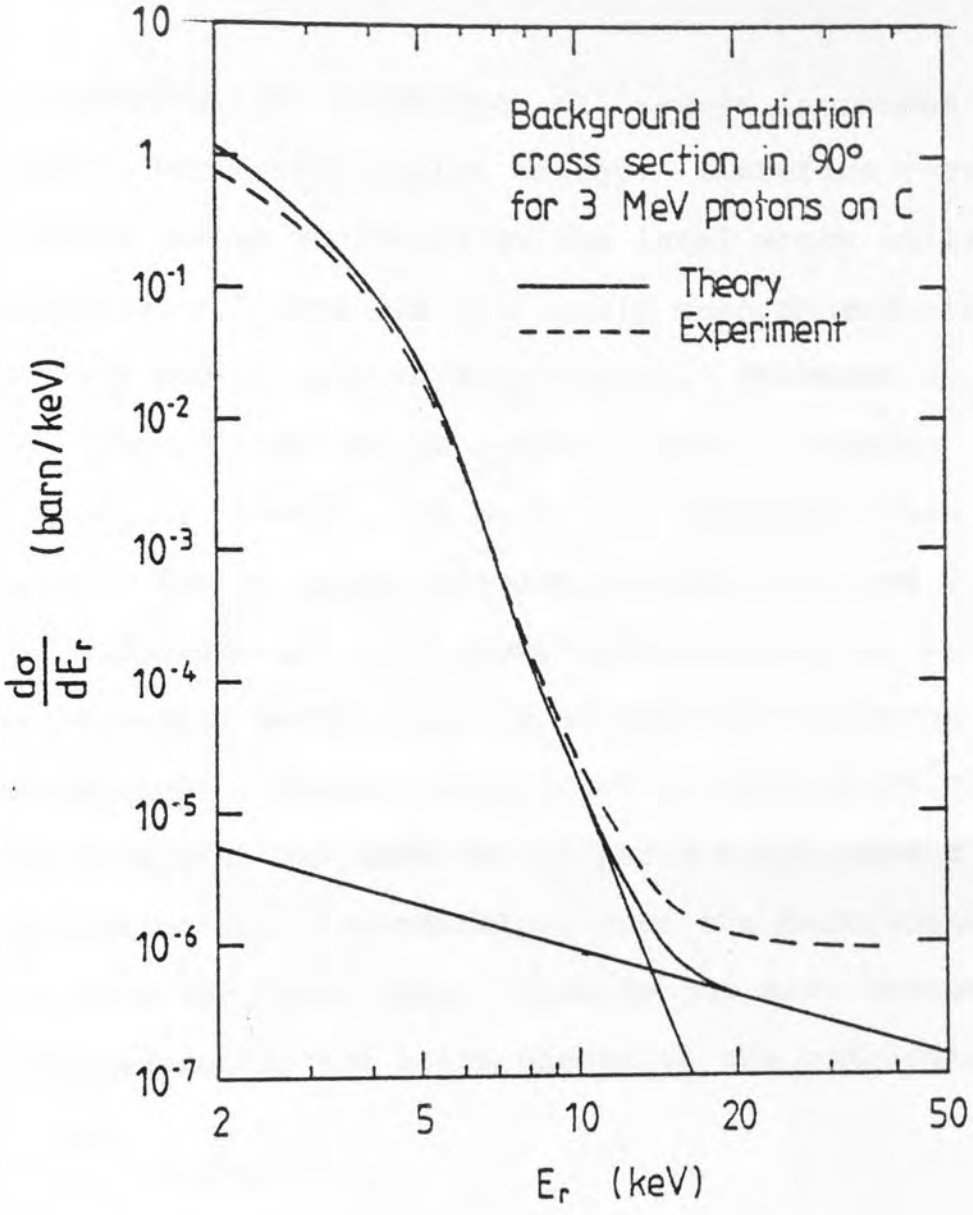

Figure (2.5) Experimental and theoretical background radiation cross-section for thin sample. (Folkmann et al. (1974a))

compton scattered γ-rays may become a serious source of background even for proton beams of 1 MeV.

Generally, the production of γ-rays increases with increasing bombarding proton energy. Therefore γ-ray background can be minimised to the level where still characteristic X-rays can be clearly seen by reducing the bombarding proton beam to some extent. Folkmann et al. (1974b) showed that the background, due to Compton scattering of γ-rays, was much more important than the background due to proton bremsstrahlung for 3 and 5 MeV proton bombardment. Above approximately 15 keV these processes become more important than electron bremsstrahlung. Heavier ions, such as alpha particles and oxygen ions with the same energy per a.m.u., have a larger cross-section for γ-production, thus the background is much higher for these ions. This is the main reason why low energy protons are often chosen as the bombarding particles.

CHAPTER 3

THICK TARGET ANALYSIS BY PIXE

3.1 INTRODUCTION

The comparative merits of thin and thick targets, their advantages and disadvantages, are indicated in this chapter. In particular, quantitative analysis by PIXE of thick composite targets together with their matrix effects are discussed. The formalism of the direct X-ray production in a thick target and a correction scheme for secondary excitation processes, if radiation is generated in the target capable of fluorescence excitation, are discussed in detail.

A computer programme has been written to calculate the X-ray yield from each element present in a target and to calculate the enhancement effect factor in thick binary alloys. Finally,the choice of different data bases used for enhancement calculationsare discussed.

3.2 THICK VERSUS THIN TARGETS

Proton induced X-ray emission (PIXE) analysis has been applied mostly to the analysis of thin targets, (e.g. environmental, biological and medical targets), Walter and Willis (1974), Johansson and Johansson (1976), Saied . (1981) and Johansson et al. (1981). These targets, although offering the possibility of increased sensitivity,are difficult and often tedious to prepare, and run a high risk of contamination. The use of thick targets,which are less prone to these

problems,are increasingly being used,(alloys, rock and mineralised tissue such as teeth), Ahlberg et al.(1975,1976),Bauer et al. (1978),Cohen et al.(1980) and Khaliquzzaman et al.(1981).

The terms thin and thick targets have to be defined with respect to the typical bombarding beam energy and target composition. The advantages of using a thin target is that the energy loss of the proton beam traversing it and the absorption of X-rays in leaving the target are often negligible, consequently the ionization cross-section $\sigma_I(E_o)$ can be taken as that at incident energy E_o of the incident proton beam. Campbell (1977) has adopted a more formal definition of a thin target as one in which the effective cross-section $\sigma_I(E)$ is 5% less than the cross-section at incident energy E_o, $\sigma_I(E_o)$.

For thin targets the number of characteristic Kα X-rays ΔI_i, arising from an element i per incident proton of energy E_o is given by:

$$\Delta I_i = n_i . w_i R_i \sigma_{I,i}(E_o) \Delta t \quad \text{photon/proton} \qquad (3.1)$$

where n_i = number of atoms of element i per unit volume,

$\sigma_{I,i}(E_o)$ = ionization cross-section of element i for proton bombardment

w_i = the X-ray fluorescence yield of element i

R_i = Kα/K total intensity ratio for the ith element

Δt = target thickness.

A thick target is defined as being sufficiently thick to completely stop the proton beam. Hence, account has to

be taken of the energy loss of the proton beam in the target and the attenuation of the emitted X-ray in passing through it. Campbell (1977), in his criterion, considered that several mg/cm^2 of biological material constitutes a thick target, for 2-4 MeV protons. While Willis et al. (1977), found that for a proton energy of 3 MeV, the dividing line between thin and thick targets for biological material is about 1 mg/cm^2.

A target can be described as a thin target if the thickness of the target is such that the energy loss of the protons in traversing it is negligible, so that the X-ray production cross-section $\sigma(E)$, which is energy dependent, can be taken as that at the incident energy E_o, and negligible attenuation of X-rays is produced from the element of interest in the target matrix.

In the case of metallic targets, for example pure Fe, X-ray absorption is the dominant criterion which determines the thickness. If the emitted X-rays are attenuated in the target by several per cent, for example, 2-4%, then the thickness of the target can be calculated to be 0.125 - 0.253 mg/cm^2. If the absorption of X-rays is significant, say larger than 4%, then the target is considered a semi-thick or thick target.

Thick targets are usually easier and faster to prepare since the actual thickness is not important and the preparation procedures involve less risk of contamination. A variety of targets has been irradiated by different workers with no preparation other than mounting them on a suitable target support.

Thick target analysis by PIXE was first employed a few years after Johansson et al. (1970) demonstrated the applicability of thin target analysis. The technique for thick target analysis is fast and requires only minimal target preparation. A target, for example a thick tissue section or metallic alloy, is just mounted in a holder and irradiated directly, consequently, the risk of introducing contamination is minimised.

A study of the feasibility of applying PIXE anlaysis for the quantitative determination of trace elements in thick targets has been performed by a number of authors including Gray et al. (1973), Ahlberg and Akselsson (1975,1976), Bauer et al. (1978), Khaliquzzaman et al. (1981) and Lagarde et al. (1983).

The calculation of the elemental composition from the X-ray yield is considerably more difficult for a thick target than for a thin one, due to the following matrix effects, Khan and Crumpton (1981):

(1) Since the energy of the incident particles decreases while they traverse the target, the X-ray production cross-section does not remain constant. The proton energy varies from its maximum incident energy E_o, right down to zero when it is stopped completely in the target.

(2) The X-rays produced within the target layers are attenuated in traversing the thickness of the sample on their path to the detector.

(3) The X-rays produced by the main body of the sample, the matrix, may produce X-rays of interest by secondary fluorescence of the atoms, (enhancement effect).

The advantages and disadvantages of thin and thick targets have been discussed by a number of authors including, Johansson and Johansson (1976), Willis et al. (1977) and Campbell (1977).

To obtain the total X-ray yield from a thick target the yield from an elementary layer, given by equation (3.1) has to be integrated over the entire particle path. This requires a knowledge of the composition of the matrix as well as the distribution of the trace elements.

For thick homogeneous targets the number of characteristic Kα X-rays I_i follows from the integration of equation (3.1) over the target thickness.

$$I_i = n_i w_i R_i \int_o^t \sigma_{I,i}(X)\, dX$$

$$= n_i w_i R_i \int_{E_o}^{E_f} \sigma_{I,i}(E)/S_m(E)\, dE \qquad (3.2)$$

Since the energy of the bombarding particle decreases as it penetrates the target, equation (3.2) is more conveniently expressed in terms of energy rather than that of the thickness, where

X = penetration depth in the target

t = path length in the target

dE = differential energy loss

E_o = incident proton energy

E_f = final proton energy

The matrix absorption of characteristic Kα X-rays in the target (self absorption)can be accounted for by the introduction of a transmission factor T_2 in equation (3.2). The number of characteristic Kα-X-rays emanating from an element i, transmitted in the direction of the detector is given by;

$$I_i = n_i w_i R_i \int_{E_o}^{E_f} \frac{\sigma_{I,i}(E) . T_2(E)}{S_m(E)} dE \quad \text{photon/proton} \qquad (3.3)$$

where $T_2(E) = \exp(-\mu_{m,s} . \rho . y)$, is the transmission of X-rays out of the target at depth y with a mass attenuation coefficient of the target of $\mu_{m,s}$ and a density of ρ.

The path length y along which the X-rays emerge before detection clearly depends on the angle of observation, as shown in Figure (3.1) , where the path length y can be calculated from the following equation, $y = \frac{\cos\theta}{\cos\phi} X$, and X can be calculated from the range equation of the proton beam, $X = \int_{E_o}^{E_f} \frac{dE}{S_m(E)}$. If the detector is positioned at an angle of a specular reflection to the beam then $\theta=\phi$ and y can be replaced by X. In the present experimental arrangement θ and ϕ were chosen as 45^o.

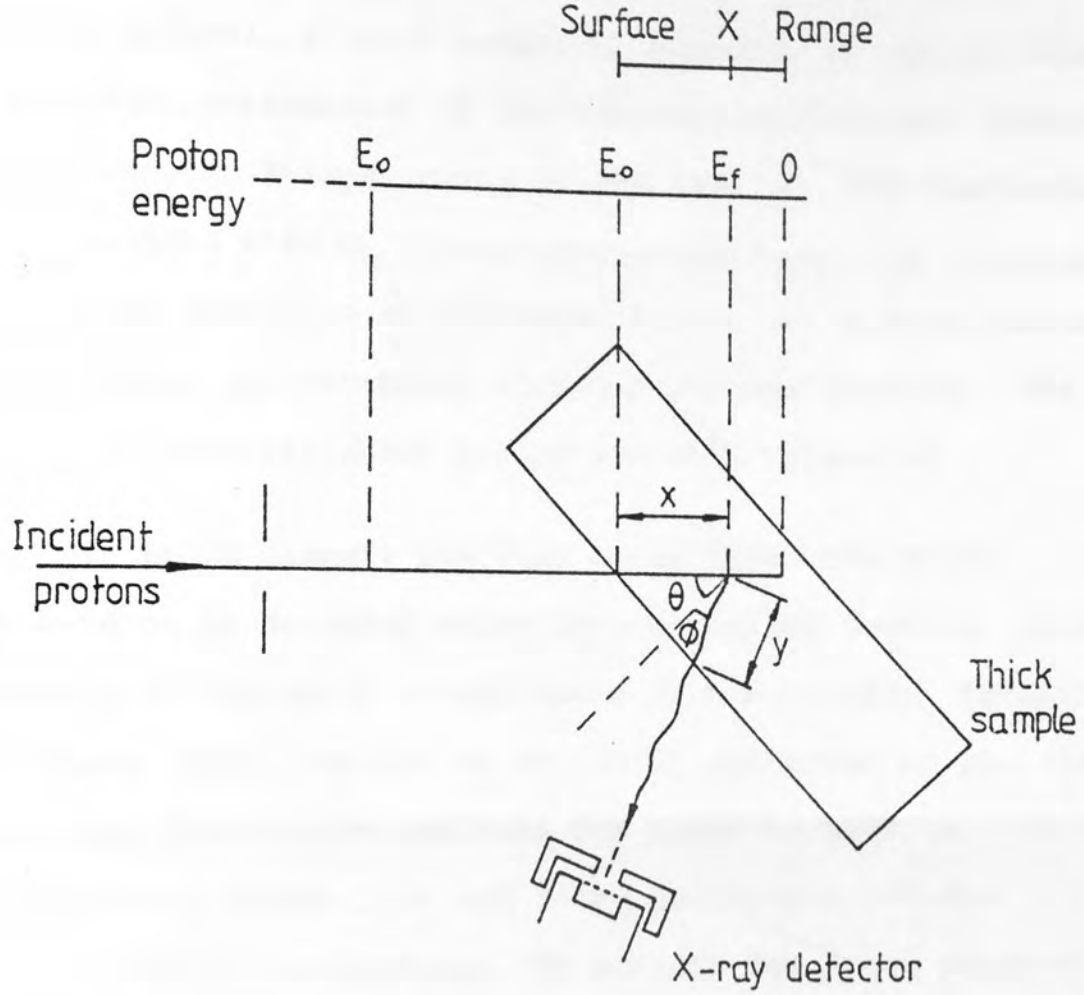

Figure (3.1) Schematic diagram of thick target irradiation.

3.3 QUANTITATIVE ANALYSIS OF THICK TARGETS BY PIXE

In general, a thick target is regarded as one in which significant attenuation of the incident protons and absorption of the emitted X-rays occurs in the sample. When bombarding thick targets with an accelerated proton beam, the continuous background radiation of scattered X-rays and bremsstrahlung from protons and secondary eletrons becomes intense. The yields of characteristic X-rays are also increased.

For trace element analysis using PIXE, the trace elements to be detected exist in a so called "matrix" which consists of the major constituents of the target. Patnaik and Dhere (1975), Willis et al (1977) and Raith et al. (1981) described quantitative analysis for thick targets in which proton energy loss and X-ray absorption effects (matrix effect) are severe. To account for X-ray absorption and the decrease in the cross-section due to the slowing down of the protons in the sample, the mass absorption coefficient and the stopping power of this matrix have to be known. The composition of the matrix can often be determined well enough for the stopping power and mass absorption coefficient for the matrix to be calculated as weighted averages of the values for the major elements, (See Section 2.5).

The area $I_{xi}(E)$ under the Kα X-ray peak corresponding to the ith element in the accumulated X-ray spectrum is given by:

$$I_{x_i}(E_o) = \varepsilon_{\alpha_i} \frac{d\Omega}{4\pi} T_1 \left[n_i w_i R_i N_p \int_{E_o}^{E_f} \frac{\sigma_{I,i}(E) T_2(E)}{S_m(E)} dE \right.$$

$$\left. + \text{secondary production} \right] \qquad (3.4)$$

where

ε_{α_i} = the efficiency of the detector for the Kα radiation of the ith element;

$d\Omega$ = the detector solid angle;

T_1 = $\exp(-\mu_{ij} t_j)$ is the attenuation of the Kα X-rays of the ith element in the ith absorber of thickness t_j, between the target and detector;

N_p = the number of incident protons with energy E_o.

Raith et al. (1981) evaluated the actual concentrations from measured X-ray spectra of thick targets by assuming the target to consist of thin layers so that the X-ray yields could be computed numerically, One problem with such calculations is the accuracy of the ionization cross-section data used in the calculations. The analysis of a standardised aluminium disk, using their computer programme, tended to give results 30% lower than the recommended composition values. Raith et al. (1981) have suggested that these errors are mainly due to systematic errors and the uncertainties of the data used for the calculations.

These authors, including Shabason et al. (1973), presented a quantitative calculation for thick targets considering primary X-ray production only. Their procedure will yield a satisfactory quantitative estimate for the composition of

the target only when the enhanced X-ray yields due to secondary excitation processes is negligible. Willis et al. (1977), have discussed the disadvantages associated with thick target analysis due to any inhomogeneties within the target, coupled with the small quantity of the material sampled by the proton beam and the difficulty in determining the quantitative yield correction factor.

A smooth sample surface must also be considered. Ahlberg and Akselsson (1976) discussed the importance of a smooth surface and estimated the effect of roughness on proton induced X-ray yields from teeth by use of a sawtooth model of the tooth surface. These calculations showed that a 4 mg/cm^2 (13 μm) matrix height difference gave less than a 5% decrease in the X-ray yield for X-ray energies above 2 keV. Recently, Cookson and Campbell (1983) presented a detailed calculation to illustrate the effect of surface defects on proton induced X-ray yields for representative combination of trace X-ray emitters homogeneously distributed in thick targets. These authors demonstrated that the X-ray yields from triangular grooves and ridges, as two types of surface defects, relative to flat surface yields are similar but have opposite results. Cookson and Campbell also demonstrated graphically the strong gain or loss of yields due to the defect angle-dependence for an iron matrix with a groove 10 μm deep as the groove angle α varied between 20° and 80°.

3.4 MATRIX EFFECTS

In thick targets, the decrease in ionization cross-section due to the slowing down of particles in the sample and the increased absorption of the X-rays generated inside the sample have been considered (given in equation (3.3)). So far, the secondary X-ray yield production due to matrix effects have been neglected in equation (3.3). Ahlberg and Akselsson (1976) have indicated that the enhancement effect is most important for elements with an absorption edge just below an intense X-ray line from a major element, and that the enhancement effect for PIXE anlaysis is less than that for X-ray induced X-ray analysis. This is because the cross-section for proton induced X-ray production is a decreasing function of the absorption edge energy and the cross-section for X-ray induced X-ray production is an increasing function of the same parameter as long as the energy of primary X-ray is higher than the energy of the absorption edge.

Ahlberg (1977) discusses the enhancement in proton induced X-ray emission anlaysis (PIXE) due to secondary excitation by bremsstrahlung, secondary electron, target-target collisions leading to ionization, Auger electron and primary induced X-rays. He concludes that the only sources of importance for secondary excitation is primary induced X-rays. Ahlberg (1977) investigated the enhancement effect as a function of proton energy and sample thickness for the Mn and Cr in the National Bureau of Standards steel

sample, SRU 1261 and obtained a satisfactory agreement between experimental results after correction for enhancement and the NBS values. His findings show a 95% agreement between the experimental results obtained from an NBS standard steel sample and the calculated values.

Van der Kam et al. (1977) have presented theoretical calculations to correct measured K-X-ray intensities for matrix effects. The results of their calculations on X-ray induced X-ray fluorescence are in agreement with the results from Ahlberg (1977).

The calculation of the secondary X-ray production correction is important only when a number of elements are present in the matrix, where the enhancement of the X-ray production of an element A by the radiation of an element B in the target has to be included. This secondary X-ray production process can only occur provided that the energy of the exciting radiation of element B is higher than the absorption edge energy of the particular shell level of element A, as shown in Figure (3.2). For example, in the case of 2 MeV protons incident on a 99.5% Ni/ 0.5% Fe alloy, the primary induced Ni Kα X-rays have an energy of 7.47 keV, which is slightly larger than the K absorption edge of iron at 7.111 keV. In this case, the probability that the 0.5% Fe is exposed to the Ni K X-rays in the sample and produces iron X-rays is high. Thus, the iron X-rays so produced may account for 55% of the total iron X-ray yield, Reuter et al. (1975).

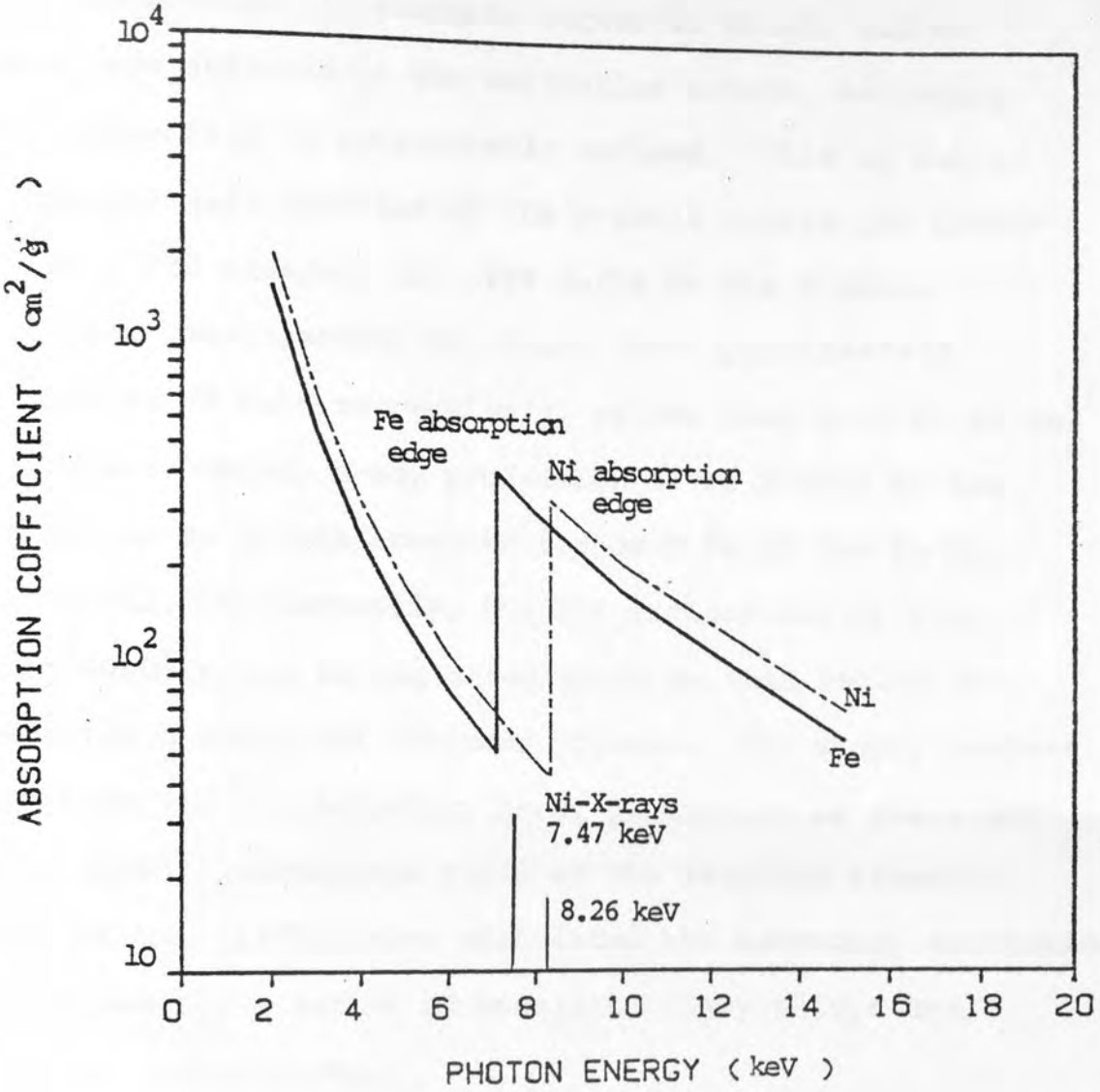

Figure (3.2) Photon absorption cross-section for Fe and Ni as a function of photon energy.

Conversely, if elements higher in atomic number than N_i are selected as the excitation source, secondary X-ray production is considerably reduced. This is due to the considerable decrease of the K-shell ionization cross-section. For example, in 99% Ge/1% Fe the K-shell ionization cross-section decreases from approximately 135 barn to 35 barn respectively, as one goes from Ni to Ge. Therefore, secondary X-ray production of Fe X-rays by the 9.88 keV Ge Kα X-rays accounts for only 8% of the Fe Kα X-ray yield. Consequently, the K→K excitations of high atomic numbers can be neglected since in this region L-ionization becomes the favoured process. For atomic numbers lower than Fe, the secondary X-ray production is small due to the small fluorescence yield of the exciting element. Reuter et al. (1975), have calculated the secondary excitation corrections for a series of metallic binary alloys and radiation combinations.

These authors have presented a detailed formulation for calculating the enhancement factor which is closely related to that employed in electron microprobe anlaysis. An accuracy of ±5% to the experimental data taken for two binary alloys has been achieved by those workers if the secondary X-ray production correction factor is appropriately applied and if the effect of the composite matrix on the stopping power is included.

Calculations throughout the work are restricted to the K→K excitation with the energy of the exciting radiation

of element B slightly above the absorption edge energy of the excited shell level of element A, because up to 40% of the total X-ray production of element A could be due to the enhancement effect, Reuter et al. (1975). The enhancement effect has also been investigated by Mommsen et al. (1979) for high energy projectiles such as 30 MeV α-particles. Theoretically dependent on X-ray energies, the elemental abundances, target thickness, and projectile energy is discussed, and it is concluded that the enhancement correction can not be neglected at low elemental abundances of elements, whose absorption edges are just below the energy of the exciting radiation of the main matrix element. Therefore, the enhancement effect has to be included in the basic calculation of the primary X-ray production originating from elements present in large amounts.

The formulation which is used in the present work for primary and secondary X-ray production is discussed in the following sections, and it can be applied to the quantitative analysis of any multi-element target assuming a homogeneous distribution of all constituents over the projectile range.

3.5 THICK TARGET FORMALISM

The thick target formulation and the correction schemes for secondary excitation processes in this section are based on the following assumptions:

(1) The target composition is homogeneous.

(2) The stopping power of the complex target is given by the weighted average of the stopping powers of the constituents, (Chapter 2, section 2.5). The effective mass attenuation coefficient for the matrix for a particular X-radiation can be obtained in a similar manner.

(3) The decrease of proton energy in the target can be treated stepwise.

(4) The excitation cross-section is given by an appropriate empirical polynomial (Chapter 2, section 2.4).

(5) The fluorescence yields W_i and relative intensity ratios R_i are well known.

(6) The isotropic emission of primary and secondary X-rays is known, Folkmann et al., (1974a).

(7) The primary induced X-rays are considered as the only source of importance for secondary excitation, Ahlberg (1977).

(8) The target is at an angle of 45^{o} with the beam and detector axis.

3.5.1 Direct X-Ray Production

Consider a uniform composite target of mass density ρ consisting of elements with atomic numbers Z_A and Z_B, atomic weights a_A and a_B, and weight fraction C_A and C_B. The number of atoms of type A per unit volume n_A is $(C_A \frac{N_o \rho}{a_A})$, where N_o is Avogadro's number.

The number of Kα-X-rays, ΔI_A per incident proton of element A in an elementary layer corresponding to the proton energy interval E to E-ΔE, Figure (3.3), is given by

$$\Delta I_A = n_A W_A R_A \sigma_{I,A}(E - \frac{\Delta E}{2}) \frac{\Delta E}{S_m(E)} \text{ photon/proton} \qquad (3.5)$$

where W_A = K-shell fluorescence yield of element A;

R_A = fraction of Kα in the K series of element A, (i.e. $K\alpha/K_{TOT}$ intensity ratio);

$\sigma_{I,A}$ = ionization cross-section at proton energy E-ΔE/2, (i.e. at the centre of the elementary layer).

$S_m(E)$ = stopping power of a composite target which is represented by the weighted average of the stopping power of all constituents.

From equation (3.5), the number of primary Kα-X-ray $I_{A,pri}$ due to proton excitation from an element A which are generated in the target and registered by the detector can be expressed as follows:

$$I_{A,pri} = C \int_{E_o}^{E_f} \frac{\sigma_{I,A}(E - \frac{\Delta E}{2})}{S_m(E)} T_2(E)\, dE \qquad (3.6)$$

where $C = n_A \frac{d\Omega}{4\pi} \varepsilon_A W_A R_A T_1$ for a given energy condition and element. The subscript pri refers to the primary X-ray production.

The expression in equation (3.6) has been coded into a computer programme. The calculation of the K-shell ionization

cross-section in the programme by any of three expressions, i.e. polynomial of Johansson and Johansson (1976), polynomial of Khan et al. (1977) and the fitted polynomial of Reuter et al. (1975) to the tabulation of Garcia et al. (1973), as discussed in Chapter 2 (section 2.4) could be employed. The proton stopping powers used in the calculation were obtained with the Anderson and Zeigler (1977) formula, while the mass attenuation coefficients used were obtained from the tables of Montenegro et al. (1978).

The integral of equation (3.6) represents the K-X-ray production over the entire particle path. These X-rays can be assumed to be emitted isotropically, Folkmann et al. (1974a).

For computer calculations, the target is represented by a set of thin layers of variable thicknesses, ΔX, parallel to the surface corresponding to a constant energy loss ΔE of the incident beam as shown in Figure (3.3). The slices are chosen thin enough so that the particle energy and the X-ray production cross-section may be taken as that at the energy $(E - \frac{\Delta E}{2})$ of each layer.

The thickness of each layer of a fixed energy loss ΔE is defined as the distance traversed by the ion in the target being slowed down from energy E_p to $E_p - \Delta E$, and can be calculated from the stopping power $S_m(E)$ for projectiles of energy $(E - \frac{\Delta E}{2})$ using the assumption

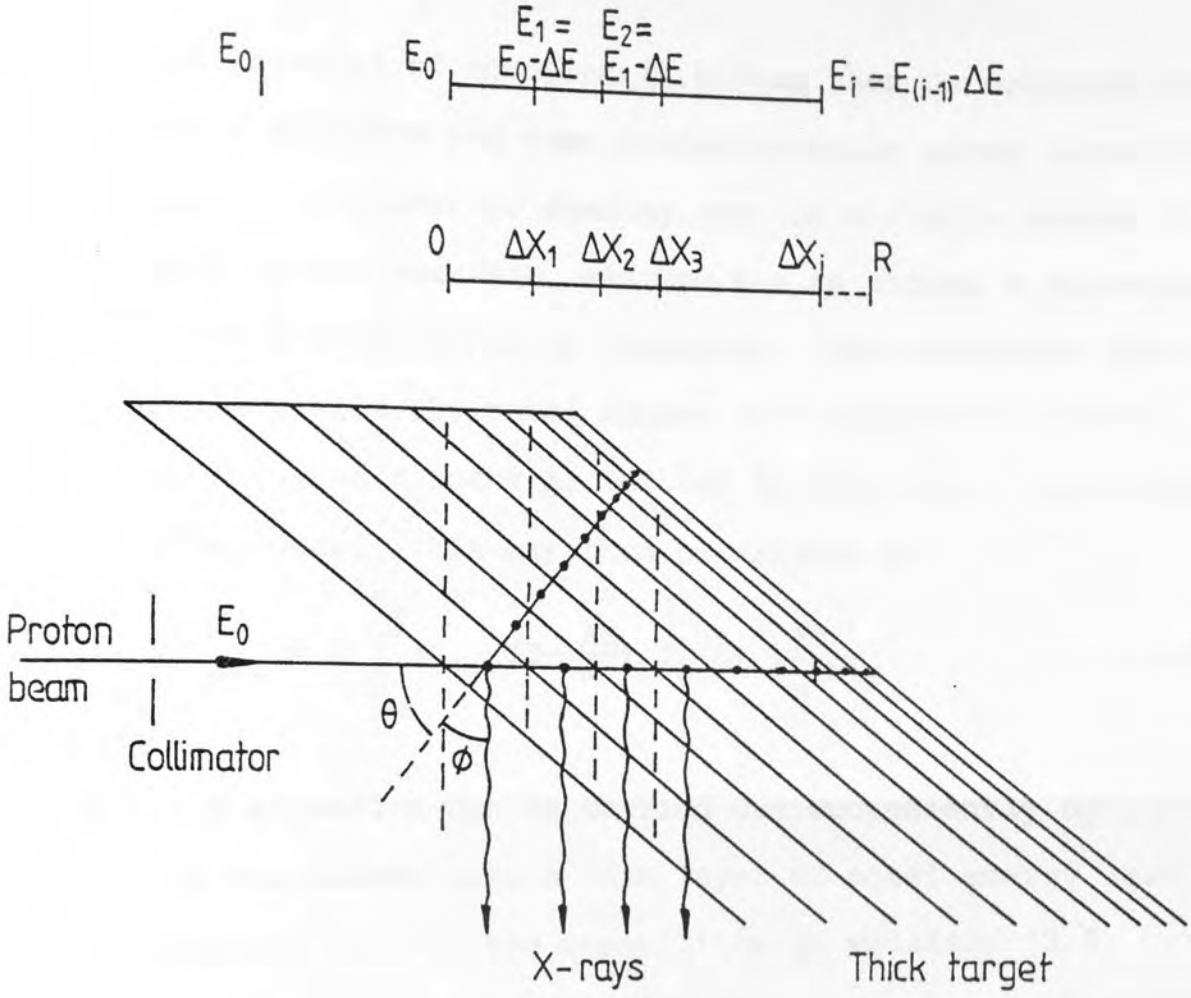

Figure (3.3) Primary X-ray production in target layers under ion bombardment.

$$\Delta X = \frac{\Delta E}{S_m(E)} \qquad (3.7)$$

The integral of equation (3.6) can then be obtained in terms of a discrete sum over infinitesimally close intervals of energy. In practice, summing over an infinite number of intervals is not possible, and one has to choose a reasonably large, but finite number of intervals. The summation over all slices yields the total number of K X-rays (Kα or Kβ) originating from element A, emitted by the target and detected by the detector. This may then be written as

$$I_{A,pri} = C \sum_{E_o}^{E_f} (\sigma_{I,A}(E - \frac{\Delta E}{2})\ T_2(E)\ \frac{\Delta E}{S_m(E)} \qquad (3.8)$$

where the summation can be carried out conveniently by dividing the target into a thin layer of equal energy loss ΔE intervals. Of all the quantitites in equation (3.8) only $\sigma_{I,A}(E - \frac{\Delta E}{2})$, $T_2(E)$ and $S_m(E)$ are a function of the ion energy E_p and can be readily computed on a small computer assuming the energy loss ΔE to be 0.05 MeV. The choice of smaller energy loss values increases the computer processing time considerably, but does not improve the results. The interval of 0.05 MeV was chosen as the interval over which the rate of energy loss may be assumed to be constant and the cross-section may be interpolated linearly.

$I_{A,pri}$ can then be obtained directly by computation.

3.5.2 Secondary Production

The intensity of the characteristic radiation of element A in a homogeneous composite target may be enhanced by secondary excitation from the X-radiation of the matrix element B in the target. As discussed earlier, this effect is favoured under certain conditions.

The primary production $\Delta I_B(i)$ of the exciting Kα-radiation of element B with energy $E_{X,B}$ in an elementary layer (i) in the target per proton corresponding to the energy interval E(i) to E(i)-ΔE of the incident beam is given by:

$$\Delta I_B(i) = n_B \, \sigma_{I,B}(E(i) - \frac{\Delta E}{2}) \, W_B \, R_B \, \frac{\Delta E}{S_m(E(i) - \frac{\Delta E}{2})} \qquad (3.9)$$

where n_B = the number of atoms of element type B/unit vol.

W_B = K-shell fluorescence yield of element B;

R_B = $K\alpha/K_{total}$ intensity ratio for the element B;

$\sigma_{I,B}$ = ionization cross-section of proton energy $E(i) - \frac{\Delta E}{2}$;

$S_m(E(i))$ = stopping power of the composite target at proton energy $E(i) - \frac{\Delta E}{2}$.

The attenuation of this primary radiation inside the matrix in the X-ray energy region is mainly attributed to the photo-electric effect leading to photoelectrons and to excited atoms. After the absorption, the excited atoms of interest, e.g. element A, will emit secondary characteristic X-rays according to the known fluorescence yield.

This radiation of intensity $\Delta I_B(i)$ is assumed to be a point source located at the centre of each layer $\Delta X(=2r_i)$ see Figure (3.4), and is absorbed in the target layers by a mechanism independent of its position in the plane of that layer as long as the beam size is small in comparison to the dimensions of the target. The fraction of $\Delta I_B(i)$ radiation from each point source at the centre of each layer is either being:

(1) absorbed in the same layer; or being

(2) transmitted and absorbed by other layers below and above it.

In the first instance, the point source has been assumed at the centre of a layer of thickness $(2r_i)$, and the point source radiation $\Delta I_B(i)$ is assumed to be isotropically emitted, Folkmann et al. (1974a). The fraction of $\Delta I_B(i)$ included between two cones of half angles is shown in Figure (3.4) as β and $\beta + d\beta$ and is given by

$$\frac{d\Omega}{4\pi} = \frac{A/r^2}{4\pi} = 2\pi r \sin\beta \frac{r d\beta}{4\pi r^2} = \frac{1}{2} \sin\beta \, d\beta \qquad (3.10)$$

where r is the height of the cone; and A is the area of the layer included between the two cones.

Therefore, a fraction of the total radiation $F_1(i)$ being absorbed in an elementary layer i due to the point source $\Delta I_B(i)$ located at the centre of the same layer of $2r_i$ thickness below the surface is given by:

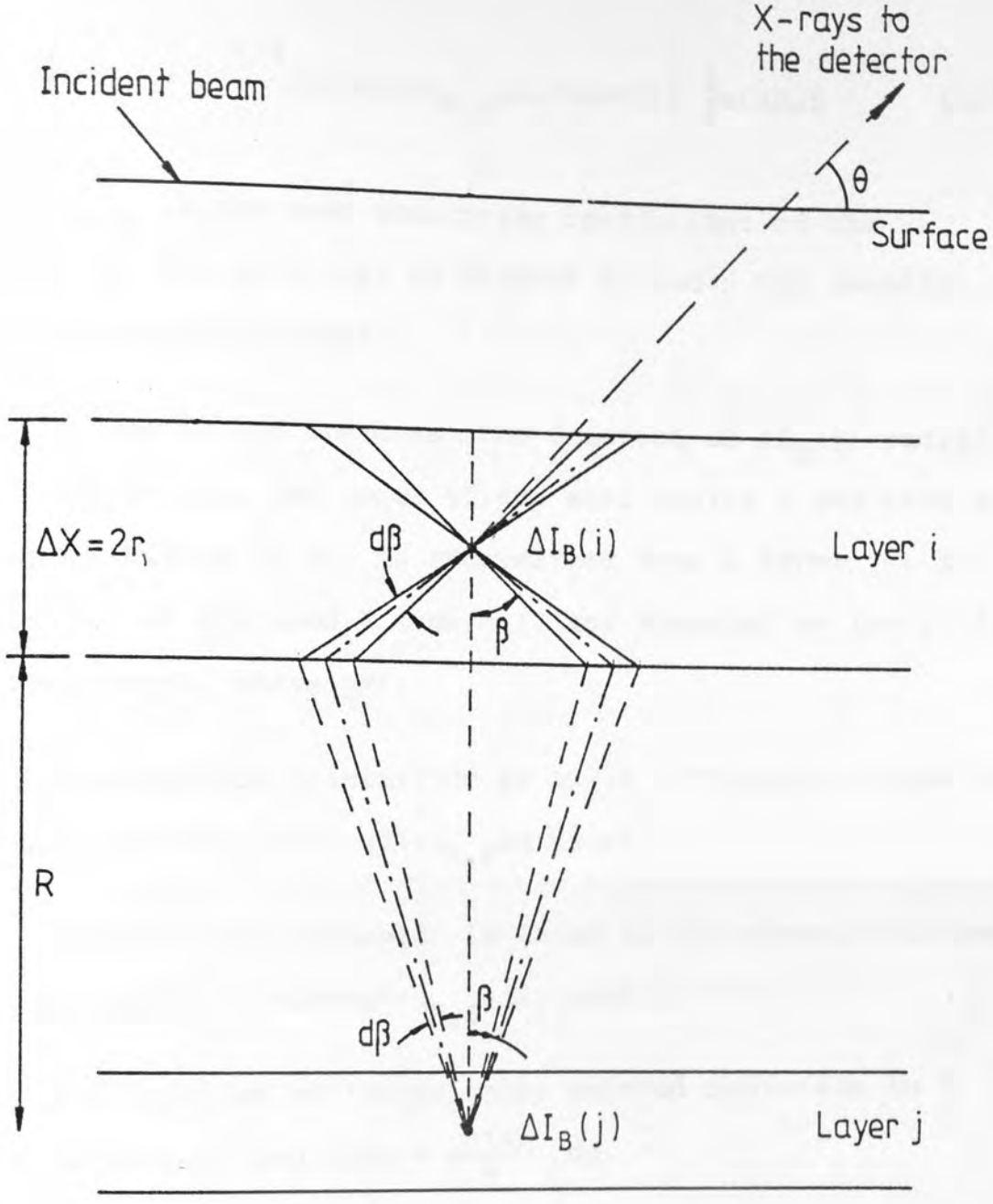

Figure (3.4) Geometry used for calculation of the secondary X-ray yield.

$$F_1(i) = 2\int_0^{\pi/2} |1-\exp(-\mu_{B,S}\cdot\rho.r.\sec\beta)| \frac{1}{2}\sin\beta d\beta \qquad (3.11)$$

where $\mu_{B,S}$ is the mass absorption coefficient of the target (S) for Kα-X-rays of element B; and ρ the density of the composite target.

In the second instance, the fraction of $\Delta I_B(j)$ radiation included between two cones of the semi angles β and β+dβ as shown in Figure (3.4), is transmitted from a layer (j) to a layer (i) at distance R from (j), and absorbed by layer (i) is considered, where $j \neq i$:

The fraction transmitted at angle β through a layer of normal thickness R = $\exp(-\mu_{B,S}\rho R \sec\beta)$.

The fraction absorbed in layer (i) of normal thickness ΔX_i at angle β = $(1-\exp(-\mu_{B,S}\rho\Delta X_i \sec\beta))$.

The fraction of isotropically emitted radiation in a cone between β and β+dβ = $\frac{\sin\beta}{2}$ dβ.

The total fraction of radiation, $F_2(j)$ absorbed in layer (i) integrated over all possible β can be written as

$$F_2(j) = \int_0^{\pi/2} \exp(-\mu_{B,S}\rho\ R \sec\beta).|1-\exp(-\mu_{B,S}\rho\Delta X_i \sec\beta|.$$

$$\frac{1}{2}\sin\beta\ d\beta \qquad (3.12)$$

The fraction of the radiation which is absorbed by the element A is

$$D_1 = C_A \mu_{B,A} / \mu_{B,S} \qquad (3.13)$$

where $\mu_{B,A}$ is the mass absorption coefficient of target element A for the Kα radiation of element B. The fraction $D_2 = \frac{\gamma_A - 1}{\gamma_A}$ of the intensity of this radiation is absorbed by the K-shell ionization of atoms A, with subsequent emission of $(W_A . R_A)$ Kα photon of element A, where γ_A is the K-absorption edge jump ratio of element A, i.e. the ratio of the mass absorption coefficient of the exciting radiation in the excited element just before and just after its absorption edge. The term $\frac{\gamma_A - 1}{\gamma_A}$ is virtually constant over a range of atomic numbers for which fluorescence is appreciable and for K→K and L→K fluorescence Reeds (1965) values of 0.88 were adopted.

The total secondary production of Kα-radiation of element A in the sample under irradiation of each primary point source of element B at the centre of each layer is given by

$$\Delta I_{A,sec(i)} = D_1 D_2 W_A R_A \sum_{i=1}^{N} \left| \Delta I_B(i) . F_1(i) + \sum_{j \neq i}^{N} \Delta I_B . F_2(j) \right| \qquad (3.14)$$

where the first term in equation (3.14) represents the secondary excitation of element A in each ith layer of ΔX thickness by its primary point source of element B in that layer, and where the second term accounts for the secondary excitation of the element A in the ith layer by the primary

source points of element B in all other layers.

Equation (3.14) is obtained in terms of a discrete sum over the finite number N of energy intervals. The summation extends from incident proton energy E_o down to 25 keV by using step of ΔE of 50 keV. $F_1(i)$ and $F_2(j)$ can be evaluated by using the exponential integral (see Appendix A).

The primary production $\Delta I_B(i)$ of the exciting Kα radiation of element B is evaluated numerically in steps of ΔE.

The fraction of the total secondary production of the Kα-radiation of element A, i.e. those which emerge from the target in the direction of the detector corrected for the target attenuation $T_2(i)$ is given by:

$$I_{A,sec} = C. \sum_{i=1}^{N} \left| (\Delta I_B(i).F_1(i) + \sum_{j \neq i}^{N} \Delta I_B(j)\ F_2(j)) * T_2(i) \right| \qquad (3.15)$$

where

$C = \frac{d\Omega}{4\pi}\ \varepsilon D_1 D_2\ W_A R_A$ = constant

$T_2(i)$ = the attenuation of the Kα X-rays of element A in the matrix emerging along a path length y from the centre of each layer.

Thus, the ratio of X-rays from element A due to excitation of X-rays from element B, $I_{A,sec}$, and the number of X-rays from element A due to primary excitation from protons, $I_{A,pri}$

is known as the enhancement caused by an element B on an element A and is given by

$$E_{n(B,A)} = \frac{I_{A,sec}}{I_{A,pri}} \qquad (3.16)$$

Therefore, the total Kα yield of element A due to primary production and secondary production can be calculated. Finally, the ratio of the total Kα X-ray yield of element A to that of element B can be determined. This is corrected for the solid angle, the absorption of the emitted radiation along its path to the detector and the efficiency ε of the detector.

3.6 ENHANCEMENT DETERMINATION

A large number of computer codes have been written in recent years to evaluate the characteristic X-ray yields and the enhancement due to matrix effects from thick targets bombarded by protons, following Reuter et al. (1975).

In the present work, a computer programme has been developed to evaluate the characteristic X-ray yield from thick metallic alloys bombarded by protons based on the previous formulations (section 3.5).

This programme was written in BASIC to be run on a PET 8043, with a 32k memory. The programme is listed in Appendix B.

The programme uses cross-sections and stopping powers

calculated from polynomial fits as discussed in Chapter 2 section 2.4 and 2.5. Input includes the incident proton energy E_o and lowest energy E_f of proton for X-ray production, and the fixed energy loss ΔE which is used together with the stopping power $S_m(E)$ to find the thickness of each layer ΔX. For flexibility, the coefficients A_i and B_i used in the stopping power equations for elements A and B respectively, are input at the beginning. The input also includes the binding energies B_A and B_B of the atoms in the composite target, the absorption coefficients $\mu_{A,i}$ and $\mu_{B,i}$ for the relevant characteristic X-rays, which is used with a logarithmic interpolation procedure to obtain the attenuation for any given X-ray energy; the concentrations of C_A and C_B; the densities ρ_A and ρ_B; the K-shell fluorescent yields W_A and W_B; and the atomic weights A_A and A_B of element A and B present in the target respectively. The detector efficiency data were also stored in the programme. After input, the calculation follows the scheme previously described without further intervention.

Reuter et al. (1975) uses constant thickness layers to evaluate an integral expression for secondary yields.

The present programme uses constant proton energy loss layers that decrease in thickness with decreasing proton energy. Instead of deriving integrals, the yield is calculated via a series of summations involving primary and secondary production in each layer. Adequate accuracy is obtained by the use of small energy steps. A simplified flow chart of the programme is shown in the following chart diagram.

Simplified flow chart for x-ray yield and matrix effect evaluation programme.

Flow chart symbols	Meaning
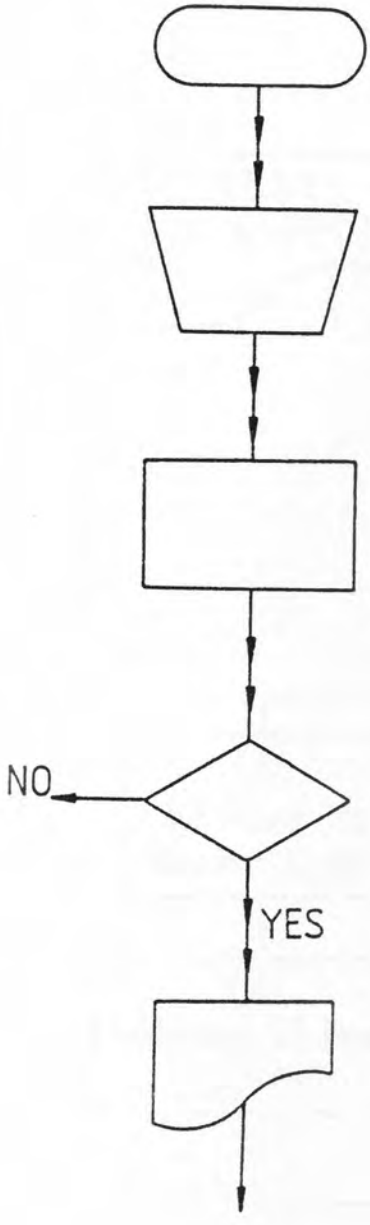	Beginning and end of the flow chart.
	Input
	Calculation
	Decision
	Print

The arrowed line indicates the order in which the various actions are to be carried out.

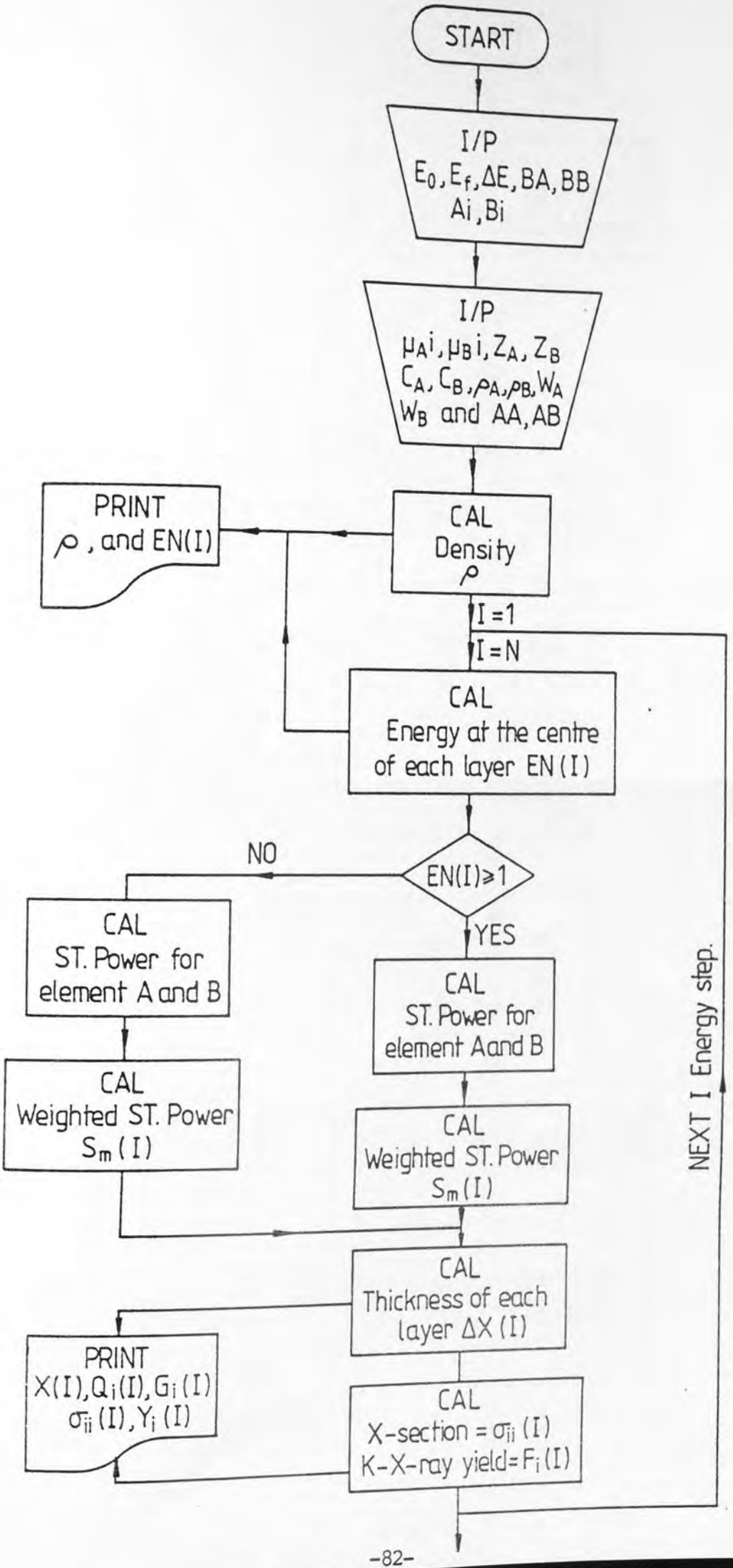
START
I/P
$E_0, E_f, \Delta E$, BA, BB
Ai, Bi
I/P
$\mu_A i, \mu_B i, Z_A, Z_B$
$C_A, C_B, \rho_A, \rho_B, W_A$
W_B and AA, AB
CAL
Density
ρ
PRINT
ρ, and EN(I)
I = 1
I = N
CAL
Energy at the centre
of each layer EN(I)
EN(I)≥1
NO
YES
CAL
ST. Power for
element A and B
CAL
ST. Power for
element A and B
CAL
Weighted ST. Power
$S_m(I)$
CAL
Weighted ST. Power
$S_m(I)$
NEXT I Energy step.
CAL
Thickness of each
layer $\Delta X(I)$
PRINT
$X(I), Q_i(I), G_i(I)$
$\sigma_{ii}(I), Y_i(I)$
CAL
X-section = $\sigma_{ii}(I)$
K-X-ray yield = $F_i(I)$

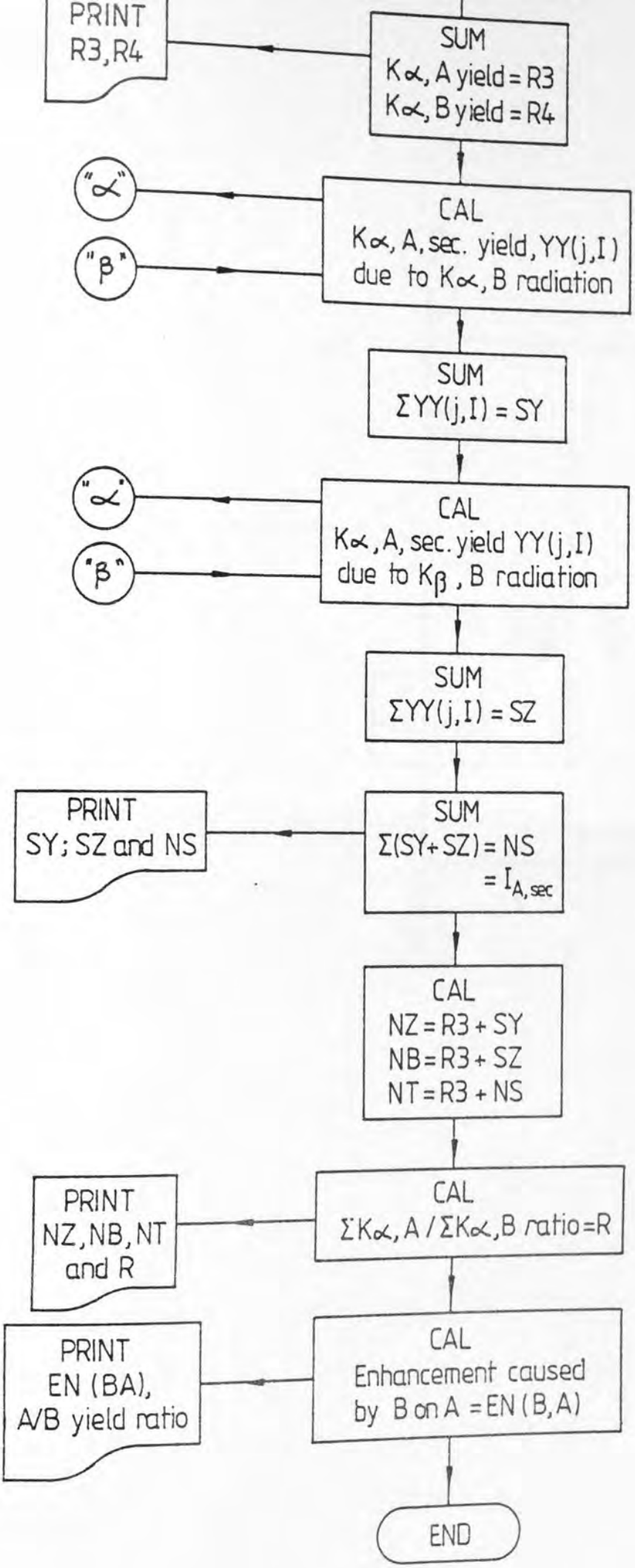
PRINT
R3, R4
SUM
Kα, A yield = R3
Kα, B yield = R4
"α"
"β"
CAL
Kα, A, sec. yield, YY(j,I)
due to Kα, B radiation
SUM
ΣYY(j,I) = SY
"α"
"β"
CAL
Kα, A, sec. yield YY(j,I)
due to Kβ, B radiation
SUM
ΣYY(j,I) = SZ
PRINT
SY; SZ and NS
SUM
Σ(SY+SZ) = NS
= I A, sec
CAL
NZ = R3 + SY
NB = R3 + SZ
NT = R3 + NS
PRINT
NZ, NB, NT
and R
CAL
ΣKα, A / ΣKα, B ratio = R
PRINT
EN (BA),
A/B yield ratio
CAL
Enhancement caused
by B on A = EN (B,A)
END

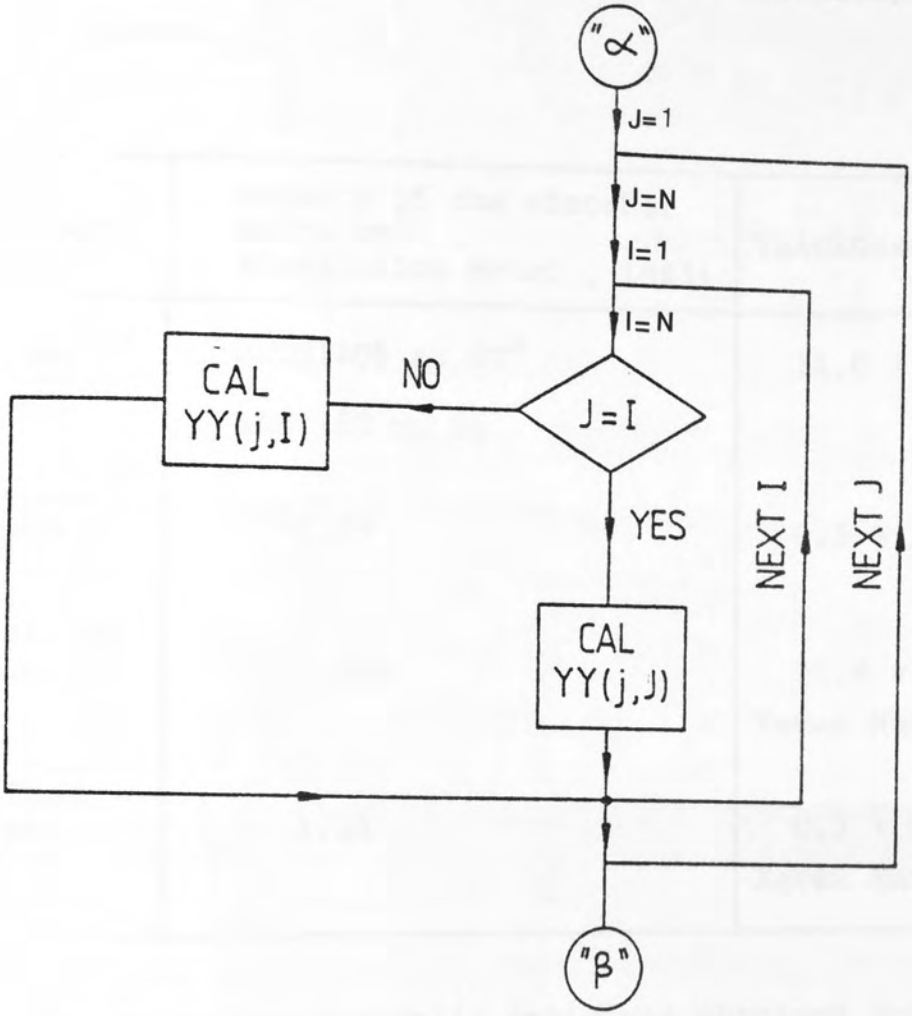
"α"
J=1
J=N
I=1
I=N
CAL
YY(j,I)
NO
J=I
YES
NEXT I
NEXT J
CAL
YY(j,J)
"β"

The data used to correct the attenuation of the Kα-X-rays of elements A and B between target and detector was as follows:

Absorber	Density of the absorber in gm/cm^3 (Goodfellow Metal , 1983)	Thickness in cm
Air Gap	0.001205 at 20^o and 760 mm Hg	11.0 ± 0.05
Melenex Window	1.39	0.5×10^{-2}
Beryllium Window	1.848	12.4×10^{-4} Kevex Manual (1975)
Silicon Crystal	2.33	0.3 ± 0.05 cm Kevex Manual (1975)

The value for the solid angle was obtained from the equation

$$\Omega = \frac{\text{Area of detector } (A_d)}{r^2}$$

where r is the detector to target distance. The diameter of the lead aperture placed in front of the Be window of the detector was accurately measured to give the value for A_d. The values used for A_d and r are,

A_d = 0.1238 cm ± 0.005

r = 11 cm ± 0.05.

hence,

$$\Omega = (1.023 \pm .014) \times 10^{-3} \quad \text{steradians}$$

assuming that the intrinsic efficiency ε is one for E_X less than 10 keV down to 4 keV.

The programme prints out the weighted average stopping power, $S_m(I)$, the thickness of each layer ΔX; and the correction factor. The ionization cross-section and the yield for element A and B respectively. These have been printed out over each step of a fixed energy loss ΔE. The programme also prints out the total $K\alpha$ secondary yield of element A due to $K\alpha$ and $K\beta$ X-radiation of element B. Finally, the programme calculates the total $K\alpha$,A to $K\alpha$,B yield ratio which in turn can be compared with the experimental observations.

The computer programme used approximately 8k of memory which adequately held and performed all these calculations in a running time of approximately 25 minutes.

3.7 DATA BASE STUDIES

3.7.1 Validation of the Present Computer Calculations

After presenting the method of calculating the X-ray yields of a composite target with inclusion of the enhancement effect, verification of the present computer calculations was needed. This was achieved by comparing the present work with the published data of Reuter et al. (1975).

The computer programme was modified according to the experimental arrangement of Reuter et al. (1975) so that direct comparison could be made. The incident beam on the target was set to 90^{o}, instead of the 45^{o} employed in the present work, and the emitted X-rays from the target were observed at an angle of 52.5^{o}. This modified programme was then employed to calculate the enhancement factor for Fe in Fe-Ni alloys bombarded by 2 MeV protons. This combination of alloy was chosen because the nickel photons have an energy just above the critical excitation edge energy of Fe , resulting in a large secondary excitation. Thus, the magnitude of the enhancement factor for different concentrations of Fe could be demonstrated.

It should be noted that Reuter et al. (1975) do not give any reference or data for the mass attenuation coefficient employed in their calculations. The present work employs the data of Montenegro et al. (1978); these data were obtained by fitting a third degree polynomial to the compilation of Storm and Israel (1970). This data has been generally used by the majority of workers in the field. The formulae of Reuter et al. (1975) were employed for the ionization cross-sections and stopping power.

In the present calculations, the target is divided into thin parallel layers of varying thicknesses, ΔX, corresponding to a constant energy loss of the incident beam in the sample rather than dividing the target into layers of equal thicknesses,

which is the approach adopted by Reuter et al. (1975).

The energy loss interval ΔE was chosen to be small enough so that the thickness of the corresponding layer was thin. The production of K X-rays by protons at the centre of each layer was calculated, as was the absorption of these X-rays on their way out of the target, as well as the influence of all other layers on that particular one. Calculations were performed for eight different concentrations of Fe and Ni.

To show the magnitude of the enhancement of Fe Kα intensity in the presence of Ni, the results of the computations for Fe-concentrations ranging from $0.5\% \lesssim C_{Fe} \lesssim 80\%$, bombarded by 2 MeV protons, are illustrated in Table (3.1).

At low Fe-concentrations, i.e. up to 10%, the present calculations tend to give results systematically higher than Reuter's calculations by approximately 10%. Above 10% Fe-concentrations, the present results are higher by up to 16% compared with Reuter'S results. A graphical comparison of the percentage enhancement factor of the present results and Reuter's results for Fe-content in the Fe/Ni alloy bombarded with 2 MeV protons is shown in Figure (3.5).

It is clear from Figure (3.5) that the results of the present calculations follow the same trend as Reuter's, but are systematically higher in magnitude.

C_{Fe} (wt %)	C_{Ni} (wt %)	Enhancement Factor = $(I_{sec,Fe}/I_{pri,Fe})$		Percentage Difference
		Reuter et al.(1975) (For normal beam)	Present work (For normal beam)	
0.50	99.5	0.55	0.60	9
1.0	99.0	0.54	0.59	9
2.5	97.5	0.51	0.56	9
5.0	95.0	0.46	0.51	10
10.0	90.0	0.39	0.43	10
20.0	80.0	0.28	0.32	13
40.0	60.0	0.16	0.18	12
80.0	20.0	0.034	0.040	16

Table (3.1) Comparison of the enhancement factor in the present calculations with illustrative calculations of Reuter et al. (1975) for Fe/Ni alloys bombarded by 2 MeV protons.

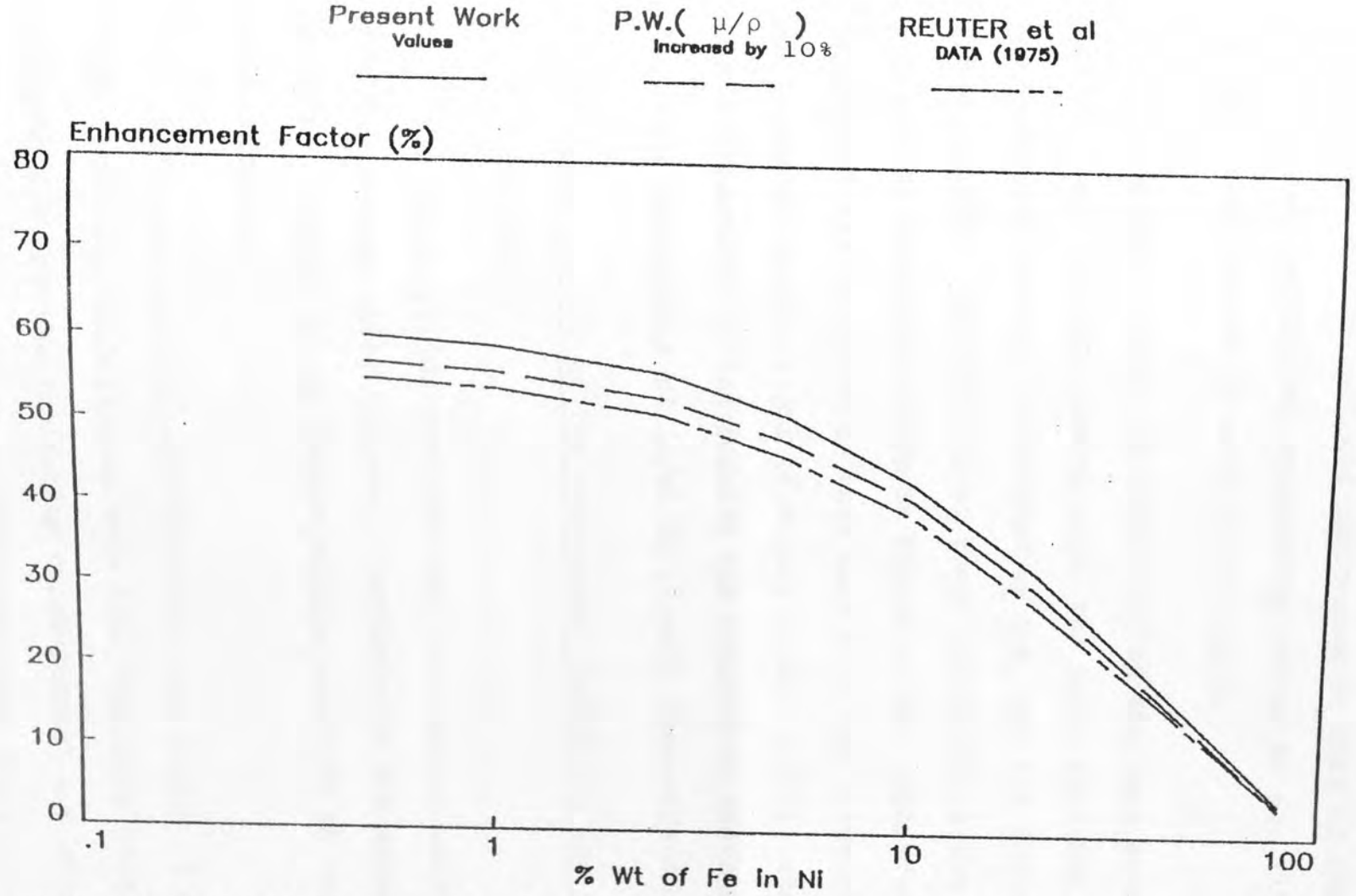

Figure (3.5) Graphical comparison between the present evaluation of the enhancement factor in % of the Fe K_{α} X-rays in dependence on Fe-concentration in weight % in Fe/Ni alloys, and Reuter et al. (1975) data.

The difference in the model used in the present work compared with Reuter's model may be attributed partially to the discrepancy stated above. The discrepancy may be due in part to the unstated references or data of the mass attenuation coefficient employed by Reuter et al. (1975), an important factor in such calculations.

In order to show the importance of the mass attenuation coefficient for such comparisons, the (μ/ρ) employed in the present work were all increased by 10%, and the enhancement recalculated. The results of these calculations are shown plotted as the dashed line in Figure (3.5). Satisfactory agreement was obtained in this case with the illustrative enhancement calculations of Reuter et al. (1975), where the discrepancy in the results was reduced on average to 5%. The importance of (μ/ρ) is clearly demonstrated.

3.7.2 Sensitivity of the Enhancement Factor to the Choice of Data

The X-ray yields predicted by the computer calculations for the binary alloy targets, together with the enhancement effects, depend on the choice of data employed in the calculations.

To illustrate the sensitivity of the choice of data base employed, calculations were done employing different polynomials for the ionization cross-section and stopping power. For the ionization cross-sections, the polynomials

of Johansson and Johansson (1976), Khan et al. (1977) and Reuter et al. (1975) have been employed. For the stopping power calculations, the fitted polynomials to the tabulated data of Anderson and Zeigler (1977), and the fitted formula of Reuter et al. (1975) to the data of Northcliffe and Schilling (1970) have been used.

The X-ray yield, for Fe and Ni in Fe/Ni alloys, for different concentrations of Fe, bombarded with 2 MeV protons have been calculated using the above polynomials in the programme. The combinations of the stopping power and the cross-section's polynomials employed in the present calculations are listed in Table (3.2), together with the different concentrations of Fe in Fe/Ni alloys considered. The results of the computer calculations for X-ray yield enhancement due to the matrix effect is given in Table (3.3). This shows three columns each employing a particular cross-section polynomial with different stopping polynomials. The data obtained from the computer calculations using a particular cross-section data base, indicate that there is no significant difference in the calculated enhancement factor for different stopping power polynomials. This was expected since the stopping power of the combinations for Fe/Ni alloys do not differ by more than 2% on average in the proton range of $0.05 \lesssim Ep \lesssim 2$ MeV.

This is illustrated for 1% Fe/99% Ni in Figure (3.6). However, the use of different cross-section polynomials produces differences in the calculated enhancement factor

Set Number	Stopping Power polynomial using	Cross-section polynomial using
1	Reuter et al. (1975)	Reuter et al. (1975)
2	Anderson and Zeigler (1977)	Reuter et al. (1975)
3	Reuter et al. (1975)	Johansson (1976)
4	Anderson and Zeigler (1977)	Johansson (1976)
5	Reuter et al. (1975)	Khan et al. (1977)
6	Anderson and Zeigler (1977)	Khan et al. (1977)

C_{Fe} wt %	0.1	0.5	1	2.5	5	10	20	40	80
C_{Ni} wt %	99.9	99.5	99	97.5	95	90	80	60	20

Table (3.2) Data base employed in the present calculations for Fe/Ni alloy at different concentrations of Fe.

Stopping Power Equation / X-selection Equation		Reuter et al. (1975) / Reuter et al. (1975)	Anderson and Zeigler (1977) / Reuter et al. (1975)	Reuter et al. (1975) / Johansson (1976)	Anderson and Zeigler (1977) / Johansson (1976)	Reuter et al. (1975) / Khan et al. (1977)	Anderson and Zeigler (1977) / Khan et al. (1977)
C_{Fe} wt %	C_{Ni} wt %	CALCULATED ENHANCEMENT FACTOR (En) = $I_{Fe,sec}/I_{Fe,pri}$)					
0.1	99.9	0.61	0.61	0.63	0.63	0.64	0.64
0.5	99.5	0.60	0.60	0.62	0.62	0.63	0.63
1.0	99.0	0.59	0.59	0.61	0.61	0.62	0.62
2.5	97.5	0.56	0.56	0.57	0.57	0.58	0.58
5.0	95	0.51	0.51	0.52	0.52	0.53	0.53
10.0	90	0.43	0.43	0.45	0.45	0.45	0.45
20.0	80	0.32	0.32	0.33	0.33	0.33	0.33
40.0	60	0.18	0.18	0.18	0.18	0.19	0.19
80.0	20	0.04	0.04	0.041	0.041	0.042	0.042

Table (3.3) The enhancement factor results at different data base employed in the present calculations for Fe/Ni alloys bombarded by 2 MeV protons (Normal incidence).

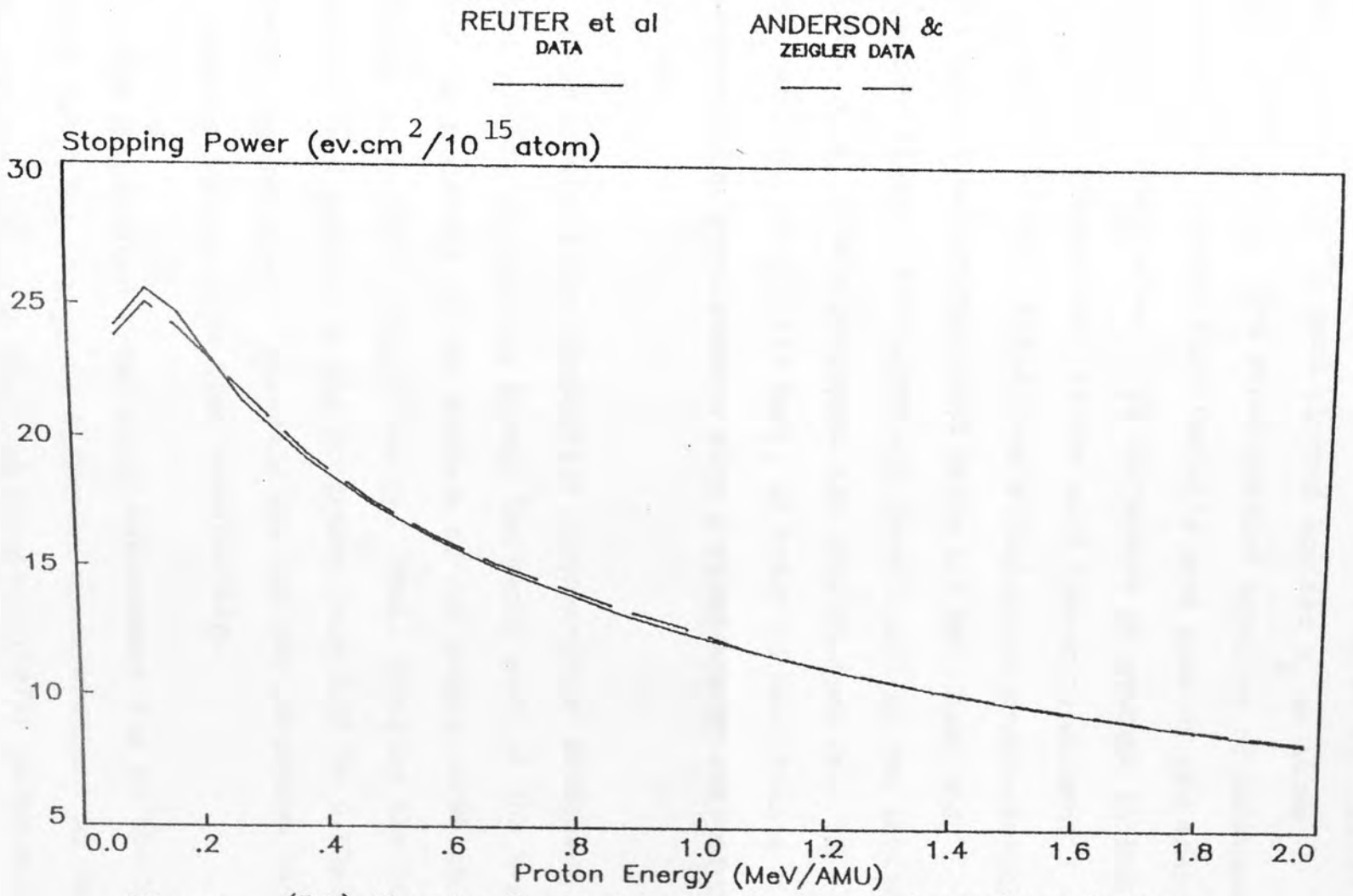

Figure. (3.6) Stopping Power Data for Protons in (1%Fe/99%Ni) Alloy

which vary from 2% to 5%.

The data of the ionization cross-section from the formula given by Johansson (1976), Reuter et al. (1975), and Khan et al. (1977) were plotted against E_p as shown in Figure (3.7). The cross-section equation of Johansson is about 10% higher than Reuter's over most of the energy range, and this gives a 2% difference on average in the calculated enhancement factor when comparing columns 1 and 2 in Table (3.3). Since Khan's ionization cross-section data cannot be extrapolated below 1.3 MeV, Khan and Crumpton (1981), the upper and lower limit of the incident proton beam in the programme has been changed from (2 - 0.05 MeV) to (2 - 1.275 MeV), in order to meet Khan's cross-section requirements with a fixed energy loss of 0.05 MeV.

Since the X-ray production cross-section decreases rapidly with decreasing energy the major part of the X-ray yield is produced in the surface of the sample in which the protons lose 30% of their energy. Thus, changing the lower limit of the energy in the programme from 0.05 to $0.6E_p$ does not affect the outcome markedly and has the advantage that it reduces computation time considerably.

The calculated X-ray yield enhancement due to the Ni effect in Fe/Ni alloys at different concentrations of Fe was determined, using Khan and Crumpton (1977) polynomials, to be systematically higher by 4% on average over the calculated results using Reuter's polynomials and by less

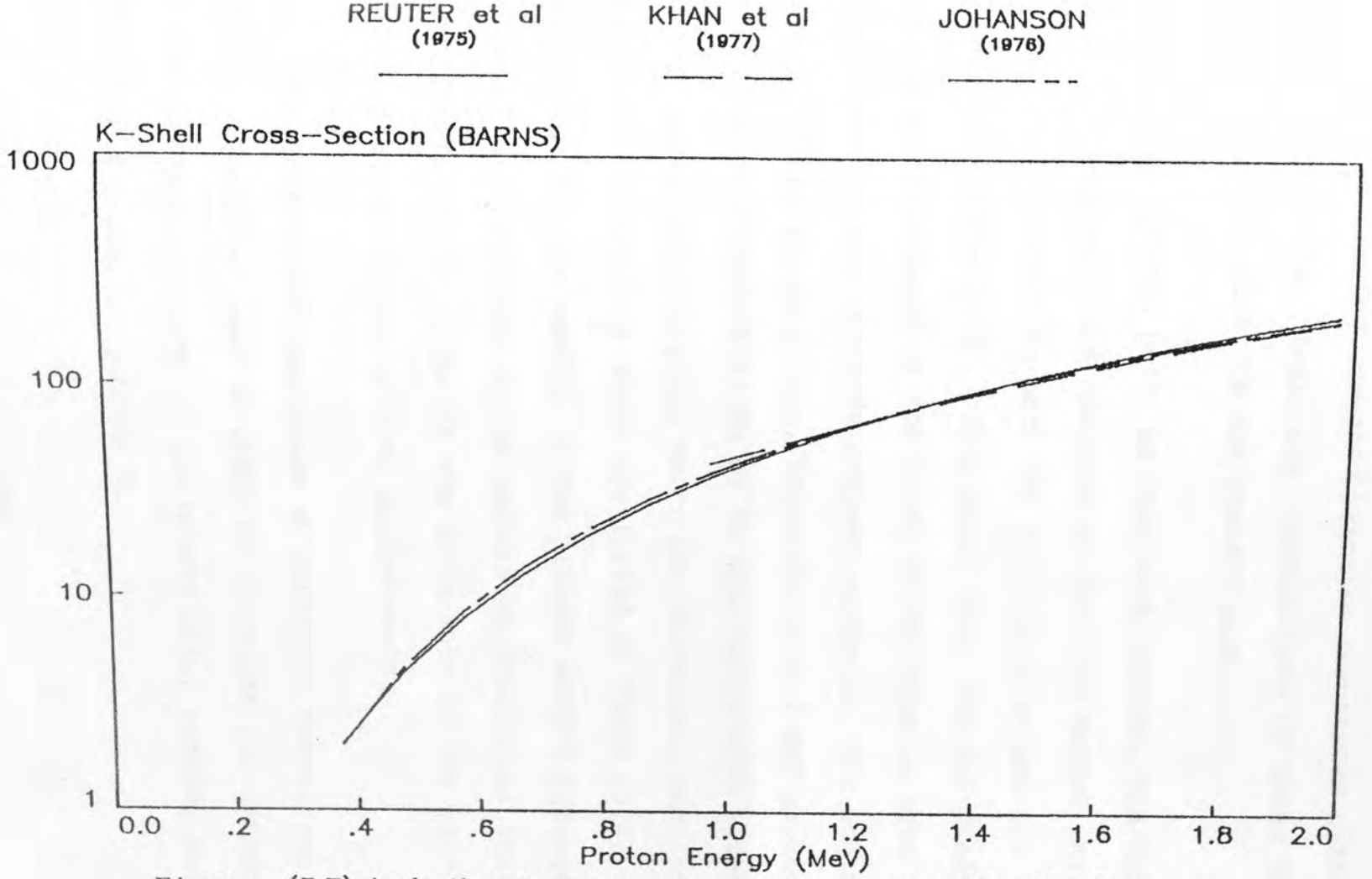

Figure. (3.7) Ionization Cross-Section for Protons in .5%Fe/99.5%Ni Alloy

than 2% on average using Johansson's (1976) polynomials.

The results in Table (3.3) are in good agreement using different combinations of the data bases studied in this section, considering the uncertainties associated with these polynomials. Thus, any combinations of these data bases can be adopted for the present work.

In the present work, as previously stated, the target holder arrangement was designed so that the target inclined at 45^{o} with respect to both the incident beam and the X-ray detector, Figure (3.3). This means that, the thickness of the target traversed by the X-ray is the same as that penetrated by the incident charged particle. The enhancement factor in the Fe/Ni alloys, bombarded with 2 MeV protons, at different concentrations of Fe was calculated according to the above configuration using the references mentioned above, the results of which are listed in Table (3.4). The difference in the results of the present work's arrangements Table (3.4), compared to the results at the normal incident beam, Table (3.3) is due to the difference in the path length of the emitted X-rays in both arrangements.

The enhancement magnitude at different bombarding energies and the procedure used in order to determine the concentrations of the elements present in the binary alloy samples will be discussed further in Chapter 6.

C_{Fe} wt %	C_{Ni} wt %	Enhancement Factor = En(Ni,Fe)
		In the present work arrangements
0.1	99.9	0.64
0.5	99.5	0.63
1.0	99	0.62
2.5	97.5	0.58
5.0	95	0.53
10.0	90	0.45
20.0	80	0.33
40.0	60	0.183
80.0	20	0.040

Table (3.4) The enhancement factor results for Fe/Ni alloys bombarded by 2 MeV protons, calculated according to the present experimental work arrangement.

CHAPTER 4

DEVELOPMENT OF AN ON-DEMAND BEAM PULSING SYSTEM

4.1 INTRODUCTION

Lithium drifted silicon detectors, Si(Li), employed for the detection of characteristic X-rays in PIXE analysis, rely on amplifiers with relatively long pulse shaping time constants of 2 to 8 μsec in order to obtain optimum energy resolution. The long electronic time constant however, leads to a low count rate limitation, typically less than 1000 counts per second. This, in turn, often results in long measuring times or the acceptance of poor statistical precision. Alternatively, one has to accept the loss of optimum resolution which is a major feature of such an analytical technique.

At high count rates, (above 1000 counts per second) the probability exists that while one pulse is being processed, another pulse arrives, resulting in an overlap of the two pulses in the main amplifier. This results in a corresponding distortion of the final X-ray spectrum. Peak centroid shift and peak broadening is also associated with high count rates as well as pulse pile-up effects. These are due to the problems that can occur with the stability of the DC level of the amplifier, Woldseth (1973) and Gedcke (1972).

Commercial pulse pile-up rejector (P.P.R.) units can be utilised to prevent the recording of these distorted pile-up

pulses. But they run into difficulties of a practical nature as the counting rate is increased above 1 kPPS, Khan and Crumpton (1981).

Figure (4.1) demonstrates three types of pile-up pulses that may occur. In the case of Figure (4.1a) the second photon is detected and arrives at the main processing amplifier (Kevex 4500P) before the first pulse reaches the first half of its processing time. These events cause leading edge pile-up. Therefore,the amplitude of both pulses is distorted, and both events are rejected by the PPR unit, thus extending the period for which the electronics is inoperative.

If the second pulse arrives after the first pulse has crossed its peak amplitude and is in the second half of its processing time, (trailing edge) as shown in Figure (4.1b), the pulse height of the first pulse is not distorted so that only the second pulse has to be rejected. The third type of pile-up, Figure (4.1c), is known as sum pile-up and occurs when two pulses are sufficiently close together in time so that the PPR is unable to suppress these closely spaced events. This results in the formation of a single pulse, the height of which is the sum of the individual pulses, Khan and Crumpton (1981).

The Kevex Model 4590 pulse pile-up rejector is designed to provide rejection of the distorted pulses as already described. A fast amplifier with good pulse per resolution

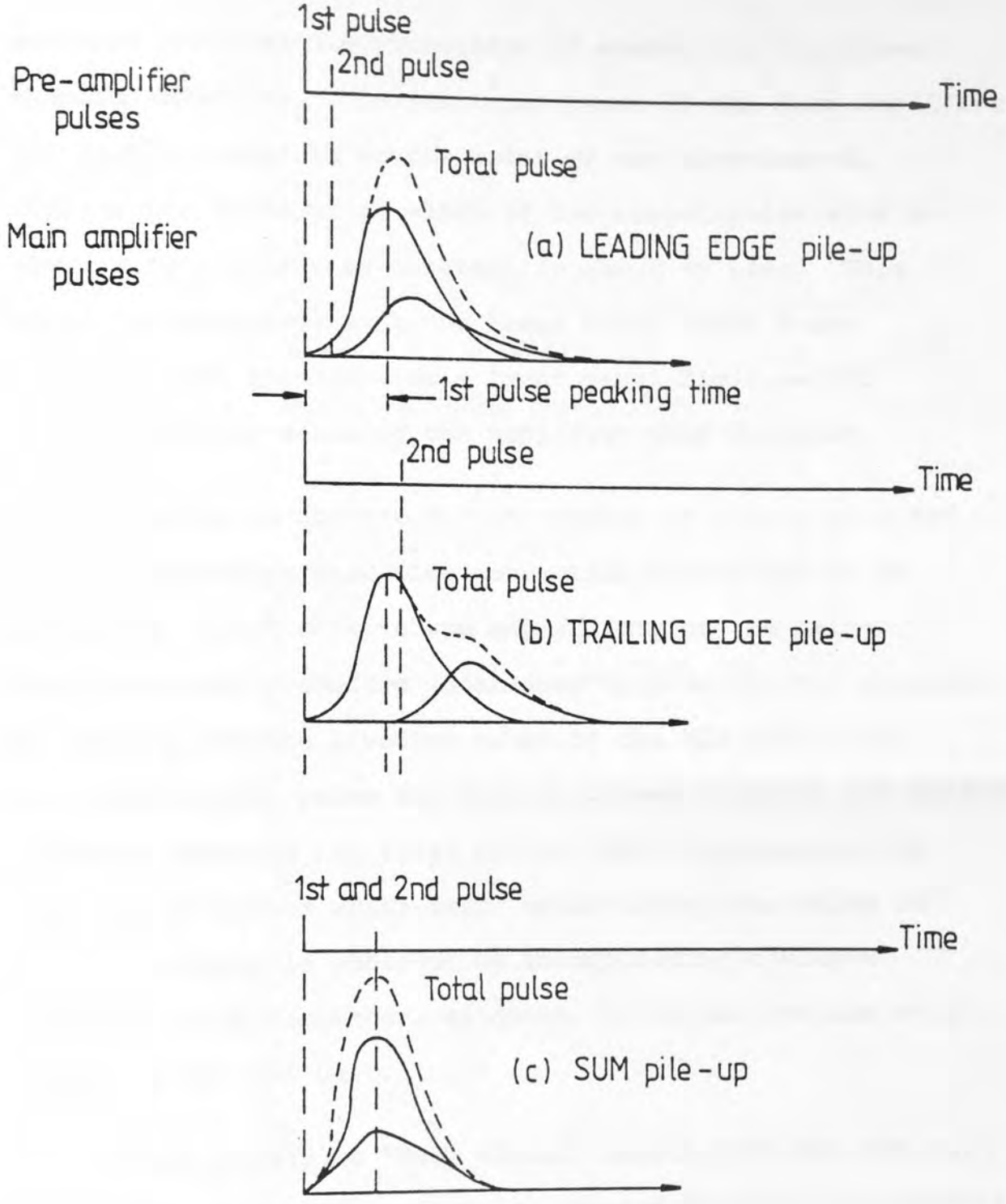

Figure (4.1) Pulse Pile-up effect due to (a) Leading Edge , (b) Trailing Edge, and (c) Sum Pile-up.

provides the time discrimination of events for the slower shaping amplifier. The resolving power of the fast amplifier and discriminator is of the order of one microsecond, whereas the total pulse width of the shaped pulse with an eight microsecond time constant is about 80 μsec. This model is compatible with the Kevex Model 4500P X-ray amplifier and incorporates a front panel digit switch (1 to 9 μsec) for matching the amplifier time constant.

In order to correct for the number of counts rejected by this system, a dead time correction factor has to be extracted, which adds to the uncertainty of the method. The correction procedure (discussed by Khan (1975)) consists of holding off the livetime clock of the MCA until the next undistorted pulse has been processed whenever the pile-up rejector discards the first pulse. The compensation for the loss of pulses which occur while a previous pulse is being processed is achieved by incorporating a simple livetime clock corrector, Woldseth (1973) and Jenkins et al. (1981) in the PPR unit.

Alternatively, a "busy signal" output from the PPR with either busy high +5V or busy low +0V can be used for correcting the dead time of the system, Khan (1975).

4.2 PILE-UP REDUCTION BY PULSED EXCITATION

The X-ray detection system employed in this work suffers a major disadvantage with respect to the count rate limitations regarding pile-up difficulties. These problems

arise because the long shaping time constants, which are required to limit the noise, make the system vulnerable to pulse pile-up effects for pulses which arrive at random intervals.

An alternative approach to the problem would thus be to derandomise the arrival of pulses as illustrated by Jaklevic et al. (1972). These authors used a grid-modulated X-ray tube to pulse the exciting beam in an X-ray fluorescence system and showed that the maximum output count rate for a given processor could be increased by a factor of 4. The basic principle of the technique is to turn off the source of X-rays as soon as a single X-ray photon is detected so that the electronics can process the pulses without interruption. When the measurement is complete and the system is ready for pulse processing, the source is switched on and the cycle repeats. Statham et al. (1974) demonstrate the essential difference between continuous and pulsed beam operations applied to an idealised conventional system with extendible dead time as shown in Figure (4.2).

In the continuous beam case, pulses which arrive during the processing time cannot be measured and merely extend the period (τ) for which the electronics is "dead". If the input counting rate (n_I) is high enough, the dead time will eventually reach 100% and no output will occur from the amplifier. The system is paralysed, Jenkins (1981). In contrast, the switching beam diagram shows that no pulses are lost, the dead time period (τ) is never prolonged and

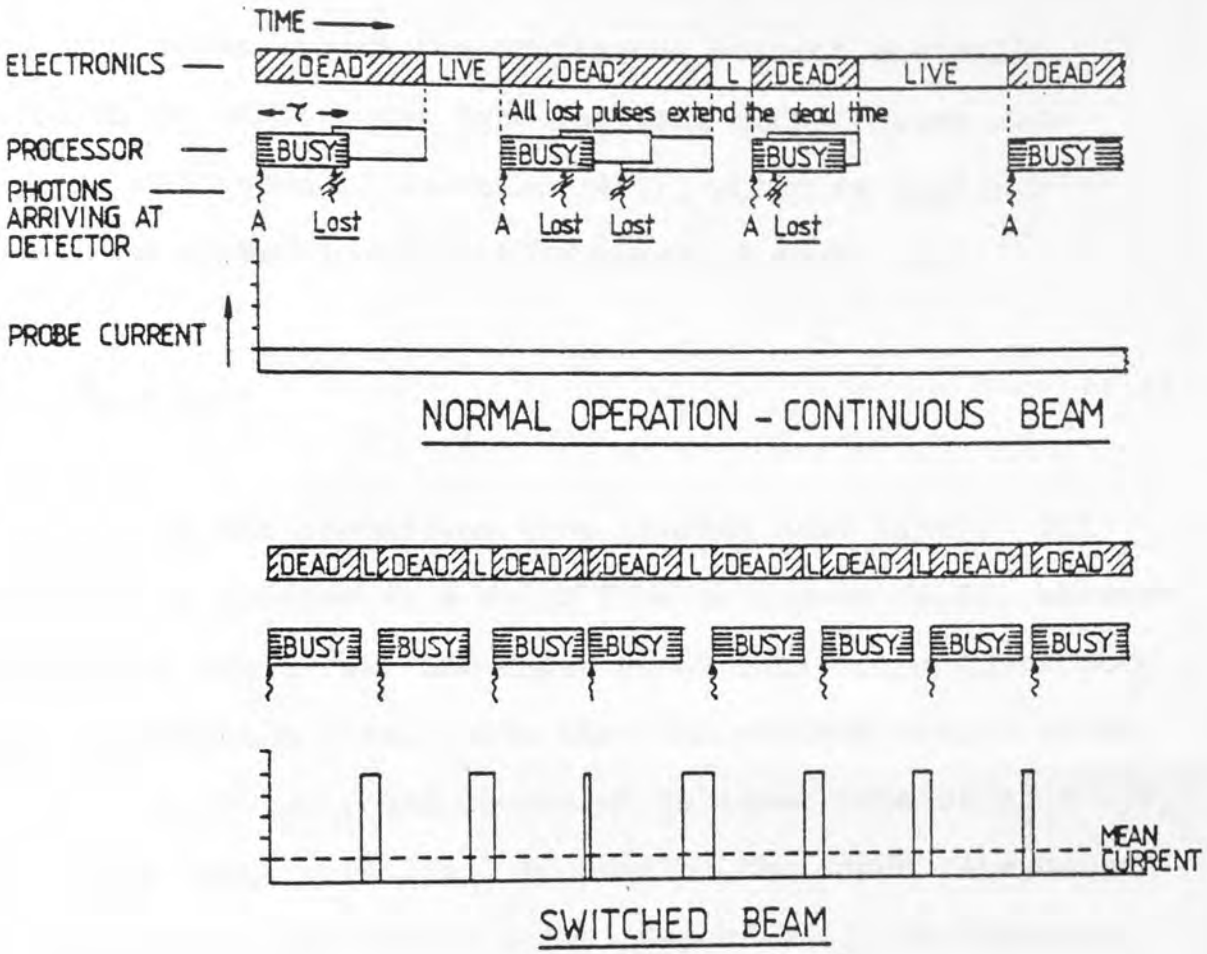

Figure (4.2) Diagrammatic representation of system operation with continuous and pulsed beams. (Statham et al. (1974))

the maximum output is much higher, although still limited, by the time required to measure a single pulse.

The general form for continuous current operation in terms of input count rate (n_I) and output count rate (m_o) is described in equation (4.1), which is applicable to the idealised system with extendable dead time:

$$m_o = n_I e^{n_I \tau_d} \qquad (4.1)$$

where τ_d is the processing time (system dead time). This equation is plotted as a solid line in Figure (4.3), between the output count rate and input count rate for a continuous beam irradiation case. Note that the maximum output count rate is, $m_o = 1/e\tau_d$ and occurs at an input rate of $n_I = 1/\tau_d$. Up to the input rate $1/\tau_d$, increasing the input rate causes an increase in the output rate. Beyond $1/\tau_d$, an increase in n_I causes a decrease in the output rate. For this reason, the extending dead time is often termed paralysable dead time.

With the paralysable system, there are always two possible input count rates corresponding to a given output rate as shown in Figure (4.3). Thus, the maximum output rate obtained in the pulsed mode is increased by a factor e over that of the continuous excitation, assuming that the dead time in both cases are equivalent. However, Jaklevic et al. (1972), reported that this is not a valid comparison if one uses the PPR circuit with continuous

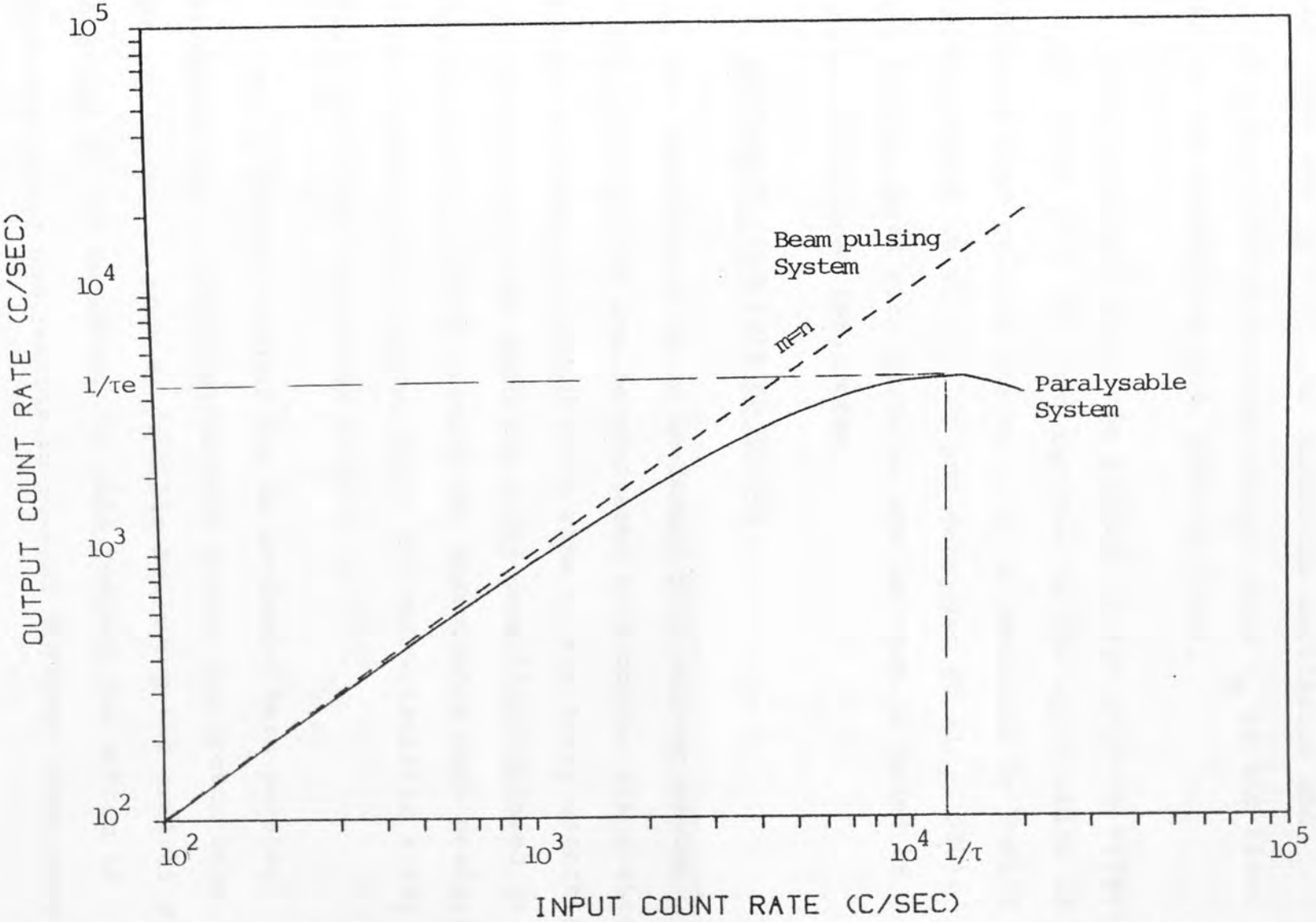

Figure (4.3) Theoretical variation of the output count rate m as a function of the input count rate n, with and without beam pulsing.

excitation which results in a longer effective dead time for equivalent minimum pulse separations. The equivalent dead times are $\tau_d = 3\tau_p$ for continuous excitation and $\tau_d = 2\tau_p$ for pulsed X-ray excitation, where τ_p is the first half of the processing time (peaking time).

In the present work, the problem of the pile-up effect at a high count rate has been improved by the application of an on-demand beam pulsing system, such as evaluated by Cahill (1975), Mingay et al. (1978) and Malmqvist et al. (1982). This method, used with particle accelerators, is based on electrostatic beam deflection.

4.3 ON-DEMAND BEAM PULSING SYSTEM

The development of an on-demand beam pulsing system in the present work was necessitated by problems associated with pulse pile-up at a high count rate in the X-ray detector data handling system. With the X-ray detection employed in this work, the pile-up problem was unavoidable when analysing thick binary alloy targets, where the characteristic X-ray yield generated from these targets is high.

The procedure adopted for an on-demand beam pulsing technique was to electrostatically switch the proton beam off the target as soon as possible following the arrival of an X-ray at the detector. In this respect, the system is self-regulating and results in several distinct advantages in PIXE analysis:

(i) An optimum count rate and an analysis time approaching one third of that for commercial pulse pile-up rejectors.

(ii) No dead time correction is required since the detector is "live" during the periods when the beam is on target.

(iii) For a given beam current, maximum yield from a target is generated with minimal target damage. This may be important when analysing biological tissues which are easily damaged by beam bombardment.

(iv) At a high count rate, the signal-to-noise ratio and energy resolution remains acceptable.

(v) Maximum statistical accuracy can be achieved.

The on-demand beam pulsing system developed as part of this study has been implemented on the PIXE beam line on the 3 Mv Dynamitron accelerator at the joint Birmingham Radiation Centre. The detailed design and technical description of this system is discussed in the following sections.

4.4 REQUIREMENT OF THE BEAM PULSING SYSTEM

An appropriate on-demand beam pulsing system comprises,

(1) A proton beam deflection system

(2) Beam collimators and a beam stop

(3) Suitable beam pulsing electronics.

The design of these features depends to a large extent on the specific beam line configuration and application. The

design philosophy and details for the present system are discussed in the following subsections.

4.4.1 Deflection of Ion Beam

The most satisfactory way of removing the proton beam from the target is to deflect the beam away from collimating slits. This deflection of the proton beam can be accomplished in either of two ways. In the first approach, switchable electrostatic fields can be established at a suitable position along the proton path by using high voltage parallel plates. The second approach establishes a magnetic field from two coils symmetrically arranged on the beam line. This field may be set up at right angles to the direction of the deflection, Plouns (1978) and Duffin (1980).

Electrostatic deflection has been adopted in the present work for the simple reason that the capacitances and inductance of the deflecting plates can be very small, while the distributed capacitance and inductance of deflecting coils cannot be small, particularly with a large number of coil turns (i.e. the load will be inductive and the switching will be slow).

Generally, for accelerators operating up to a few MeV, electrostatic deflection systems are preferable because they store a smaller amount of energy than the magnetic one; consequently, they can be switched faster. It must also be noted that the electrostatic system is much more economical. Indeed, an electrostatic field is produced in

a space without power consumption, while energy is required for producing a magnetic field due to resistive losses in the windings.

4.4.2 Electrostatic Deflection System

The electrostatic deflection theory and the details of the electrostatic deflection system are fully discussed in this section.

Basically, two parallel deflecting plates can be placed in the beam transport tube between which the proton beam either passes on its way towards the target or is deflected away from the target when a suitable potential difference exists between the plates.

When an X-ray event is detected, a pulse is generated at the output of the preamplifier, which in turn triggers the electronics to ground one of the deflecting plates, where these plates are both initially kept at the same potential. A transverse electric field is therefore applied between the plates forcing the beam to be deflected from the target and onto a beam stop aperture.

In order to design a deflection system, the following facts must be noted.

When a charged particle, having a charge +q and mass m, is in a uniform electric field of intensity E, the particle experiences a force in the direction of the field of magnitude

$$F = qE \tag{4.2}$$

where the field between the plates is given by

$$E = \frac{V_{AB}}{d} \tag{4.3}$$

V_{AB} is the potential difference applied to the deflecting plates and d is the separation between the plates. This expression may be used for plates of lengths much greater than the spacing, when little error is caused by neglecting the distortion of the field at the ends of the plates. If all other forces on the particle are negligible compared with the one given in equation (4.2), the particle will spend a time t $(= \frac{X}{V_X})$ undergoing a transverse acceleration (qE/m) over a portion of its path equal to the length of the plates ℓ, i.e. $X=\ell$ where X is a length in the horizontal direction and V_X is the velocity of the particle. The path of the particle over this length is parabolic and the displacement from the axis is given by

$$h = \frac{1}{2}at^2 = \frac{1}{2}\frac{qE}{m}\frac{X^2}{V_X^2} \tag{4.4}$$

Therefore

$$h_1 = \frac{1}{2}\frac{qE}{m}\frac{\ell^2}{V_X^2} \tag{4.5}$$

where h_1 is the displacement of the particle from the axis over the path length ℓ of the plates. Beyond the deflecting plates, the path of the particle is a straight line because the charge moves in field free space. The beam is therefore deflected through an angle α and the value of h_2 is L tanα, where h_2, L and α are defined in Figure (4.4). The slope of this

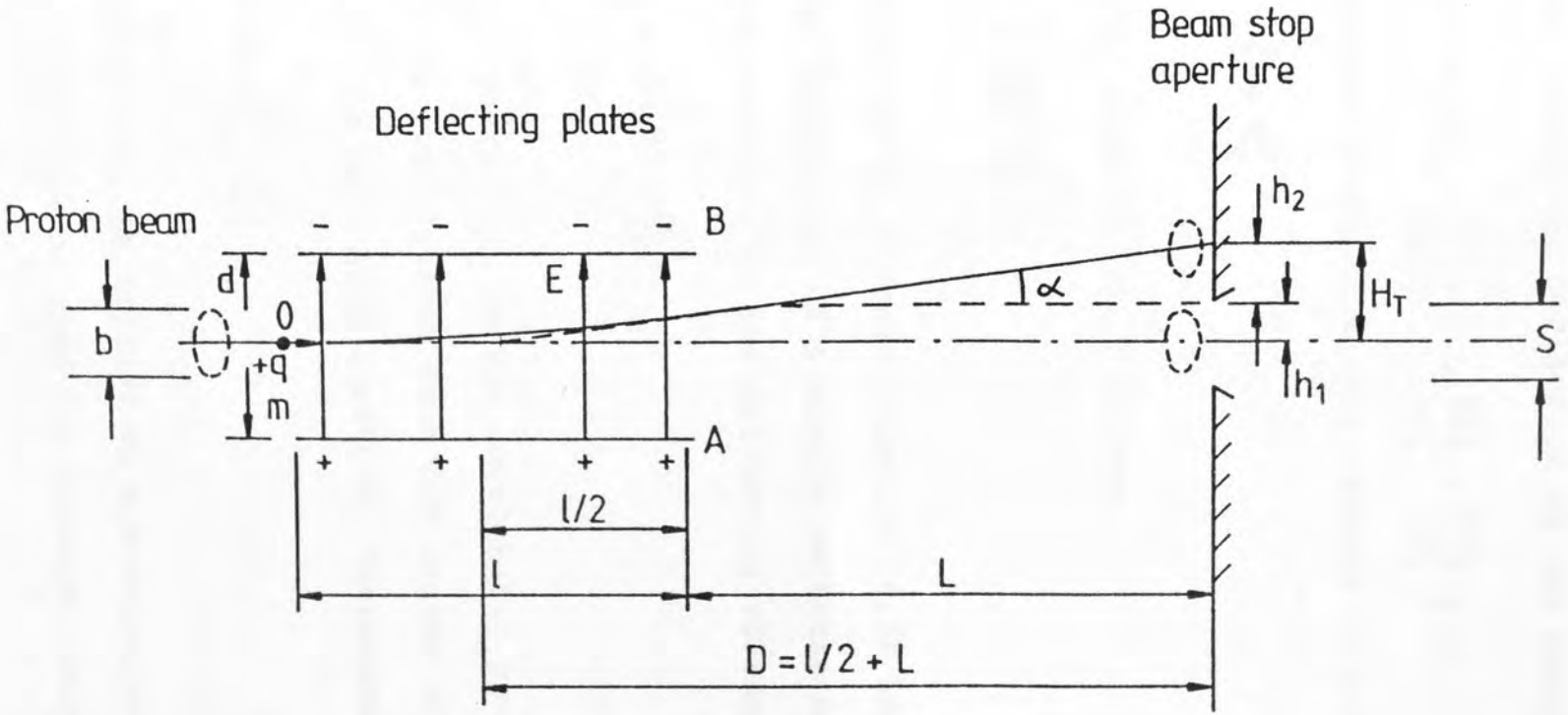

Figure (4.4) Motion of positive charge particles in uniform electrostatic fields (perpendicular to E).

straight line is

$$\tan\alpha = \left(\frac{dh}{dX}\right)_{X=\ell} = \frac{qE\ell}{mV_X^2} \tag{4.6}$$

Therefore, the total deflèction of the beam, H_T is

$$H_T = h_1+h_2 = \frac{qE\ell^2}{2mV_X^2} + L\,\frac{qE\ell}{mV_X^2} = \frac{qE\ell}{mV_X^2}\left(\frac{\ell}{2}+L\right) \tag{4.7}$$

The classical value of kinetic energy is given by

$$K = \frac{1}{2}\, m\, V_X^2 \tag{4.8}$$

Therefore, equation (4.7) becomes

$$H_T = \frac{qE\ell}{2K}\left(\frac{\ell}{2}+L\right) \tag{4.9}$$

Elimination of E, between equation (4.3) and (4.9), relates the total deflèction of a single particle needed at the beam stop aperture to the deflecting voltage.

$$H_T = \frac{q\ V_{AB}}{K}\left(\frac{\ell D}{2d}\right) \tag{4.10}$$

$K=q\ V_{ACC}$, where V_{ACC} is the accelerator potential, and $D(=\frac{\ell}{2}+L)$ is the distance from the centre of the deflecting plates to the beam stop aperture. Therefore

$$H_T = \frac{V_{AB}}{V_{ACC}}\left(\frac{\ell D}{2d}\right) \tag{4.10a}$$

Equation (4.10a) is applied to non-relativistic particles and can therefore be used for protons, deuterons and alphas up to a few MeV.

In order to estimate the deflection voltage required

for optimum geometry, consider the case shown in Figure (4.4) where an undeflected beam of broadness b, is incident on the centre of the beam stop aperture of width s.

At the beam stop aperture, the shift, H_T, of the beam from the central line should be $>(b+s)/2$, in order that the whole beam is deflected away from the slit.

The minimum deflecting voltage $V_{AB,min}$ can be derived from equation (4.10a) and written as follows:

$$V_{AB,min} = \frac{2V_{ACC}H_T d}{\ell D} \qquad (4.11)$$

Therefore, ℓ and D should be taken as large as possible to minimise $V_{AB,min}$. Also, for a smaller d, $V_{AB,min}$, becomes smaller.

In practice, the gap d and the length of the deflectors ℓ, are limited by the beam line arrangement and also by the maximum capacitance permissible between the plates in order to achieve fast switching of the beam. The beam diameter, b, was chosen to be 1 cm, therefore the slit width s was adjusted to be equal to the beam diameter, (1 cm). Consequently, minimum shift of the beam, H_T at the slit $(=\frac{b+s}{2})$ is equal to 1 cm. The available space restricted ℓ and D to approximately 50 and 90 cm respectively.

The maximum spacing between the plates d should be

$$d = 2(\frac{b}{2} + h_1) \qquad (4.12)$$

where

$$h_1 = \frac{\ell/2}{D} H_T = 0.278 \text{ cm.}$$

Therefore, the minimum spacing $d = 2(\frac{b}{2} + \frac{\ell/2}{D}.H_T) = 1.56$ cm. Practically, d was chosen to be 2.5 cm to ensure that the beam does not touch the plates. The estimated capacity between deflection plates is approximately 7 pF and the supports and leads will increase this value by about a factor of 2.

The minimum voltage needed to deflect particles accelerated by a potential of 3 MV off the target under the above conditions is 3.75 kV from equation (4.11). This value for the deflection voltage is the minimum possible value since the edge of the deflected beam first touches the edge of the slit. An increase from 3.75 kV to 4.25 kV increases the total shift of a 3 MV beam to 1.13 cm, giving a margin of 0.13 cm between the edge of the deflected beam and the slit. h_1 now becomes 0.314 cm and the minimum plate spacing is calculated to be 1.63 cm. Consequently, the chosen d=2.5 cm remains satisfactory. It should be noted that the deflection will be larger for a lower energy beam. Therefore, to avoid the beam hitting the plates when deflected, equation (4.11) can be written as follows to estimate the plate voltage at different accelerator potentials in order for the deflection to remain constant:

$$V_{AB,min} = \text{plate voltage for 3MV particle} \times \frac{\text{operating potential (MV)}}{3 \text{ MV}}$$

where the accelerator potential versus plate voltage is given in Table (4.1).

Accelerator Potentials MV	Minimum Plate Voltages kV
3.0	4.25
2.5	3.54
2.0	2.83
1.5	2.13
1.0	1.42

Table (4.1) Minimum plate voltages for different accelerator potentials.

Technical Description of Deflection Plates

In the current PIXE beam line, between the focussing magnet and the scattering foil, two beam deflecting plates have been installed. These plates are made of a fine polished stainless steel 50 cm long, 4 cm wide and 2.5 cm apart. The side edges of these plates were bent to strengthen them and to reduce the edge effect. Four vacuum, high voltage leadthroughs are used to hold the plates in one of the standard beam transport tubes (diameter = 4 inch). These leadthroughs are manufactured from materials especially selected for their electrical and vacuum properties (Edwards Vacuum Leadthroughs type 7D). The cross-sectional and

front elevation design of the deflecting plates are shown in Figures(4.4a) and (4.4b) respectively. These plates were fabricated at the Radiation Centre workshop and then installed in the beam line as shown in Figures (4.4c) and (4.4d).

4.4.3 Apertures for PIXE Beam Line

In order for the beam pulsing to operate correctly, the position of the beam has to be accurately controlled within the beam tube. This is accomplished by installing different sets of apertures at different stages on the beam line for monitoring and defining the beam to the target. These apertures are carefully designed according to their purpose and position on the beam line, these are:

(a) X-Y Aperture

The beam was accelerated vertically downward from the accelerator and deflected through 90^{o} in two stages by suitable bending magnets. This required a device for alignment and monitoring of the beam before it passes through the second bending magnet. This was accomplished by inserting water cooled tubes, Figure (4.5a), to form an aperture of about 2 cm^2. This aperture was the result of the positioning of four stainless steel tubes,each with an external diameter of 3.6 cm with a copper block cut, bevelled and welded on to their ends, Figure (4.5b). These tubes were accommodated in a stainless steel rectangular box with a 2" tube on each of its opposite side faces for

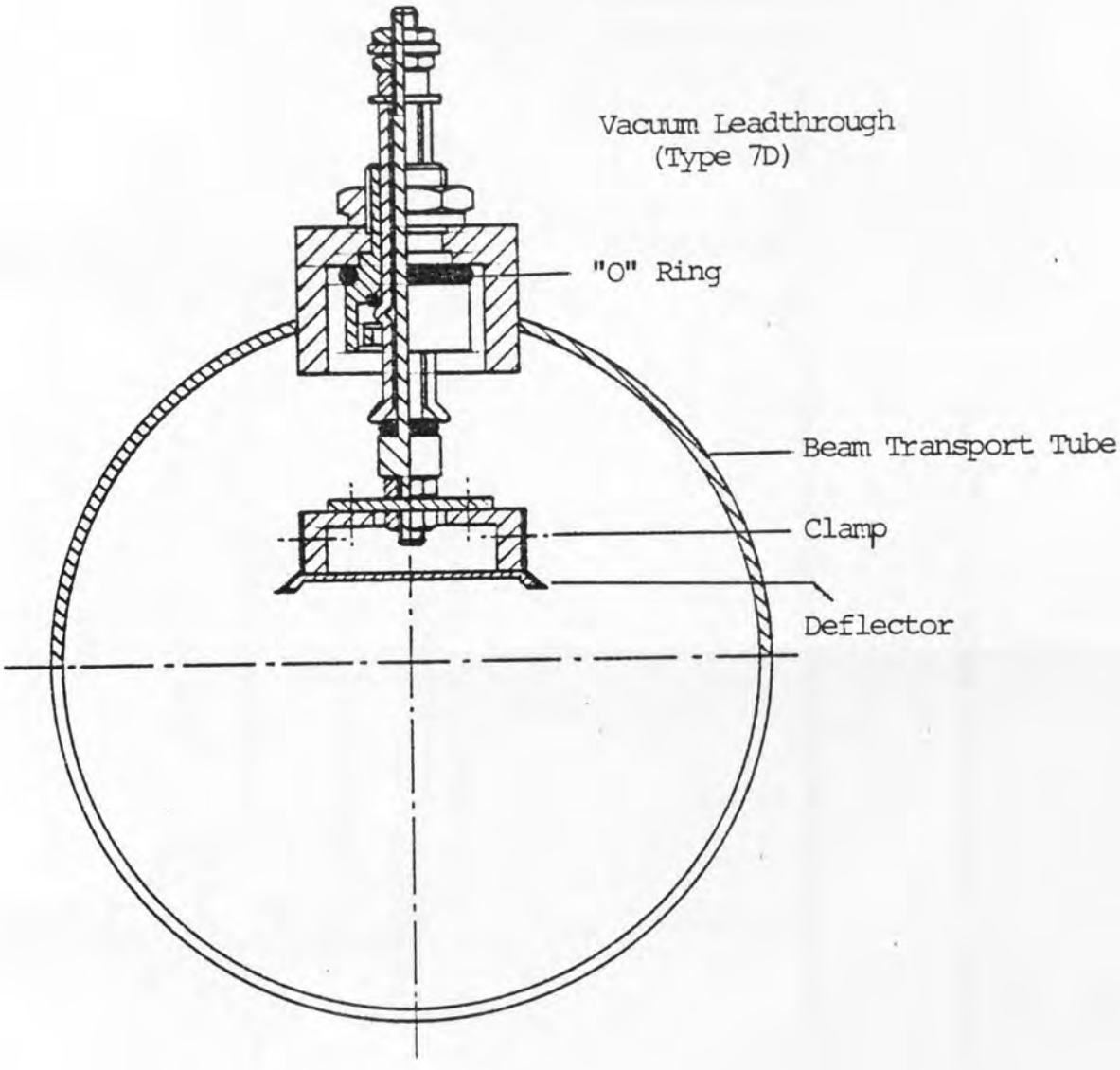

Figure (4.4a) The cross-section design of the deflecting plates

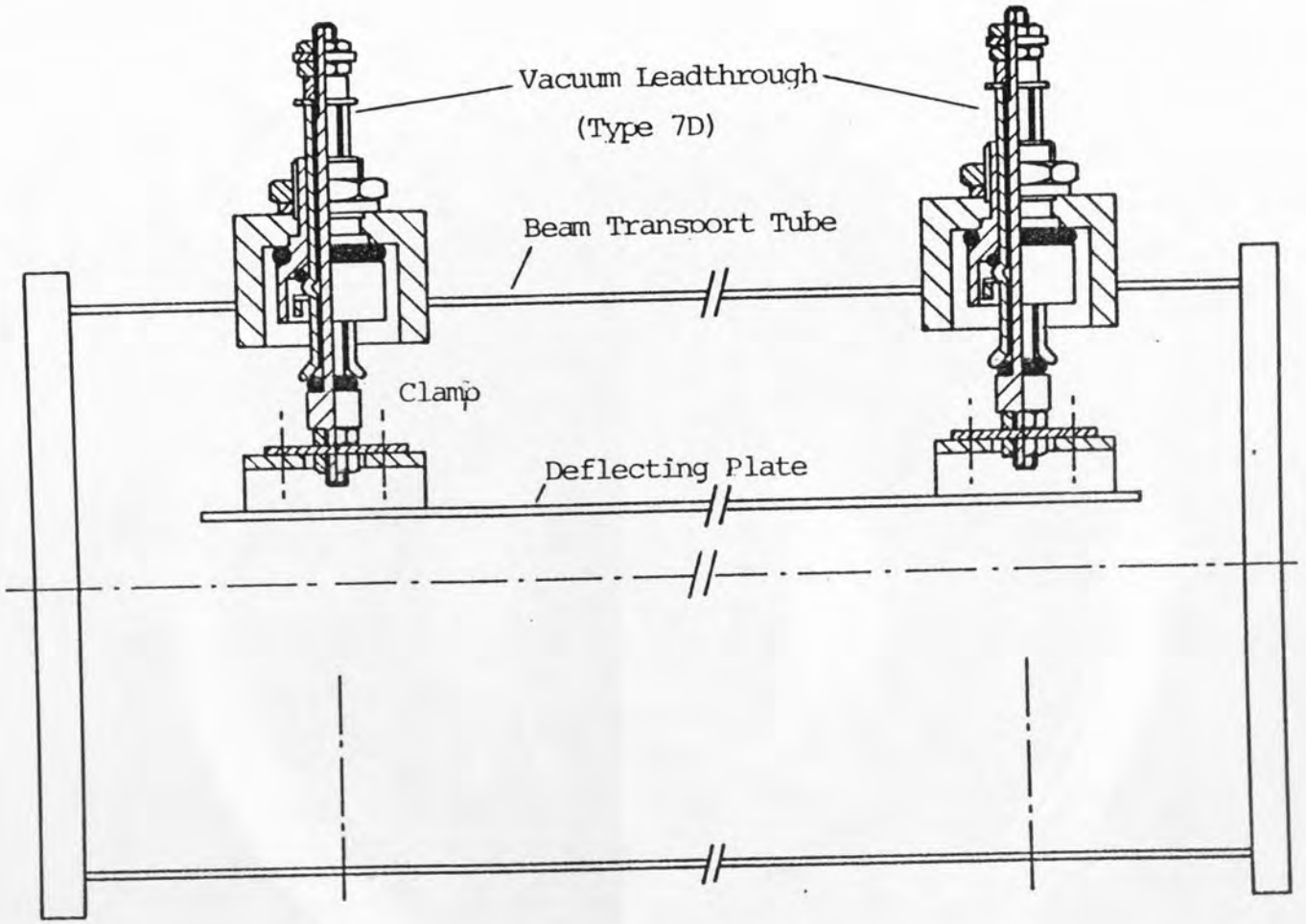

Figure (4.4b) The front elevation design of the deflecting plates.

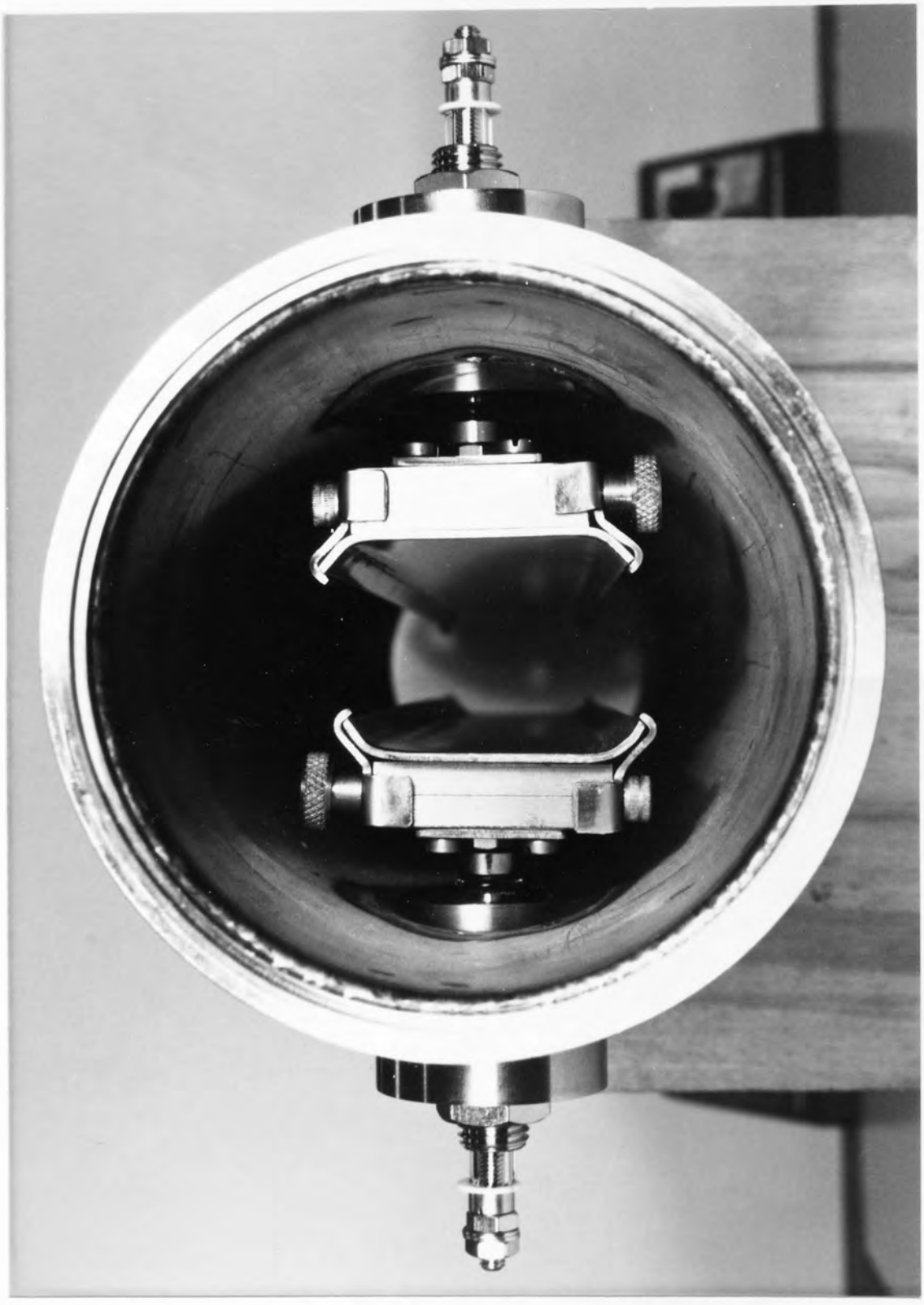

Figure (4.4c) A photograph of the deflecting plates arrangement.

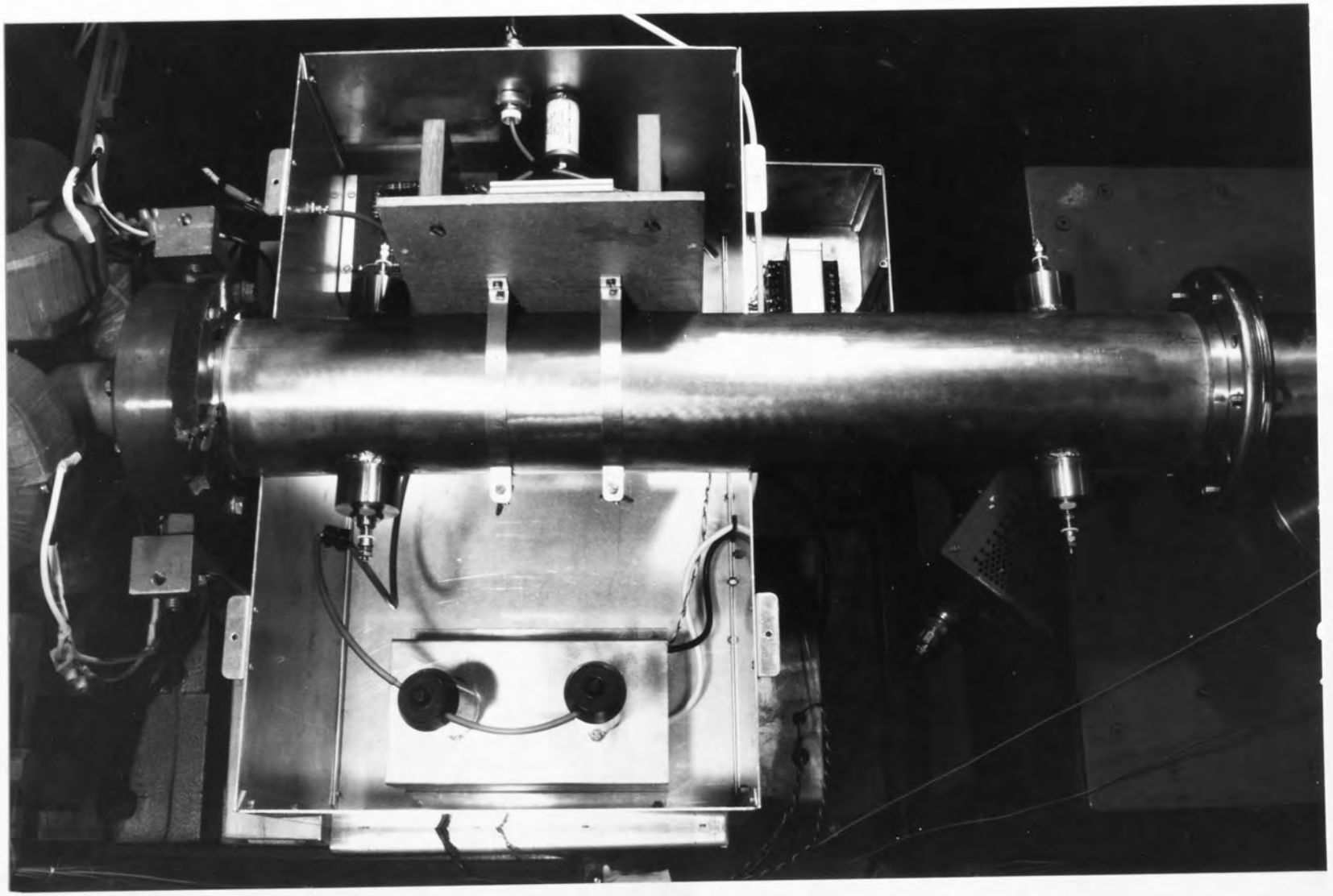

Figure (4.4d) A photograph of the deflection system installed in the beam line.

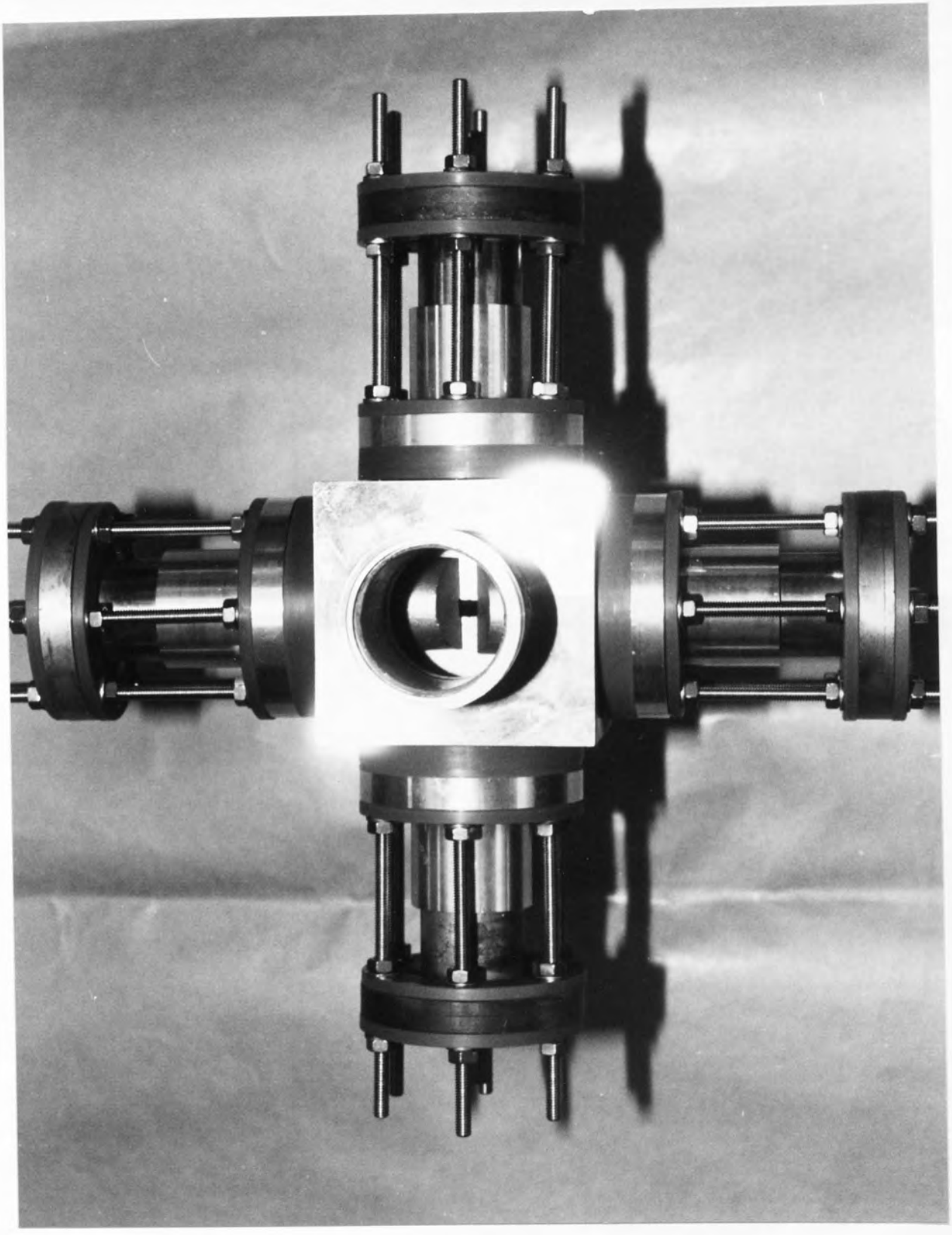

Figure (4.5a) A photograph of the X-Y aperture design.

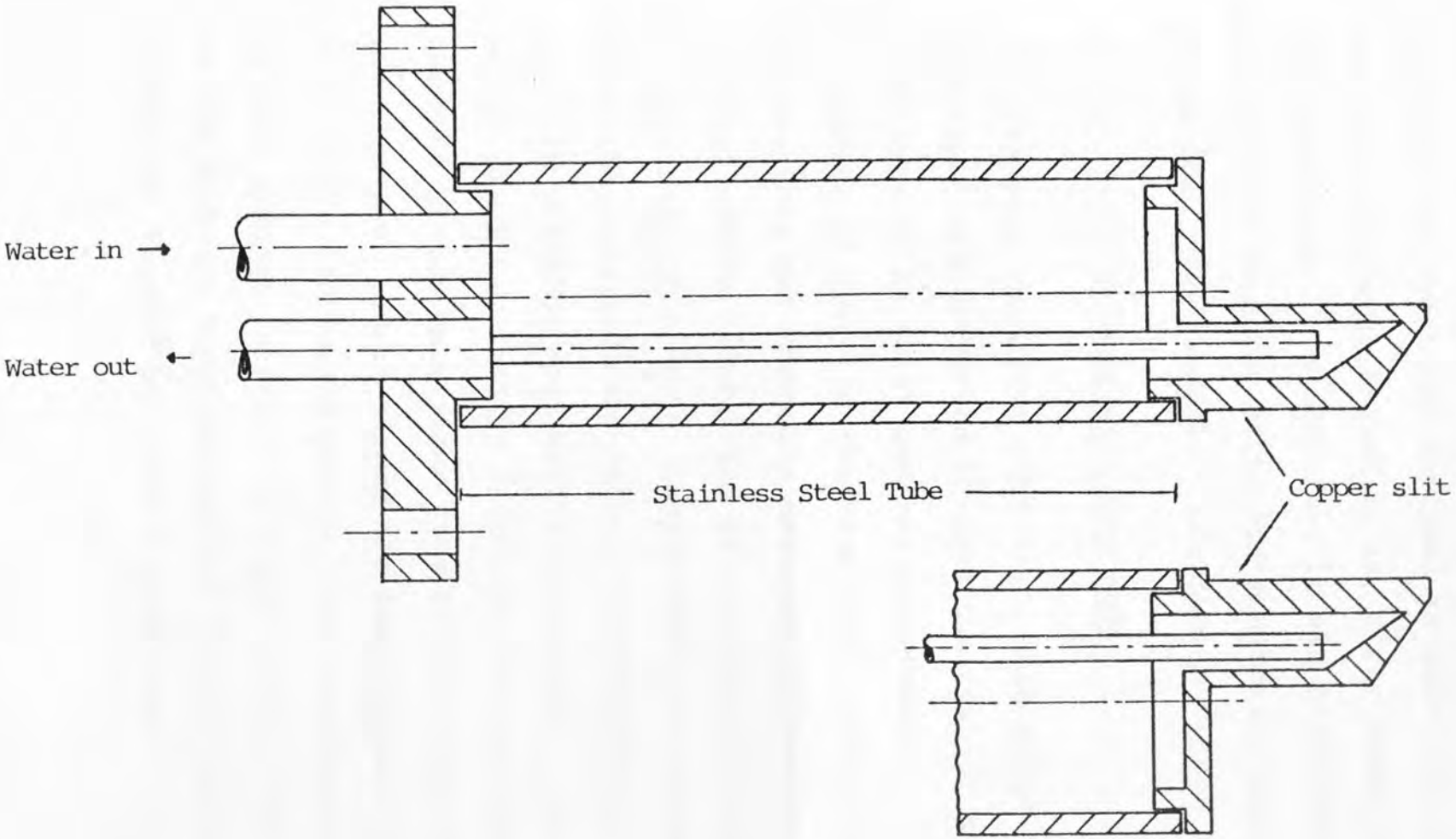

Figure (4.5b) The assembly of the adjustable tubes with a copper slit at the end of each tube.

connections to the rest of the beam line, 40 cm above the second bending magnet as shown in Figure (4.6a). This apparatus was specially designed to take into account the heat dissipation generated by any stray beams hitting the aperture's edge. In addition, it was electrically insulated and isolated from the earth for monitoring purposes. One of the four tube assembly is shown in Figure (4.6b).

(b) 4" to 2" Reducer with Aperture

The beam transport tube up to this stage of the beam line was 2" in diameter and because the rest of the beam line is a 4" tube, a 2" to 4" reducer was needed. Due to the limitation of space in the beam room, a 2 to 4 inch reducer and aperture was specially designed for use in place of a standard reducer, resulting in a saving of 6cm of space. This reducer, made of a 1.5" copper block, was accommodated directly after the quadrupole and before the deflecting plates with a 0.5 cm defining aperture in the middle. Likewise, a large copper block was used to dissipate the heat caused by the incident proton beam since this is not water cooled. The aperture was used to direct the beam through the central line of the deflecting plates. The cross-sectional design of this reducer is shown in Figure (4.7). The alignment of the aperture with the central line of the deflecting plates was checked by using a laser beam.

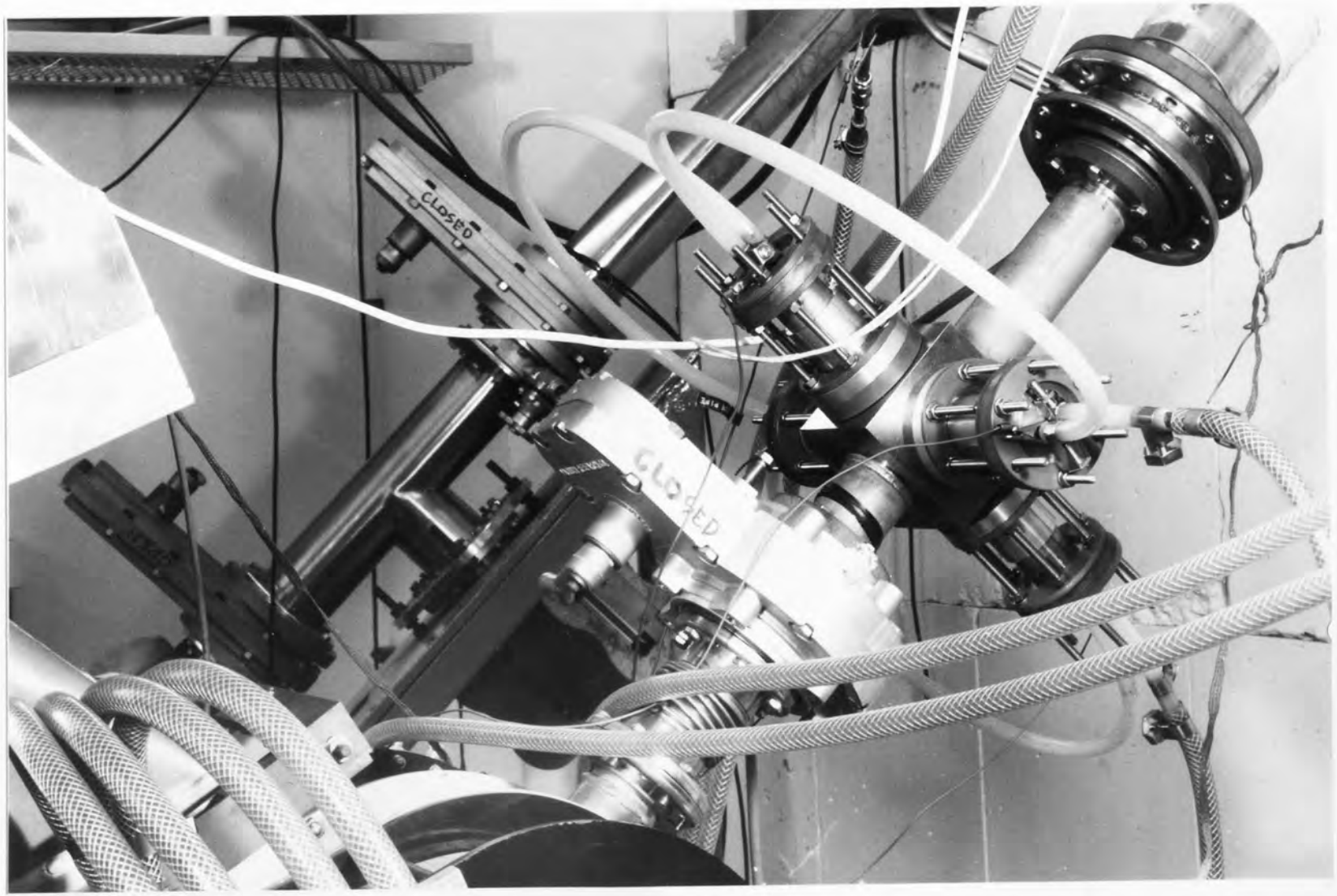

Figure (4.6a) A photograph of the X-Y aperture connected to the rest of the beam line.

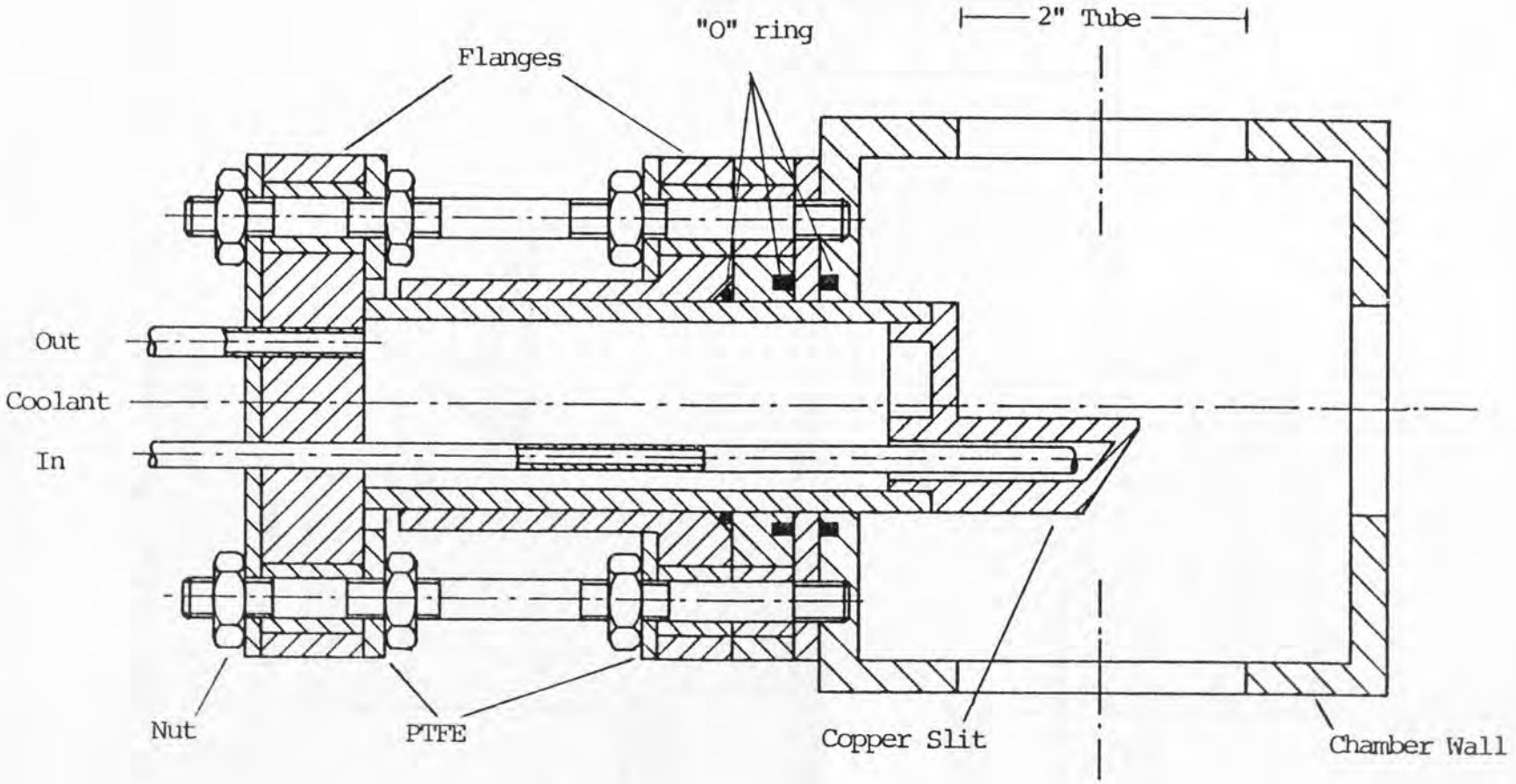

Figure (4.6b) Cross-sectional view of four slit collimator assembly.

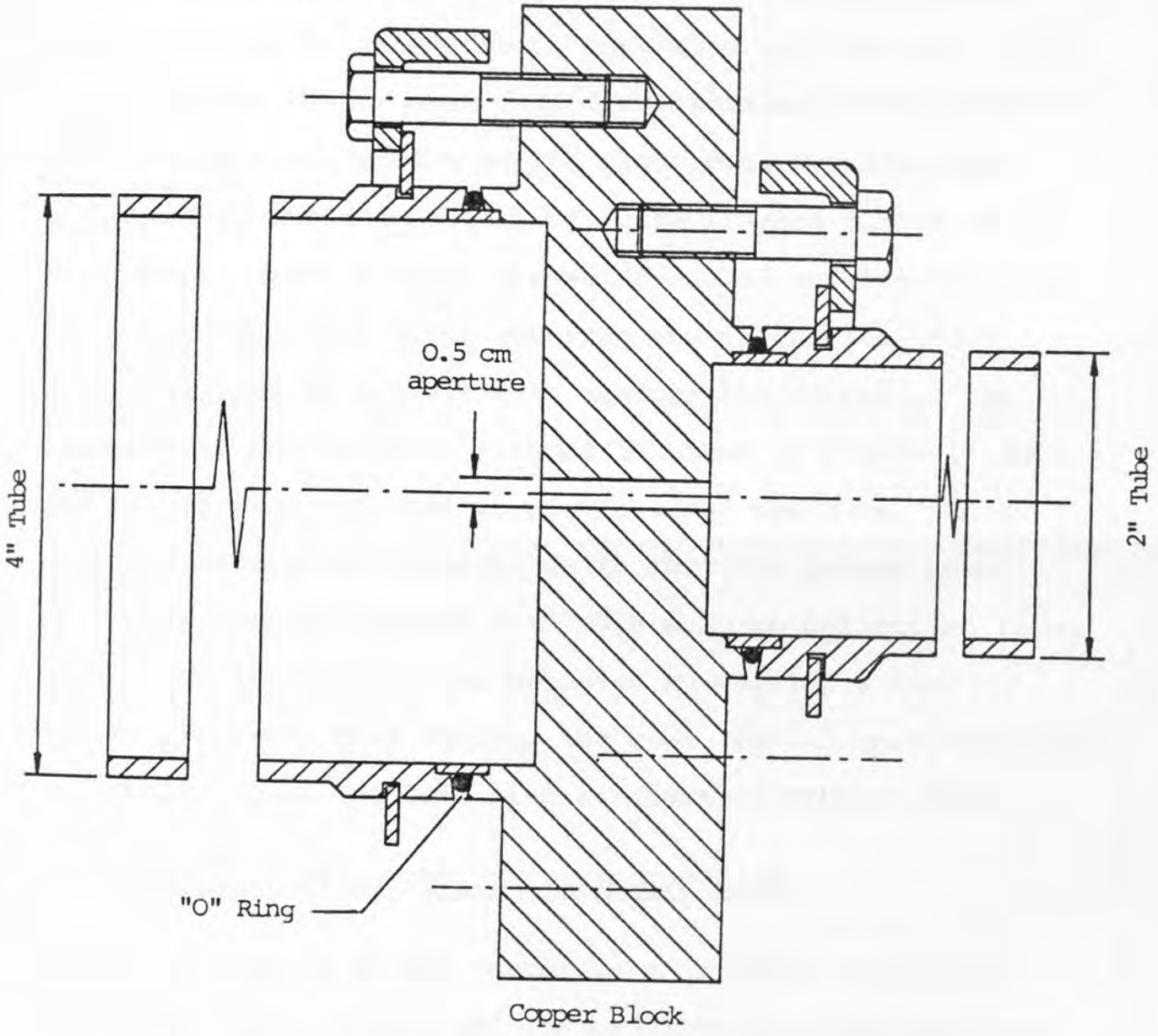

Figure (4.7) 4" to 2" Reducer with aperture assembly.

(c) X-Y Beam Stop Aperture

A beam stop was required on to which the beam could be deflected for a time proportional to the processing time of the X-ray signal. Four sets of arm slits were designed which could be located at the scattering foil chamber, at about 90 cm from the centre of the deflecting plates. This apparatus was constructed from four stainless steel fingers each 1.5 cm I.D., with a copper block cut, bevelled and welded on to the end of each of these fingers to act as the beam stop. These fingers are water-cooled and electrically insulated from each other and from the earth, i.e. each finger is used as a monitor to measure the current. The assembly of one of these fingers is shown in Figure (4.8a) and it has been adjusted to give a 1 cm^2 aperture. This aperture was carefully adjusted so that the proton beam must pass through without hindrance when no deflection takes place. This alignment was achieved by passing a fine horizontal laser beam through the beam line. This component was installed in the beam line as shown in Figure (4.8b).

4.5 INSTALLATION OF THE NEW PIXE BEAM LINE

During the last few years, work on Aston beam line commenced on the design and construction of a new PIXE and Rutherford back scattering (R.B.S.) analysis beam line. The construction of the on-demand beam pulsing system and multiple sample facility has been implemented on the Aston beam line on the 3 MV Dynamitron accelerator. The proton

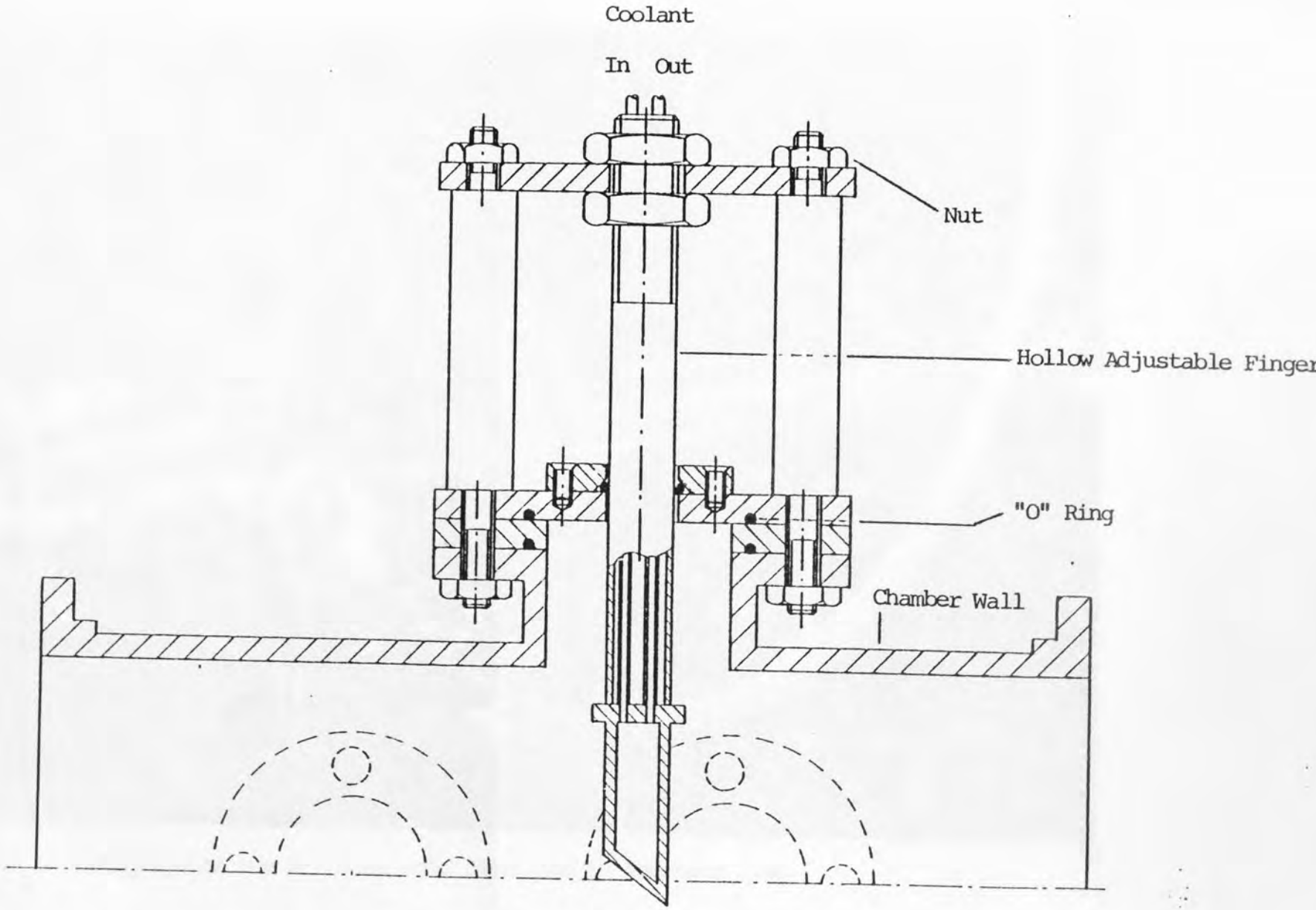

Figure (4.8a) Assembly of the beam dump aperture.

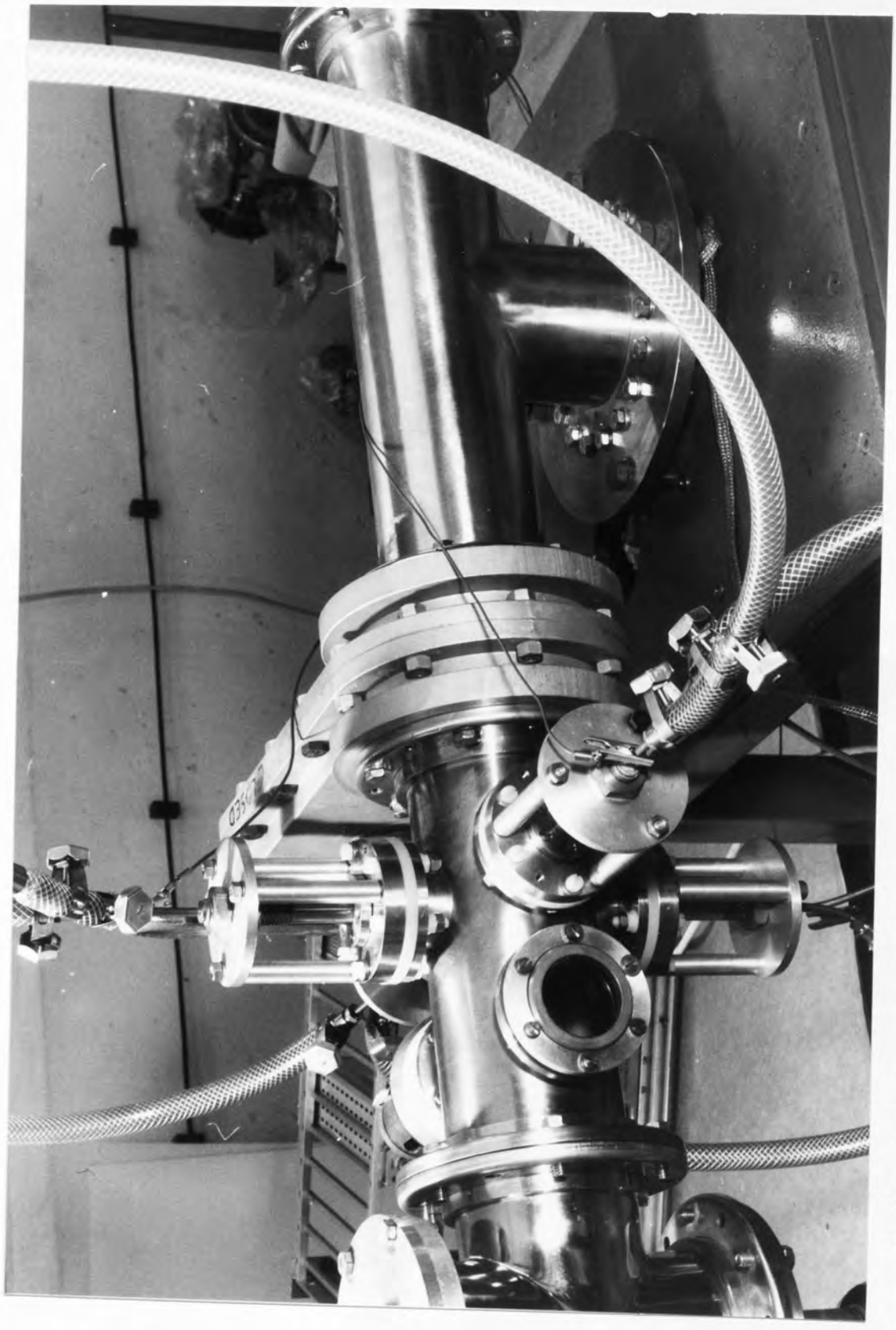

Figure (4.8b) A photograph of the X-Y beam stop installed in the beam line.

beam was accelerated vertically downward and deflected through 90^{o} in two stages by suitable bending magnets. The beam was then focussed using a quadrupole pair of focussing magnets and then collimated .

The main features of the new beam line elicit the following comments and are illustrated in Figure (4.9).

(1) The new on-demand beam pulsing system and its optimum counting rate capability enable a thick sample to be analysed more readily, and very good pile-up suppression has been achieved.

(2) With the new target chamber, better sensitivity can be achieved because the detector can be brought very close to the target which improves the efficiency of the collection of X-rays. The automatic remote control target changer accommodates 80 targets, and thus allows a maximum number of targets to be analysed sequentially with a minimum of machine down time.

(3) It allows for a normalization of measured spectra to the total beam charge without dead time corrections.

(4) It is fully automated.

(5) Minimum target damage, which is important for thin biological samples and other heat sensitive samples.

A photograph of the general irradiation facility is given in Figure (4.9a).

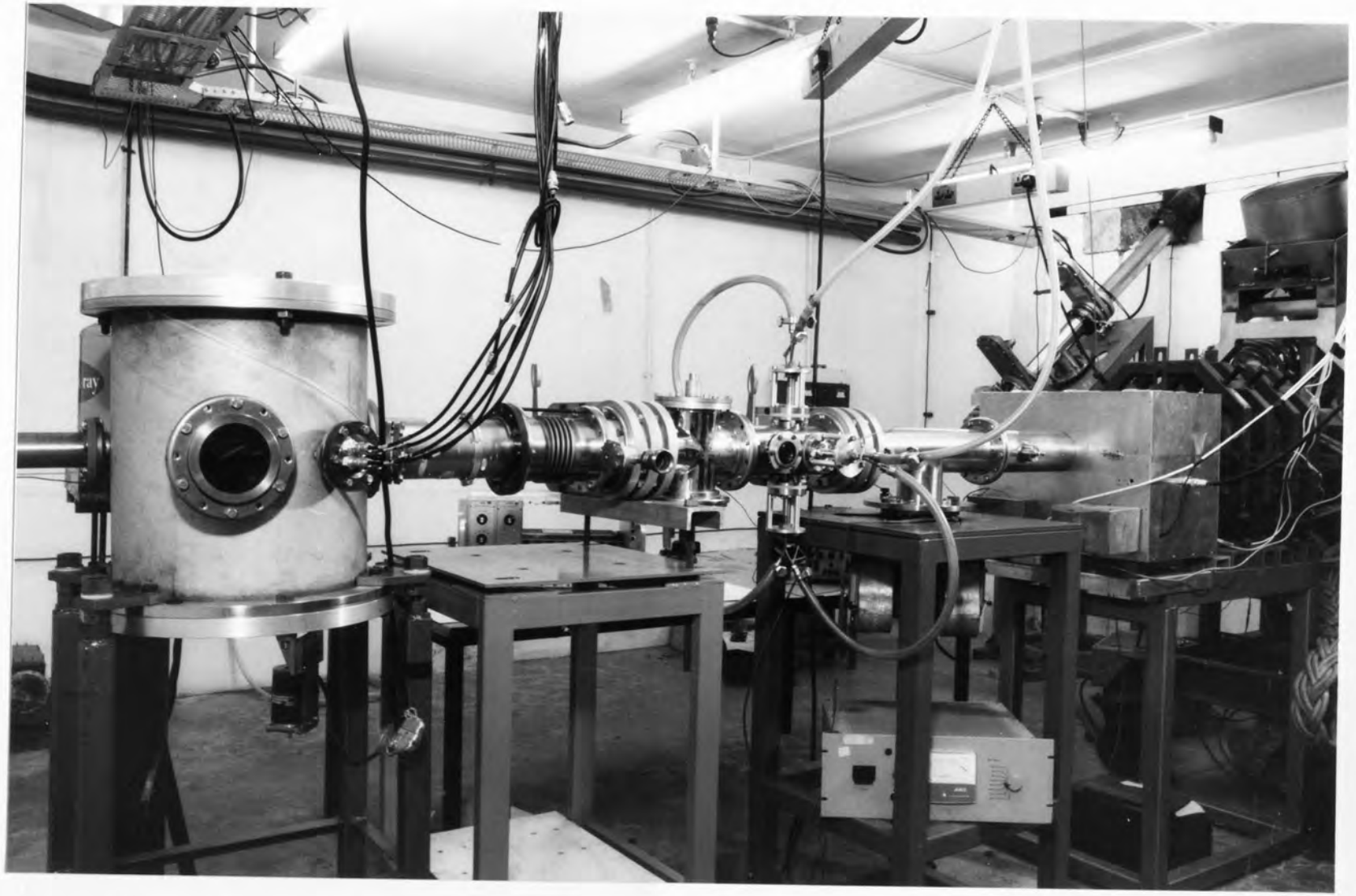

Figure (4.9a) A photograph of the PIXE facility.

4.6 THE ELECTRONIC SYSTEM FOR BEAM PULSING

Several electronic circuits have been investigated in the current study to find a satisfactory way to control the switching of the E.H.T. applied to the deflecting plates.

In order to reduce the chance of pulse pile-up, the propagation delay time from the instant of the first detected event to the time at which the beam is effectively deflected off the target should be minimised. A method of switching the beam off the target is thus required which will, ideally, complete the cycle in less than a microsecond, so as to offer some advantage over the PPR unit as discussed earlier. A number of electronic circuit designs, needed to control the deflection, are discussed in detail in this section. Figure (4.10) illustrates the block diagram of the on-demand beam pulsing electronics employed in the present work.

The proton beam passes through a set of two deflecting plates which are normally both at a high positive potential. Whenever an event is detected, the resulting pre-amplifier signal is shaped by the fast amplifier and discriminator unit. Then, with a variable pulse stretcher, the pulse is stretched to allow the total deflection time of the beam to be controlled. The resulting signal triggers the beam pulsing electronics (BPU), which grounds one of the deflecting plates. The deflected beam is stopped in a beam dump collimator (Section 4.3.3 (c)) for a period of time, until

the main amplifier and multichannel analyser shapes and analyses the signal

Both high voltage switching and time base transistors were tried as switching elements. Two configurations were tried on each of these switching elements. The first consisted of a single transistor with a grounded emitter, and the second, a Darlington pair. Each had a resistive collector load, with a small (25 pF) capacitor to represent the deflecting plates. The Darlington circuit had a switching time of about 8 μsec and the single transistor had a minimum switching, plus delay time before switching, of 2 - 5 μsec. Charge storage in the base was thought to be responsible for the slow response time, which was in excess of the desired time of less than one microsecond.

A high power high voltage thermionic valve (PL 519) was tried and found to have a delay time of less than 200 nsec and a switching off time of less than 500 nsec. This was then developed into a switching circuit (BPU) that could be triggered by a TTL logic signal. The description of the circuit used in the present work follows. The electronic circuit of the beam pulsing unit (BPU) consists of a high speed optocoupler (HCPL - 2601). This unique integrated circuit provides maximum DC and AC circuit isolation while achieving TTL compatibility. The isolation and coupling of this device is achieved with a typical propagation delay of 95 nsec. The output of this device is fed into two parallel VMOS - Field Effect Transistors. VMOS - is a

majority carrier device, and its charge carriers are controlled by an electric field. Their switching delay time is small, (several nsec). The high input impedance and the high speed of VMOS makes it ideal as a switch, as it will interface any driver capable of a 5V - 30V swing to nearly any load requiring high current. Furthermore, the lack of failure from secondary breakdown means that it can withstand high voltage currents simultaneously.

CMOS-logic makes an ideal driver for VMOS since no interface components are required. The switching speed is increased when several CMOS-gates are paralleled to increase the drive current to the VMOS F.E.T.

A logic low to the input of the CMOS,(4011B), turns ON the device while a logic high turns the device OFF. These logic gates are introduced between the optocoupler and the VMOS, (VN88AF).

The drain of each VMOS device is connected to the cathode of two parallel power tubes (PL519). These power tubes are connected to one of the deflecting plates in order to achieve a faster switching off time. With a positive 5 volt on the Gate (G) of the VMOS devices, the drains (D) of the same devices will switch on the power tubes, make them conducting, and discharge one of the deflecting plates to the ground. These plates are normally both maintained at a voltage of 2.5 - 3 kV. The electronic circuit diagram of the BPU has been built as shown in Figure (4.11). This circuit is triggered by a +5 volt fast rising step pulse of 0.5 μsec

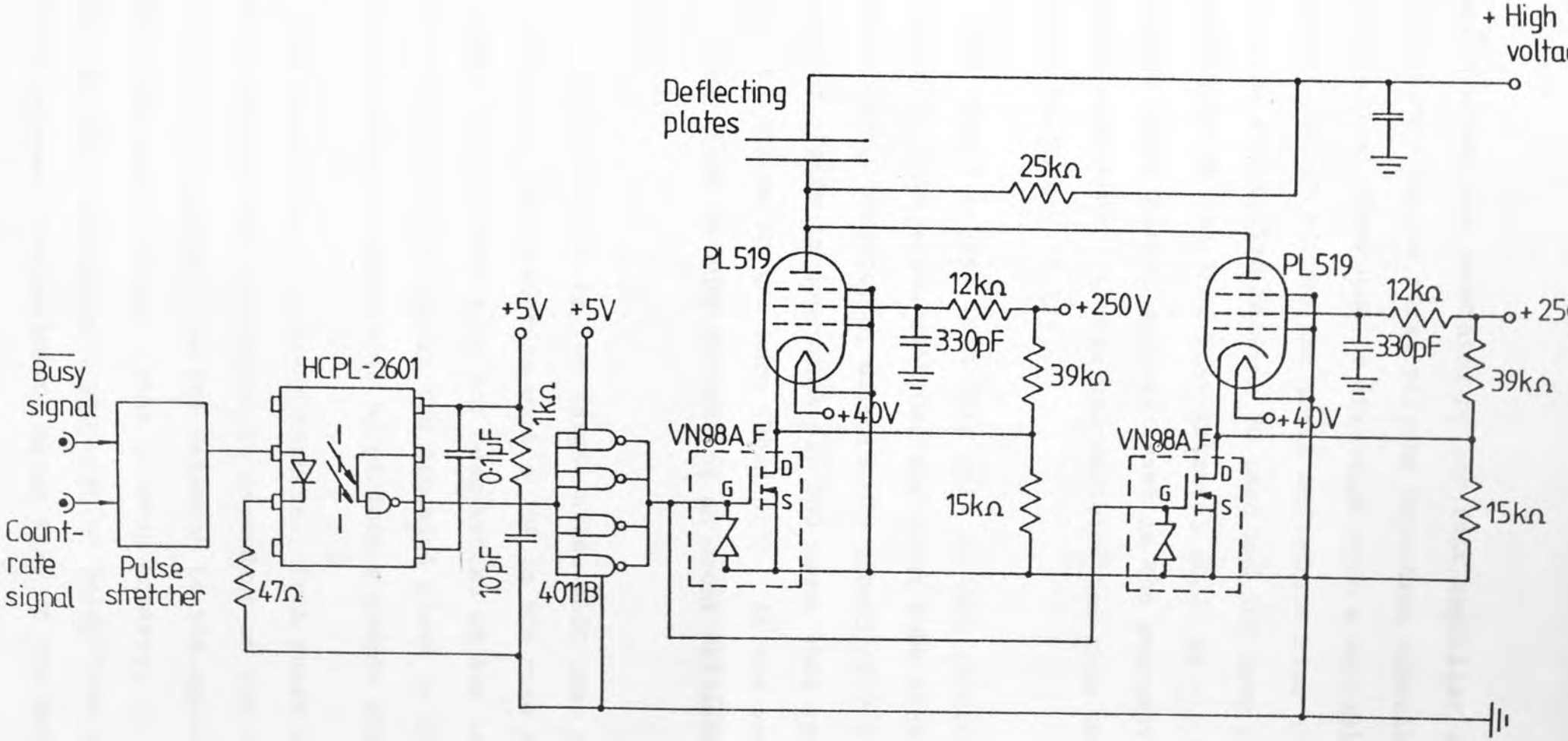

Figure (4.11) Electronic circuit of the beam pulsing unit (B.P.U.).

duration which was generated by the fast amplifier and discriminator in the pulse pile-up rejection circuit. The control signal generated is stretched with a variable pulse stretcher, which allows the total deflection time of the beam to be controlled between 20 μsec and 100 μsec plus the duration of the long busy interval (0.25 ms - 1 ms) following every pulsed optical reset in the pre-amplifier. A simple electronic circuit was designed for this purpose as shown in Figure (4.12).

The output signal from this unit in turn controls the beam pulsing unit which switches the power tube into a state of heavy conduction, effectively grounding one of the deflecting plates in approximately 300 nsec; this results in the deflection of the beam (Beam Off). At the same time as the amplifier is busy processing an event deflection is maintained.

The beam returns to the target after ~100 μsec and the beam intensity then recovers with a 10% to 90% rise time of 5 μsec. The longer time for beam return is due to the longer time needed to return the grounded plate to its initial potential rather than to perform a sudden grounding.

The time delay τ (pile-up interval) from pulse initiation to beam removal from the target is dependent on the time constant of the system from the detector to the application of the deflection voltage. This pile-up interval is given by the sum of the electronic propagation delay time of the detection system, the switching delay time of the deflection

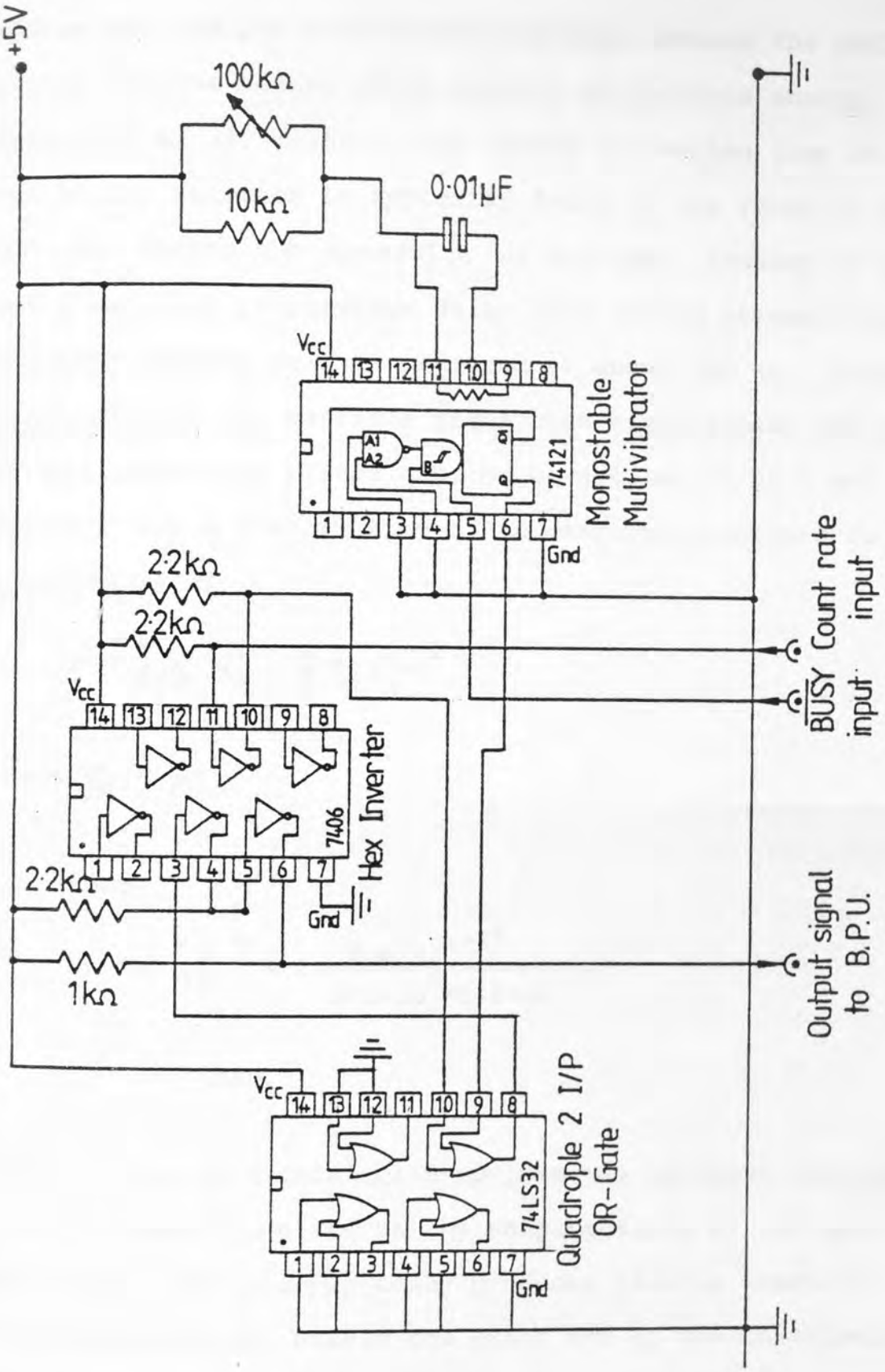

Figure (4.12) Simple electronic circuit of the variable pulse stretcher.

system and the particle transition time between the deflection plates and the target which depends on particle energy, Malmqvist et al. (1982). The charge collection time in the Si(Li) detector is typically lying in the range of 25 to 100 nsec during the detection of an X-ray, Jenkins et al. (1981). The electronic propagation delay time of the preamplifier and beam pulsing unit is measured at about 700 ns. This, combined with the particle transition time between the centre of the deflecting plates and the target, which at 2 MeV protons, has a transit time t is measured according to equation (4.8)

$$K = \frac{1}{2} m_p V_X^2 = \frac{1}{2} m_p \left(\frac{L'}{t}\right)^2$$

where $V_X = \frac{L'}{t}$

Therefore

$$t = L' \left(\frac{m_p}{2k}\right)^{\frac{1}{2}} = 2\left(\frac{1.67\times10^{-27}}{2\times2\times10^{6}\times1.6\times10^{-19}}\right)^{\frac{1}{2}}$$

$$t = 102 \text{ nsec.}$$

This results in a total pile-up interval of about 900 nsec which is small compared to the shaping times of the main amplifier. The pile-up delay produces pile-up counts at energies which are nearly the exact sum of the contributing X-ray energies, the effect of which gives rise to discrete pile-up peaks in PIXE spectra. This may lead to erroneous results if an energy overlap between a trace element peak and a pile-up peak occurs.

4.7 TARGET CHAMBER AND SAMPLE-DETECTOR GEOMETRY

A new versatile target chamber for the PIXE analysis work was installed at the end of the Aston beam line, (designed by Phull (1982) private communication) as shown in Figure (4.13). The chamber was constructed from helically wound stainless steel tube of 14" nominal diameter. Several ports are available in the chamber. The Si(Li) detector port used for X-ray detection, is situated at 90^{o} or 135^{o} to the beam direction. The detector port window is fitted with a 50 μm Melinex window through which the X-rays from the target can be detected.

Facilities for inclusion of silicon surface barrier detectors in the system for beam monitoring and target thickness measurements are also available. In this chamber, an automatic remote control target changer is mounted allowing the sequential analysis of 80 targets without breaking the vacuum, and thus allowing a maximum target throughput with a minimum of machine down time. Better signal-to-noise ratio can be achieved with such a system because it is designed so that the detector can be brought very close to the irradiated target, in or outside the vacuum chamber.

Thick targets typically of 25 mm × 25 mm and 0.1 mm thickness, are mounted on the central recessed target holder. These target holders are made of pure Al of 2.5 cm × 2.5 cm and 2 mm thickness and are specifically designed so they can be mounted in conventional 5 cm × 5 cm slide mounts,

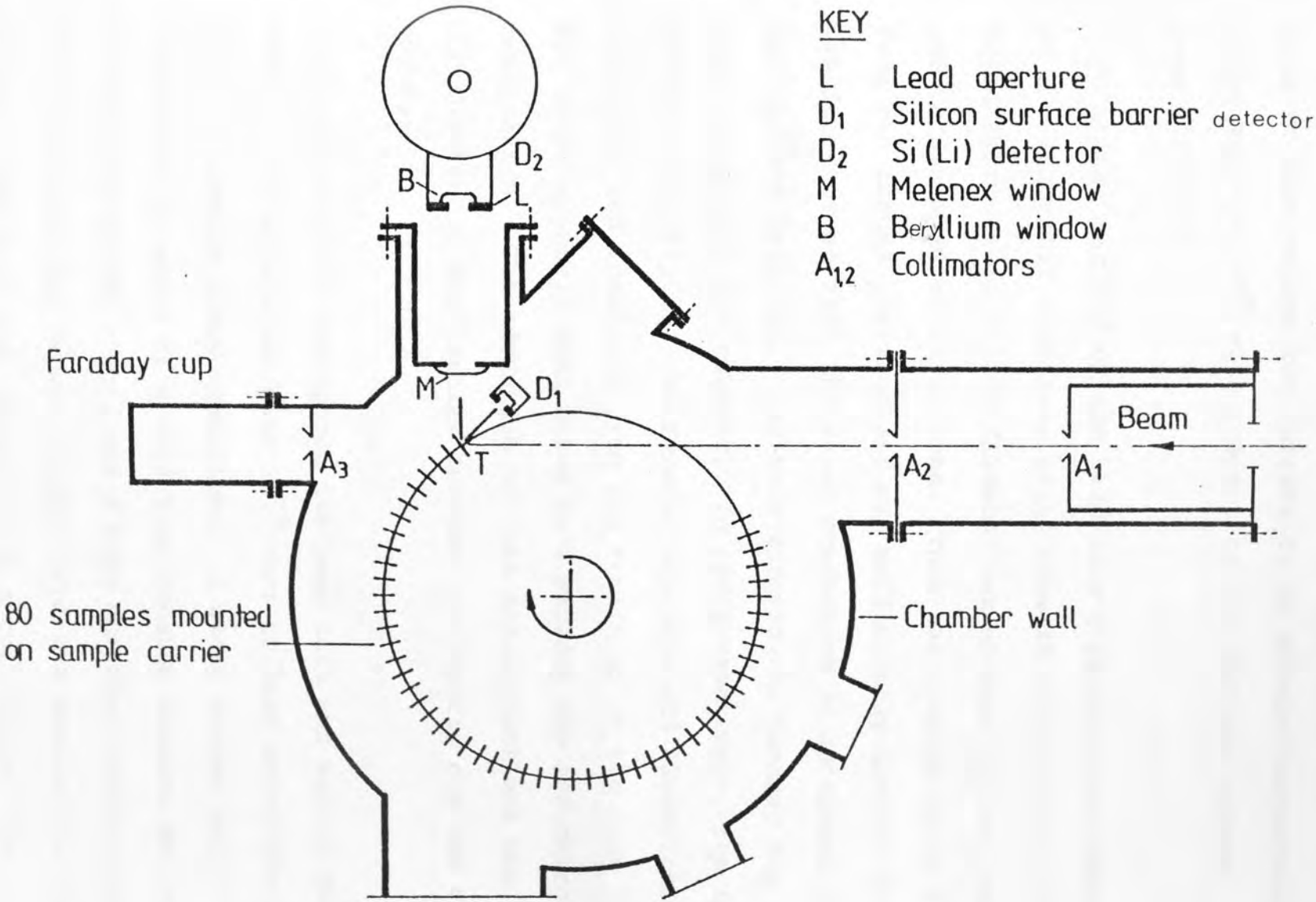

Figure (4.13) Target chamber assembly with multi-sample facility.

80 of which can be carried in a typical slide changer. This in turn guides the targets to be mounted sequentially at an angle of 45^{o} with respect to the incident proton beam direction.

At the far end of the beam line a Faraday cup consisting of a cylindrical stainless steel tube 44 cm long with a fixed aperture of 1.5 cm diameter was mounted at the open end to minimise electron loss. This was located about 15 cm from the target position and was sufficiently distant from the detector so that the X-ray production in and around the cup was not detected. For thin targets, the Faraday cup was used to monitor the current. In the present work, the target chamber assembly and the Faraday cup were all electrically connected and insulated from the remainder of the beam line. The whole assembly then acted as a Faraday cup for charge integration. The advantage of this arrangement was the elimination of the leakage between the Faraday cup and the chamber.

The pressure throughout the beam tube and target chamber was usually maintained near 10^{-5} torr or less using the ion pump to provide clean conditions. A clean system was maintained by means of a cold trap located between the two vacuum gate valves. This was a hand operated vacuum lock which isolated the target chamber from the accelerator vacuum system. The cold trap consisted of a cylindrical tube maintained at liquid nitrogen temperature through which the beam passed. The cold trap reduced condensation of

hydrocarbons on the target and the vapour pressure which protected the accelerator vacuum.

Two collimators preceding the target chamber served to define the incident beam, selecting the central and intense portion. The beam collimator consisted of two tantalum apertures, A_1 and A_2, of 2 and 4 mm in diameter respectively. The aperture A_2, nearest to the target, defined the beam area at the target while A_1, which was electrically connected to A_2, prevented the multiple scattering of protons in the beam line from reaching the target chamber. Also A_2 prevented the secondary electrons released at A_1 from reaching the target chamber. The collimation arrangement A_1 and A_2 precisely defines the beam and can be altered to suit the experimental conditions, and it is continuously monitored by an electrometer in the control room.

The alignment of the collimation system and the centre spot of the target is accomplished with the aid of a laser beam. The laser beam is set up in the same direction as that of the proton beam, and is incident on a plane mirror in place of a target. The specular reflection from the mirror is observed at 90° to the beam direction on a mark on the wall approximately 3 m away from the chamber and in line with the axis joining the chamber and detector.

4.8 DATA ACQUISITION AND ANALYSIS

The data acquisition system used in the present work has been described by Khan (1975), Saied (1981) and Mahrak (1983), and the electronic system concerning the on-demand beam pulsing operation is described earlier in this chapter. Consequently, only a brief description of the acquisition system will be given here.

A block diagram of the data acquisition system and the electronics of the on-demand beam pulsing for the X-ray measurements are schematically shown in Figure (4.14).

A lithium drifted silicon, Si(Li) ,detector detects the X-rays emitted from the target under proton bombardment. Each X-ray entering the Si(Li) detector gives rise to an electrical pulse which is proportional to the energy of the X-ray. These charge pulses were then collected by the applied potential of 1000 Volts. The KEVEX 2002 pulsed optical feedback pre-amplifier, which is an integral part of the detector assembly, integrates the charges produced in the detector and presents them as a voltage signal to the amplifier using a cooled field effect transistor (FET), while retaining the proportionality between the energy deposited and the pulse height. To maintain the DC level, pulsed optical feedback was employed. The output of the preamplifier was coupled to a spectroscopy amplifier (model Kevex 4500P) and to a fast amplifier and discriminator unit. In the first loop the pulses were shaped and amplified before being

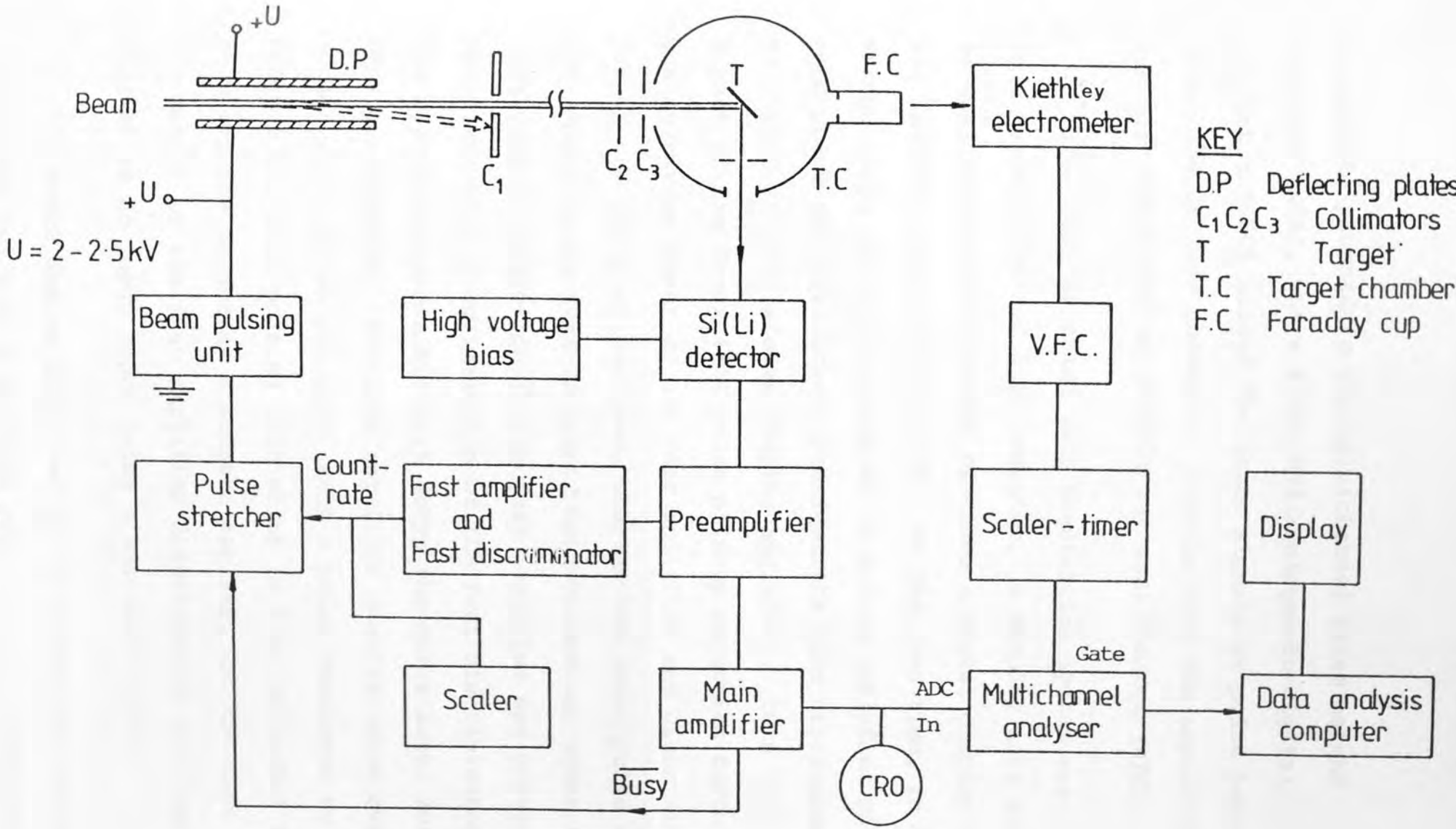

Figure (4.14) Block diagram of the electronics for the X-ray, current integration system and on-demand beam pulsing system.

allowed to proceed to the multichannel pulse height analyser (MCA), where a 200 MHZ analogue-to-digital converter (ADC) sorted the input signals by pulse height into 1024 or 2048 channels. Signals from the amplifier are also monitored on cathode ray oscilloscope (CRO).

This computer based data acquisition system was interfaced to a Hewlett-Packard 2100 computer. A display unit working in conjunction with the ADC provided a visual display of the spectrum being accumulated. At the same time, in the second loop, the pulses, coupled to a fast amplifier with good pulse per resolution, provided the time discrimination of events for the slower shaping amplifier. This unit is a part of the Kevex 4590 pulse pile-up rejection circuits. The resolving power of the fast amplifier and discriminator was of the order of one μsec, whereas the total pulse width of the shaped pulse with an 8μsec time constant was about 80 μsec. Some pile-up rejection in the fast amplifier was provided by pulse width discrimination of the fast discriminator. The discriminator is set just above the noise level for best performance. The fast amplifier discriminator output (count rate) pulse was used, with a pulse stretcher to trigger the beam pulsing unit which in turn deflected the beam off the target as discussed earlier. At the same time the output of the fast amplifier discriminator unit can be counted as an input count using a suitable scaler.

The total charge collected on the target and the target chamber was fed into a Keithley electrometer which generates

a voltage signal for the charge collected. These voltage signals were fed into a voltage frequency converter (VFC), which gave a pulse chain of 10^5 HZ for 1 volt input. A decade dividing unit, taking its input from the VFC, can reduce this frequency in multiples of $\frac{1}{10}$ (i.e. from 10^5 HZ to 10 HZ) in five steps, making it suitable for counting on a scaler. The scaler and divider were linked with an automatic stop device.

Once a preset count on the scaler had been accumulated, the accumulation of the data was stopped automatically. This was directly proportional to the integrated beam charge (IBC), as calculated from the following equation:

$$\text{IBC}(\mu c) = \text{FSD on Keithley } (\mu A) \times \frac{N_2 \text{ dividing factor}}{10k} \times \text{preset counts}$$

The accumulated spectrum data of each analysed sample was stored on a file manager (FMGR); a system for storing source information. These data can be stored on magnetic tape for further analysis at any time. At the same time, a variable software programme was already in the FMGR for spectral analysis and several terminals were available for such analysis.

The K-X-ray spectra, with such a system, are shown in Figure(4.15)for a thick copper target (Z=29) bombarded by a 2 MeV proton beam, showing the reduction of the pile-up continuum with the on-demand beam pulsing operation. The performance of such a system will be discussed in the next chapter.

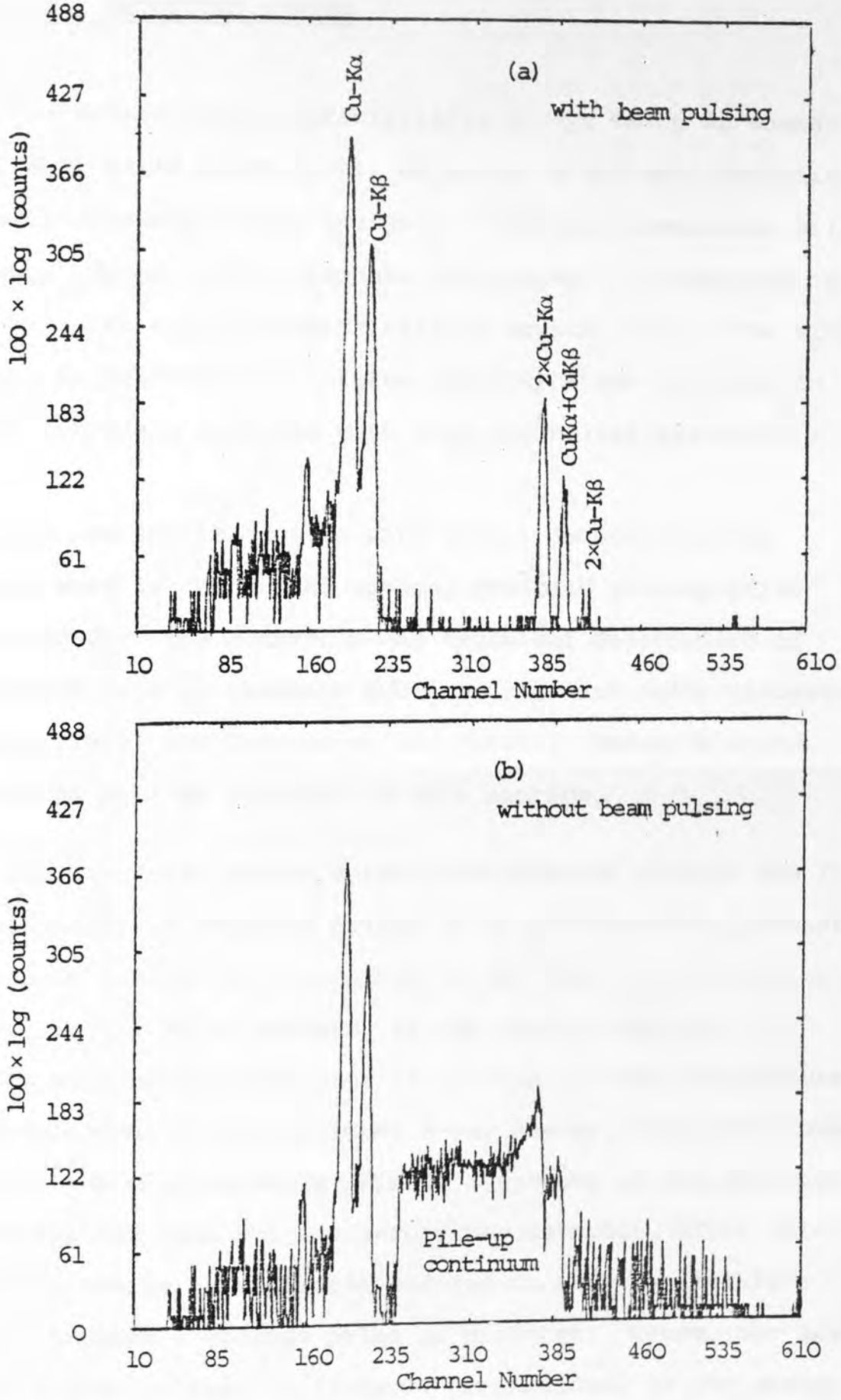

Figure (4.15) Typical K X-ray spectra obtained during equal bombardments of thick copper targets.

4.9 X-RAY DETECTION SYSTEM

The detection of characteristic X-rays using an energy dispersive solid state Si(Li) detector is now well-established in multi-elemental X-ray analysis. The high resolution Si(Li) detector (Kevex, 3201 cryogenic sub-system) comprises a 30 mm^2 area and 3 mm thick silicon crystal disc. The silicon crystal is drifted with lithium impurity atoms in order to create intrinsic material with high electrical resistivity.

The pre-amplifier used with Si(Li) detector in the present work is the pulsed optical feedback pre-amplifier (Kevex 2002). The operation and technical description of the pulsed optical feedback pre-amplifier are fully discussed by Khan (1975) and Jenkins et al. (1981). Hence, a brief discussion will be included in this section.

When an X-ray photon enters the detector through the front contact layer it interacts primarily by photoelectric processes to produce a cloud of ionization in the form of electron-hole pairs. 3.62 eV on average is the energy required to produce an electron-hole pair in silicon at room temperature and is independent of the incident X-ray energy, Khan and Crumpton (1981). The electron-hole pair is swept out of the detector by the applied bias voltage across the detector, after which the total charge is collected and fed to the pre-amplifier stage, in which a voltage pulse is produced. Hence, the level of the output voltage is linearly proportional to the energy of the X-ray absorbed in the detector.

The vacuum of the detection system is protected using a 12.4 μm beryllium window in the front of the detector. In the present work,the detector was placed outside the target chamber in a fixed position at 90^{o} with respect to the incident beam, using the specular reflection of the laser beam from the target. Lead apertures of 3.97 mm were used to define the effective detector area and to mask-off the edge effect, where the effective diameter of the detector has been measured to be about 5± 0.1 mm, Armaghani and Crumpton (1980).

The parameters related to the performance of the Si(Li) detector, such as (a) detector efficiency, (b) detector resolution, and (c) the detector linearity and energy calibration are discussed by Saied (1981), Khan and Crumpton (1981) and recently by Sokhi (1984). A brief discussion will be included here.

4.9.1 Detector Efficiency

For the present work, the use of the intensity ratio of two elements very close in atomic number,eliminates the need to know the detection efficiency absolutely.

However, if the efficiency is required to be known absolutely then it should be measured experimentally. The approach used was recently discussed by Sokhi (1984).

4.9.2 Detector Resolution

Energy resolution is one of the most important characteristics of an X-ray detection system since it sets

the limit on the ability to resolve the peaks from two adjacent elements in the periodic table.

Throughout the work, the resolution of the Mn-Kα line from an Fe^{55} source was measured at full width of the energy peak at half its maximum height (FWHM) to be 174±7 eV at 5.898 keV at 1000 CPS, Figure (4.16) showing the Mn k-X-ray lines.

A comparison of the working resolution with an earlier measurement of 164 eV by Sokhi (1984) showed a deterioration of about 6% of the resolution, an extent not great enough to make it unworthy of measurement in PIXE analysis.

The resolution for Kα lines of adjacent elements and Kα and Kβ lines of intermediate and high Z elements is such as to be resolved with the present system. However, Saied (1981) and Mahrok (1983) have discussed the limitation on X-ray detection of the present system due to

(i) incomplete charge collection,

(ii) high counting rate, and

(iii) the limited resolving power of Si(Li) detected making line interference unavoidable.

However, interference encountered between the Kβ of element Z and the Kα of element Z+1 and also the interference due to K and L lines of widely different Z was discussed fully by Saied (1981). Counting rate limitation and the pulse pile-up problem have been improved by the application of on-demand beam pulsing system as discussed earlier in this chapter.

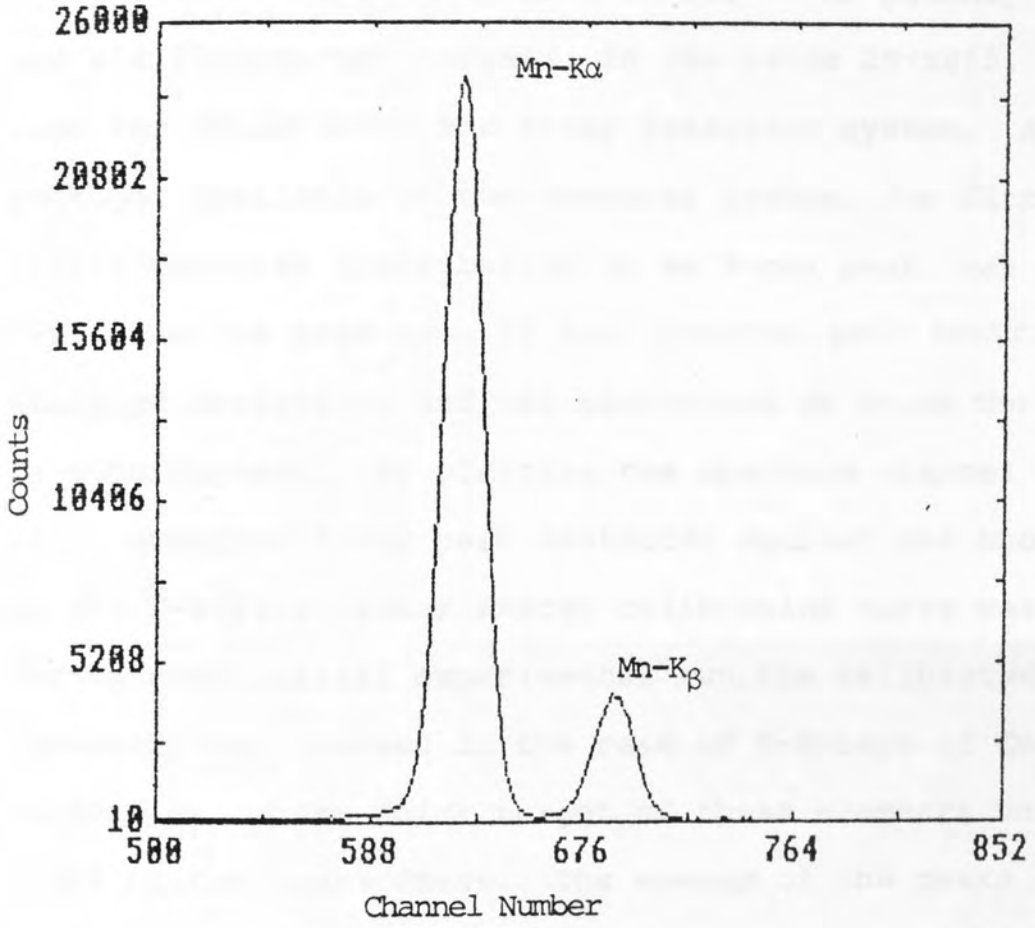

Figure (4.16) Mn K X-rays detected with a Si(Li) detector using Fe^{55} sources.

4.9.3 Energy Calibration of the System

The energy calibration of a detection system is essential for identification of elements represented by peaks in a spectrum . The X-ray spectra from a variable X-ray source, consisting of a 10 mCi ^{241} Am primary source and six fluorescent targets, in the range $29<z\leq65$, were used for calibrating the X-ray detection system. A software package, available on the computer system, for fitting a single Gaussian distribution to an X-ray peak, was used to determine the peak area of the spectra, peak centroids, standard deviations and the background on which the X-ray peak is superimposed. By plotting the spectrum channel number of observed X-ray peak centroids against the known energy of the X-ray, a linear energy calibration curve was obtained. During each initial experimental run, the calibrated linearity was checked in the case of K-X-rays of Cu and Fe, emitted by a pure thick target of these elements under 2 MeV proton bombardment. The energy of the peaks was found to lie on the line, interpolated between the peaks from 10 mCi ^{241}Am source, as shown in Figure (4.17).

With a least square method the following equation was obtained by fitting a linear model to the data.

$$Y_X \text{ (keV)} = 0.1926 + 0.0372\ X \qquad (4.13)$$

where Y_X is the X-ray energy and X is the centroid of the X-ray peak. The linear-correlation coefficient, r, may be calculated to estimate the degree of linear correlation.

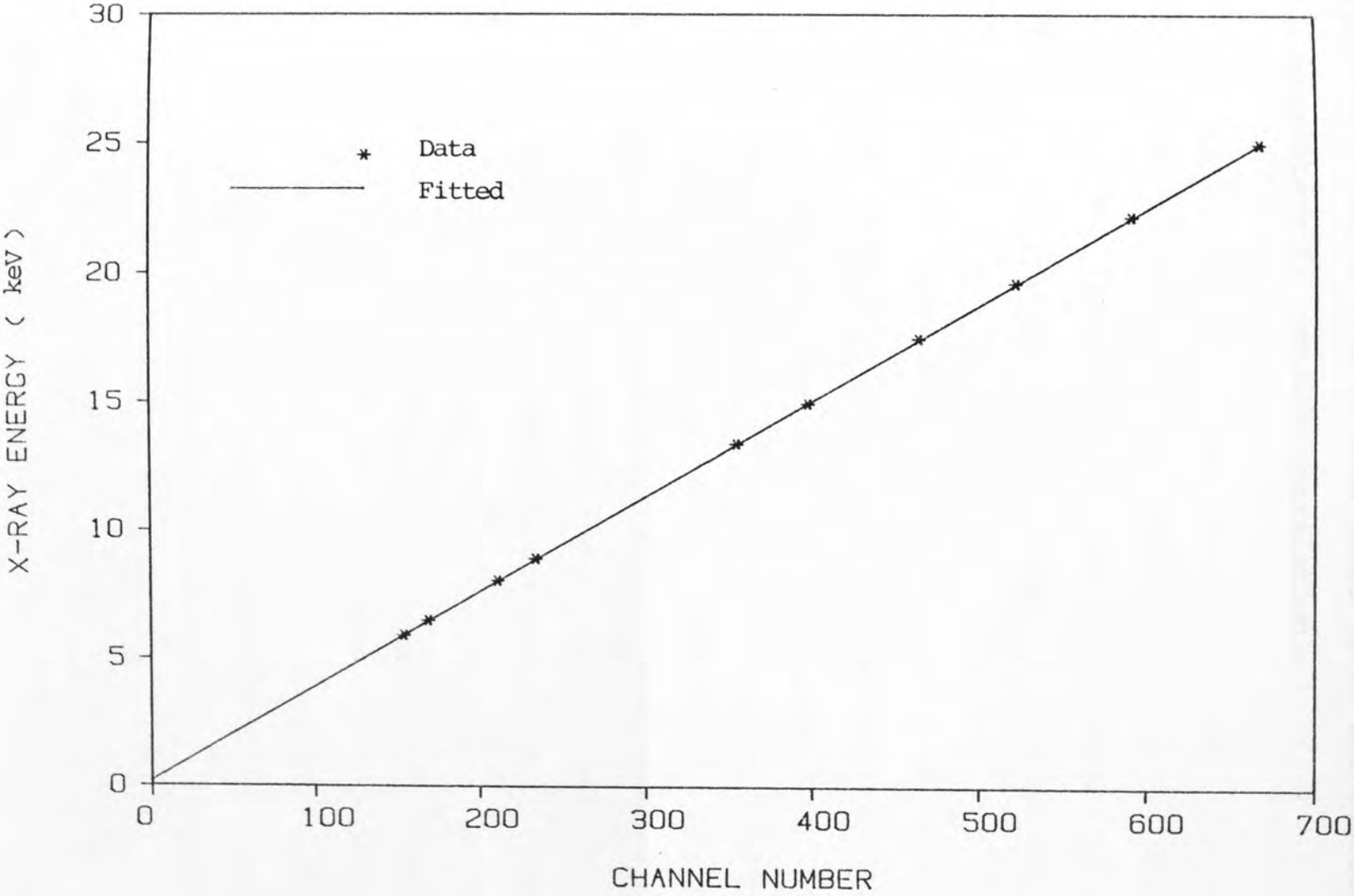

Figure (4.17) Energy calibration curve (error bars were omitted since they were smaller than the symbol size)

A value of 0.9999 was obtained for equation (4.13). The value of r ranges from 0, when there is no correlation, to ±1, when there is complete correlation.

CHAPTER 5

PERFORMANCE OF ON-DEMAND BEAM PULSING SYSTEM

5.1 INTRODUCTION

Pulse pile-up phenomena can cause severe problems in analysing a spectrum. The pulse pile-up is the continuum which extends from just above the characteristic X-ray peaks to the pile-up doubling peaks which represent an energy equivalent to twice the original peak energy. In this energy region, this continuum weakens the statistical precision and detection limit for trace element analysis.

Saied (1981) has shown that interference between the strong Ca Kα line (3.62 keV) in kidney stone samples produces a pile-up peak at 7.38 keV, which may be misinterpreted as the Ni Kα line (7.48 keV) as shown in Figure (5.1); at the time, all elements between Ca Kα - line and its doubling peak could not be identified and quantified satisfactorily. This effect can be minimised by either decreasing the counting rate (to less than 1000 c/sec) which increases the analysis time required to obtain the same statistical accuracy, or by reducing the shaping time constant of the amplifier which degrades the energy resolution (Chapter 4, section 4.1). This operational parameter may have to be selected as a compromise consideration. A commercial P.P.R. can also be used to reduce this effect.

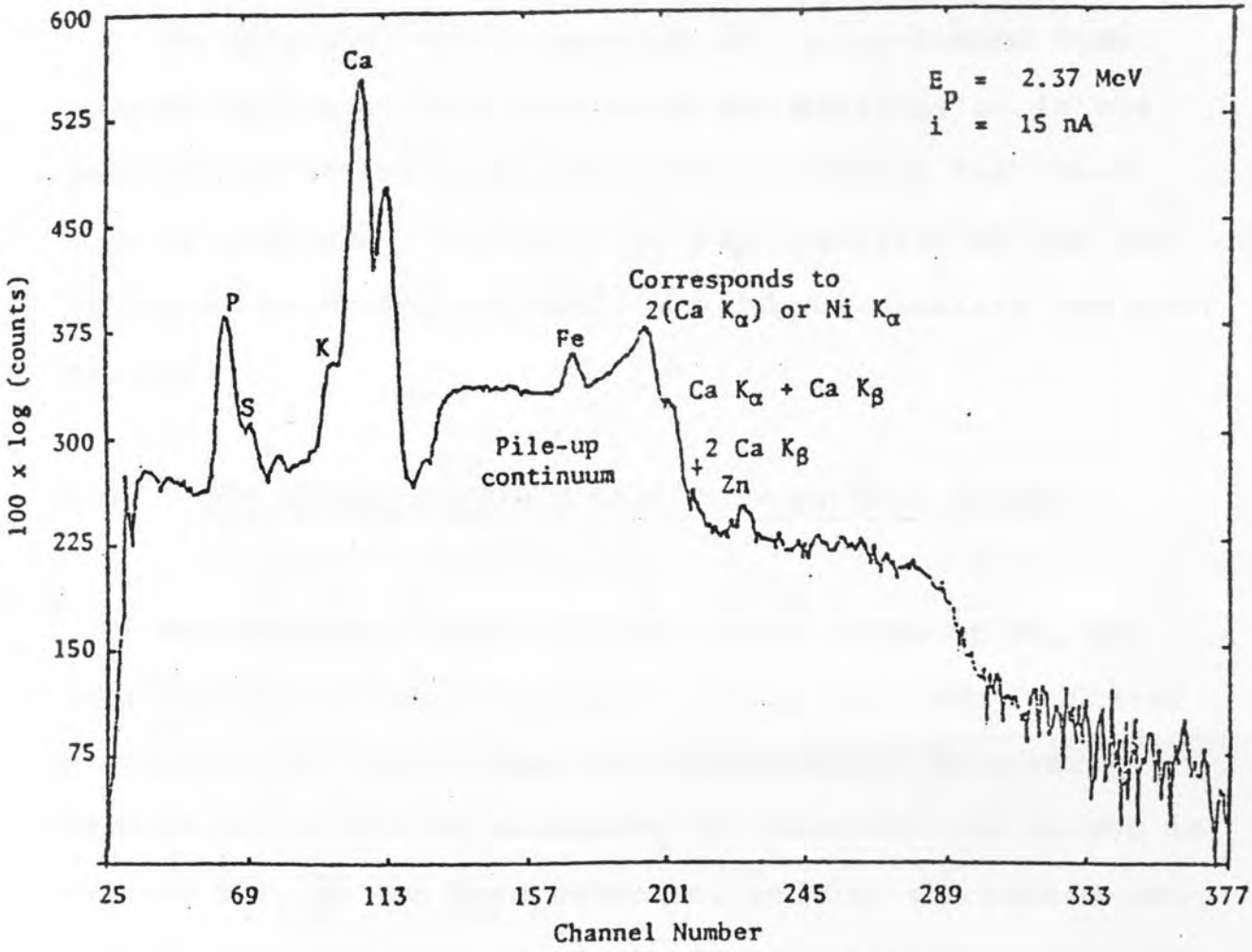

Figure (5.1) PIXE spectrum of bladder stone. Accumulated at high count rate, the effect of pile-up of Ca peak is shown, starting from Ca X-ray energy up to twice that energy. (Saied (1981)).

In this chapter, the signals of the on-demand beam pulsing system are discussed.

In addition, the properties of the on-demand beam pulsing system are evaluated and the degradation in the performance of the X-ray detection system at high count rate is indicated. To test the applicability of the new system as an analytical tool, the reproducibility has been studied.

5.2 THE SIGNAL SEQUENCE WITH BEAM PULSING SYSTEM

The on-demand beam pulsing system (Chapter 4), can greatly improve the performance of the most sophisticated processing unit for pulses by a solid-state detector. This is the method of switching the beam off the target as soon as a pulse has been detected, so that the pulses can then be measured with no possibility of interference. The beam is switched back on to the target again after a time τ_d at which time the electronics are ready to process another pulse. The resultant waveforms and logical signals produced by the detection system, the processing unit, and the beam pulsing unit are discussed as follows.

The Kevex 2002 pulsed optical pre-amplifier integrates the charges produced in Si(Li) detector and presents them as a voltage signal to the amplifier. The

voltage, in the first stage of the pre-amplifier, (FET), is allowed to build-up in a step formation to a certain level, at which point a level sensor triggers a light emitting diode, Figure (5.2). Light shines momentarily on the FET drain gate junction and makes it conductive and the capacitance discharges. The Kevex 2002 pre-amplifier gives an output with negative reset pulses, Figure (5.3a). The pre-amplifier detector signal is split (see Figure (4.10)) into pulses fed:

(1) to the main amplifier to amplify and process them in order to make them compatible with the subsequent data analysis and storage system. The amplifier uses a long shaping time constant for efficient noise suppression. The total width of the shaped pulse (τ_d) is 10 times the time constant, Figure (5.3b). The output pulses are flat topped and of 2 μsec duration, Figure (5.3c).

(2) and to the fast amplifier and discriminator circuit of the PPR unit. A fast pulse of 0.5 μsec duration is generated by this unit (count rate), Figure (5.3d).

A pulse stretcher unit (see Chapter 4) stretches the fast pulses in a time corresponding to the long shaping time τ_d of the main amplifier, and is further extended for every pulsed optical reset time, Figure (5.3e). In

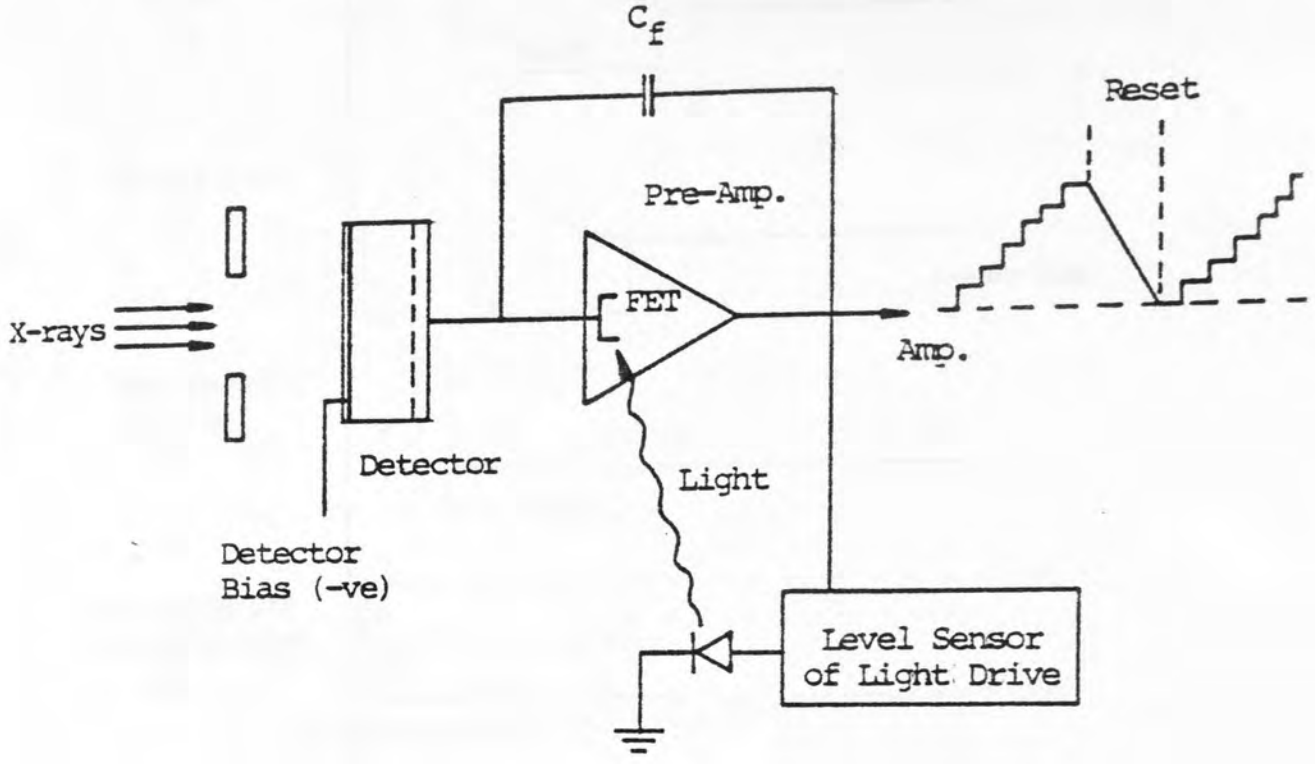

Figure (5.2) Pulsed optical feedback pre-amplifier (Kevex 2002)

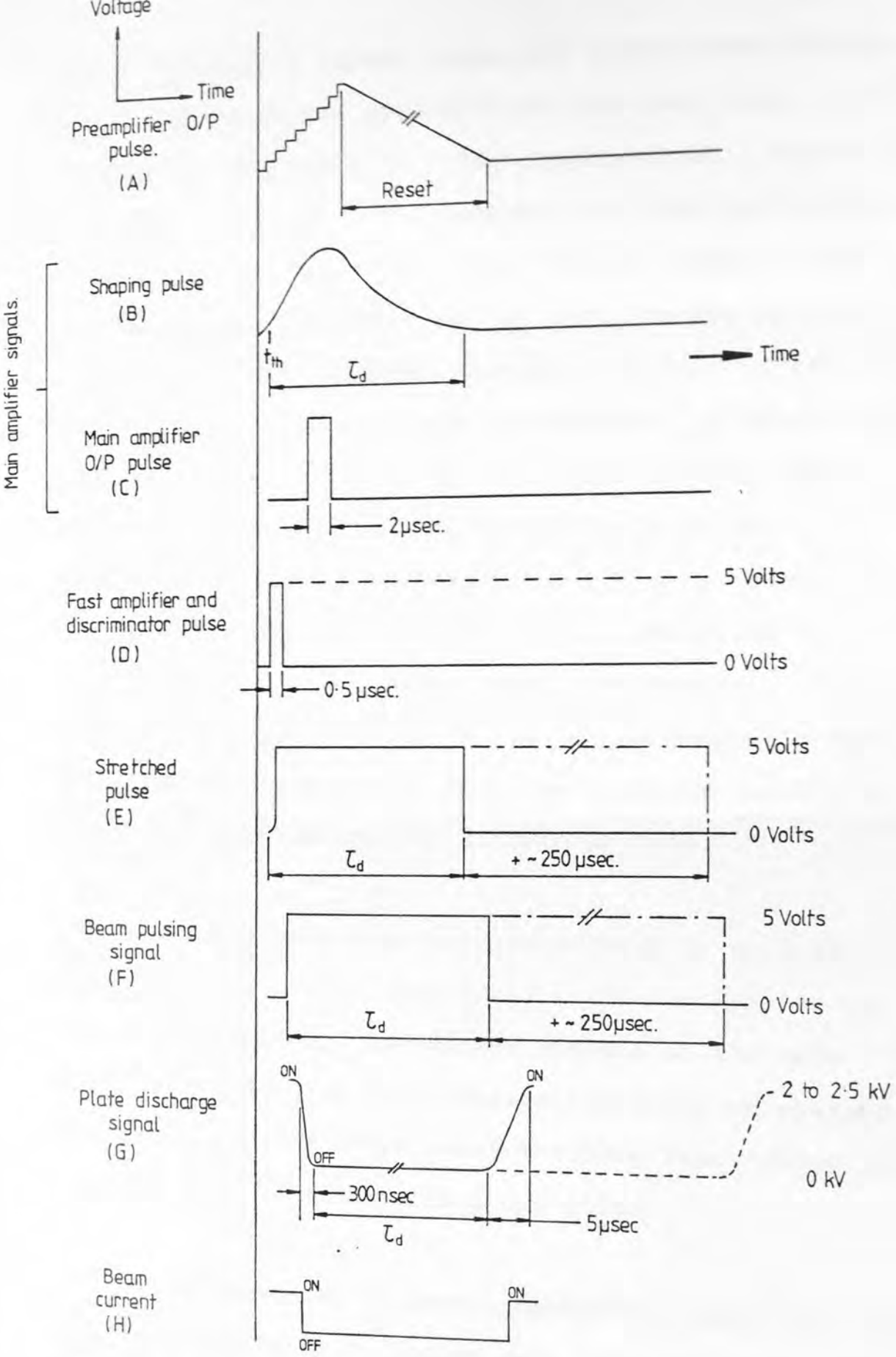

Figure (5.3) Signals occurring in the X-ray detection system during the beam pulsing operation.

order to prevent ground loops and common mode signals, a high speed response opto-isolator has been used, (see Chapter 4, section 4.5). The output signal, Figure (5.3f) from this unit, in turn, controls the beam deflection (Chapter 4, section 4.5). The voltage signal on one of the plates was monitored on the oscilloscope and showed that the plate discharges in about 300 ns, Figure (5.3g). Each time an X-ray is detected, it causes the proton beam to be deflected to a well-shielded beam stop. This beam is maintained on the beam stop for a time proportional to the processing time of the X-ray signal. During this time, further events will not occur. After this, the beam is automatically returned to the target to produce a new X-ray. Figure (5.3h) shows that the measured current on Keithley is zero during the deflection time.

The great advantage of beam pulsing is demonstrated in Figure (5.4), when bombarding a thick copper target with 2 MeV protons. The output signals of the main amplifer shown on an oscilloscope and their corresponding X-ray spectrum are taken under the same input count rate with and without beam pulsing operation.

It is important to have a method to check that the beam is being fully deflected away from the target and stopped by the beam dump when an event arrives at the X-ray detector. This is done by feeding the detector signal

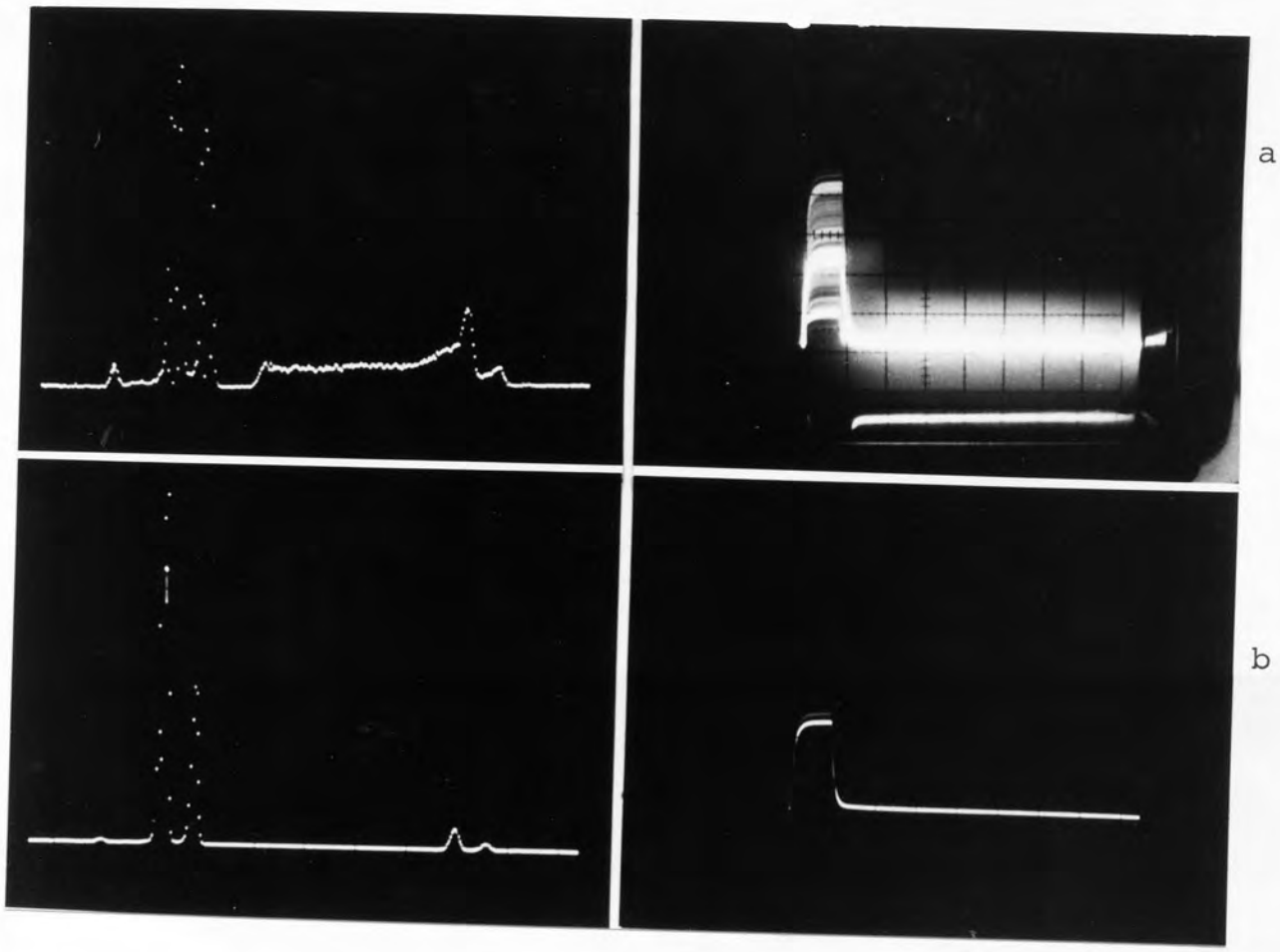

Figure (5.4) The display of typical PIXE X-ray pulses and spectrum from thick copper target bombarded with 2 MeV protons

(a) Without beam pulsing operation

(b) With beam pulsing operation using 8 μsec amplifier time constant.

from the first stage of amplification to an oscilloscope in the data collection room in such a way that this signal triggers the oscilloscope. When the system is working correctly in the beam pulsing mode, a pulse is seen followed by about an 80 μsec interlude, and then additional pulses are seen at quasi-random intervals centred around multiples of 80 μsec, Figure (5.5a and 5.5b). If the system is operating poorly or not at all, pulses will arrive continuously from the detection system as shown in Figure (5.5c).

5.3 PROPERTIES OF ON-DEMAND BEAM PULSING OPERATION WITH X-RAY AMPLIFIER (KEVEX 4500P)

The properties of the beam pulsing system (B.P.S.) have been investigated by bombarding a thick copper target with 2 MeV protons, with an amplifier shaping time constant of 2, 4 and 8 μsec.

The beam-off time corresponds to the total pulse width of the shaped pulse (20 to 80 μsec duration) and to the pulsed optical reset time. This has been accomplished by using the stretcher unit (see Chapter 4). Thus, the actual beam-off time is long enough to allow for a maximum pulse processing time in the amplifier and multi-channel analyser (MCA) and to prohibit counting losses with beam pulsing. Therefore, dead time corrections are not required for the normalisation of measured spectra to the total beam charge.

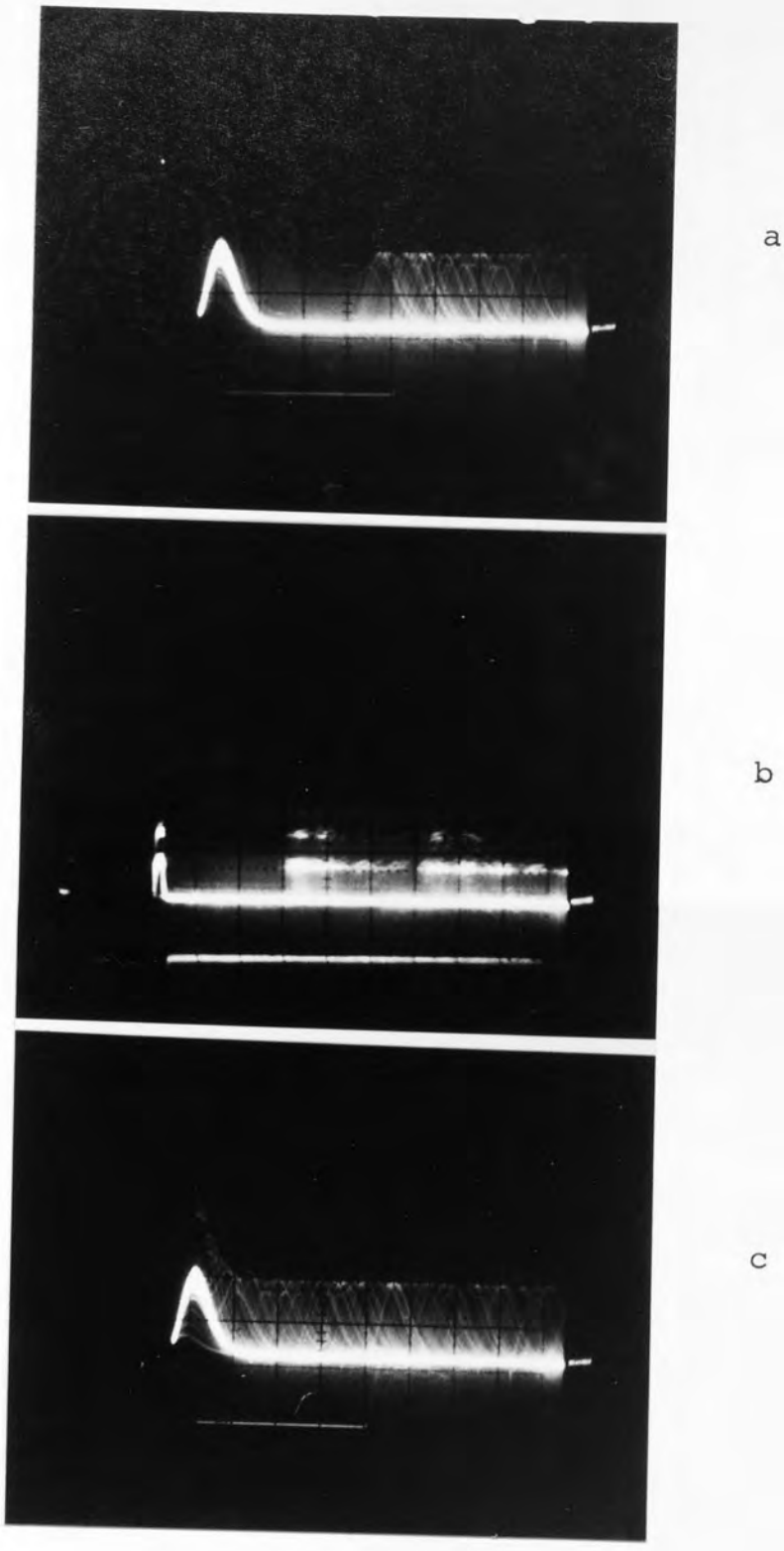

Figure (5.5) Fast amplifier signal which detects each X-ray event at the first stage of the 4525P processer (count rate) shows,

(a,b) - with beam pulsing operation

(c) - without beam pulsing operation

The number of pulses per unit of time is recorded using a suitable scaler to set the fast discriminator threshold just above noise level and is called the input count rate. The output count rate is defined as the number of counts processed by the MCA per unit time.

The characteristics of the beam pulsing system have been evaluated by observing the proton-induced X-ray emission from spectroscopically pure elements under a variety of conditions, with and without beam pulsing. A typical X-ray emission spectrum obtained using a thick copper target bombarded with 2 MeV protons is shown in Figure (5.6), under

(a) continuous proton bombardment and no pulse pile-up rejector,

(b) on-demand beam pulsing irradiation and no pile-up rejection (Kevex 4500P Amplifier), and

(c) the simultaneous use of on-demand beam irradiation and electronic pile-up rejection (Kevex 4525P Amplifier),

where the total input count rate in each spectrum is about 4500 count per second. In Figure (5.6b), a drastic suppression of the continuous pile-up can be observed with on-demand beam pulsing irradiation as compared to Figure (5.6a). The system cannot of course remove sum and triple sum peaks which are dependent on the counting rate and the

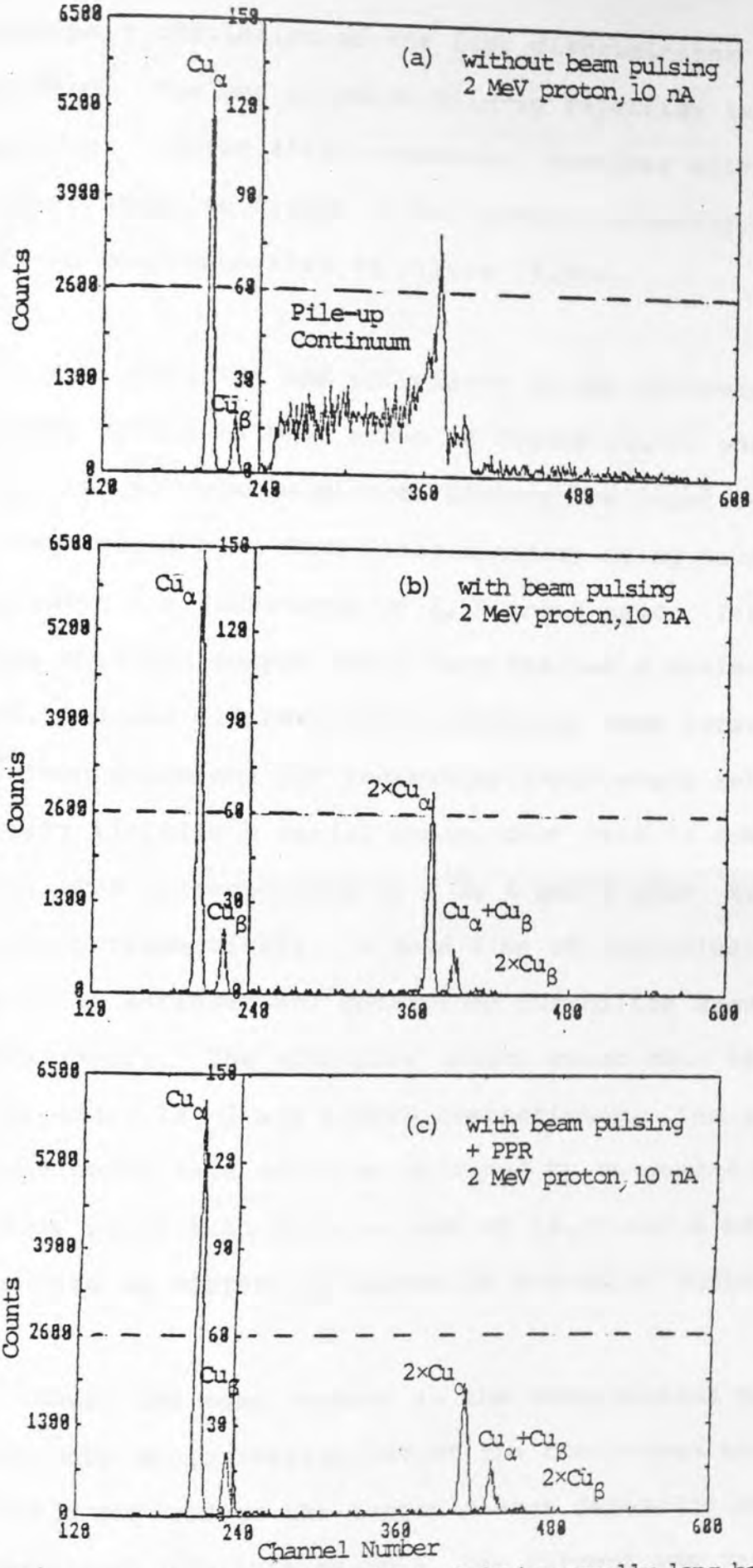

Figure (5.6) The spectra obtained during equally long bombardments of thick Cu-target using an amplifier time constant of 8 μsec.

pulse-pair resolution of the fast discriminator employed. The use of pulse pile-up rejection in the main amplifier (Kevex 4525P processor) together with on-demand beam irradiation Figure (5.6c) gives a slightly lower pile-up continuum than in Figure (5.6b).

The operation and efficiency of the on-demand beam pulsing system is best shown in Figure (5.7), where the output count rate is plotted against the input count rate as determined by a fast discriminator, using main amplifier time constants of 2, 4 and 8 μsec. Figure (5.7) shows that the output count rate reaches a maximum of 14.5, 8.3 and 4.5 kPPS with continuous beam irradiation, and then decreases for increasing input count rate, thereby limiting a useful input count rate to some 23, 13 and 7 kPPS corresponding to a 2, 4 and 8 μsec time constant respectively. A dead time of approximately 50% has to be suffered and determined during the above measurements. The effective output count rate is recorded to be about 13, 7 and 4 kPPS respectively. The same output count rate could be obtained by on-demand beam pulsing which also gives a rate of 13, 7 and 4 kPPS and in this case no current is wasted in producing photons.

Thus, the mean current in the beam pulsing situation needs only approximately 50% of the continuous beam value and this may reduce the target damage depending on the target used. In this example, the current was recorded

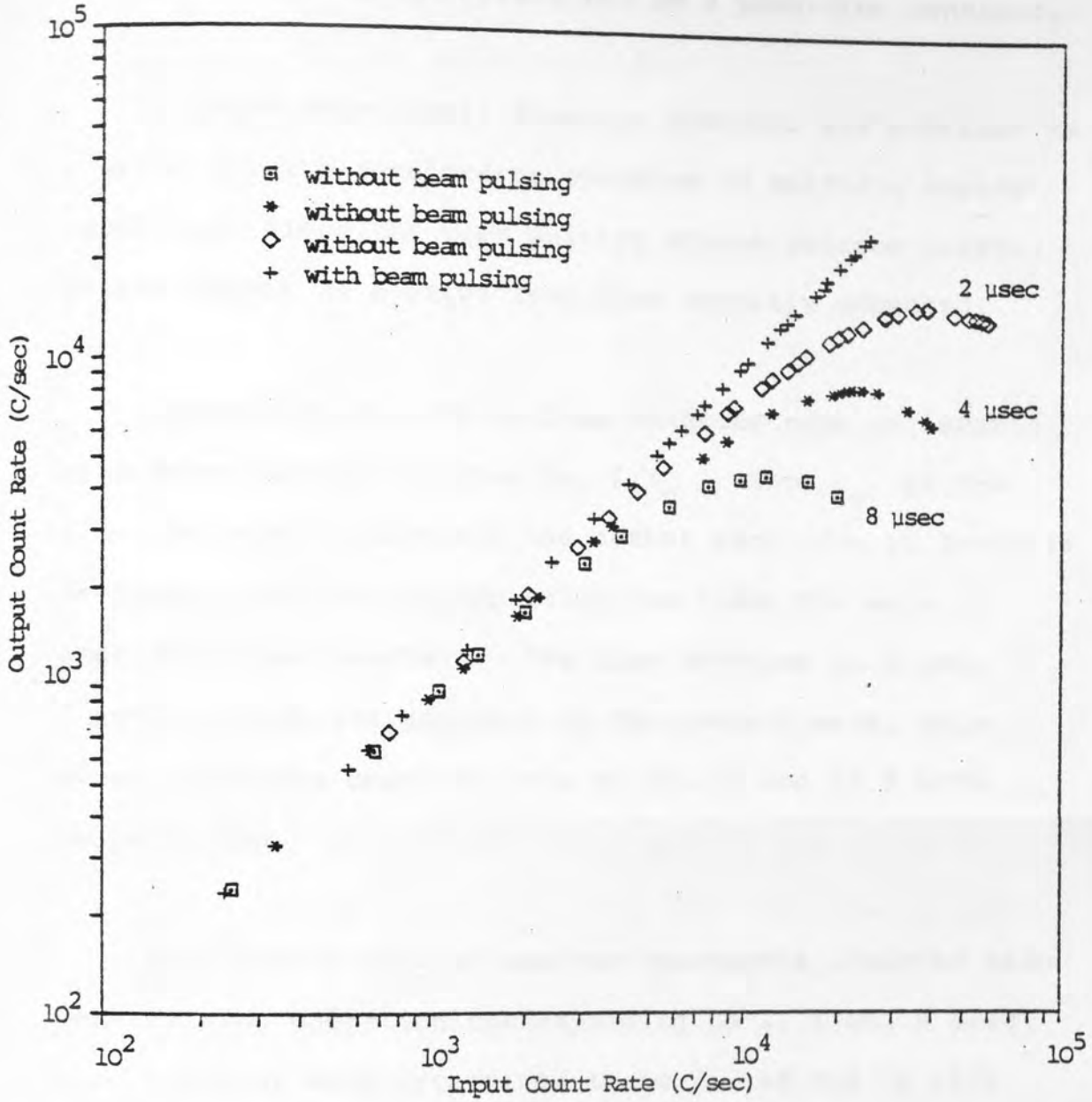

Figure (5.7) The observed total count rate from Cu target plotted against the input count rate at different amplifier time constants, with and without beam pulsing operation.

for both the continuous and pulse beam irradiation to be 17 nA and 10 nA respectively for an 8 μsec time constant.

A count rate signal from the detector was provided as a guide for the accelerator operator to maintain steady conditions since the beam pulsing system reduces current on the target to a value less than normally expected.

Theoretically, the maximum counting rate achievable with beam pulsing is given by $1/\tau_o$, where τ_o is the time the beam is kept off the target each time an X-ray is detected, and this is typically ten times the main amplifier time constant. For time constant 2, 4 and 8 μsec , which are employed in the present work, this gives a maximum counting rate of 50, 25 and 12.5 kPPS respectively.

Experimentally, the maximum countingrate achieved with beam pulsing operation corresponding to 2, 4 and 8 μsec time constant were determined to be 25, 18 and 10 kPPS respectively. The discrepanciesbetween the experimental maximum count rate achieved with beam pulsing operation and the theoretical one were due to:

(a) the uncertainty in the time constants employed which is in order of ±5%;

(b) the uncertainty associated with τ_o, which was adjusted by the stretcher unit in order to keep the beam off the target for the time of 10 × the amplifier time constant employed;

(c) the time delay in switching the beam back on the target, which was typically a few μsec.

All these factors can add to the actual beam off time and limit and the maximum counting rate as stated above.

Figure (5.8) shows the theoretical curve for the maximum output count rate with beam pulsing operation against the time constant. For a 2 μsec time constant, the change in the count rate for a 1 μsec change in time constant is of the order of 46%, whereas the percentage change in maximum ouput count rate per μsec at 8 μsec time constant is only 13%. This demonstrates the sensitivity of the maximum output count rate for different time constants employed in the present system.

In addition, the performance of Si(Li) detectors deteriorates at high count rates. Peak centroid shifts and resolution degradation are observed in the spectrum. These effects are discussed in the next section.

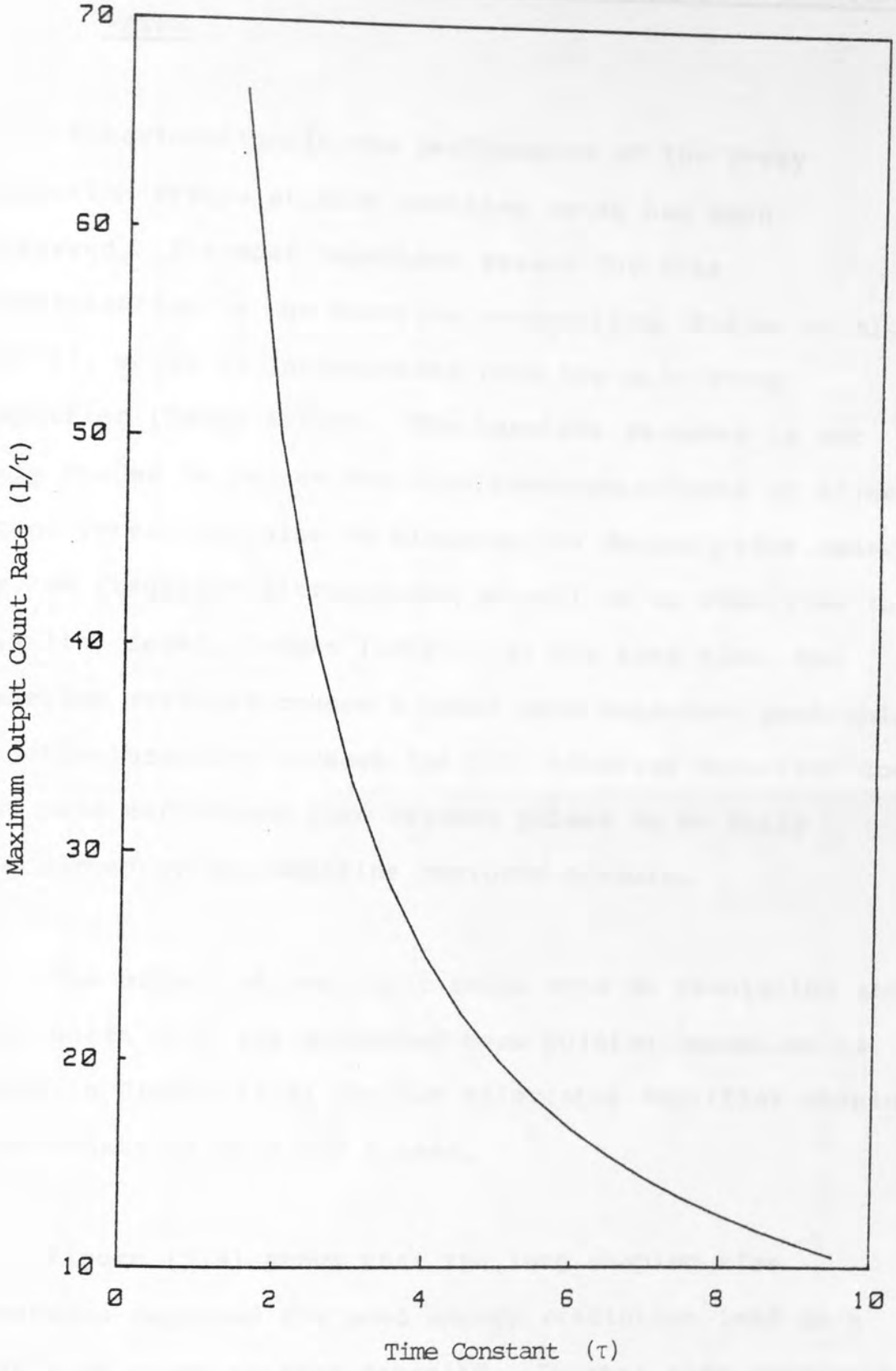

Figure (5.8) Variation of the maximum output count rate ($1/\tau$) at different amplifier time constant (τ) calculated with beam pulsing condition.

5.4 ENERGY RESOLUTION AND PEAK SHIFT AT HIGH COUNTING RATES

Deterioration in the performance of the X-ray detection system at high counting rates has been observed. The most important reason for this deterioration is the baseline restoration, Gedcke et al. (1971), which is incorporated into the main X-ray amplifier (Kevex 4500P). The baseline restorer is not only needed to reduce the line broadening effects of higher count rates, but also to minimise the degradation caused by low frequency microphonics as well as to stabilise the baseline level, Gedcke (1972). At the same time, the baseline restorer causes a count rate dependent peak shift and line broading because the D.C. blocking capacitor does not have sufficient time between pulses to be fully discharged by the baseline restorer circuit.

The effect of the input count rate on resolution and peak shift with the on-demand beam pulsing operation is shown in Figure (5.9) for two selectable amplifier shaping time constants of 8 and 2 μsec.

Figure (5.9) shows that the long shaping time constants required for good energy resolution lead to a poor high counting rate capacity. Shorter time constants allow higher count rates at the expense of energy resolution. The rapid degeneration of resolution at high

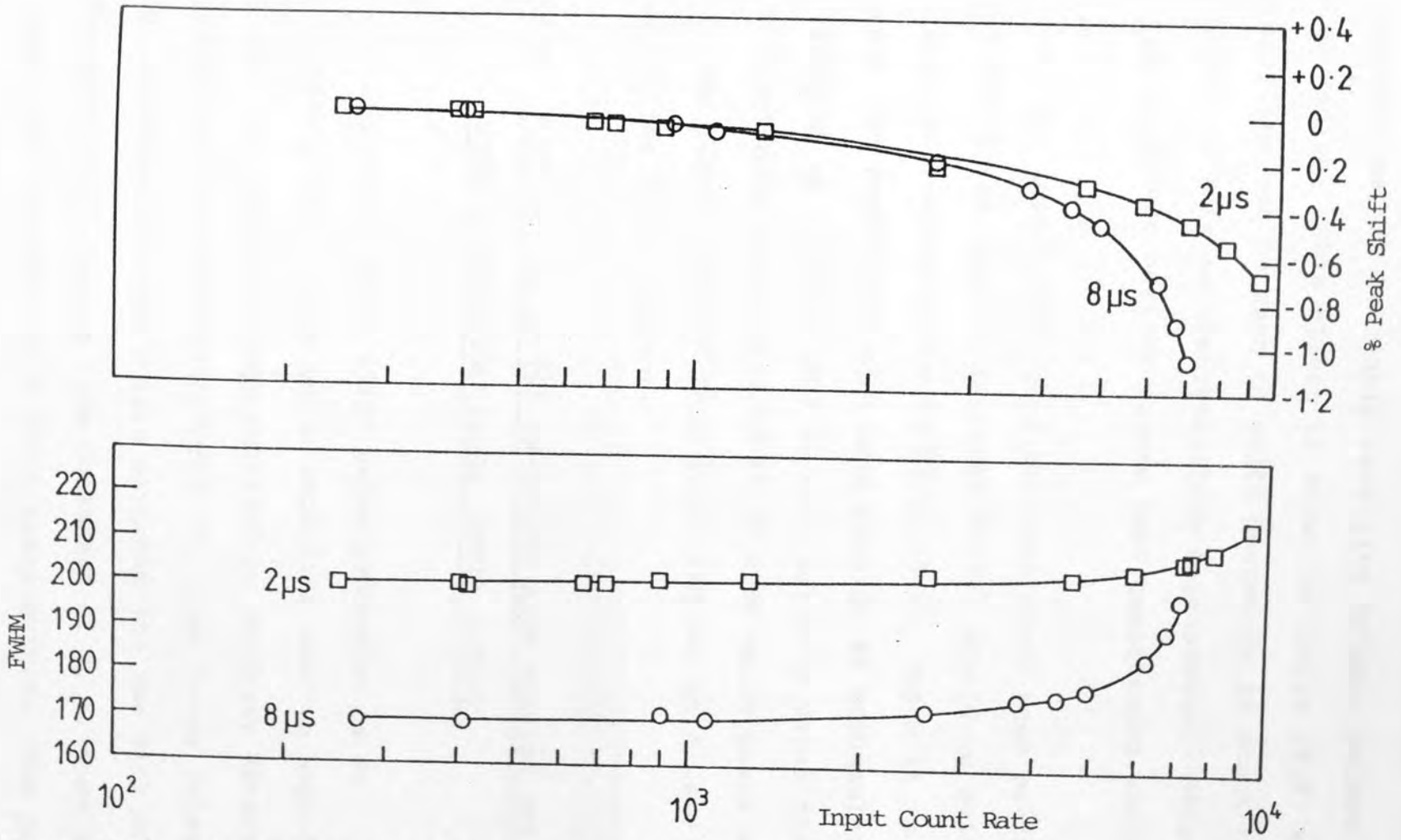

Figure (5.9) FWHM and % peak shift as a function of input count rate for a Kevex 4500P main amplifier with beam pulsing operation using two different amplifier time constants.

count rates is caused by the baseline restorer losing control as the available base line between pulses begins to vanish. This effect is shown in Figure (5.9) where the baseline can be seen to shift downwards at about the same counting rate as the resolution degenerates. This effect can introduce serious errors into qualitative analysis.

The improvement over the continuous beam performance of the X-ray amplifier (Kevex 4500P) should be evident from the results given in Table (5.1), where it is seen that the resolution with beam pulsing at accummulation rates of up to 7.49 kPPS is only slightly worse then with a continuous input-rate of 14.64 kPPS which gives an accummulation rate of only 4.35 kPPS for an 8 μsec amplifier time constant.

5.5 PROPERTIES OF THE ON-DEMAND BEAM PULSING OPERATION WITH A PULSE PROCESSOR (KEVEX 4525P)

The Kevex model 4525P pulse processor is an adjustable gain X-ray pulse amplifier used to amplify, shape and process pulses provided by an X-ray detector. The pulse processor transforms the input X-ray pulses into square-shaped output pulses suitable for use with MCA. The amplifier shaping time constants of 2, 5, 6 or 8 μsec are selected by a front panel switch. The pulse processor also provides leading and trailing edge rejection as well as live-time correction of input pulses

	Input Count Rate (kPPS)	Output Count Rate (kPPS)	Cu Kα Peak	
			FWHM(eV)	Peak Centroid (Channel) No.
Continuous Beam Irradiation	4.03	2.88	174.0	196.0
	7.11	3.97	178.0	195.0
	8.69	4.10	185.0	195.0
	14.64	4.35	194.0	194.0
Beam Pulsing Operation	4.65	4.60	178.0	198.0
	7.49	7.38	199.0	193.0
	8.45	8.33	222.0	192.0
	9.64	9.51	233.0	191.0

Table 5.1 Performance of the Kevex 4500P amplifier with and without beam pulsing, for an 8 μsec amplifier time constant.

by employing a unique "pulse pile-up rejector" with a live time corrector circuit. A symmetric baseline restorer circuit provides precise and rapid base line stability to minimise peak shift and resolution deterioration at high count rates. The Kevex (4525P) processor provides a beam blanking signal during the processor dead time. With this capability, the beam pulsing system can be directly activated. In this case there is no need for the pulse stretcher unit. The throughput curves of the processor Kevex 4525P with and without pulsing operation are shown in Figure (5.10).

Without beam pulsing operation, Figure (5.10), the input count rate during which an approximately 50% dead time has to be suffered, is limited to 4 kPPS and the output rate is recorded to be about 2.3 kPPS corresponding to the 8 μsec processor time constant. The use of the electronic pile-up rejection circuit in the Kevex 4525P processor eliminates the pile-up continuum completely, except the sum and triple sum peaks, and improves the situation with respect to the rate at which the energy resolution degrades with increasing count rates. This is a distinct advantage of the Kevex 4525P processor over the 4500P amplifier at normal operation. On the other hand, the count rate capability of the 4525P processor is reduced to approximately 60% at normal operation compared with the 4500P amplifier, this is because the rejection of the X-ray signals distorted by pile-up on either the

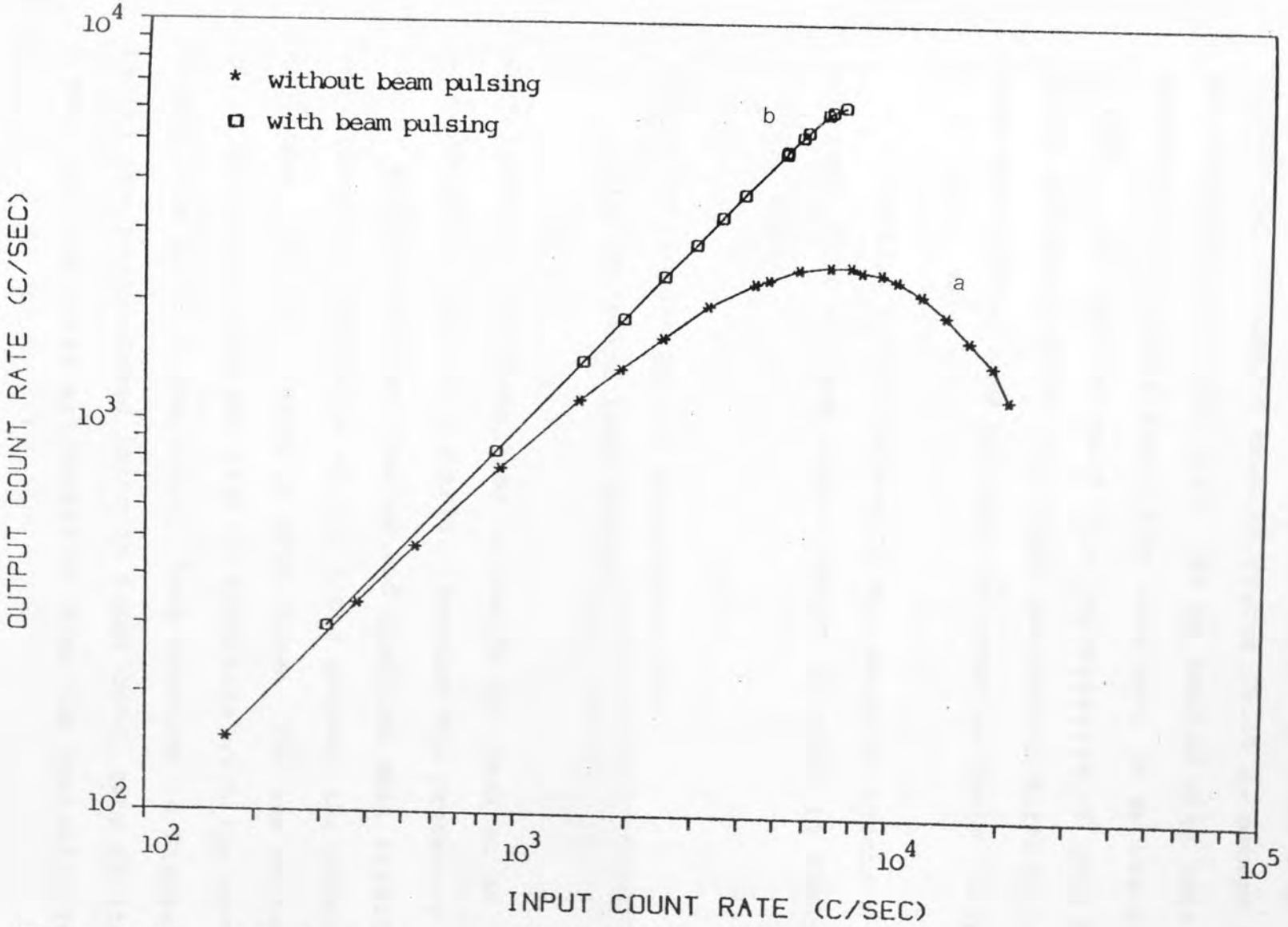

Figure (5.10) Throughput curves for Si(Li) X-ray detection system with and without beam pulsing, using the processor Kevex 4525P, (T.C. = 8 μsec)

leading edge or trailing edge causes this difference in the count rate capability. With the on-demand beam pulsing operation, the improvement of tne count rate capability is clearly seen in Figure (5.10), except that the maximum count rate which can be reached with this processor using an 8 μsec time constant, is approximately 6 kPPS. The maximum count rate capabilities of both Kevex 4500P and Kevex 4525P with their percentage differences, with and without beam pulsing, is shown in Table (5.2).

A typical proton-induced X-ray emission spectrum obtained using a thick copper target is shown in Figure (5.11), under

(a) continuous proton bombardment, and
(b) the on-demand beam pulsing.

Both spectra are normalised to the Cu Kα peak at an accumulation rate of 2.3 kPPS. Because the processor (Kevex 4525P) provides leading and trailing edge rejection and live time correction of the input pulses, the pile-up continuum can not be seen in both cases. The sum peaks still exist but they are less in magnitude with the on-demand beam pulsing operation. Each spectrum in Figure (5.11) was accumulated under an input count rate of 4500 c/sec, and the total accumulation time was typically 10 sec.

Type of Processor	Continuous Beam Irradiation		Beam Pulsing Operation	
	I/P CR at Maximum O/P CR (kPPS)	Maximum O/P CR (kPPS)	I/P CR at Maximum O/P CR (kPPS)	Maximum O/P CR (kPPS)
Kevex 4500P (with 8 µsec T.C.)	12.5	4.5	10.0	10.0
Kevex 4525P (with 8 µsec T.C.)	6.6	2.5	6.6	6.6
Percentage Difference	62%	57%	41%	50%

Table 5.2 Comparison in Count Rate Capabilities using different types of processors at the same 8 µsec amplifier time constant.

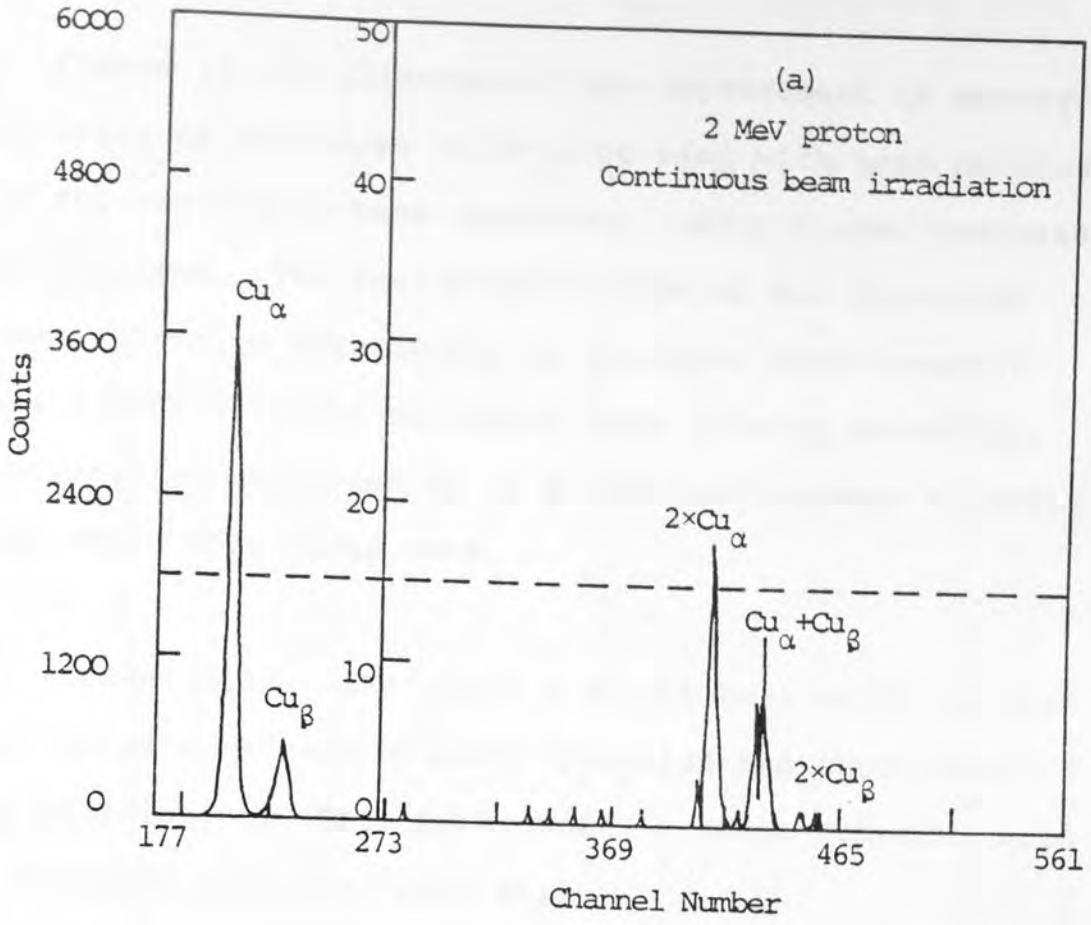

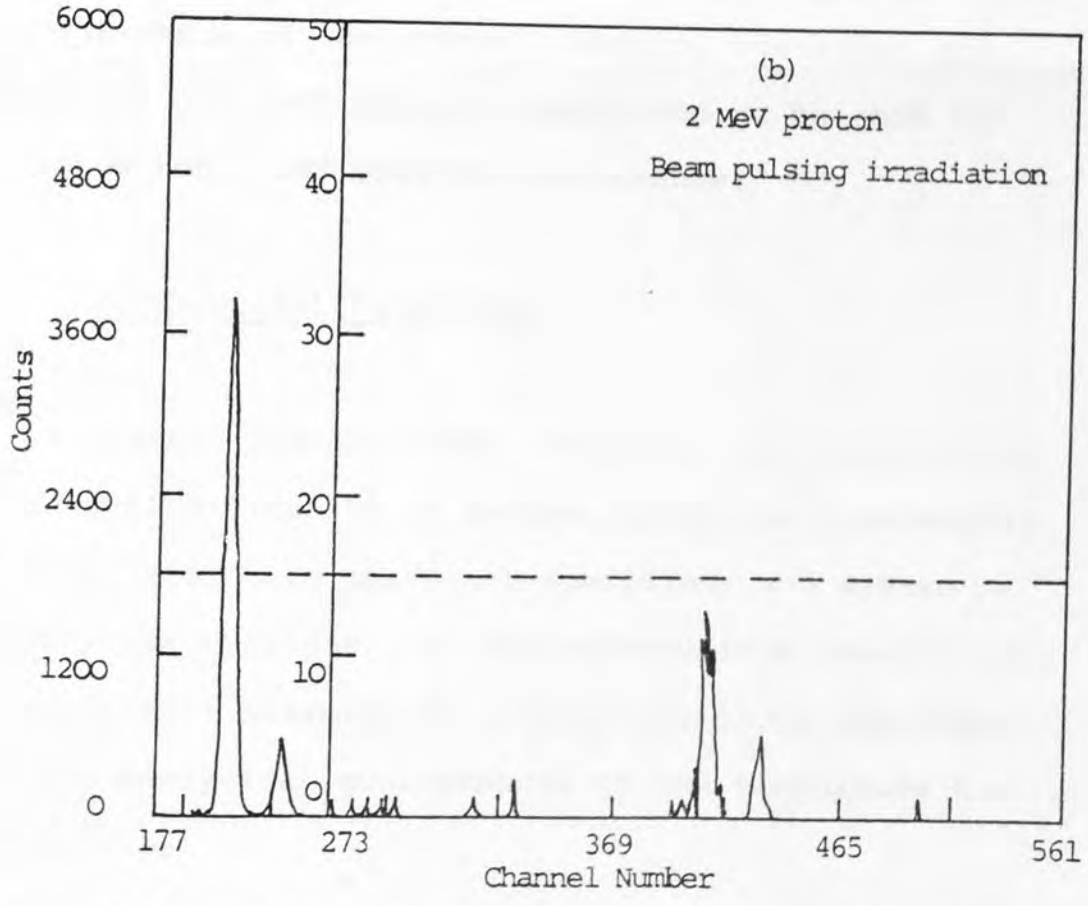

Figure (5.11) Typical X-ray spectrum obtained using a thick copper target with processor Kevex 4525P.

Figure (5.12) illustrates the improvement in energy resolution of the Kevex 4525P processor with beam pulsing over the continuous beam operation, using 8 μsec processor time constant. The energy resolution of the detection system starts to deteriorate at an input count rate of above 2 kPPS with the on-demand beam pulsing operation. Deterioration continues up to 6 kPPS and becomes slightly worse above this count rate.

Figure (5.12) also shows a slight peak shift at high count rates with beam pulsing operation and continuous beam irradiation. This peak shift is small compared with the previous amplifier peak shift.

The basis of the system's design, operation and properties are sufficiently understood to be able to extract a total and optimum performance.

5.6 REPRODUCIBILITY STUDIES

In proton induced X-ray analysis, the precision of the analytical results is determined by the statistical counting error when operating conditions and system geometry are constant. As non-reproducible results make any analytical measurement unreliable, it is important that the analytical measurements of the techniques are reproducible.

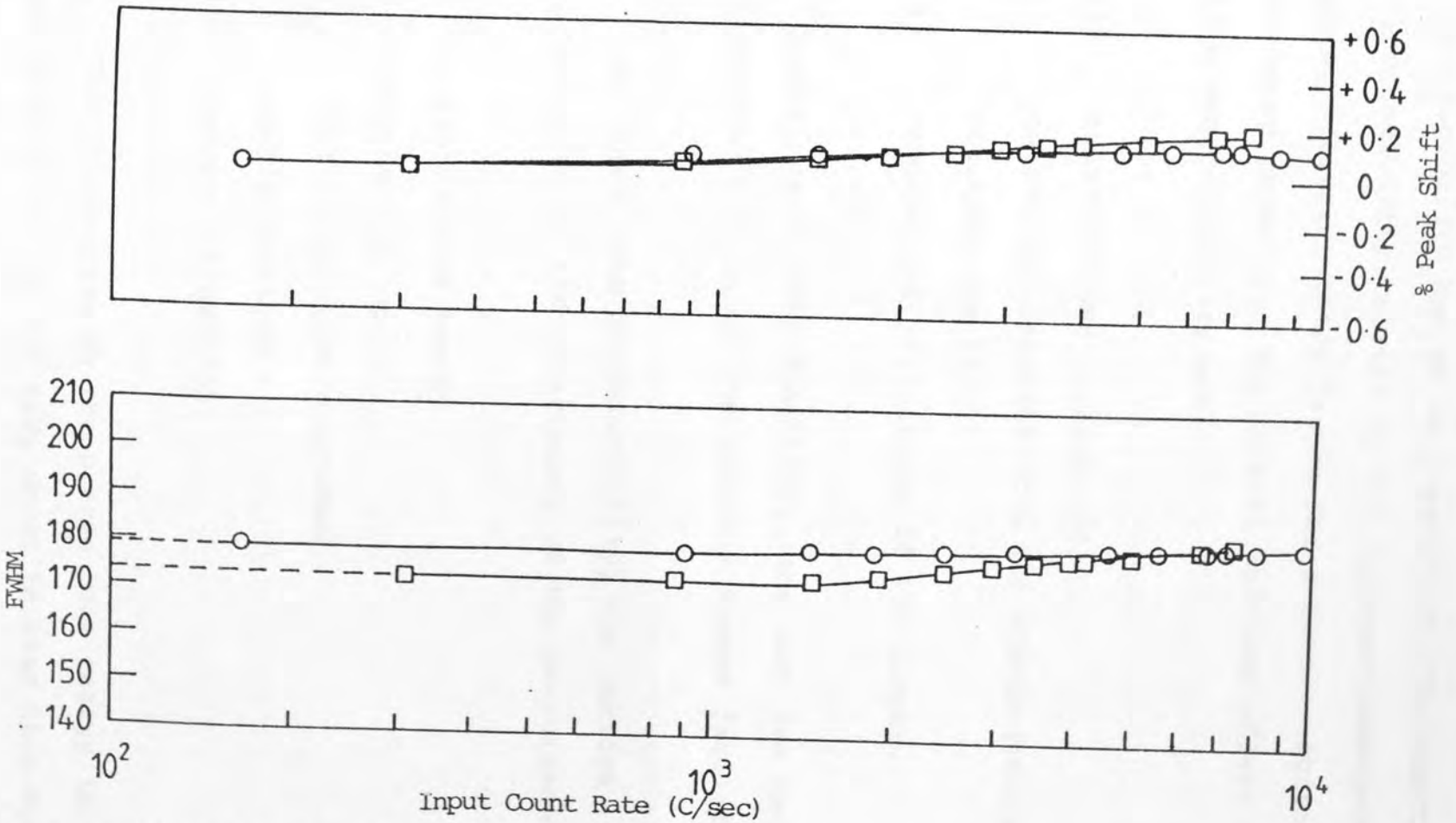

Figure (5.12) FWHM and % peak shift as a function of input count rate for a Kevex 4525P processor operation, using 8 μsec processor time constant.

□ with beam pulsing O without beam pulsing

Because the beam line is newly constructed, system reproducibility has to be identified. The short term reproducibility relates to the repeated measurements made on a particular thick target for a fixed target-sample-detector geometry. The factors that may affect the long term reproducibility are:

(1) switching the machine off
(2) moving the detector from its stable position
(3) rotating the target
(4) removal and reinsertion of the target.

With the new chamber facilities, the last two factors are eliminated because of the reliable system facilities.

In short term reproducibility, the factors contributing to the uncertainty of the measurement are:

(1) proton beam energy
(2) pulse pile-up
(3) peak integration programme
(4) sample position
(5) charge integration.

The uncertainty in the proton beam energy is usually less than 10 keV at 2.0 MeV, which is less than 0.5% of the beam energy. This uncertainty produces less than a 3% uncertainty in the photon yield per proton from thick

targets as it varies as E_p^6 .

The uncertainty in the X-ray detection was insignificant as pulse pile-up was reduced by the on-demand beam pulsing system. The peak integration programme may introduce up to a 10% uncertainty if the peak region is not properly selected. However, in the reproducibility studies for each target this region was kept nearly constant, hence, the only uncertainty is due to counting statistics.

The uncertainty due to sample position is insignificant as the standard target does not move during the measurement. The total uncertainty due to the charge collecting system is difficult to quantify. Although the uncertainty due to the Keithley electrometer is 1% at full scale deflection, the instrument has a high input impedance, typically $10^6 \Omega$ on the μA range. Hence, leakage currents are important and may change as the experiment is being performed.

In the present work, care was taken to ensure that leakage impedance was very much less than electrometer impedance. An alternative approach is to employ a beam monitor as described by Mitchell et al. (1980), which eliminates the need for accurate charge measurements. The method uses the backscattered yield from a thin calibrated foil for monitoring MeV ion beam doses. The principle of

this method involves interposing a thin self-supporting foil between the ion beam and the target. The foil must be thin enough to permit all of the beam to pass through without any significant energy loss. These authors have indicated that the foil must be thin enough so that they do not appreciably increase the uncertainty in the beam energy by energy straggling effects. Furthermore, angular straggling must be small enough so as to ensure that all of the transmitted beam reaches the target within a reasonable spot size.

5.6.1 Precision and Reproducibility of On-Demand Beam Pulsing System

To check the reliability of the on-demand beam pulsing system developed in the present work as an analytical tool, the precision of the system behaviour was assessed. For checking the reliability and reproducibility of the on-demand beam pulsing system the throughput curve was measured under identical experimental conditions several times over a period of 3 months. The reproducibility of the throughput curve was therefore investigated and compared with the previous curve (solid line) as shown in Figure (5.13) for an 8 μsec time constant. Figure (5.13) shows that a good agreement can be obtained in the throughput curves with continuous and pulsed beam operation and indicates the reliability of the system. Because of the statistical

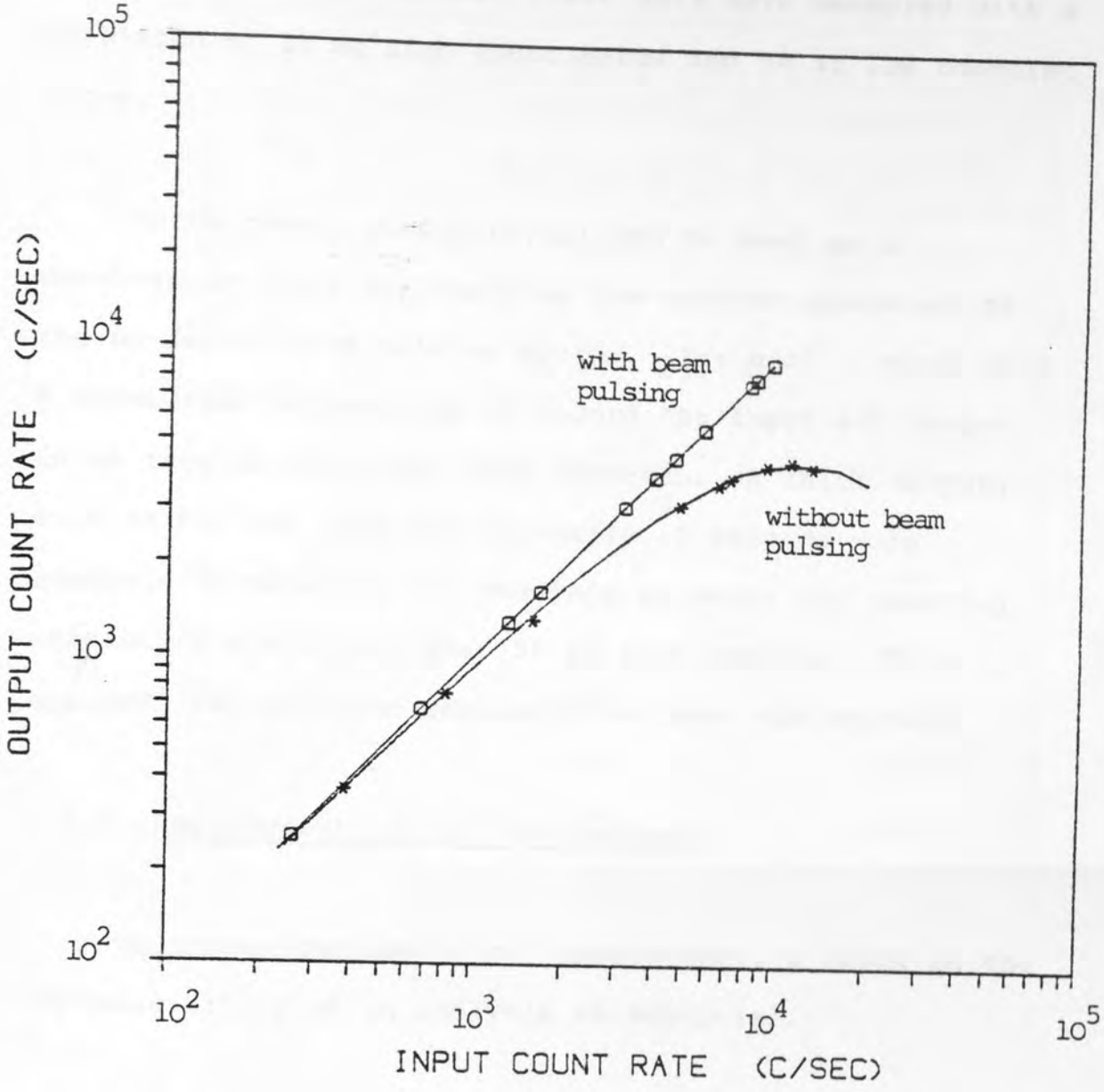

Figure (5.13) The reproducibility of the throughput curves of the PIXE system, with beam pulsing and without beam pulsing operation. (T.C. = 8μsec)

uncertainty of the counts, these data were measured with a precision of 1% at high count rates and 5% at low counting rates.

Furthermore, Figure (5.13) can be used as a calibration curve for checking the correct operation of the on-demand beam pulsing system. For such a check only a short time is required to record the input and output count rate at different beam currents. A thick target, such as Cu, was used and typically 10 seconds were adequate to obtain a few readings in which the counting statistics are better than 5% on each reading. This approach was employed regularly to check the system.

5.6.2 Reproducibility of the Analysis

To assess the analytical consistency, a check on the reproducibility of an analysis is essential.

Experiments were carried out on standard thick binary alloys and afforded a good test of the system's reproducibility. No external uncertainties were introduced from target formation or caused by problems of uniformity and stability of these targets. The standard targets listed in Table (5.3) were analysed in order to test the reproducibility of the results.

A set of three binary alloy targets was placed in the

Reading Number	Sample Type		
	Ni_{80}/Cr_{20}-alloy	$Fe_{87.5}/Cr_{12.5}$-alloy	Fe_{64}/Ni_{36}-alloy
	Cr Kα Counts	Fe Kα Counts	Ni Kα Counts
1	35234 ± 198	131274 ± 382	22916 ± 196
2	35656 ± 199	132211 ± 382	22931 ± 195
3	35362 ± 199	130953 ± 381	22425 ± 192
4	35260 ± 198	132835 ± 383	22880 ± 196
5	35267 ± 199	133448 ± 384	22518 ± 196
6	34740 ± 197	134442 ± 384	22410 ± 193
7	35076 ± 198	132907 ± 383	22498 ± 193
8	35090 ± 198	130150 ± 380	22560 ± 194
9	35856 ± 200	129805 ± 378	22915 ± 193
10	35566 ± 200	132630 ± 382	22297 ± 192
Mean	35310	132066	22635
SD	320	1485	248
C.V.	0.91%	1.12%	1.09%

C.V. = Coefficient of Variance = $\frac{SD}{Mean} \times 100$

Table 5.3 Reproducibility of Analysis of Standard Alloys.

newly-designed chamber. The target was aligned at 45° to the incident proton beam by using a laser beam. Once the beam had stabilised at a beam current of 5 nA at 2 MeV protons, the total X-ray counts under the Kα peak were recorded for a fixed preset charge. This was repeated several times and each time counts were taken.

Table (5.3) gives a list of results for the Kα X-ray yields which are corrected for background. These results were taken with the beam pulsing system operational and employing a counting rate of 3000 counts per second. The statistical error of the counts in Table (5.3) was kept below 1%.

Assuming the distribution of the X-ray counts is normal, (in fact the distribution is Poisson and can only be approximated to a normal distribution if the number of counts is greater than 30) and denoting the standard deviation of the sample of counts by S, then 68.27% of the counts should lie within the ±1S range limit, 95.45% within the ±2S limit and 99.73% within the ±3S limit. For most of the experimental runs, the X-ray counts lie within the ±2S limit. Within each set of readings the results were reproducible.

Different alloys from the same composition were prepared in order to perform a comparison in terms of the ratio between the major elements. The advantage of this

ratio technique is that it does not require accuracy in the sample thickness, size and weight. In addition, systematic errors are eliminated. Therefore, two sets of targets, Fe_{64}/Ni_{36} and Ni_{80}/Cr_{20} alloys were made ready for this test.

The mass ratios, Fe/Ni and Ni/Cr represented by their X-ray peaks, were determined. These sets of data, shown in Table (5.4), include the mean ratios and their relative standard deviations. It should be noted that the comparison of the mean values as well as the relative standard deviation of each ratio of different sets shows that an acceptable reproducibility was achieved.

A typical PIXE spectrum from analysis of these alloys is shown in Figure (5.14).

Consequently, it may be concluded that the reproducibility of the system with the on-demand beam pulsing operation is reliable.

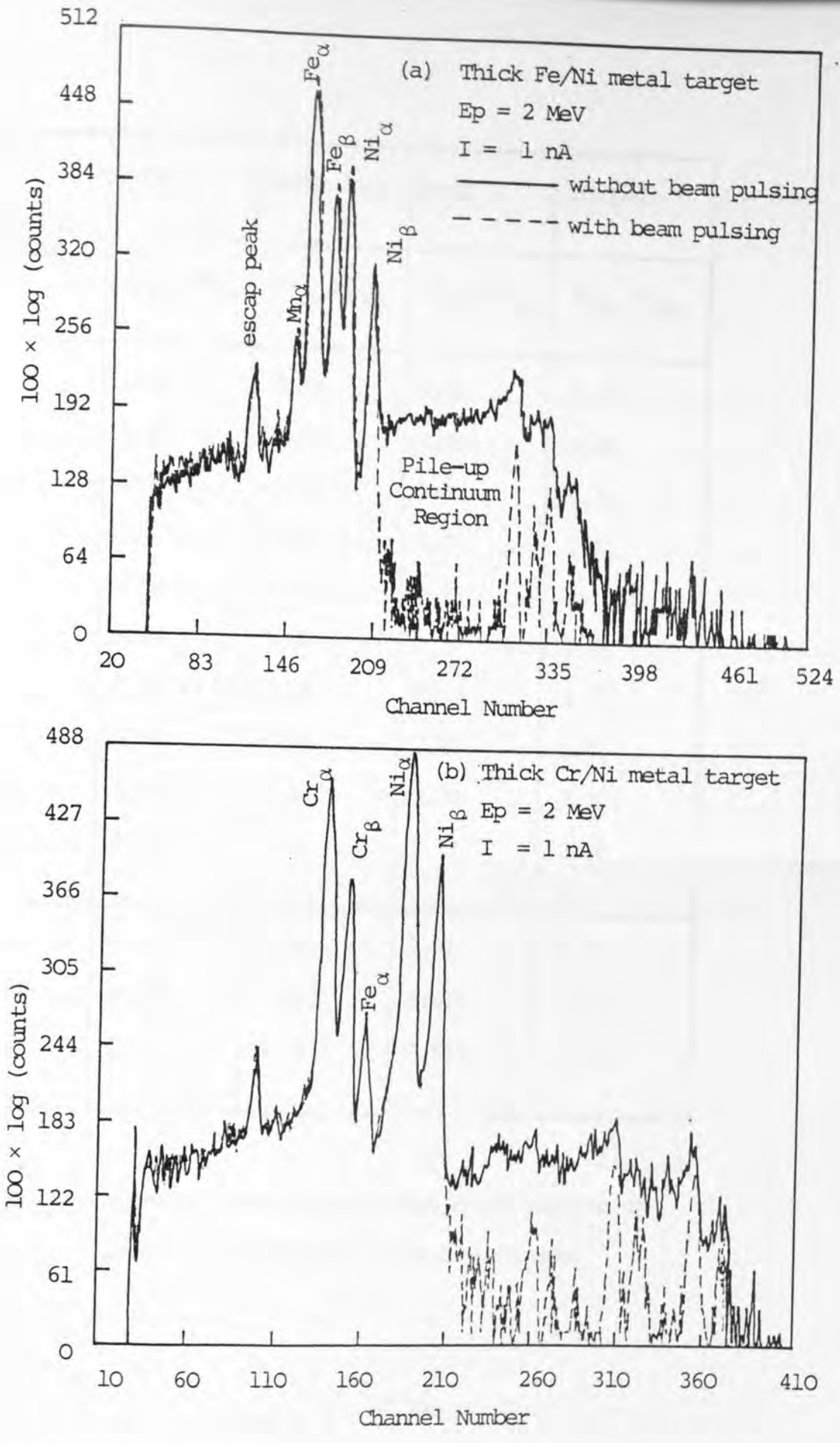

Figure (5.14) Typical PIXE spectrum from analysis of Fe_{64}/Ni_{36} and Cr_{20}/Ni_{80} thick metal alloys, with and without beam pulsing operation

Reading Number	Group 1	Group 2	Group 1	Group 2
	$Fe_{K\alpha}/Ni_{K\alpha}$	$Fe_{K\alpha}/Ni_{K\alpha}$	$Ni_{K\alpha}/Cr_{K\alpha}$	$Ni_{K\alpha}/Cr_{K\alpha}$
1	5.56	5.46	2.70	2.69
2	5.52	5.67	2.68	2.68
3	5.55	5.54	2.72	2.72
4	5.67	5.56	2.73	2.71
5	5.54	5.56	2.72	2.73
6	5.64	5.48	2.70	2.71
7	5.44	5.60	2.70	2.71
8	5.54	5.54	2.72	2.71
9	5.42	5.58	2.70	2.72
10	5.42	5.50	2.72	2.68
Mean	5.53	5.55	2.71	2.70
SD	0.085	0.061	0.015	0.017
C.V.	1.54%	1.1%	0.55%	0.63%

Table 5.4 Intensity Ratio Obtained for Thick Targets of Binary Alloys from Two Different Groups.

CHAPTER 6

APPLICATION OF PIXE ANALYSIS TO THICK METAL TARGETS

6.1 INTRODUCTION

In this chapter, the calibration of the system is studied theoretically and experimentally in order to establish the reliability of the theoretical evaluation of the X-ray yields for thick pure elemental standards for different proton energies. Furthermore, PIXE-methods for quantitative analysis of thick targets are discussed.

The intensity ratios for Fe/Ni and Cr/Fe binary alloys have been determined theoretically for different concentrations of the element of interest. The secondary X-ray production process (enhancement effect) and other matrix effects have also been included in these calculations. These calculations were verified experimentally using a number of standard alloys. The intensity ratios were plotted against the concentrations of the element of interest to be as a calibration curve for a particular binary alloy combination.

These calibration curves were then employed in the determination of the elemental composition of Fe and Cr in Fe/Ni and Cr/Fe sample directly from their measured intensity ratio using protons of 2 MeV. The determined compositions of Fe and Cr in Fe/Ni and Cr/Fe samples are

discussed and compared with the given composition in this chapter.

The magnitude of the enhancement effect for different concentrations of Fe and Cr in Fe/Ni and Cr/Fe alloys has been investigated. The projectile energy dependence of the enhancement is also discussed.

Finally, the chapter discusses the use of the Rutherford backscattering technique to investigate the depth distribution of Mo in an Fe-steel sample containing Cr and Mo using 2.8 MeV α-particles.

6.2 SYSTEM CALIBRATION FOR PURE ELEMENTAL STANDARDS

The PIXE technique of trace analysis has been applied to many types of thin and thick targets to perform quantitative measurements by many authors, including Mangelson et al. (1977) and Johansson (1977, 1981), Bauer et al. (1978) and Raith et al. (1981). Furthermore, qualitative information and the relative quantities of elements present in the sample may be determined on-line during the collection of data.

In thick target experiments with PIXE, the correlation of the X-ray yield with the concentration of the element is dependent on the matrix of the target.

The number, $I_x(E_o)$, of characteristic X-rays of an element of the atomic number Z and atomic weight A detected during the bombardment with protons of energy E_o on a pure thick target is given by

$$I_x(E_o) = N_p \int_{E_o}^{E_f} n_i \frac{\sigma_p(E)}{S(E)} T_2 \, dE \qquad (6.1)$$

The above symbols are defined in Chapter 3, where however, S(E) and $\sigma_p(E)$ are the stopping power and production cross-section of the target under bombardment. The absorption of the characteristic X-rays in the target (self absorption) has been accounted for by introducing the transmission factor T_2 in the integral.

If the X-rays are detected in a solid angle Ω steradian by a detector of efficiency ε including absorption losses, T_1, in the chamber exit window, air passage and detector front window, then the yield $I_x(E_o)$ can be written as:

$$I_x(E_o) = N_p \, \varepsilon \, \frac{\Omega}{4\pi} \, T_1 \int_{E_o}^{E_f} \sigma_p(E) \, n_i \, \frac{T_2}{S(E)} \, dE \qquad (6.2)$$

or

$$I_x(E_o) / (N_p \, \varepsilon \, \frac{\Omega}{4\pi} \, T_1) = \int_{E_o}^{E_f} \sigma_p(E) \, n_i \, \frac{T_2}{S(E)} \, dE \qquad (6.3)$$

Therefore,

$$I_x(E_o) \; / \; (N_p \; \varepsilon \; \frac{\Omega}{4\pi} \; T_1) = F_{XZ} \qquad (6.4)$$

where F_{XZ} is the "calibration factor" which is constant for a given element Z, X-ray transition, primary proton energy and geometry.

Two possible methods of obtaining the F_{XZ} values of equation (6.4) are available. They are:

(i) Theoretical evaluation of F_{XZ} values

(ii) Experimental evaluation of F_{XZ} values using pure elemental thick standards.

6.2.1 Theoretical Evaluation of F_{XZ} values

The F_{XZ} values were calculated semi-empirically since most of the parameters in the F_{XZ} expression, equation (6.3) can be obtained from published data. In equation (6.3) the calibration factor (F_{XZ} value) is expressed as:

$$F_{XZ} = \int_{E_o}^{E_f} \frac{\sigma_p(E)}{S(E)} \left(\frac{N_o \rho}{A}\right) T_2 \, dE \qquad (6.5)$$

A computer programme was written to facilitate evaluation of equation (6.5) which determines the primary X-ray production along the particle path at different depths of the target, as well as X-ray attenuation by the

target material in the direction of the detector. As discussed in Section 3.5, the targets were generally assumed to consist of successive thin layers of a fixed energy loss.

The X-ray yield of a target is then calculated by summing the yields of the successive layers, taking into account the energy loss of the incoming particle as a function of depth and the absorption of the X-rays by the target material in the direction of the detector. Thus, the F_{XZ} value was calculated for 8 elements in the range of $22<Z<47$ and for three proton beam energies.

To accomplish this, the following input parameters were used:

(i) the upper and lower limit of the incident proton beam energy (E_o and E_f);
(ii) the density and atomic number of each element, and
(iii) the coefficients needed for the calculation of the stopping power, the production cross-section and the X-ray attenuation.

The ionization cross-section and the stopping power employed were computed from the polynomial of Johansson and Johansson (1976) and Anderson and Ziegler (1977) respectively. The absorption of the outgoing X-rays in the target was also considered in the calculations using

the appropriate absorption coefficient taken from the compilation of Montenegro (1978).

In trace analysis, the use of the production cross-section, $\sigma_p(E)$, is of more interest than the ionization cross-section, though these are related to each other through the fluorescence yield, the values of which are taken from Bambynek et al. (1972) or Krause (1979).

The values calculated as described above, are tabulated in Table (6.1) at three different proton bombarding energies. The uncertainties in the calculated F_{XZ} value, taken from the parameters involved in equation (6.5), are discussed as follows:

The error in the Avogadro's number, atomic weight and density are negligible. The uncertainty in the fitted function of the ionization cross-section of Johansson and Johansson (1976) is within the experimental error of Akselsson and Johansson (1974) which varies from 4% to 11% depending on the element. The fluorescence yields of Bambynek et al. (1972) and their uncertainty have been used in these calculations. At most they differ by only 2% from the values given by Krause (1979) for the elements given in Table (6.2), this factor adds further uncertainty to the calculation of the F_{XZ} value. The main source of uncertainty comes from the mass attenuation coefficient, ±10% is quoted for photon energies up to 6 keV and a ±3%

Proton Energy / Element	Calculated F_{XZ} (Photon/Proton)		
	1.5 MeV	2.0 MeV	2.5 MeV
Ti_{22}	$(3.82 \pm 0.49) \times 10^{-3}$	$(9.81 \pm 1.27) \times 10^{-3}$	$(18.29 \pm 2.4) \times 10^{-3}$
Fe_{26}	$(1.25 \pm 0.047) \times 10^{-3}$	$(3.63 \pm 0.14) \times 10^{-3}$	$(7.62 \pm 0.29) \times 10^{-3}$
Ni_{28}	$(7.16 \pm 0.53) \times 10^{-4}$	$(2.18 \pm 0.12) \times 10^{-3}$	$(4.79 \pm 0.33) \times 10^{-3}$
Cu_{29}	$(5.39 \pm 0.20) \times 10^{-4}$	$(1.68 \pm 0.06) \times 10^{-3}$	$(3.77 \pm 0.14) \times 10^{-3}$
Zn_{30}	$(3.99 \pm 0.28) \times 10^{-4}$	$(1.27 \pm 0.08) \times 10^{-3}$	$(2.91 \pm 0.20) \times 10^{-3}$
Zr_{40}	$(2.26 \pm 0.15) \times 10^{-5}$	$(8.39 \pm 0.46) \times 10^{-5}$	$(2.22 \pm 0.12) \times 10^{-4}$
Mo_{42}	$(1.36 \pm 0.11) \times 10^{-5}$	$(5.13 \pm 0.30) \times 10^{-5}$	$(1.38 \pm 0.08) \times 10^{-4}$
Ag_{47}	$(3.89 \pm 0.19) \times 10^{-6}$	$(1.53 \pm 0.15) \times 10^{-5}$	$(4.26 \pm 0.26) \times 10^{-5}$

Table (6.1) The calculated F_{XZ} values of the present system for $Ti \leq Z \leq Ag$ at three bombarding energies.

Element	W From Bambynek et al. (1972)	W From Krause (1979)	Percentage Difference
Ti_{22}	0.219 ± 0.018	0.214	2.0%
Fe_{26}	0.347 ± 0.008	0.340	2.0%
Ni_{28}	0.414 ± 0.028	0.406 ±5-3%	1.95%
Cu_{29}	0.445 ± 0.009	0.440	1.13%
Zn_{30}	0.479 ± 0.030	0.474	1.05%
Zr_{40}	0.730 ± 0.032	0.730 ± 3%	0
Mo_{42}	0.746 ± 0.032	0.765 ± 2%	0.13%
Ag_{47}	0.830 ± 0.025	0.831 ± 2%	0.13%

Table (6.2) Comparison of two published fluorescence yield values with their uncertainties and percentages of difference for elements $22 \leq Z \leq 47$.

above 6 keV, Storm and Israel, (1970), though its effect may be small because it does not enter as a multiplicative term.

The fitted stopping power formula of Anderson and Ziegler (1977) at high energies (above 1 MeV) are accurate to 1% and 5% at 500 keV. No error was assumed in connection with $K\alpha/K_{total}$ values to separate the $K\alpha$ intensities since these were calculated from the theoretical values for the $K\beta/K\alpha$ ratio of Scofield (1974).

The total uncertainty , E_T, in the calculated F_{XZ} value can be obtained by combining the uncertainties in the normal manner, the overall uncertainties in the calculated F_{XZ} values were estimated to be 3-10% for $Fe \leq Z \leq Ag$ and rising to 13% for Ti over all the protons energy used.

6.2.2 Experimental Evaluation of F_{XZ} Values using Elemental Thick Standard

In order to provide a check for the theoretical evaluation of F_{XZ} values, an experimental determination was made.

In the present experiments, eight pure elemental standard targets from Goodfellow Metals Co., were analysed for their K-Lines. These targets were thick enough to

stop the beam completely. The characteristic K X-ray (I_x) peak was measured and normalised to the number of incident protons, and was corrected for the efficiency, the solid angle and the absorption of the emitted X-rays on its way to the detector.

The experimental F_{XZ} values were then determined from

$$I_x(E_o) \; / \; N_p \; \varepsilon \; \frac{d\Omega}{4\pi} \; T_1 \qquad (6.6)$$

where N_p is the number of protons that are incident on the target during the measurements.

The solid angle, subtended by the detector, was kept fixed during the experimental period and was determined by the geometry of the experimental set up. This was achieved by introducing a lead collimator of 0.3 ± 0.05 cm thickness in front of the detector with a precise diameter aperture of 3.97 ± 0.04 mm, obtained by using vernier calipers, thereby allowing an uncertainty of less than 0.5%. The target-aperture distance was measured to be 15 ± 0.05 cm.

A fraction of the emitted X-rays from the target are absorbed by the following absorbers:

(i) The chamber Melinex window

(ii) the air path between the Melinex window and the detector, and

(iii) the detector combination of the beryllium vacuum window, the gold layer on the front of the crystal, and a silicon "dead layer".

The silicon crystal has a gold layer with an approximate thickness of 200A° on both sides which acts as an electrical contact, and a comparatively thin silicon dead layer the thickness of which is not given by the manufacturer. The X-rays employed in this work are typically in the energy range of 6-22 keV and the absorption of these X-rays in the gold layer and Si-dead layer is negligible.

The fraction of X-rays transmitted through the absorbers as stated above was calculated as:

$$T_1 = e^{-\Sigma \mu_i x_i} = e^{-[\mu_{air} x_{air} + \mu_m x_m + \mu_B x_B]} \qquad (6.7)$$

where μ_{air}, μ_m and μ_B are the mass absorption coefficients of air, Melinex, and beryllium respectively, and where X_i's are the thickness that X-rays must transverse.

The μ_m of Melinex $(C_{10} H_8 O_4)_n$ was calculated from the coefficient μ_i for the constituent elements according

to the weighted average (equation (2.21)). The same equation was applied to find μ_{air}. The μ_B was taken from Storm and Israel (1970).

The values of the detector efficiency ε were calculated for each X-ray energy using the following equation

$$\varepsilon = (1 - e^{-\mu_{Si} x_{Si}}) \, e^{-\mu_B x_B} \qquad (6.8)$$

where μ_{Si} and x_{Si} are the mass absorption coefficient and the thickness of the silicon crystal and $e^{-\mu_B x_B}$ represents the absorption correction for the beryllium detector window.

The results of the thick target X-ray yield measurements of the 8 elements for the three bombarding energies are listed in Table (6.3), and plotted as a function of the atomic number as shown in Figure (6.1). The dots in the graph represent the experimental results and the solid lines represent the theoretical data. Satisfactory agreement was obtained between the calculated F_{XZ} values in Table (6.1) and the experimental determination of F_{XZ} values in Table (6.3) as shown in Figure (6.1).

These observations confirmed the reliability of the theoretical evaluation of F_{XZ} values for pure thick metal

Proton Energy / Elements	Experimental F_{XZ} values (Photon/Proton)		
	1.5 MeV	2.0 MeV	2.5 MeV
Ti	$(3.77 \pm 0.38) \times 10^{-3}$	$(9.59 \pm 0.96) \times 10^{-3}$	$(17.3 \pm 1.7) \times 10^{-3}$
Fe	$(1.27 \pm 0.42) \times 10^{-3}$	$(3.57 \pm 0.12) \times 10^{-3}$	$(7.49 \pm 0.24) \times 10^{-3}$
Ni	$(7.21 \pm 0.23) \times 10^{-4}$	$(2.22 \pm 0.07) \times 10^{-3}$	$(4.68 \pm 0.15) \times 10^{-3}$
Cu	$(5.32 \pm 0.17) \times 10^{-4}$	$(1.63 \pm 0.05) \times 10^{-3}$	$(3.82 \pm 0.12) \times 10^{-3}$
Zn	$(4.12 \pm 0.136) \times 10^{-4}$	$(1.28 \pm 0.04) \times 10^{-3}$	$(2.83 \pm 0.09) \times 10^{-3}$
Zr	$(2.34 \pm 0.096) \times 10^{-5}$	$(8.74 \pm 0.33) \times 10^{-5}$	$(2.21 \pm 0.08) \times 10^{-4}$
Mo	$(1.48 \pm 0.064) \times 10^{-5}$	$(5.53 \pm 0.21) \times 10^{-5}$	$(1.44 \pm 0.05) \times 10^{-4}$
Ag	$(4.17 \pm 0.26) \times 10^{-6}$	$(1.67 \pm 0.07) \times 10^{-5}$	$(4.51 \pm 0.18) \times 10^{-5}$

Table (6.3) The measured F_{XZ} values of the present system at three bombarding energies.

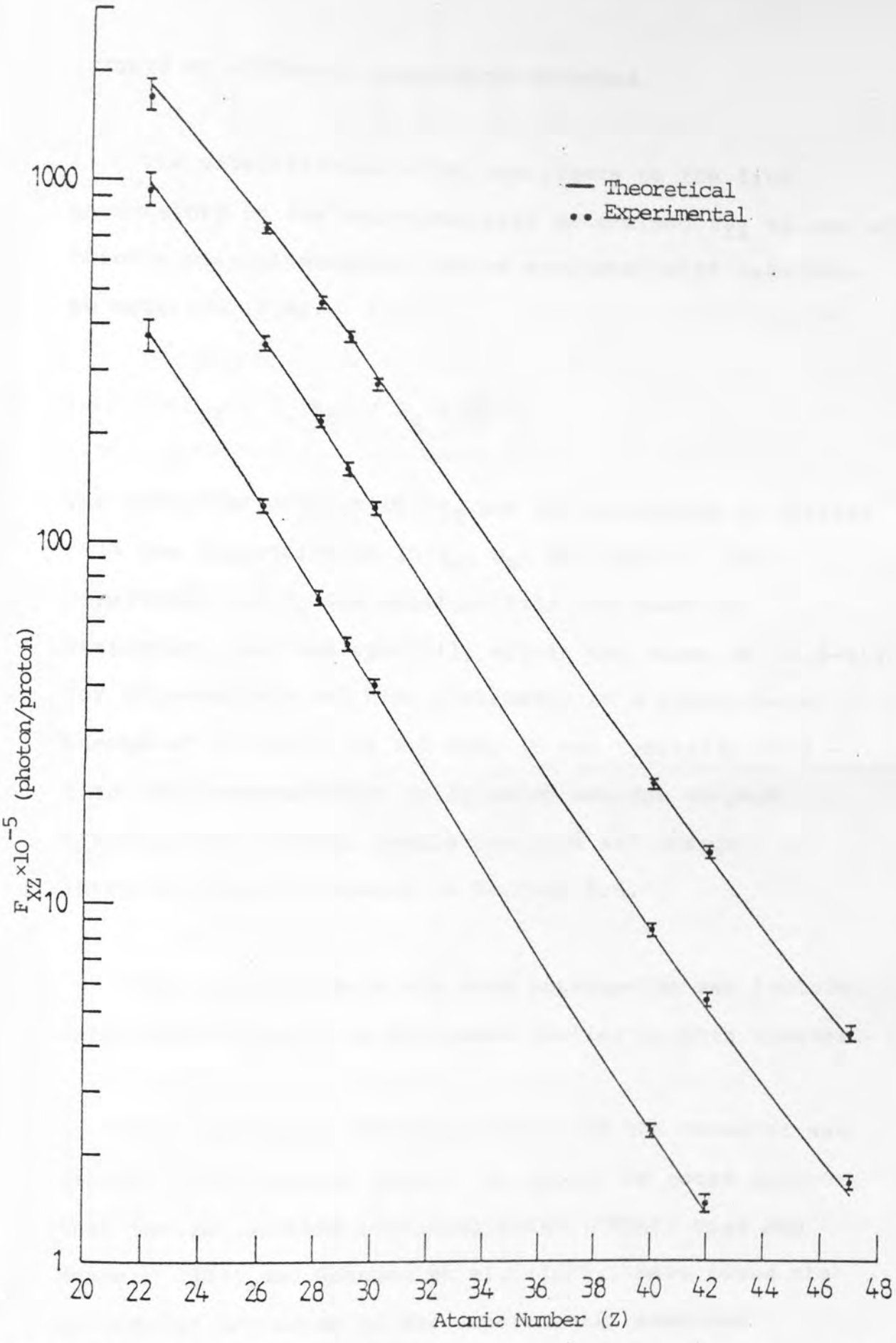

Figure (6.1) Thick target yield of Kα radiation from various pure matrices vs. atomic number at different bombarding energies.

targets at different bombarding energies.

The uncertainties which contribute to the final uncertainty in the experimentally determined F_{XZ} values of thick elemental standard can be evaluated with reference to equation (6.6).

$$F_{XZ} = I_x(E_o) \; / \; N_p \; \varepsilon \; \frac{d\Omega}{4\pi} \; T_1$$

The precision with which F_{XZ} can be determined is derived from the uncertainties in I_x, N_p, $d\Omega$ and ε. The uncertainty of I_x was obtained from the counting statistics, and was typically within the range of (0.5-5)% for intermediate and high Z elements at a proton beam energy of 1.5 MeV. At 2.5 MeV, it was typically (0.3 - 2)%. The uncertainties in I_x which are due to peak fitting, beam energy, sample position and charge integration are discussed in Section 5.6.

The uncertainty in the mass attenuation was included when calculating T_1 as discussed earlier in this chapter.

The calculated efficiency (ε), of the detector was assumed to be without error. It should be noted however, that several authors including Sokhi (1984), Dias and Renner (1982) and Johnson et al. (1978), have noted the systematic deviation of the experimental measured efficiency values from theoretically calculated values.

The overall uncertainty in the measured F_{XZ} values were estimated to be 3% - 10% for Ti<Z<Ag.

The experimental to theoretical ratio for F_{XZ} value is shown in Table (6.4) at 1.5, 2.0 and 2.5 MeV for the eight elements, showing a good agreement for all elements. These ratios are plotted as a function of the atomic number for three proton bombarding energies as shown in Figure (6.2).

6.3 THICK COMPOSITE TARGET MEASUREMENTS

The use of the proton induced X-ray emission technique allows quick non-destructive quantitative analysis of many types of targets with high accuracy and sensitivity. It is ideally suited to the analysis of metal alloys.

For certain elemental combinations, the X-ray yield is enhanced since the X-rays generated for one element are just above the K-absorption edge energy of the other elements, resulting in an increased yield.

Thus, when analysing a thick complex target the value of $I_x(E_o)$ is more complicated and the calculation of the elemental composition from the X-ray yield is considerably more difficult to obtain for a thick target than for a

	(Experimental/Theoretical) F_{XZ} Ratio At		
Elements	1.5 MeV	2.0 MeV	2.5 MeV
Ti	0.987 ± 0.163	0.970 ± 0.164	0.946 ± 0.164
Fe	1.016 ± 0.050	0.984 ± 0.051	0.983 ± 0.05
Ni	1.007 ± 0.081	1.018 ± 0.063	0.977 ± 0.076
Cu	0.987 ± 0.049	0.970 ± 0.049	1.013 ± 0.049
Zn	1.033 ± 0.078	1.008 ± 0.072	0.973 ± 0.076
Zr	1.035 ± 0.078	1.042 ± 0.067	0.996 ± 0.065
Mo	1.088 ± 0.092	1.078 ± 0.070	1.044 ± 0.069
Ag	1.070 ± 0.080	1.09 ± 0.107	1.060 ± 0.073

Table (6.4) The experimental/theoretical ratio for F_{XZ} values at different proton beam energies for 8 elements ranging from $Ti \leq Z \leq Ag$

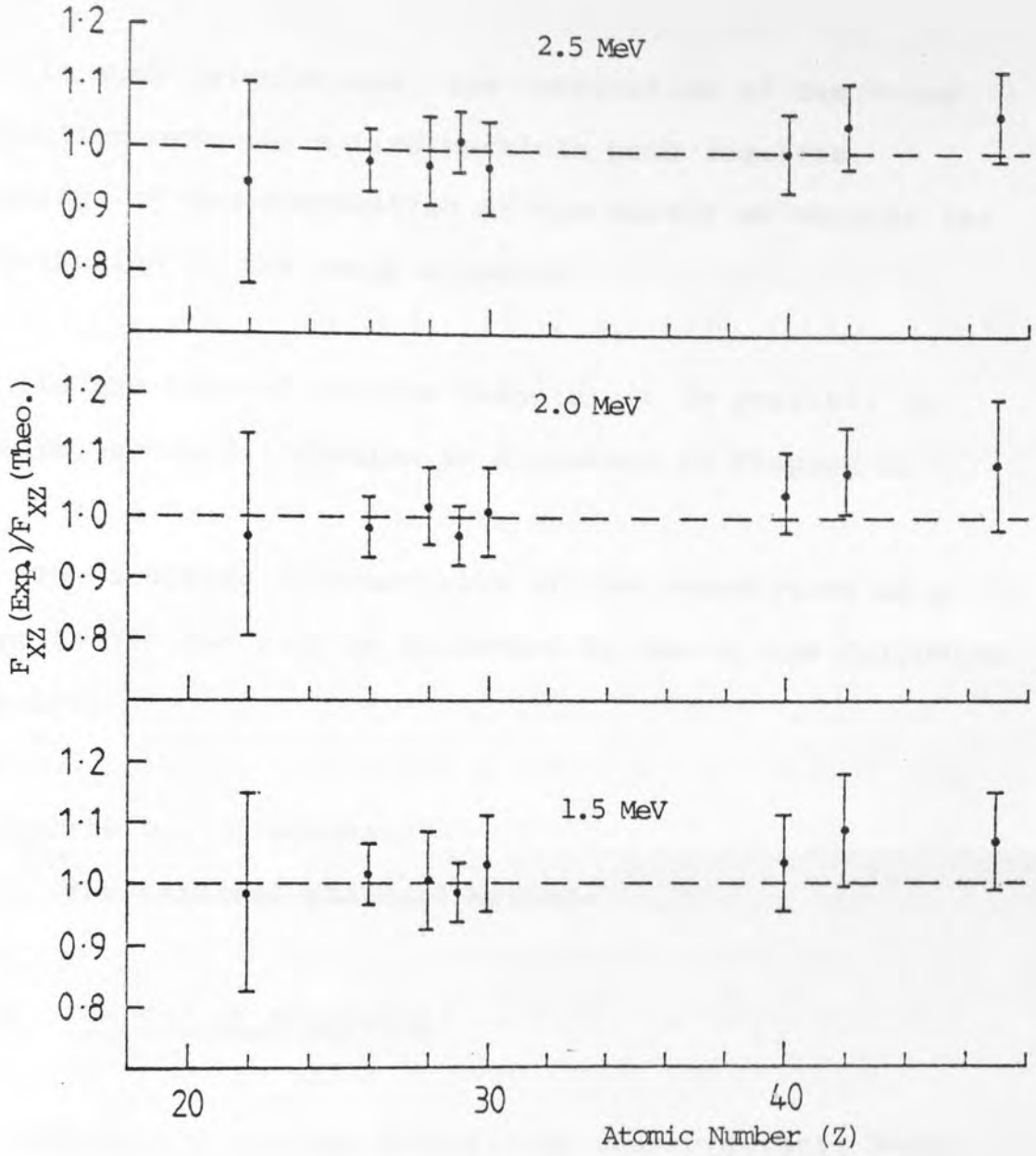

Figure (6.2) Experimental to theoretical F_{XZ} ratio of 8 pure matrices plotted against their atomic number Z at different bombarding energies.

thin one, (see Chapter 3).

In such calculations, the integration of the X-ray production over the entire particle path requires knowledge of the composition of the matrix as well as the distribution of the trace elements.

In the case of uniform targets, it is possible to perform such a calculation as discussed in Chapter 3.

The absolute determination of the composition of a thick target can also be performed by one of the following methods:

(i) the use of standards
(ii) the internal standard method.

6.3.1 The Use of Standards

Assuming a uniform target, the characteristic X-ray yield from the element i in a thick composite target can be calculated from equation (3.4), (neglecting the secondary production in this argument), and can be written as follows:

$$I_i(E) = N_p \varepsilon_{\alpha,i} \frac{d\Omega}{4\pi} T_1 W_i R_i \int_{E_o}^{E_f} n_i \sigma_{I,i}(E) \frac{T_2}{S_m(E)} dE \qquad (6.9)$$

The absolute values of the ionization cross-section $\sigma_{I,i}$, are only known with an accuracy of 10% and the geometrical factors ($\varepsilon_{\alpha,i}$, $d\Omega$ and T_1) are often difficult to estimate accurately. The determination of the elemental concentration from the published cross-section data cannot be done with a high degree of accuracy, Deconninck et al. (1975).

However, the use of a standard target of known composition is another possible method of facilitating the analysis of thick targets. The standard and the target to be analysed must contain similar relative amounts of major elements. When bombarding the target and the standard sequentially with protons of a fixed energy, their X-ray yield per incident proton can be measured with the same geometry in order to avoid systematic error in the measurements of Ω, ε_α, T_1 and uncertainties in the data of $\sigma_p(E)$ ($= \sigma_{I,i} W_i R_i$) . The ratio of the X-ray yield of the element in a sample and standard can be expressed as:

$$\frac{I_{sp}(E_o)}{I_{st}(E_o)} = \frac{N_{sp}}{N_{st}} \frac{\int_{E_o}^{E_f} \sigma_p(E) \frac{dE}{S_{m,sp}(E)} T_2}{\int_{E_o}^{E_f} \sigma_p(E) \frac{dE}{S_{m,st}(E)} T_2'}, \qquad (6.10)$$

where N_{sp} and N_{st} are the number of atoms per unit volume of the sample and standard, respectively; $S_{m,sp}(E)$ and $S_{m,st}(E)$ are the stopping power of the sample and standard; T_2 and T_2' are the absorption correction factors

for the sample and standard. The integrals are evaluated as discussed in Chapter 3 for the particular geometry employed. Consequently, equation (6.10) can be used to obtain N_{sp} in case of homogenous samples.

However, in case of a small amount of heavy Z elements present in light element matrices, the absorption for the K-radiation of the high Z elements can be neglected, reducing equation (6.10) to:

$$\frac{I_{sp}}{I_{st}} = \frac{N_{sp}}{N_{st}} \frac{\int_{E_o}^{E_f} \sigma_p(E) \frac{dE}{S_{m,sp}(E)}}{\int_{E_o}^{E_f} \sigma_p(E) \frac{dE}{S_{m,st}(E)}} \qquad (6.11)$$

Consequently, equations (6.10) or (6.11) can be used to obtain N_{sp}, once the integrals are evaluated.

The applicability of these equations, considering the effect of different single element matrices, has been discussed by Deconninck et al. (1975).

6.3.2 The Internal Standard Method

The internal standard method can be employed in the determination of trace elements, if the targets are in the form of homogeneous powders or liquids. A reference material of known quantity can be introduced directly into the sample and used as an internal standard to determine

its X-ray yield. The concentration of the element of interest can be obtained by comparing the X-ray yields from that element with the standard. It should be noted however, that the addition of the standard to the analysed sample must not induce any appreciable difference in the X-ray attenuation or in the stopping powers $S_{m,st}(E)$ and $S_{m,sp}(E)$ if meaningful results are to be obtained. Many authors, including Khaliquzzaman et al. (1981, 1983), Deconninck (1977), Lin et al. (1979) and Clayton (1981) have used both or one of these methods to determine the elemental composition in biological, liquid, geological and metal samples. The present study is primarily concerned with metallic binary alloys. In order to determine the absolute amounts of trace elements from measured thick target yields, one has either to use an appropriate reference material or to calculate the X-ray yield absolutely. Since suitable standards are often not available or are expensive to obtain the concentrations of trace elements can be calculated from their X-ray yields relative to that of the matrix.

In actual application, a calibration curve for the relative X-ray yields at different trace element concentrations should be established first. This method and its applications are discussed in the following sections.

6.4 STUDIES ON BINARY ALLOYS

The intensity of the characteristic X-rays emitted from an element in alloys or compounds bombarded by a proton beam is, in general, not simply a function of the concentrations and absorption coefficients of the various elements in the compound. There is, in general, an additional dependency on the differences between the atomic numbers of the elements present in the alloy or compound. This effect, often termed the "enhancement effect" is due to the fact that the characteristic spectra of elements of higher Z are sufficiently energetic to excite the spectra of elements of lower Z, (see Section 3.4). The added contribution to the intensity of the spectra of lower Z, or enhancement (secondary fluorescence), may be highly significant. Indeed, under certain conditions, more than 50% of the total intensity could be due to the enhancement, (see Table 3.1) The theoretical formulas of the fluorescent X-ray intensities (the primary and secondary fluorescent X-rays) have been discussed fully in Section 3.5. The basic assumptions of the formulae are that the specimen is homogeneous, thick, and has a smooth surface; and that the penetration of radiation obeys the exponential law.

6.4.1 Theoretical Evaluation of the Intensity Ratio in Binary Alloys

For a thick target, A_xB_y, the number ($I_{x,A}$) of characteristic X-rays under the Kα-peak corresponding to the element A and the number of secondary fluorescence X-rays, $I_{A,sec}$, which are enhanced by the characteristic K X-radiation of element B, can be obtained from equation (3.4) and is given as:

$$I_{x,A}(E_o) = C_{1,A}[n_A W_A R_A N_p \int_{E_o}^{E_f} \frac{\sigma_{I,A}(E)}{S_{m,A}(E)} T_2(E)\, dE + I_{A,sec}] \qquad (6.12)$$

where $C_{1,A}$ is the geometrical factor ($= \varepsilon_{\alpha,A} \frac{d\Omega}{4\pi} T_1$), $I_{A,sec}$ is the secondary production of the Kα-radiation of element A by Kα and Kβ radiation of element B, and n_A is the number of atoms per unit volume of element A ($= \frac{N_o \rho}{A} C_A$).

Given that

$$n_A W_A R_A N_p \int_{E_o}^{E_f} \frac{\sigma_{I,A}(E)}{S_{m,A}(E)} T_2(E)\, dE = I_{A,pri} \quad ,$$

equation (6.12) can be written as

$$I_{X,A}(E_o) = C_{1,A}[I_{A,pri} + I_{A,sec}] \qquad (6.13)$$

where $I_{A,pri}$ refers to the primary production of the Kα-

radiation of element A.

OR

$$I_{X,A}(E_o) = C_{1,A}\, I_{A,pri}\left[1 + \frac{I_{A,sec}}{I_{A,pri}}\right] \qquad (6.14)$$

where $\left(\frac{I_{A,sec}}{I_{A,pri}}\right)$ is known as the enhancement factor; $E_n(B,A)$ see Section 3.5.2.

Therefore,

$$I_{X,A}(E_o) = C_{1,A}\, I_{A,pri}\left[1 + E_n(B,A)\right] . \qquad (6.15)$$

Consequently, the number, $I_{X,B}$, of the characteristic X-rays of element B per incident proton generated in a complex target can be written as

$$I_{X,B}(E_o) = C_{1,B}\, I_{B,pri} . \qquad (6.16)$$

The intensity ratio of the element A to that of the matrix element B in an alloy or compound can be obtained by dividing equation (6.15) by equation (6.16):

$$\frac{I_{X,A}(E_o)}{I_{X,B}(E_o)} = \left[\frac{I_{A,pri}}{I_{B,pri}}\left(1 + E_n(B,A)\right)\right] \times \frac{C_{1,A}}{C_{1,B}} . \qquad (6.17)$$

The right hand side of equation (6.17) can be determined theoretically after substituting the appropriate values of $C_{1,A}$ and $C_{1,B}$. The left hand side of the same equation

can be determined experimentally after integrating the appropriate Kα-peaks.

The theoretical formula of the fluorescent X-ray intensity (the primary for element A and B, the secondary for element A only) was discussed in Section 3.5 and actual calculations were made for Fe/Ni and Cr/Fe alloys at different concentrations of Fe and Cr respectively. The computer programme, as discussed in Section 3.6, has been worked out to include the calculation stated above. Since the intensity of fluorescent X-rays emitted from an element in alloys or compounds is a function of the weighted fraction of the element and also of the coexistent element, Shiraiwa and Fujino (1966), the resultant Kα-intensity ratio of Fe/Ni and Cr/Fe with and without inclusion of the secondary fluorescent X-rays of Fe and Cr is plotted against the weight fraction of the concentration of Fe and Cr in Fe/Ni and Cr/Fe alloys as shown in Figures (6.3) and (6.4) respectively. These curves represent the theoretical calibration curves for any combination of Fe/Ni and Cr/Fe alloys for 2 MeV proton beam bombardment. In these alloys, the secondary X-ray production of the K X-rays of interest becomes significant in cases where the energy of the primary induced matrix X-rays lies just above the absorption edge of the element of interest, as shown in Figure (6.5) for the Cr/Fe alloys. In this case, the primary induced Fe Kα X-rays have an energy of 6.403 keV, which is slightly larger than the K-

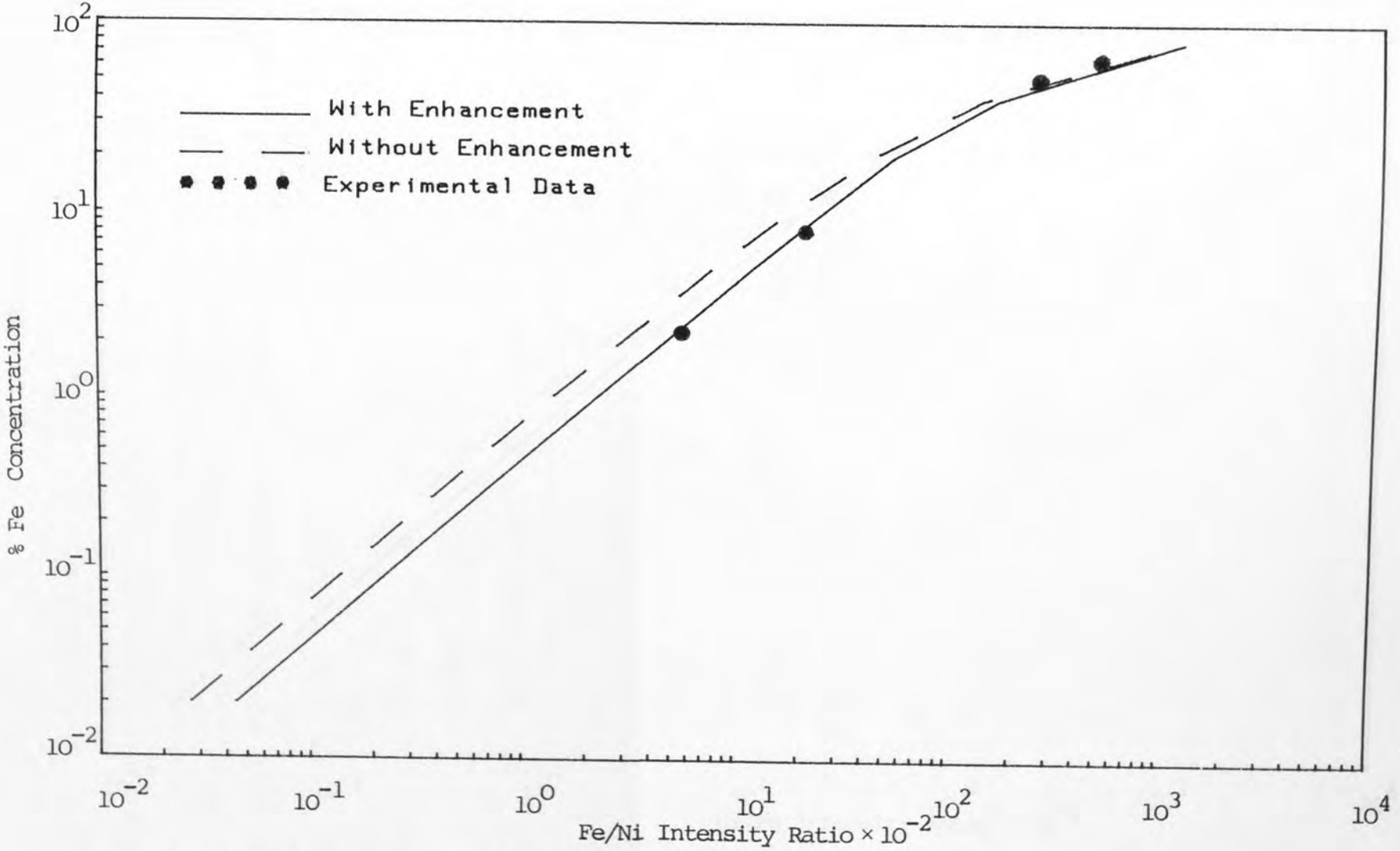

Figure (6.3) Calibration curves used to estimate the % elemental composition of Fe in Fe/Ni alloys bombarded at 2 MeV protons.

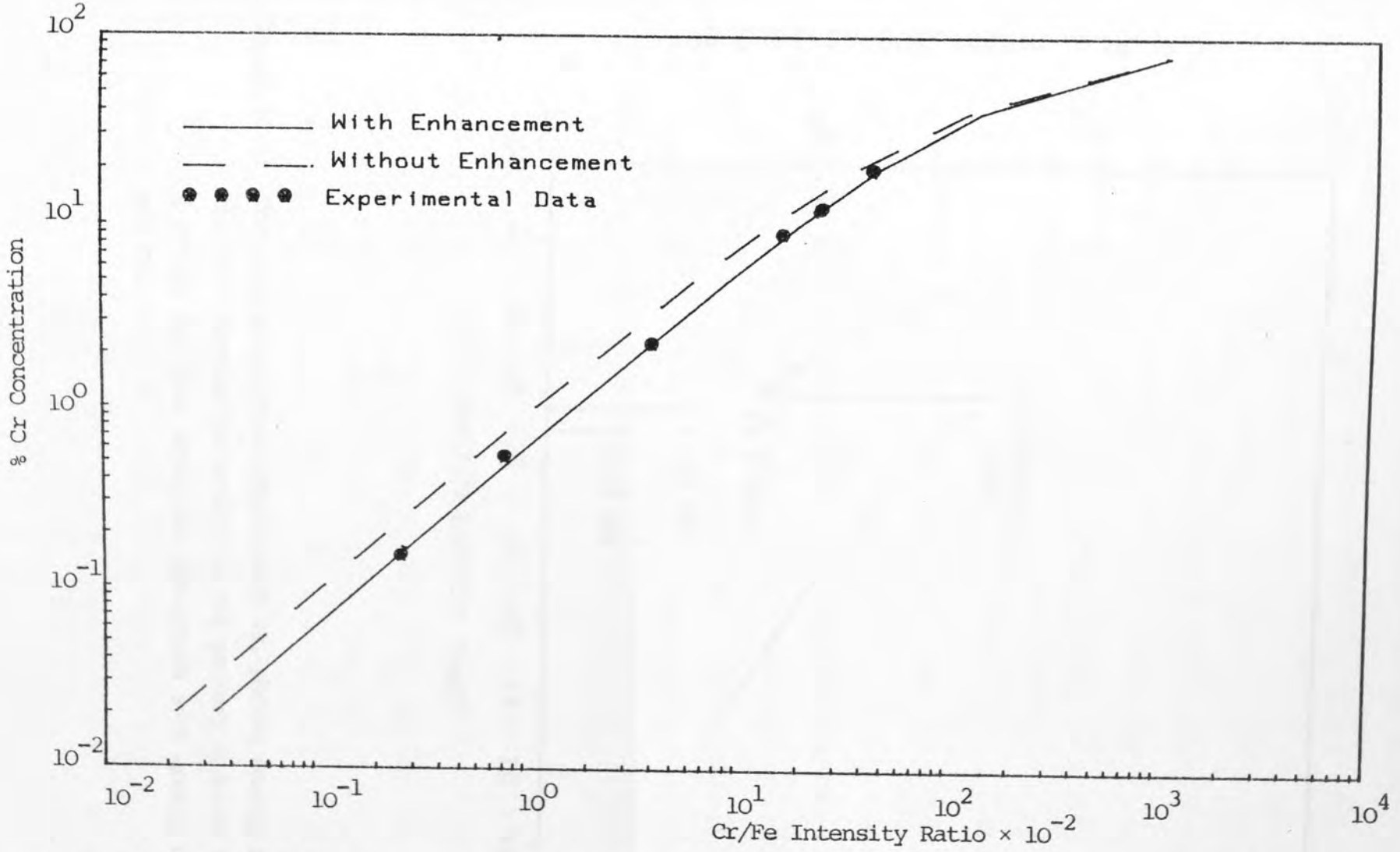

Figure (6.4) Calibration curves used to estimate the % elemental composition of Cr in Cr/Fe alloys bombarded at 2 MeV protons.

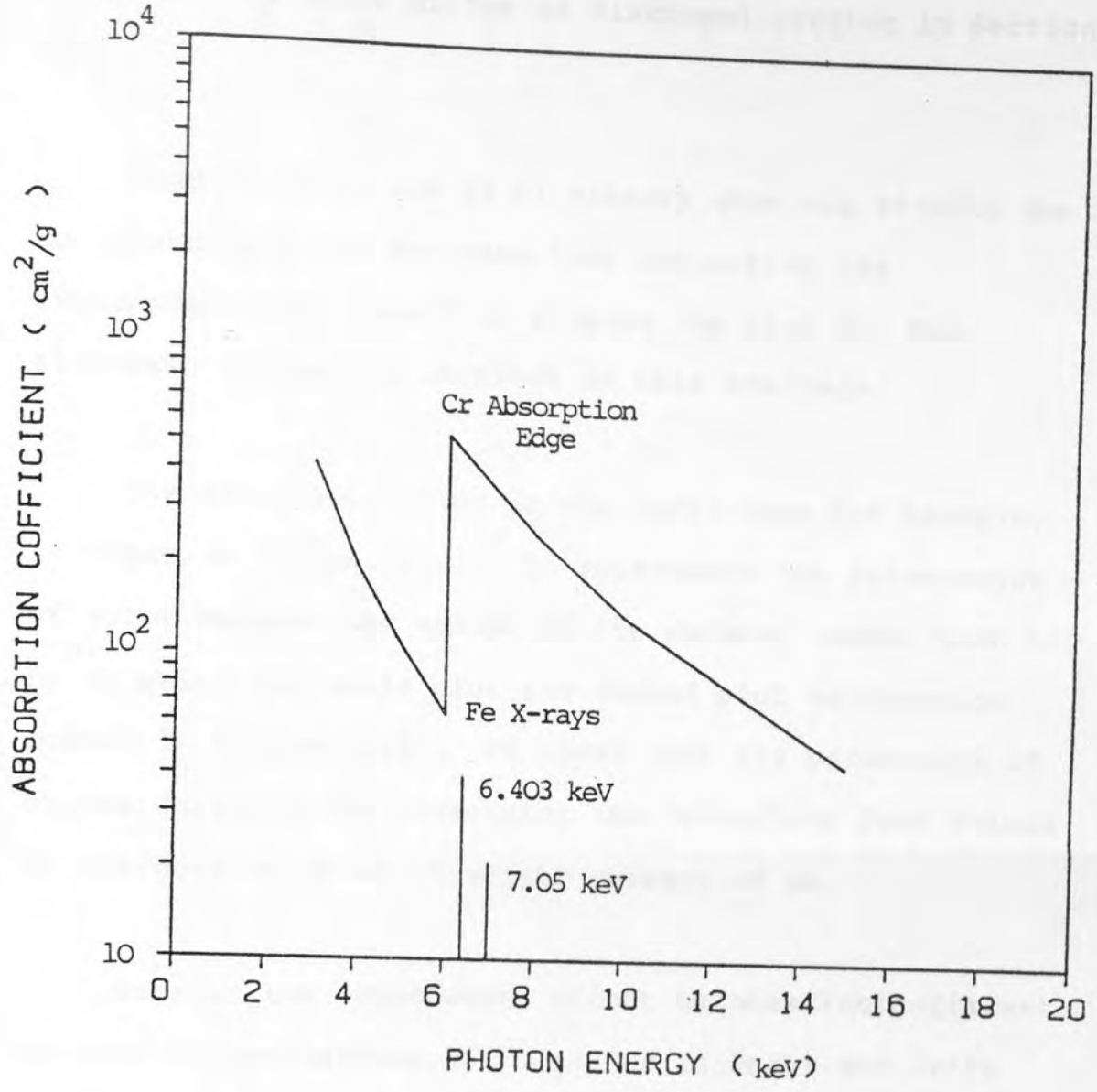

Figure (6.5) The mass attenuation coefficient vs. photon energy for the Cr. Showing the energy of the primary induced Fe K X-rays are just above the absorption edge energy of the Cr.

absorption edge of Cr at 5.988 keV. This is also applicable to Fe/Ni alloys as discussed earlier in Section 3.4.

Figures (6.3) and (6.4) clearly show the effects due to enhancement and indicate that neglecting the enhancement will result in a value too high for the elemental content of interest in this analysis.

The analytical error in the Fe/Ni case for example, is shown in Figure (6.6). It represents the percentages of error between the values of the deduced composition of Fe by using the solid plot and dashed plot calibration curves in Figure (6.3). It shows that the percentage of errors decreases by increasing the Fe-content from values of 60% down to 2% at 64 weight percent of Fe.

Because the enhancement effect becomes insignificant at high concentrations of Fe and Cr in Fe/Ni and Cr/Fe alloys, there will only be negligible differences in the calculated intensity ratio with or without inclusion of the enhancement effects.

Using the solid plots in the calibration curves will lead to direct measurements of the concentration of Fe and Cr in the unknown Fe/Ni and Cr/Fe alloys' samples through their measured intensity ratio.

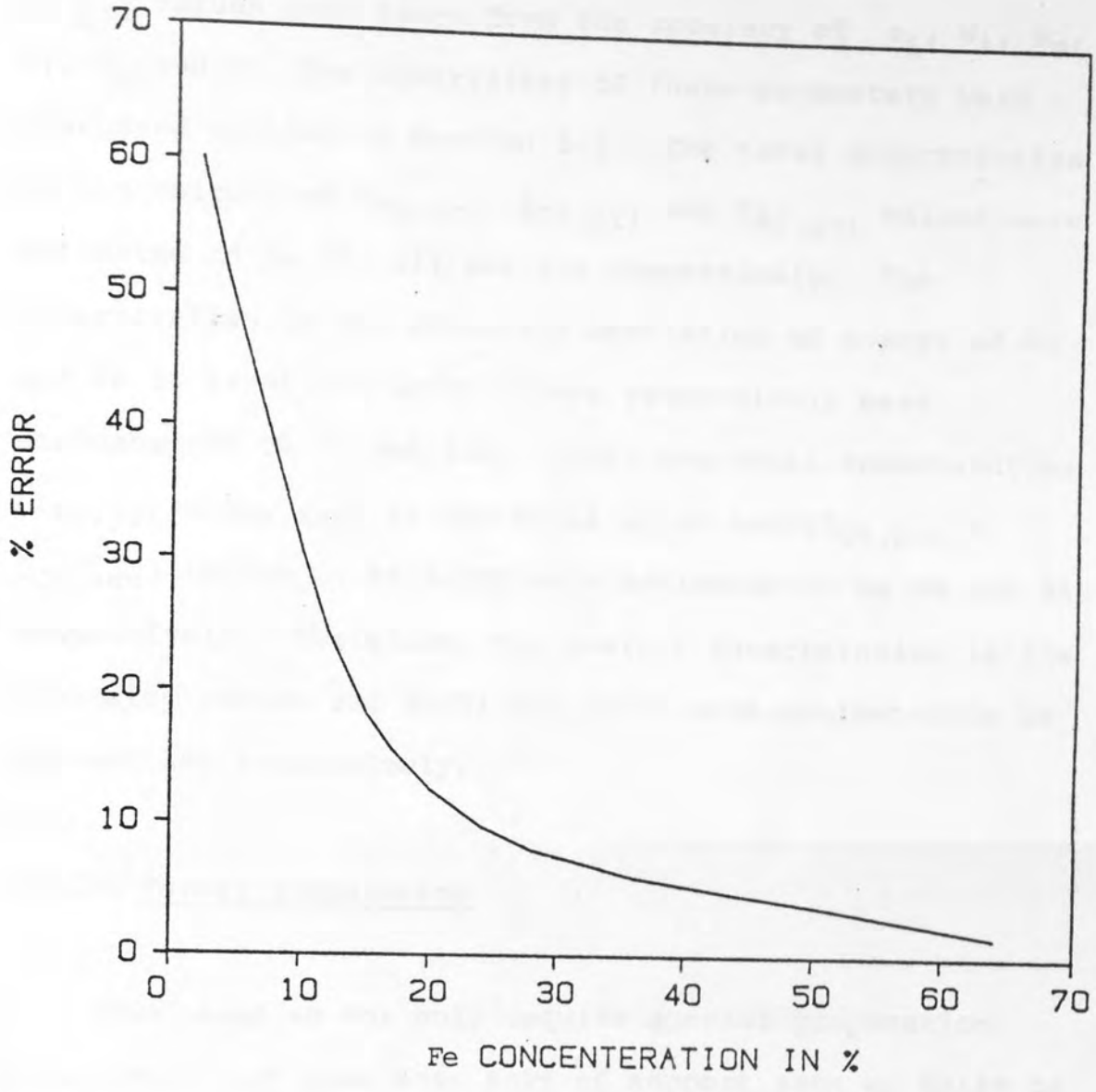

Figure (6.6) Percentage error in the Fe concentration with PIXE neglecting the enhancement effect in a Ni-matrix in dependence on the given Fe concentrations, for Ep = 2 MeV.

The errors in the calculated $I_{A,pri}$, $I_{A,sec}$ and $I_{B,pri}$ values were taken from the accuracy of σ_i, W_i, S_m, T_1, T_2 and E. The uncertainty of these parameters were discussed earlier in Section 5.2. The total uncertainties in the calculated $I_{Fe,pri}$, $I_{Cr,pri}$ and $I_{Ni,pri}$ values were estimated to be 7%, 11% and 11% respectively. The uncertainties in the secondary excitation of X-rays of Ni and Fe in Fe/Ni and Cr/Fe alloys respectively were estimated to be 9% and 10%. Thus, the total uncertainties ($I_{Fe,pri} + I_{Fe,sec}$) in the Fe/Ni alloy and ($I_{Cr,pri} + I_{Cr,sec}$) in the Cr/Fe alloy were estimated to be 6% and 8% respectively. Therefore, the overall uncertainties in the intensity ratios for Fe/Ni and Cr/Fe were estimated to be 12% and 10% respectively.

6.4.2 Target Preparation

Thin samples not only require special preparation techniques, but also some sort of support such as Mylar or polycarbonate membrane prior to its presentation to the proton beam for analysis. Many authors including Campbell (1977), Mangelson et al. (1977), Kivits (1980) and Khan and Crumpton (1981), have reviewed a number of methods for sample preparations depending on the type of sample.

Certain samples are suited to direct irradiation without any preparation, including hair, teeth and metal alloys, Valkovic et al. (1975), Ahlberg and Akselsson

(1976).

In the present work, thick binary alloys have been analysed. Some of the samples required were supplied by their manufacturers in wrought form, or the samples had to be cut to a suitable size. In either case, surface irregularities were encountered.

Surface irregularities act as heterogeneities in the path of the primary exciting X-rays and have an even greater effect on the secondary fluorescent X-rays. The effect of the surface irregularities are severe only when low energy X-rays are being measured. Thus, in order to ensure that errors were not introduced from improper surfaces, most of the metallic samples were polished prior to PIXE analysis.

A summary of the polishing method used on these metallic alloy samples follows.

The wrought samples supplied by MBH Co. were cut into pieces 25×25 mm and 1 mm thick. These samples were mounted by using a cooled mounting compound, (Resin base), which hardens by the chemical reaction between the constituents. The samples were first placed on moulds. Enough mounting compound was then poured so that the upper part of the samples was covered. This was left for 10-20 minutes, or until the compound hardened. Once hardened,

the lower part of the samples was polished on a water cooled rotating wheel on which was mounted varying degrees of emery paper, starting with a coarse grit P180 and moving in stages to the very fine P1200. The samples were then cleaned with the ultrasonic-cleaner to remove any possible contamination on their surfaces.

After this, the samples were polished with a 6μm diamond to remove the P1200 emery grit scratches. At this stage, the sample surfaces had a mirror like quality. Finally, the samples were cleaned and polished with 1μm diamond.

After carefully cracking the mount with a vice, the samples were removed from these mounts, and were subsequently mounted on a suitable target holder ready for analysis.

6.4.3 Experimental Measurements and Comparisons

In addition to the theoretical evaluation of the intensity ratio of the element A to that of the matrix element B, an experimental determination was made to check these calculations and the validity of the approximation in the determination of the secondary excitation.

Ten thick standard binary alloys of Fe/Ni and Cr/Fe, containing Fe and Cr at different concentrations were

obtained from Goodfellow Metals Co. and MBH Analytical Limited, for testing the method. The standards obtained from Goodfellow Metal Co. were smooth, homogeneous and thick enough to stop the proton beam. The standards obtained from MBH Co. were in the form of wrought alloys. Those wrought alloys were specially prepared before mounting them onto the target holders, see Section 6.4.2. Analytical data was supplied with each standard, as listed in Table (6.5), but was not accurately certified by the suppliers.

Most of the standards in Table (6.5) contain not only Fe and Ni in Fe/Ni alloys or Cr and Fe in Cr/Fe alloys but also other impurities such as Mn, Cu, Co and Mo. These impurities make the analysis very complicated, especially if they exist at high concentrations. In the present work, standards were chosen to have the least possible amount of these impurities in order to make a direct comparison between the theoretical and experimental intensity ratio of the element of interest.

The spectrum taken from the standard number 6, for example, is shown in Figure (6.7). The Mn-lines interfere and overlap with the Cr and Fe lines, and the Fe Kβ escape peak interferes with the Cr Kα line. The number of counts under the Fe Kα and Cr Kα peaks was determined with very good peak fitting procedures, provided by one of the programmed facilities of the on-line computer. The

No.	Composition in % / Standard Alloys	C %	Mn %	Si %	Cr %	Fe %	Ni %	Cu %	Mo %	Source
1.	Fe/Ni/Cu (Monel 400)	0.15	-	<0.5	-	<2.5	bal	31	-	Goodfellow Metal Co. (UK)
2.	Fe/Ni/Cr (Inconel 600)	<0.15	<1	0.5	15.5	8	bal	<0.5	-	Goodfellow Metal Co. (UK)
3.	Fe/Ni	-	-	-	-	50	50	-	-	Goodfellow Metal Co. (UK)
4.	Fe/Ni (Invar)	<1	<1	<1	-	bal	36	-	-	Goodfellow Metal Co. (UK)
5.	Plain Carbon Steel (12M64)	1.03	0.42	0.38	0.15	bal	0.08	0.03	0.007	MBH-Analytical Ltd.
6.	Low Alloy (12M54)	0.66	0.81	0.23	0.5	bal	0.46	0.078	0.175	MBH-Analytical Ltd.
7.	Fe/Cr/Mo	-	-	-	2.25	bal	-	-	0.5	Goodfellow Metal Co. (UK)
8.	Fe/Cr/Mo	-	-	-	9	bal	-	-	1.0	Goodfellow Metal Co. (UK)
9.	Fe/Cr (AISI 410)	<1.5	<1	<1	11.5-13.5	bal	-	-	-	Goodfellow Metal Co. (UK)
10.	Fe/Cr/Ni (AISI 302)	<1.6	<2	-	17-20	bal	7-11	-	-	Goodfellow Metal Co. (UK)

Table (6.5) The analytical data of the standards as given by the manufacturers.

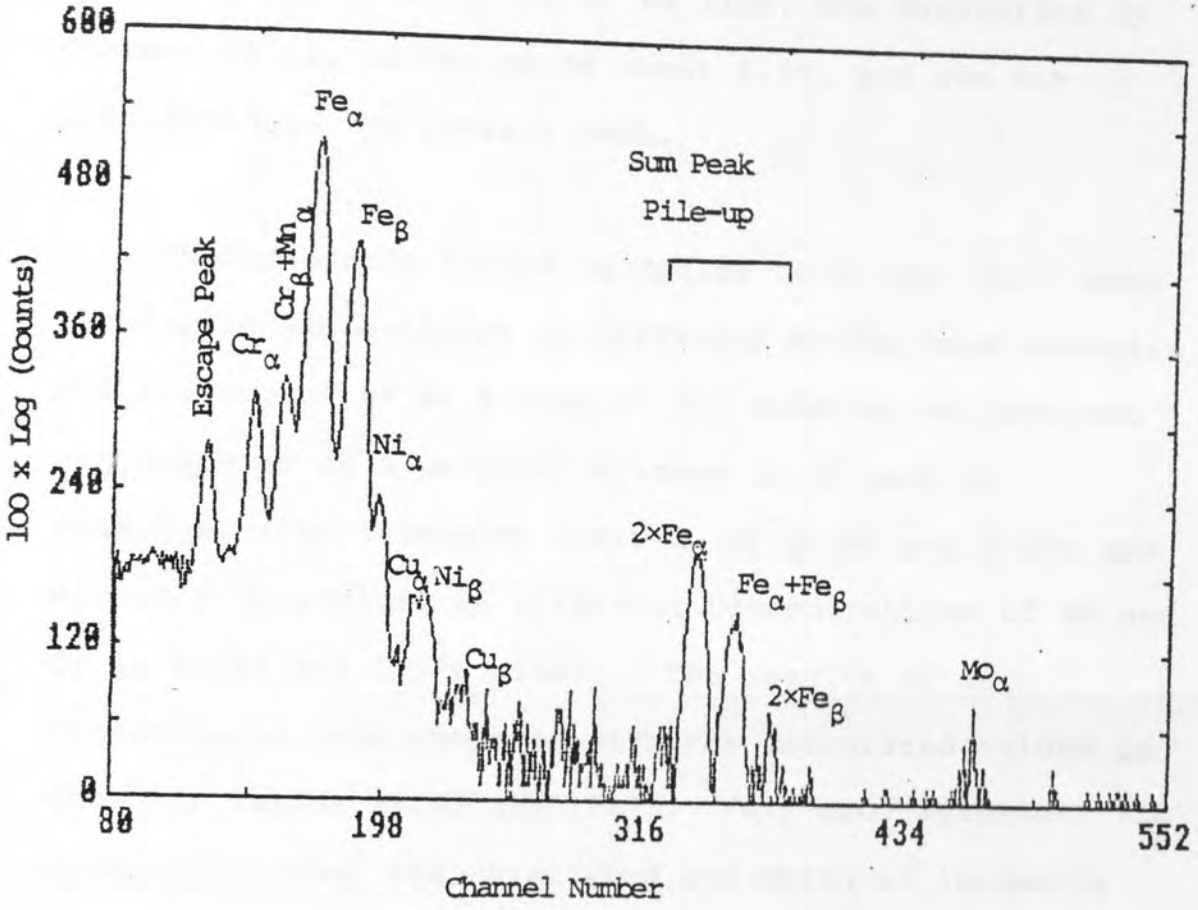

Figure (6.7) PIXE spectrum from analysis of 1 mm thick low alloy steel metal (12M54).

intensities of Fe Kα and Cr Kα was obtained with an uncertainty of less than 5%. Since all the lines sit on high backgrounds, especially on the lower energy side of the strong Fe Kα line, the contribution of the Fe Kβ escape peak to the Cr Kα line, was determined by Mommsen et al. (1979) to be about 4.5%, and are not considered in the present work.

The standards listed in Tables (6.6) and (6.7) were irradiated sequentially at different proton beam energies, and the number of Kα X-rays of the elements of interest was measured as a weighted average of 10 sets of readings. The intensity ratio R, of Fe/Ni and Cr/Fe was directly determined at different concentrations of Fe and Cr in Fe/Ni and Cr/Fe alloys. The results of such measurements were compared with the calculated values as shown in Tables (6.6) and (6.7). Very good agreement was obtained between the calculated and measured intensity ratios of Fe/Ni and Cr/Fe. The percentage difference between the theoretical and experimental intensity ratios varies between 10% down to less than 1%. The high percentage difference in some samples is due to either the existence of the impurities at high concentrations or due to existence of one element of interest at very low concentration which makes the determination of its peak more difficult. The intensity ratio data for the 2 MeV proton bombardment were plotted as filled circles in Figures (6.3) and (6.4).

Standard	2.5 MeV		% differ-ence	2.0 MeV		% differ-ence	1.5 MeV		% differ-ence	1.0 MeV		% differ-ence
	$(Fe/Ni)_{thr}$	$(Fe/Ni)_{exp}$		$(Fe/NI)_{thr}$	$(Fe/Ni)_{exp}$		$(Fe/Ni)_{thr}$	$(Fe/Ni)_{exp}$		$(Fe/Ni)_{thr}$	$(Fe/Ni)_{exp}$	
* $Fe_{2-2.5}/Ni_{65}/Cu_{31-33}$	0.058	0.052	12%	0.060	0.055	8.7%	0.062	0.056	10%	0.063	0.058	8.6%
* $Fe_8/Ni_{72}/Cr_{16}$	0.194	0.192	1%	0.201	0.206	2.5%	0.209	0.203	2.9%	0.215	0.209	2.8%
Fe_{50}/Ni_{50}	2.75	2.77	0.7%	2.52	2.50	0.8%	2.29	2.31	1%	2.10	2.18	3.7%
Fe_{64}/Ni_{36}	5.36	5.53	3%	4.79	4.80	0.2%	4.25	4.31	1.5%	3.79	3.94	4%

* The concentrations of Fe and Ni in Fe/Ni alloys were used as given, and correcting for the major impurities when calculating the intensity ratios. Whereas they normalised to 100% when calculating the enhancement factor.

Table (6.6) Comparison between the calculated and measured Fe/Ni intensity ratio at different proton bombarding energy.

No.	Standard	*C_{Cr} %	*C_{Fe} %	2.5 MeV		% diff-erence	2.0 MeV		% diff-erence	1.5 MeV		% diff-erence	1.0 MeV		% diff-erence
				$R_{th.}$	$R_{exp.}$		$R_{th.}$	$R_{exp.}$		$R_{th.}$	$R_{exp.}$		$R_{th.}$	$R_{exp.}$	
1.	12M64	0.15	99.85	2.49×10^{-3}	2.57×10^{-3}	3.2%	2.6×10^{-3}	2.62×10^{-3}	0.8%	2.69×10^{-3}	2.72×10^{-3}	1%	2.72×10^{-3}	3.08×10^{-3}	12%
2.	12M54	0.53	99.47	8.67×10^{-3}	8.0×10^{-3}	8%	9.04×10^{-3}	8.10×10^{-3}	11%	9.34×10^{-3}	8.60×10^{-3}	8.2%	9.45×10^{-3}	8.8×10^{-3}	7%
3.	Fe/Cr/Mo	2.26	97.74	0.038	0.037	3%	0.039	0.040	2.5%	0.040	0.039	2.5%	0.041	0.042	2.4%
4.	Fe/Cr/Mo	9.01	90.91	0.170	0.162	5%	0.172	0.163	5%	0.174	0.167	3.5%	0.174	0.168	3.5%
5.	AISI 410	12.5	87.5	0.249	0.242	3%	0.249	0.247	1%	0.250	0.240	4%	0.248	0.241	3%
6.	AISI 302	19.57	80.43	0.448	0.433	3%	0.440	0.425	3.5%	0.431	0.417	3%	0.421	0.415	1%

Table (6.7) Comparison between the calculated and measured Cr/Fe intensity ratio at different proton bombarding energies.

* The concentration of Cr and Fe in the Cr/Fe alloys are calculated so that they add up to 100% since the concentration of the other coexistent elements in these standards are very small amount.

In order to determine the concentration of Fe and Cr in the Fe/Ni and Cr/Fe test alloy samples obtained from the Goodfellow Metal Co. and MBH Co., the samples were treated in a similar manner as the standards and the intensity ratio of Fe/Ni and Cr/Fe were determined at 2 MeV protons.

The concentration of Fe and Cr in the Fe/Ni and Cr/Fe samples were determined directly from their calibration curves, Figures (6.3) and (6.4). The results are summarised in Table (6.8) and are compared with the given composition of Fe and Cr respectively. The given concentration of Fe, Ni and Cr in Fe/Ni and Cr/Fe alloys are assumed to add up to 100% since the concentrations of the other coexistent elements in these samples are very small. These given concentrations were used to calculate the intensity ratio listed in Table (6.8).

The samples containing impurities at high concentrations of elements other than Fe, Ni and Cr in Fe/Ni and Cr/Fe alloys were treated individually as follows:

(i) the computer programme had to be modified in order to include the effect of high concentration impurities on the stopping power and the mass absorption coefficient corrections, when

No.	Test Sample A/B	Source	Given Composition of element A in %	Intensity Ratio at 2 MeV protons		Deduced Composition of element A in %
				Theoretical	Experimental	
1.	Fe/Ni (high permeability magnetic alloy)	Goodfellow Co. (1982)	16%	0.40±12%	0.38±1%	15±1%
2.	Cr/Fe (162-AA)	MBH Co. (1983)	2×10^{-2}%	3.39×10^{-4}±10%	3.65×10^{-4}±6%	2.20×10^{-2}±6%
3.	Cr/Fe (En 26 Wrought steel)	British Standard 970 - (1955)	0.68%	1.16×10^{-2}±10%	1.14×10^{-2}±3%	0.66±3%
4.	Cr/Fe (En 24 Wrought steel)	British Standard 970 - (1955)	1.19%	2.04×10^{-2}±10%	1.98×10^{-2}±2%	1.15±2%
5.	Cr/Fe (En 31 Wrought steel)	British Standard 970 - (1955)	1.32%	2.28×10^{-2}±10%	2.27×10^{-2}±2%	1.35±2%
6.	Cr/Fe (9% Cr)	Goodfellow Co. (1982)	9%	17.2×10^{-2}±10%	16.3×10^{-2}±2%	8.6±2%

Table (6.8) The deduced concentrations of Fe and Cr in Fe/Ni and Cr/Fe alloys respectively, directly from the calibration curves Figures (6.3) and (6.4) using the experimentally determined intensity ratios.

calculating the intensity ratio; and,

(ii) the concentrations of the elements of interest had to be normalised to 100% when calculating the enhancement factor.

These effects may increase the uncertainty in the determination of the actual concentration of Fe and Cr in Fe/Ni and Cr/Fe alloys. For example, in a 65% Ni/33% Cu/2% Fe alloy, the complete neglect of the tertiary fluorescent X-rays of Fe, due to Cu-K lines, was calculated to be 30% when their concentrations (i.e. Fe and Cu) were normalised to 100%. This caused a 22% difference between the given composition and the deduced composition. By correcting for this effect, the composition of Fe could be determined within a 5% difference.

In pure binary alloys, such as Fe_{50}/Ni_{50} and $Cr_{0.68}/Fe$ or alloys containing small amounts of impurities such as $Cr_{2.25}/Fe_{97.25}/M_{0.05}$ the deduced composition of Fe and Cr was determined to be within 3% of the given composition. Thus, the method discussed in this section can be used to determine the concentration of the major elements in binary metallic alloys with an accuracy, in general, better than ±5%.

6.5 ENHANCEMENT MAGNITUDES IN Fe/Ni AND Cr/Fe ALLOYS

After presenting the method of calculation of the intensity ratio in metallic binary alloys with inclusion of the enhancement effect, and after comparing the results with the measured intensity ratio of some Fe/Ni and Cr/Fe samples of known compositions, it is very important to present the magnitude of the enhancement factor of the Fe and Cr Kα-lines in Fe/Ni and Cr/Fe alloys respectively.

Generally, the enhancement magnitude is calculated according to the procedure discussed in Section 3.5. In the Fe/Ni alloy, for example, the enhancement of the Fe Kα line, due to the excitation of the primary X-rays from Ni Kα and Kβ lines at different concentrations of Fe using 2 MeV protons, is illustrated in Table (6.9) and in Figure (6.8). Also, the enhancement in the Cr/Fe alloy has been determined in a similar way as shown in Table (6.10) and Figure (6.9).

At low Fe concentrations in a Fe/Ni alloy, Fe is exposed to an intense flux of exciting Ni Kα-radiation, so that nearly 64% of the total Fe Kα-radiation is due to the secondary excitation processes. If the Fe abundance in the Ni-matrix is increased, the primary Fe-intensity increases where as the Ni radiation decreases. The enhancement of the Fe-Kα line due to the excitation of the primary X-rays from Ni Kα and Kβ lines decreases as shown

Concentrations wt%		Enhancement of Fe-K_α Lines		Total Enhancement of Fe-K_α
C_{Fe}	C_{Ni}	Due to Ni-K_α	Due to Ni-K_β	
0.02	99.98	0.570	0.0704	0.640
0.05	99.95	0.569	0.0702	0.639
0.10	99.90	0.568	0.0702	0.638
0.50	99.50	0.560	0.0692	0.628
1.00	99.00	0.550	0.0680	0.620
5.00	95.00	0.470	0.0600	0.530
10.0	90.00	0.400	0.0500	0.450
20.0	80.00	0.290	0.0400	0.330
40.0	60.00	0.160	0.0200	0.180
80.0	20.00	0.036	0.0048	0.041

Table (6.9) Enhancement of the Fe K_α line due to the exctitation of the primary X-rays from Ni K_α and K_β lines at different concentrations of Fe.

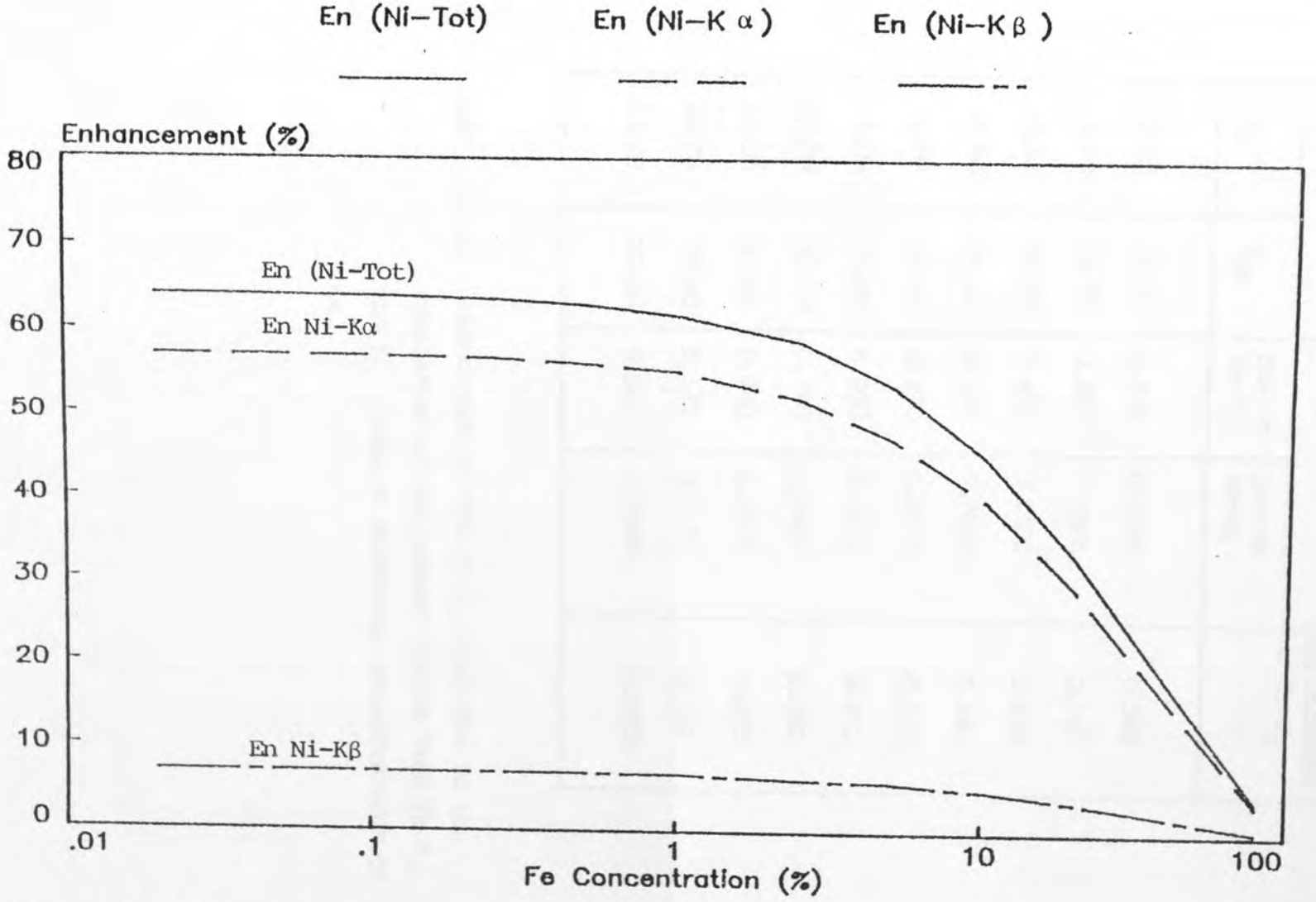

Figure (6.8) Percentage intensity enhancement of the Fe Kα line in dependence on the Fe concentration in weight % in a Ni-matrix. The excitation due to the Ni Kα and Kβ lines are shown separately.

Concentrations wt%		Enhancement of Cr-K_α		Total Enhancement of Cr-K_α
C_{Cr}	C_{Fe}	Due to Fe-K_α	Due to Fe-K_β	
0.02	99.98	0.488	0.0604	0.548
0.05	99.95	0.487	0.0603	0.547
0.10	99.90	0.486	0.0602	0.546
0.50	99.50	0.478	0.0590	0.540
1.00	99.00	0.470	0.0580	0.530
5.00	95.00	0.400	0.0500	0.450
10.00	90.00	0.340	0.0400	0.380
20.00	80.00	0.240	0.0300	0.270
40.00	60.00	0.130	0.0170	0.150
80.00	20.00	0.0287	0.00385	0.0325

Table (6.10) Enhancement of the Cr K_α lines due to the excitation of the primary X-rays from Fe K_α and K_β lines at different concentrations of Cr.

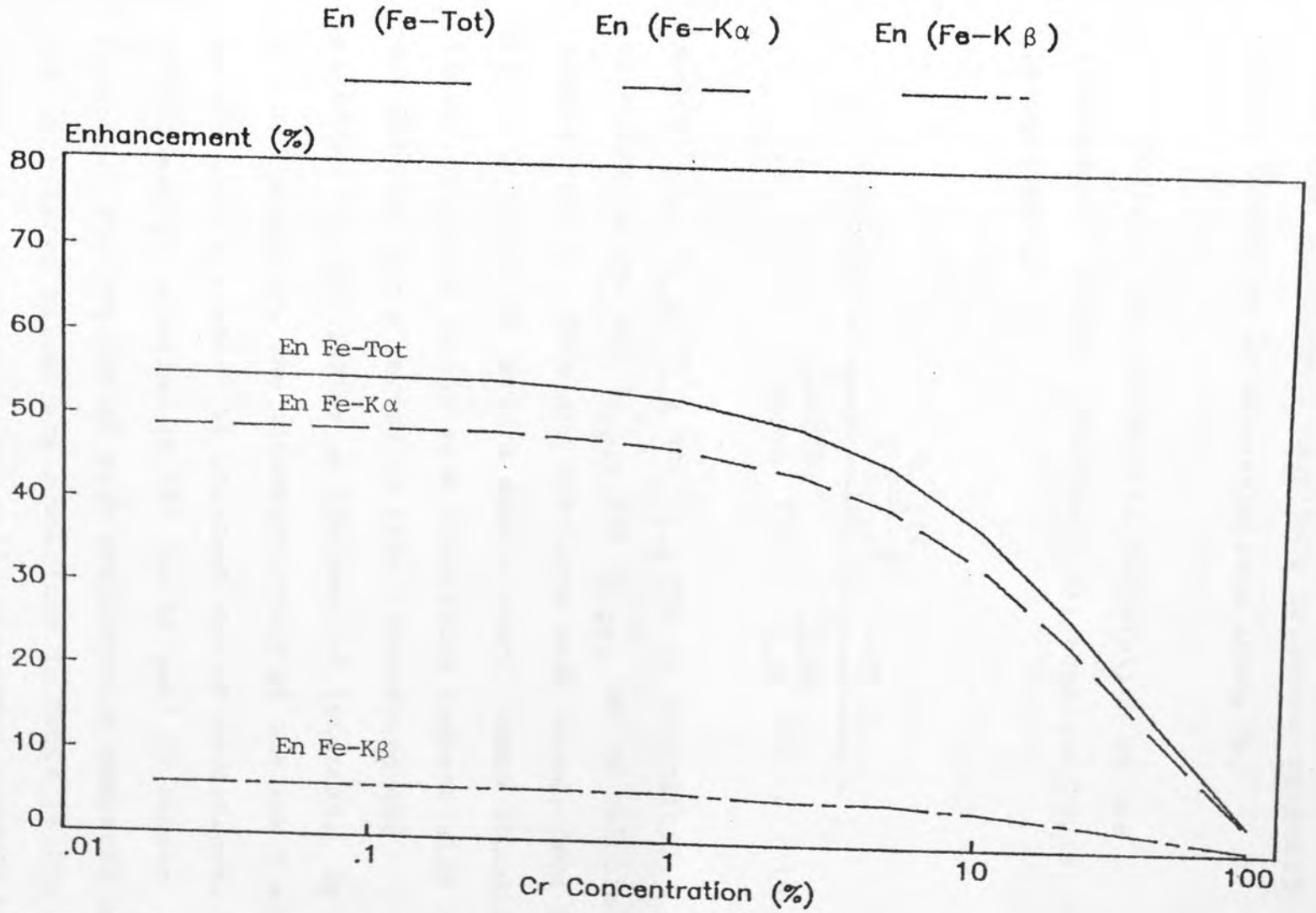

Figure (6.9) Percentage intensity enhancement of the Cr Kα line in dependence on the Cr-content in weight % in a Fe-matrix. The excitation due to the Fe Kα and Kβ lines are shown separately.

in Figure (6.8). For the Cr/Fe alloys, also shown in Figure (6.9), it is noted that as the Cr-content is increased, there is less Fe present to enhance the Cr. Thus, the enhancement magnitude decreases gradually and drops faster at Cr concentrations above 5%.

To test the theoretical calculation of the enhancement factor, (Section 3.5), equation (6.17) can be re-written as

$$En(B,A) = \frac{\left(\frac{I_{X,A}(E_o)}{I_{X,B}(E_o)}\right)_{exp}}{\left(\frac{I_{A,pri}}{I_{B,pri}}\right)_{thr} \times \left(\frac{C_{1,A}}{C_{1,B}}\right)_{exp}} - 1 \qquad (6.18)$$

where $I_{X,A}$, $I_{X,B}$, $C_{1,A}$ and $C_{1,B}$ can be determined experimentally, and $I_{A,pri}$ and $I_{B,pri}$ can be calculated theoretically. Thus [illegible] standards were chosen from Table (6.5) in order to perform such a test. Those standards listed in Table (6.11) were irradiated sequentially with 2 MeV protons for a period of time in order to get satisfactory statistics on the peak of interest. By using a fixed geometry, the intensity ratio of the low Z element to the high Z element of interest can be determined. Consequently, equation (6.18) can be used to obtain $E_n(B,A)$. The results of such measurements compared with the calculated values are summarised in Table (6.11) and indicate a satisfactory and valid agreement between the theoretical and experimental enhancement factor $E_n(B,A)$

Sample Number	Sample Type	Normalised Concentrations wt %		% $E_n(B,A)$	
		C_A	C_B	Calculated	Measured ±13%
1.	Fe/Ni	50	50	13.5±11%	13.4
2.	Fe/Ni	64	36	8.4±11%	8.7
3.	Cr/Fe	12.5	87.5	34.8±14%	33.5
4.	Cr/Fe	9.1	90.9	39.0±14%	37.0
5.	Cr/Fe/Mo	2.26	97.74	50.1±14%	51.0
6.	Cr/Fe (En 31)	1.33	98.68	52.0±14%	52.4
7.	Cr/Fe (162AA)	0.02	99.98	54.9±14%	56.0
8.	Cr/Fe (12M64)	0.15	97.85	54.6±14%	55.6

Table (6.11) Comparison between the calculated enhancement factor $E_n(B,A)$ and the experimentally determined one.using number of standard and test samples.

values.

The uncertainties in the calculated $E_n(B,A)$, for Fe/Ni and Cr/Fe alloys were determined to be 11% and 14% respectively, based on the uncertainties in the calculated intensities of Fe and Cr as detailed in Section (6.4). The uncertainty in the measured $E_n(B,A)$ using equation (6.18) for Fe/Ni and Cr/Fe alloys was determined to be about 13%.

By varying the proton energy, the thickness of the irradiated layer will change, thus, the magnitude of the enhancement will be changed. Figures (6.10) and (6.11) show the enhancement magnitude at different proton beam energies in thick Fe/Ni and Cr/Fe alloys at different concentrations of Fe and Cr respectively. As was expected, the enhancement decreases with the decreasing proton energy in the range studied from 2.5 MeV down to 1 MeV. Figures (6.10) and (6.11) illustrate the magnitude of the enhancement in the Fe/Ni and Cr/Fe alloys at different proton beam energy level.

6.6 TARGET HOMOGENEITY

Metal alloy steels are used for many applications due to their advantageous specifications, for example, a high melting point and freedom from stress corrosion up to certain temperatures. In advance gas-cooled reactors

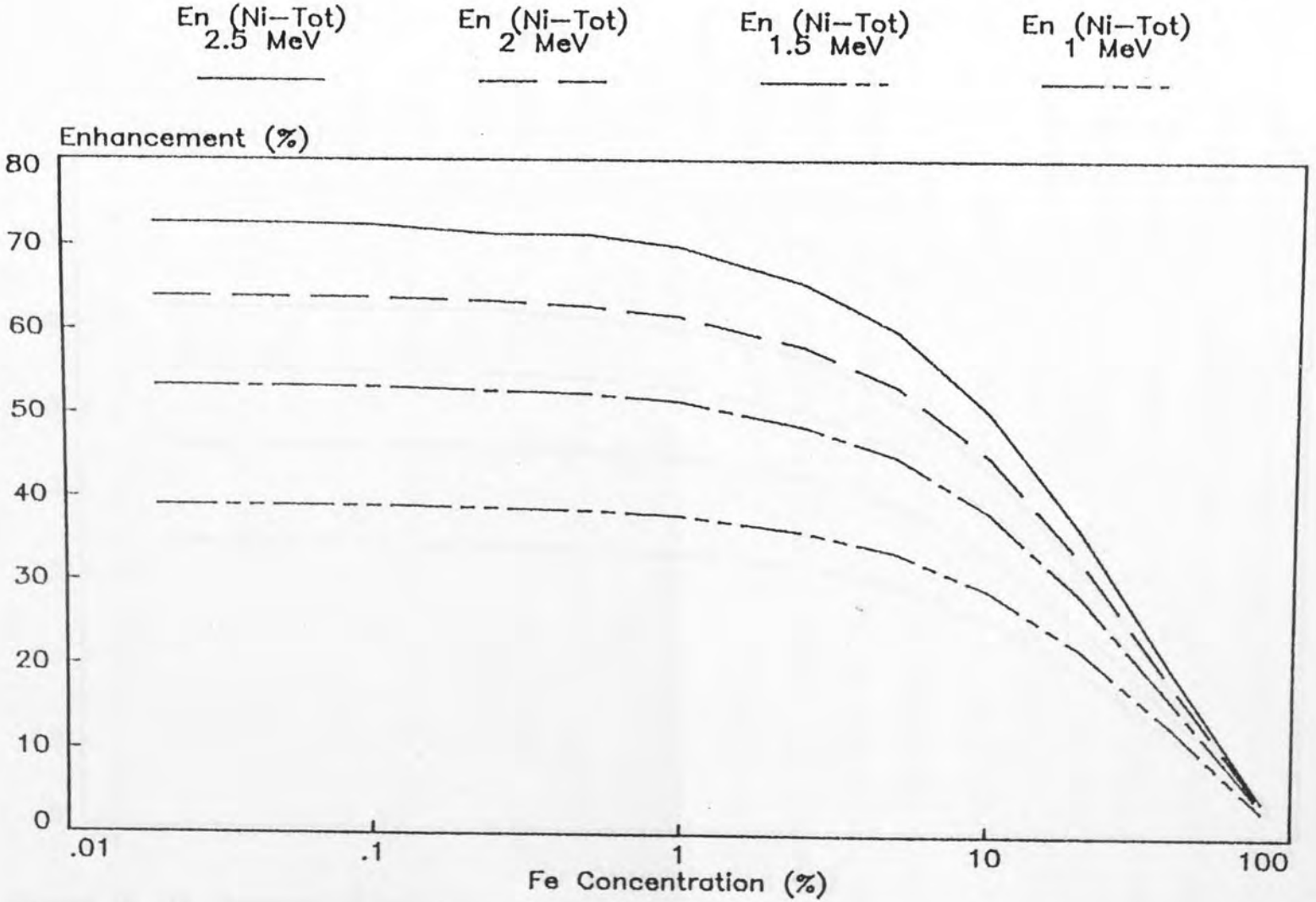

Figure (6.10) Percentage intensity enhancement of the Fe Kα line in dependence on the Fe-content in weight % in a Ni-matrix due to Ni K-radiation at different proton bombarding energies.

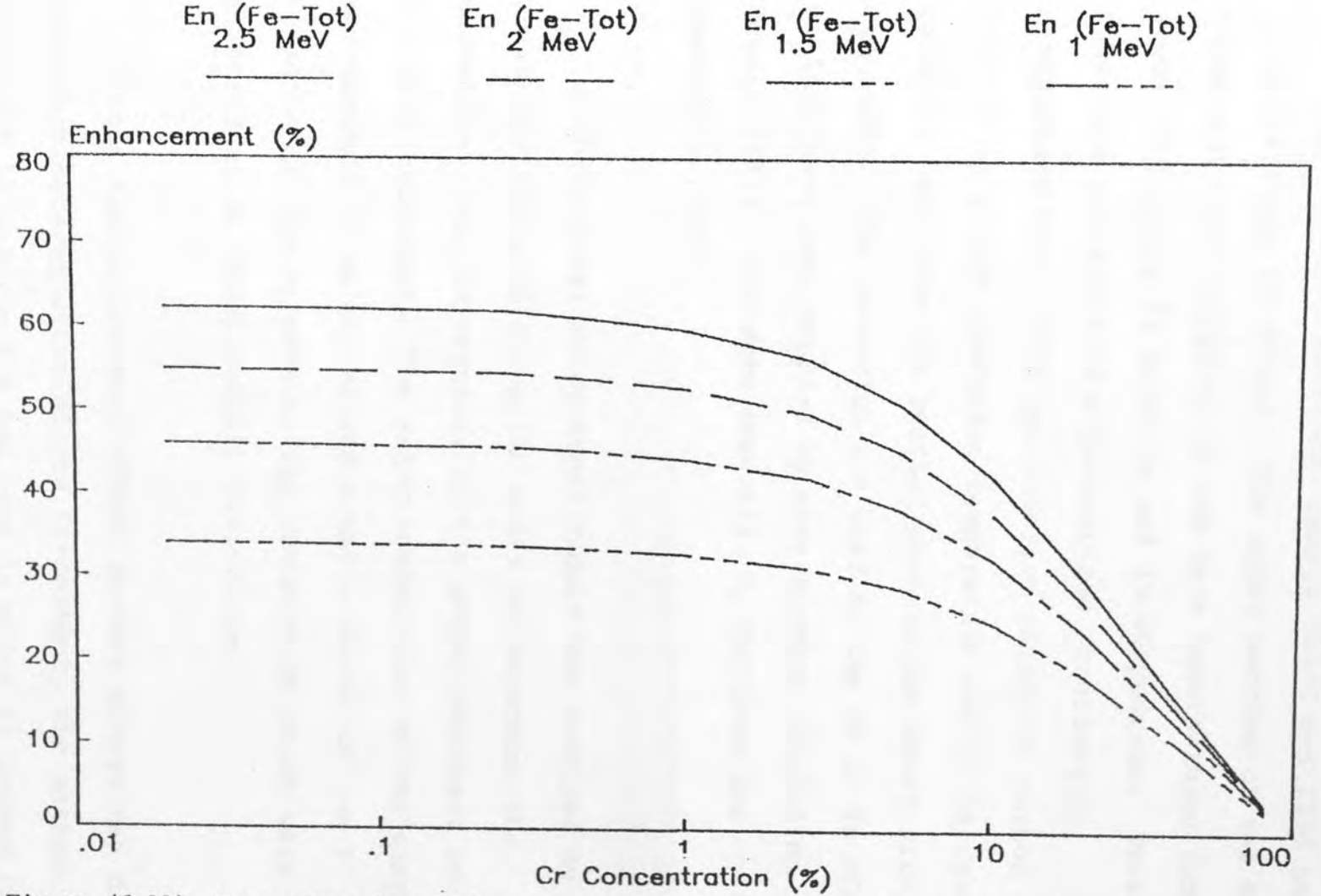

Figure (6.11) Percentage intensity enhancement of the Cr Kα line in dependence on the Cr content in weight % in a Fe-matrix due to Fe K-radiation at different proton bombarding energies.

(AGR), different types of steel were used at different stages. The AGR was designed to supply steam at the same temperature and pressure conditions as were applicable to modern non-nuclear turbines, namely 541°C and 2350 psig with one stage of reheat. The upper section of the boiler tubes and their supports in AGR were manufactured from steel containing 9% chromium and 1% molybdenum. These tubes are subjected to a pressurised, continually circulating gas. This gas consists mainly of carbon dioxide at a high operating temperature and it is used to transfer heat from the reactor core to the water within the tubes. The corrosion and wear of the 9% Cr in AGR boilers have been studied by many workers, including Newell (1972), and more recently, by Sullivan and Granville (1984).

A thick metal alloy steel sample was provided by the Tribology Research Group, in order to determine the concentrations, in percent, of the major component using the PIXE-technique. The major composition of the sample was assumed to be Cr, Mo and a small amount of low Z elements in the Fe matrix, the contents of which were supposed to be homogeneously distributed.

Since the enhancement effect in such alloys can cause incorrect determination of the Cr-content, the method discussed in Section 6.4 was used in order to determine the Cr-concentration. The sample was irradiated with 2

MeV proton beam, and a 10 nA beam current, for about 5 minutes with and without on-demand beam pulsing operation as shown in Figure (6.12). Consequently, the Cr/Fe intensity ratio was determined and by using the calibration curve, Figure (6.4), the Cr content given in percentage was obtained and found to be about 9 ± 2%.

The use of a homogeneous standard of known composition was employed to determine the Mo-concentration. The standard was chosen to have similar relative amounts of major elements in the sample.

The sample and the standard were bombarded sequentially with protons of a fixed energy. The X-ray yield per incident proton of Mo relative to the Fe were measured in the sample and standard with the same geometry in order to avoid systematic error in the measurements of the geometrical factor. Thus, the Mo-content in the sample was determined to be 1.02 ± 3%. Consequently, the major components of the sample were found to be 9% Cr and 1% Mo, with Fe as the remainder. Figure (6.12) demonstrates the importance of the on-demand beam pulsing system in such measurements.

The Tribology Research Group at Aston has conducted experiments on a similar sample by subjecting it to high temperatures.

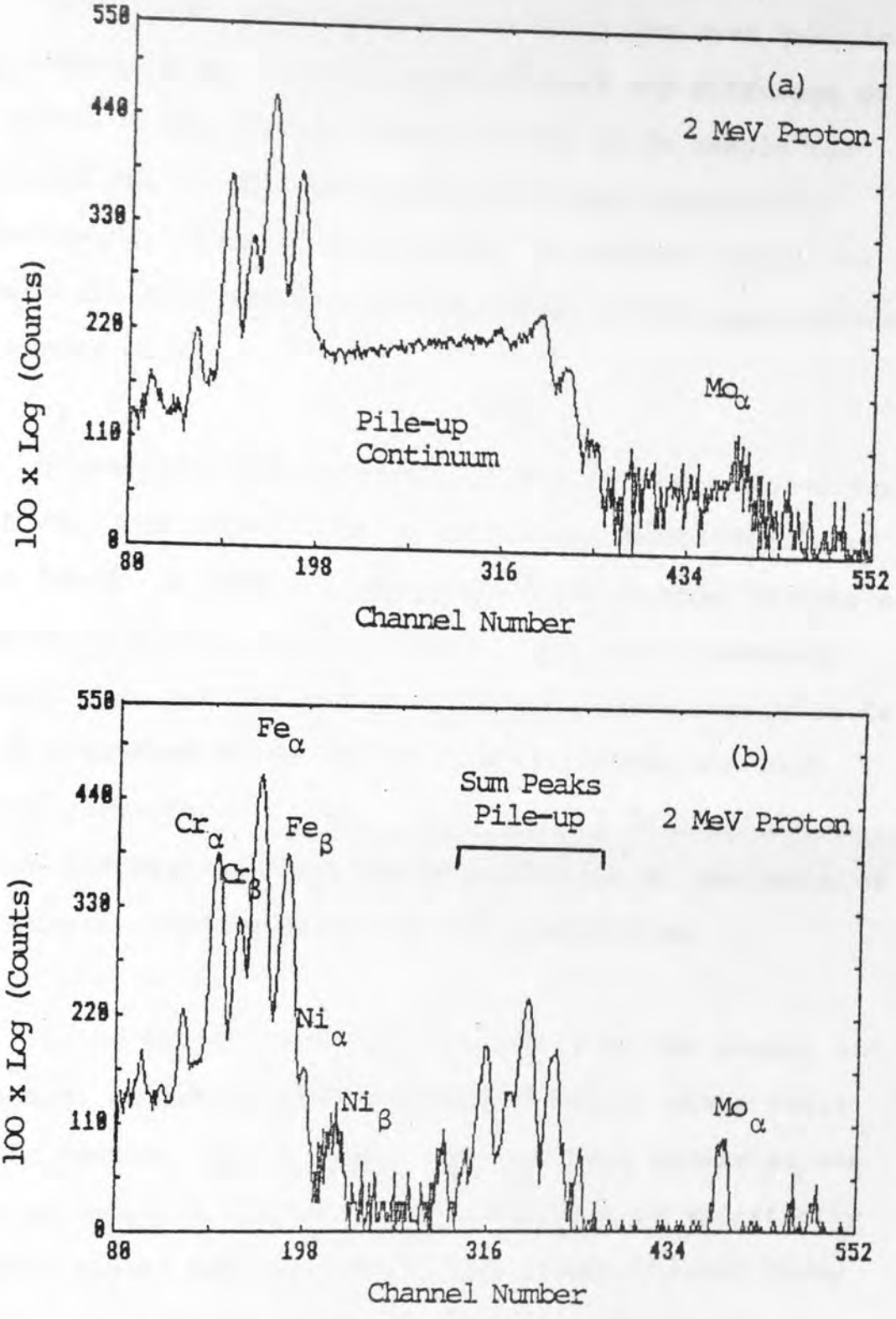

Figure (6.12) PIXE spectrum for 9% Cr-steel sample.

(a) without on-demand beam pulsing

(b) with on-demand beam pulsing operation.

Rutherford backscattering (R.B.S.) has been used in the present work to investigate whether any diffusion of Mo atoms in the surface region of the 9% Cr sample had occurred due to the above mentioned high temperature experiments, since this technique is powerful enough to obtain the depth profiles of elements in the upper micron of smooth solids.

Rutherford backscattering of 2-3 MeV α-particles has been employed extensively to obtain the depth profile of thin layers of high Z elements on thick backing targets of lighter elements, Ziegler (1975). The basic concepts, capabilities and limitation of backscattering analysis is fully discussed by Chu et al. (1978). Since the high energy particles are used, it is possible to derive information about the distribution of the depth of the sample elements using 2.8 MeV α-particles.

In the present work, the Fe and Cr in the sample and standard, cannot be distinguished by R.B.S. since their atomic numbers are so close, and they both appear as one edge as shown in Figure (6.13). The lack of specificity of this signal was resolved by the proton induced X-ray analysis techniques (PIXE) as discussed previously.

The standard employed in the PIXE analysis was also used for the R.B.S. investigation. Because Mo has a much higher atomic number (42) than the other constituents in the

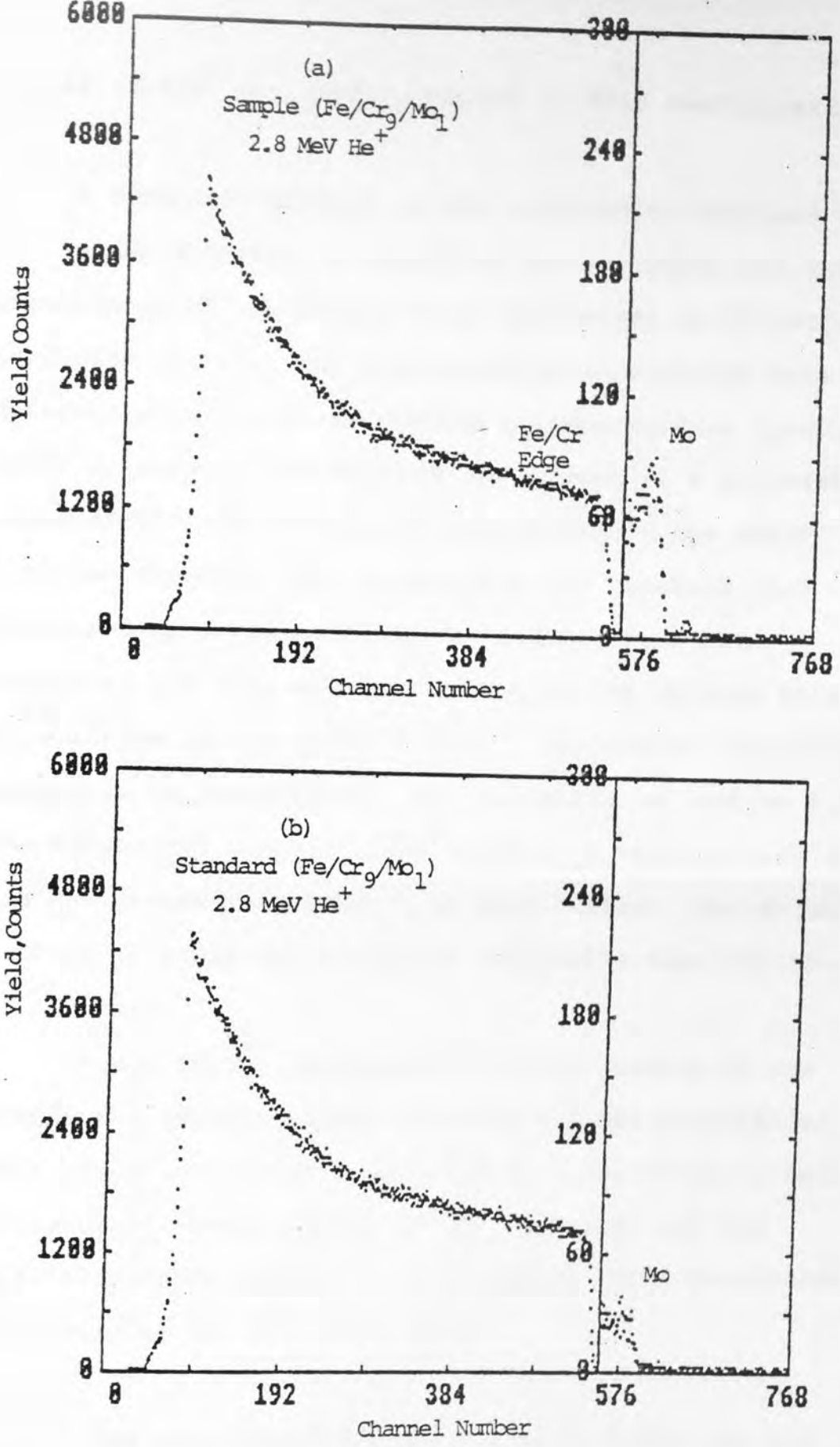

Figure (6.13) Typical RBS spectrum of 2.8 MeV He ions incident on (a) Cr-steel alloy sample (b) 9%Cr-steel alloy standard.

sample, R.B.S. was ideally suited to this configuration.

A schematic diagram of the electronics employed to enable the information regarding the thickness and the homogeneity of the sample to be determined is illustrated in Figure (6.14). The backscattered α-particles were detected with a well collimated silicon surface barrier (SSB) detector. The detector was placed at a backward angle of 135° to the beam direction within the newly designed chamber. The pulses from the detector were processed by a preamplifier and a 472A Ortec main amplifier and then fed into an MCA of the HP5406B data acquisition system (Section 4.8). The charge collection procedure is identical to that described in Section 4.8. The sample and standard were irradiated sequentially with 2.8 MeV α-particles and a 5 nA beam current, for about 60 minutes in order to accumulate acceptable edge for the Mo.

Figure (6.13) compares the R.B.S. spectra of the sample and standard bombarded with 2.8 MeV α-particles. This comparison made it apparent that the Mo-atoms had distributed homogeneously in the standard, but had diffused to the surface in the sample. This conclusion is supported by the following facts:

(1) The iron-chromium edge had shifted back in the sample. This indicates that there is a thin layer at the surface. He^+ ions lose energy in traversing

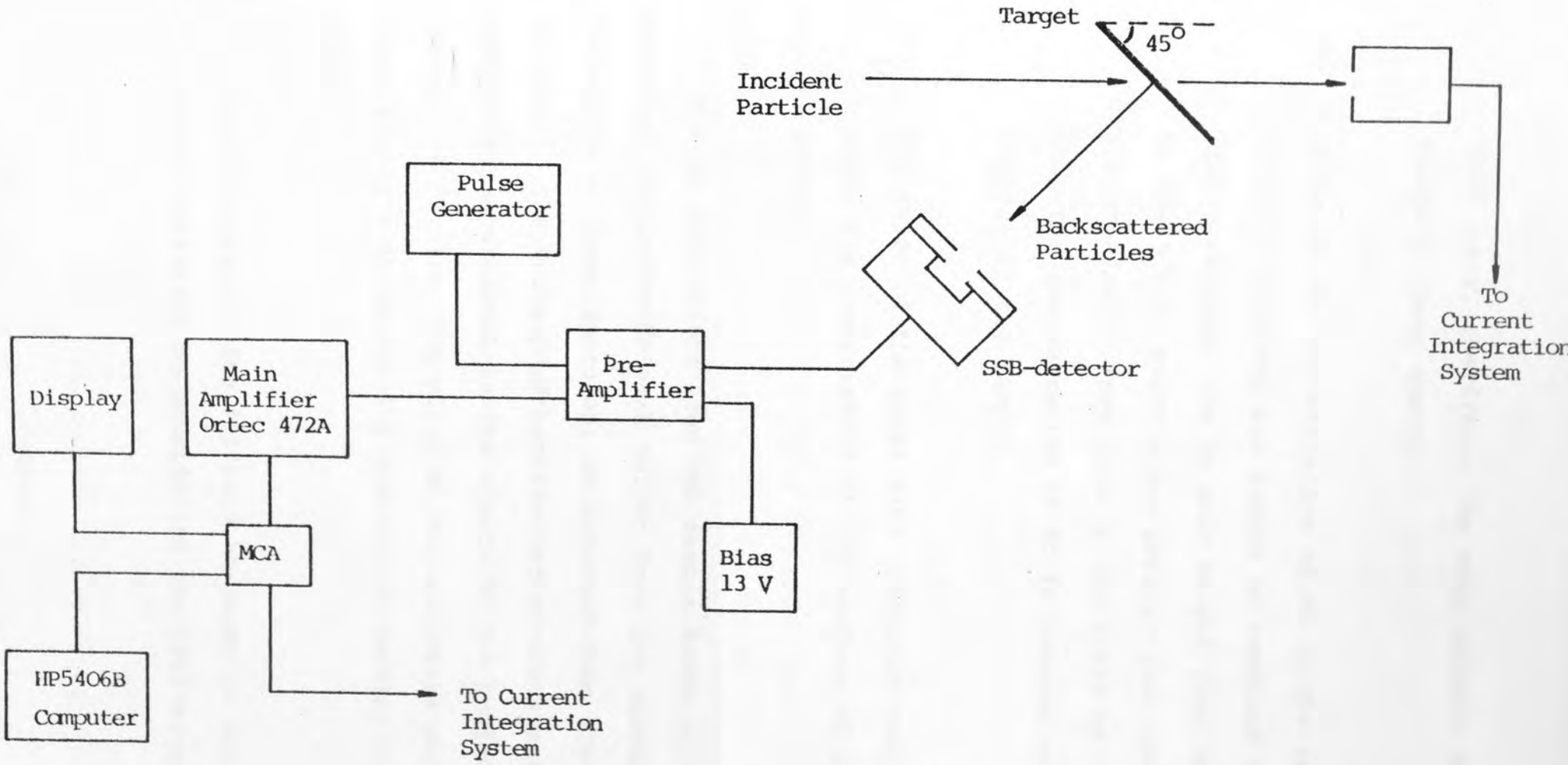

Figure (6.14) Schematic diagram of the R.B.S. system

this layer, therefore, the edge appears at a slightly lower energy.

(2) Although the concentration of Mo is the same in both the standard and sample as examined by the PIXE technique, the Mo peak height from the sample in the R.B.S. spectra was greater than that from the standard. From this it can again be concluded that the concentration of Mo is greater at the surface of the sample.

(3) The shape of the peaks also indicated that the Mo-atoms are concentrated at the surface of the sample.

The Mo peak height from the sample drops at lower energies, while the Mo peak height from the standard increases at lower energies, as expected from a homogenous material. The Rutherford backscattering cross-section is inversely proportional to the square of the projectile energy (αE^{-2}) i.e. the yield of the scattered particles rise rapidly with decreasing bombarding energy, Chu et al. (1978).

The thickness of the diffused Mo-layer in the sample can then be estimated by considering the following model.

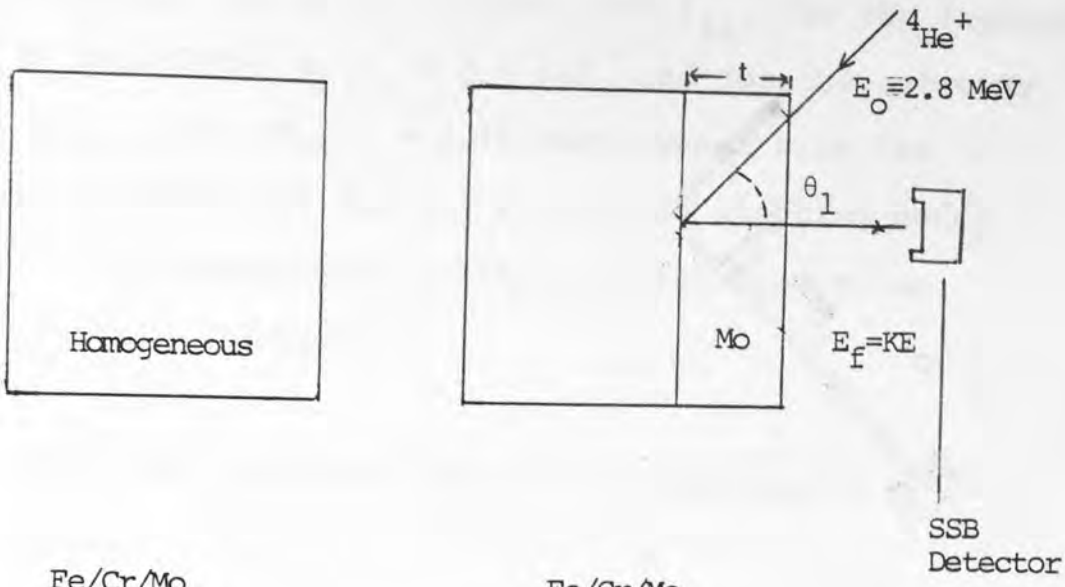

Fe/Cr/Mo
Standard

Fe/Cr/Mo
Sample

In the sample, the beam will lose energy in traversing the Mo layer. Therefore, the Fe/Cr edge will appear at a lower energy than observed in the standard.

From the spectra obtained, Figure (6.13), the Fe/Cr edge in the standard occurs at channel number 628 and the Fe/Cr edge in the sample occurs at channel number 624. The energy of the back scattered projectile in keV per channel is given from the slope of the calibration curve, Figure (6.15), to be 3.7 keV/ch. Therefore, the projectile loses 14.8 keV of energy in the inward and outward path.

From the tables given by Chu et al. (1978), the energy loss factor $[S_o]^{Mo}_{2.8}$ for the $^4H^+_e$ in Mo at various energies can be found. Therefore, by applying the surface

approximation, Chu et al. (1978), the ε_{in}, for the ingoing path is calculated at E_o = 2.8 MeV, and for the outgoing path, ε_{out}, at ($K_{Mo}E_o$ = 2.41 MeV), where K is the kinimatic factor for Mo, and ε, is the stopping power factor. The energy loss factor is calculated to be approximately 252 eV/A°.

Thus, the thickness (t) of the Mo layer

$$= \frac{\text{Energy lost by projectile}}{[\,s_o]_{2.8}^{Mo}} = \frac{14.8 \text{ keV}}{252 \text{ eV/A°}} = 59 \text{ A°}$$

These findings indicate that while the PIXE method and the R.B.S. method can not stand alone in this particular investigation to obtain complete quantitative and qualitative information about the sample, used together, they complement each other to provide the valid findings already described.

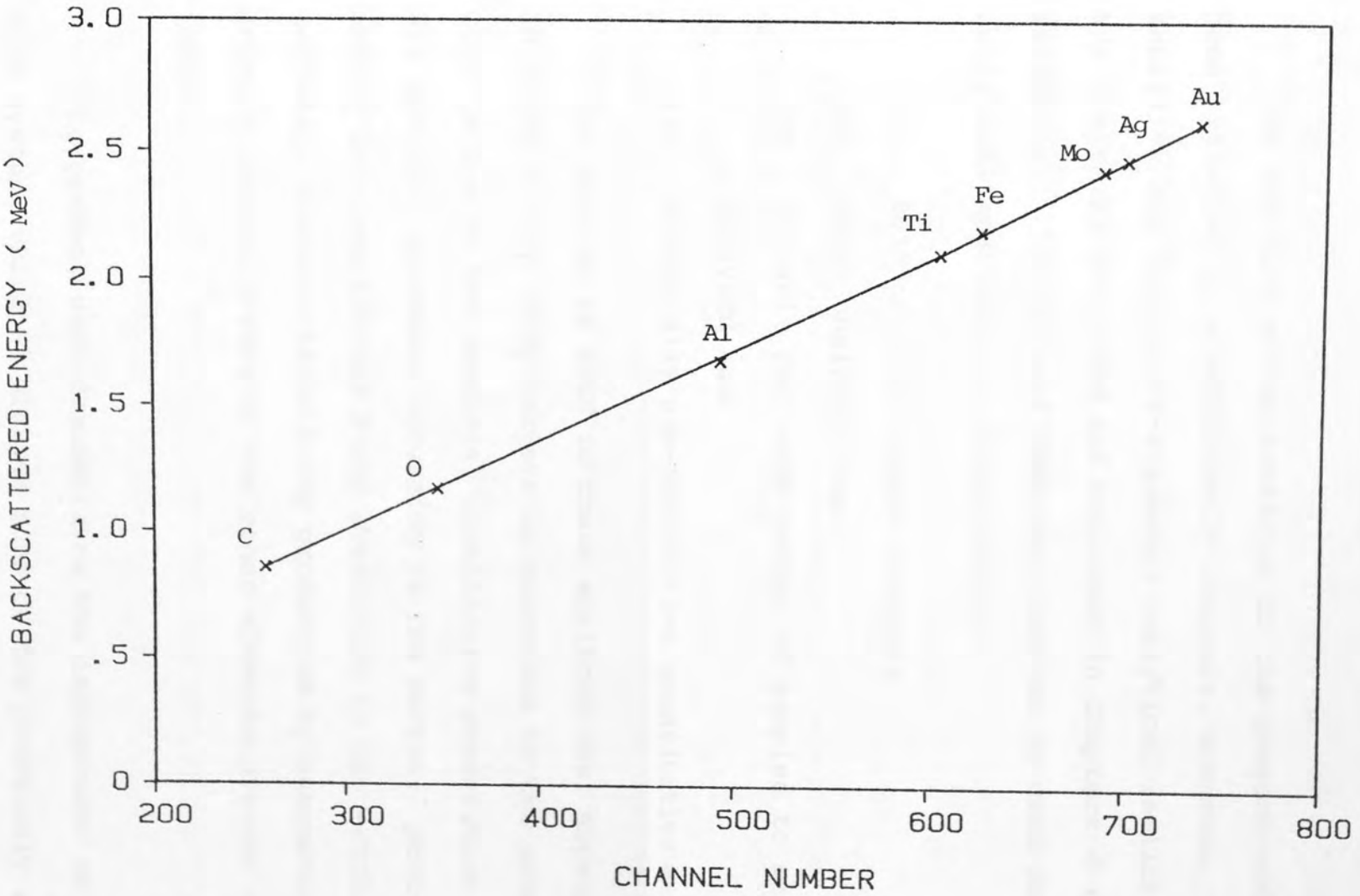

Figure (6.15) R.B.S. calibration curve. Error bars omitted since they were smaller than the symbol size.

CHAPTER 7

CONCLUSIONS

The new PIXE system developed in the present work has been verified as a sufficiently adequate, accurate, precise, sensitive and fast multi-elemental analytical facility. The system as described and evaluated in Chapters 4 and 5 respectively has several features that can be used for many analytical applications these include:

(1) thin or thick target analysis

(2) short analysis time

(3) suitable for large number of samples to be analysed and

(4) essentially non-destructive quantitative analysis.

The success of PIXE in these applications, especially in thick binary alloy targets as described in the present work is due to the accurate, quantitative description of all physical processes occurring in the target: proton-energy deceleration and X-ray absorption in the matrix; secondary characteristic X-ray production by energetic primary induced X-rays of the other elements present in the target.

The present work demonstrates the improvement to the PIXE system, which eliminates some of the previously existing limitations and leads to improved analytical capabilities.

The installation of the new beam line, incorporating the on-demand beam pulsing system, together with the new scattering chamber, with a multiple sample capability which now extends to 80 samples, will lead to complete automation of the irradiation facility. The use of the pulsed proton beam, triggered by a signal from the X-ray pre-amplifier, provides significant advantages over continuous beam excitation and removes some of the limitation experienced by previous research workers regarding the count rate limitation leading to the pulse pile-up effect.

This technique has been successfully tested and its advantages over continuous beam irradiation is demonstrated in the present study.

The remarkable performance of this technique at high counting rates has been evaluated by observing the ion-induced X-ray emission from spectroscopically pure elements under a variety of conditions, with and without beam pulsing. With the on-demand beam pulsing system operation, counting rates of up to 10, 18 and 25 kPPS corresponding to the 8, 4 and 2 μsec amplifier time constant was achieved without significant loss of pulses. This is clearly advantageous as it results in a much shorter analysis time and requires no dead time correction. In addition, a better system resolution was obtained at up to 7 kPPS. Consequently, this improves the sensitivity due to the elimination of the pile-up continuum which appears between the matrix peaks and the sum peaks. The system cannot, of course, eliminate sum and

triple sum peaks which are dependent on the counting rate and the pulse-pair resolution of the fast discriminator employed. They were, however, reduced to some extent when applying the pulse pile-up rejector unit together with the on-demand beam pulsing system. This system, with its optimum counting rate capability, will enable thick targets to be analysed more readily. Typically, 2.5 minutes were required in the present system for analysing thick binary alloys with acceptable statistical accuracy.

In general, it is a non-destructive technique and will reduce the target damage when analysing heat sensitive targets.

The target chamber has been constructed so that it permits the X-ray detector to be positioned either at 90^{o} or 135^{o} to the incoming beam whether in or outside the vacuum chamber. The improved signal-to-noise ratio of the 135^{o} position to the normally used 90^{o} position will be exploited in future analysis by other workers. The new beam line includes facilities for beam monitoring and target thickness measurements using R.B.S. spectroscopy.

The system reliability and reproducibility was checked throughout the work, and it was concluded that the present PIXE system is reliable.

A computer programme was developed in this study, to evaluate the X-ray yields from thick targets bombarded by

protons based on the procedure outlined by Willis et al. (1977) and Reuter et al. (1975). A study has been made of the X-ray yield enhancement due to matrix effects, and the senstivity of the calculations to the choice of data base employed has been investigated. Acceptable agreement has been found with the illustrative enhancement factor calculations of Reuter et al. (1975). Satisfactory agreement was obtained in the enhancement factor calculations employing different combinations of data bases from which it may be concluded that any of the polynomials considered can be used in such calculations with confidence.

Furthermore, experiments were carried out on standard thick pure metallic targets. Their Kα-X-ray peaks were determined and compared with the theoretical calculations. The results indicate acceptable agreement between the experimental and theoretical calculations.

The quantitative results obtained for thick homogeneous binary alloys indicate that the present system, as developed, has sufficient accuracy and precision to meet the needs of different thick and thin target studies.

PIXE-analysis is an ideal analytical technique for identifying the elements present in different types of samples. During the last five years, PIXE research workers at Aston University have shown remarkable progress in

demonstrating the versatility and usefulness of this technique in many different applications.

The results of this work are significant in that the use of PIXE analysis provides an improved system for future studies in thick metal sample analysis.

Finally, the utility of the system for nuclear reactions induced in the target by the incident particle can be used in further studies in order to extend the analytical capability of the system to atomic number Z less than 14.

APPENDIX A

APPROXIMATION FOR SECONDARY K-X-RAY PRODUCTION

(1) Consider a point source of radiation $\Delta I_B(i)$ at the centre of a layer (i) of 2r thickness, (see Figure (3.4)). The fraction of the absorption in the same layer i for an isotropically emitted source is given by the previously derived equation (3.11). In this equation, the β integral may be given as follows:

$$F_1(i) = \left[\int_0^{\pi/2} \sin\beta \, d\beta - \int_0^{\pi/2} \exp(-\mu_{B,S}\rho r \sec\beta)\sin\beta \, d\beta\right]$$

which reduces to:

$$F_1(i) = \left[1-\int_0^{\pi/2} \exp(-\mu_{B,S}\rho r \sec\beta)\sin\beta \, d\beta\right] \quad (A.1)$$

Let $Z = \mu_{B,S}\rho r \sec\beta$, $\qquad dZ = + \dfrac{\mu_{B,S}\rho r}{\cos^2\beta} \sin\beta \, d\beta$

Therefore

$$\int_0^{\pi/2} \exp(-\mu_{B,S}\rho r \sec\beta)\sin\beta \, d\beta = \mu_{B,S}\rho r \int_{\mu_{B,S}\rho r}^{\infty} \frac{e^{-z}}{z^2} dz$$

$$= t \int_t^{\infty} \frac{e^{-z}}{z^2} dz$$

where $t = \mu_{B,s}\rho r$

Therefore equation (A.1) becomes

$$F_1(i) = [1 - t \int_t^\infty \frac{e^{-z}}{z^2} dz] \quad (A.2)$$

Expanding the exponential integral gives:

$$\int_t^\infty \frac{e^{-z}}{z^2} dz = \int_t^\infty \frac{1}{z^2} (1 - z + \frac{z^2}{2!} - \frac{z^3}{3!} + \frac{z^4}{4!} + ...)dz$$

$$= \int_t^\infty (\frac{1}{z^2} - \frac{1}{z} + \frac{1}{2!} - \frac{z}{3!} + \frac{z^2}{4!} - \frac{z^3}{5!} + ...)dz$$

$$= [- \frac{1}{z} - \ell n\ z + \frac{z}{2!} - \frac{z^2}{2.3!} + \frac{z^3}{3.4!} - \frac{z^4}{4.5!} + ...]_t^\infty$$

(A.3)

as z becomes larger (i.e. $z \to \infty$) the upper limit of the integral becomes -0.422784, therefore

$$t \int_t^\infty \frac{e^{-z}}{z^2} dz = 1 + t\ell nt - 0.422784t$$

$$- \frac{t^2}{2} + \frac{t^3}{12} - \frac{t^4}{72} + \frac{t^5}{480} + ... \quad (A.4)$$

Hence, the solution of equation (A.4) can be substituted in equation (A.2). Therefore,

$$F_1(i) = t[-\ell nt + 0.422784 +$$

$$+ \frac{t}{2} - \frac{t^2}{12} + \frac{t^3}{72} - \frac{t^4}{480} + ...] \quad (A.5)$$

The solution of equation (A.5) is evaluated and substituted in equation (3.15) to carry on the summations.

(2) In the case of the fraction of $\Delta I_B(j)$ radiation produced in a layer (j) reaching another layer i and thickness ΔX $(=2r_i)$, where the nearest surface is at distance R from the centre of layer j as shown in Figure (3.4), (isotropic distribution is also considered). The previous derived equation (3.11). The β integral of this equation can be solved as follows:

$$F_2(j) = \int_0^{\pi/2} [\exp(-\mu_{B,S}\rho R \sec\beta)*(1-\exp(-\mu_{B,S}\rho\Delta X \sec\beta)] * \frac{1}{2} \sin\beta \, d\beta \qquad (A.6)$$

$$F_2(j) = \int_0^{\pi/2} [\exp_{B,S}(-\mu\rho R \sec\beta) - \exp(-\mu_{B,S}\rho(R+\Delta X)\sec\beta)] * \frac{1}{2} \sin\beta \, d\beta$$

let

$$z = \mu_{B,S}\rho R \sec\beta , \qquad dz = \mu_{B,S}\rho R \frac{\sin\beta \, d\beta}{\cos^2\beta}$$

and

$$y = \mu_{B,S}\rho(R+\Delta X)\sec\beta , \qquad dy = \mu_{B,S}\rho(R+\Delta X) \frac{\sin\beta \, d\beta}{\cos^2\beta}$$

Therefore,

$$F_2(j) = \frac{1}{2}\left[\mu_{B,S}\rho R \int_{\mu_{B,S}\rho R}^{\infty} \frac{e^{-z}}{z^2}\, dz\right] - \frac{\Delta I_B}{2}\left[\mu_{B,S}\rho(R+\Delta X) * \int_{\mu_{B,S}\rho(R+\Delta X)}^{\infty} \frac{e^{-y}}{y^2}\, dy\right]$$

let $t = \mu_{B,S}\rho R$ and $t' = \mu_{B,S}\,\rho(R+\Delta X)$

$$F_2(j) = \frac{1}{2}\left[\left(t \int_t^{\infty} \frac{e^{-z}}{z^2}\, dz\right) - \left(t' \int_{t'}^{\infty} \frac{e^{-y}}{y^2}\, dy\right)\right] \qquad (A.7)$$

Because

$$\int_t^{\infty} \frac{e^{-u}}{u^2}\, du = \left[-\frac{1}{z} - \ell nz + \frac{z}{2!} - \frac{z^2}{2.3!} + \frac{z^3}{3.4!} - \frac{z^4}{4.5!} + \cdot\cdot\right]_t^{\infty}$$

as z becomes larger the upper limit of the integral becomes -0.422784.

Therefore,

$$t \int_t^{\infty} \frac{e^{-u}}{u^2}\, du = 1 + t\ell nt - 0.422784t -$$

$$\frac{t^2}{2} + \frac{t^3}{12} - \frac{t^4}{72} + \frac{t^5}{480} - \ldots.] \qquad (A.8)$$

Hence, the solution of equation (A.8) can be substituted in equation (A.7), therefore,

$$F(j) = \frac{1}{2}\left[t\left(\frac{1}{t} - 0.422784 + \ell nt - \frac{t}{2} + \frac{t^2}{12} - \frac{t^3}{72} + \frac{t^4}{480} \ldots\right)\right.$$

$$\left.-\left[t'\left(\frac{1}{t'} - 0.422784 + \ell nt' - \frac{t'}{2} + \frac{t'^2}{12} - \frac{t'^3}{72} + \frac{t'^4}{480} + \ldots.\right)\right]\right]$$

(A.9)

The solution of equation (A.9) is substituted in equation (3.15) to carry on the summation. Hence, the fraction of the total secondary production of the Kα -radiation of element A can be evaluated.

APPENDIX B

```
100 REM              ************************************
110 REM              *                                  *
120 REM              * PRIMARY & SECONDARY X-RAY YIELD  *
130 REM              *    PRODUCTION IN THICK METAL     *
140 REM              *         BINARY ALLOYS            *
150 REM              *                                  *
160 REM              *                                  *
170 REM              *       BY M.A.S. ARMAGHANI        *
180 REM              *       UNIVERSITY OF ASTON        *
190 REM              *             1984                 *
200 REM              *                                  *
210 REM              ************************************
220 REM
230 REM
240 REM                   *****     VARIABLES      *****
250 REM ** LL,UL THE LOWER & UPPER ENERGY LIMITS AND S0 IS THE ENERGY LOSS STEP
260 REM ** BE,BB THE BINDING ENERGIES OF ELEMENTS A & B IN A/B ALLOY
270 REM ** A2...AF AND B2...BF ARE THE STOPPING POWER COEFFICIENTS OF A & B
280 REM ** (UN,UM,UX,UZ) & (UP,UQ,UY,UV) ARE THE MASS ATTENUATION COEFF. OF A &
290 REM **  B FOR KX AND KB RADIATION OF A & B RESPECTIVELY
300 REM ** ZA,PA,AA,W1 ARE THE ATOMIC NO.,DENSITY,ATOMIC WEIGHT AND FLUORESCENT
310 REM **  YIELD OF ELEMENT A
320 REM ** ZB,PB,AB,W2 ARE THE ATOMIC NO.,DENSITY,ATOMIC WEIGHT AND FLUORESCENT
330 REM **  YIELD OF ELEMENT B
340 REM ** CA(S),CB(S) ARE THE CONCENTRATIONS FOR TEN DIFFERENT COMBINATIONS OF
350 REM ** THE BINARY ALLOY
360 REM ********************************************************************************
370 OPEN1,4:CMD1
380 REM                   *******  MAIN PROGRAMME  *******
390 READ LL,UL,S0,BE,BB,A2,A3,A4,A5,A6,A7,A8
400 READ A9,A0,A1,AF,B2,B3,B4,B5,B6,B7
410 READ B8,B9,B0,B1,BF
420 READ UN,UM,UX,UZ,UP,UQ,UY,UV,ZA,ZB
430 READ PA,PB,W1,W2,ND,AB,AA,Z
440 N=INT(((UL+S0)-LL)/S0)+S0)
450 DIM E(N),S(N),OA(N),Y(N),W(N),OB(N),Y8(N),WB(N),SX(N)
460 DIM Q1(N),G1(N),F(N),L(N),YY(N,N),F2(N),L2(N),X(N),CA(N),CB(N)
470 DIM Q2(N),G2(N),F3(N),FF(N),EE(N),SS(N),EN(N),S1(N),S2(N)
480 FOR S= 1 TO 10
490 READ CA(S),CB(S)
500 REM ---LL,UL ARE THE LOWER &UPPER LIMITS ---S0=IS THE ENERGY LOSS STEP
510 REM---BE&BB ARE THE (B.E.)---& A(I),B(I)= ARE ST.POWER COFF.--
520 P=CA(S)*PA+CB(S)*PB
530 U0=((CA(S)*UN)+(CB(S)*UM))
540 U1=((CA(S)*UX)+(CB(S)*UZ))
550 U2=((CA(S)*UP)+(CB(S)*UQ))
560 U3=((CA(S)*UY)+(CB(S)*UV))
570 PRINT#1,"CONCENTERATION       (CA)="CA(S)
580 PRINT#1,"CONCENTERATION       (CB)="CB(S)
590 PRINT#1,"STEP                  (S)="S
600 PRINT#1,"NUMBER OF STEP        (N)="N
610 PRINT#1,"DENSITY               (P)="P
620 PRINT#1,"MASS ATT.(KX,A,SPL)  (U0)="U0
630 PRINT#1,"MASS ATT.(KX,B,SPL)  (U1)="U1
640 PRINT#1,"MASS ATT.(KB,A,SPL)  (U2)="U2
650 PRINT#1,"MASS ATT.(KB,B,SPL)  (U3)="U3
660 PRINT#1,"    "
```

```
670 PRINT#1,"     "
680 PRINT#1,"     "
690 FOR I= 1 TO N
700 E(I)=UL+S0-(I*S0)
710 EN(I)=E(I)-(S0/2)
720 EE(I)=(EN(I)*1000)/1.00727
730 REM E(I) IS THE PROTON ENERGY IN MEV,EE(I) IN KEV/AMU
740 REM EN(I) IS THE PROTON ENERGY AT THE CENTRE OF EACH LAYER
750 IF EN(I)>=1 THEN GOSUB 2920
760 IF EN(I)< 1 THEN GOSUB 3070
770 REM--- S(I)= THE WEIGHTED ST.POWER OF ALL CONSTITUENTS IN (KEV*CM↑2/MG)
780 REM--P= THE MASS DENSITY OF CMPOSIT TARGET&(PA,PB)=DENSITY OF ELEMENT A&B
790 REM---P IS IN (GR/CM↑3)--&S0 IS IN (MEV)
800 X(I)=(S0*1E21)/(S(I))
810 SX(I)=SX(I-1)+X(I)
820 X(0)=0 : SX(0)=0
830 REM ** X(I) IS THE THICKNESS OF EACH LAYER IN CM **
840 REM-U0 IS THE MASS ABSORPTION COFF.FOR THE KX RAD.OF THE ELEMENT A IN/SP
850 REM---UN=THE MASS ATTIN.COFF.OF TARGET ELEMENT A FOR KX RAD.OF ELEMENT A
860 REM---UM=THE  =    =     =   =    =       =   B  =  KX  =   =   =     A
870 REM---UX=THE  =    =     =   =    =       =   A  =  KB  =   =   =     B
880 REM---UZ=THE  =    =     =   =    =       =   B  =  KB  =   =   =     A
890 Q1(I)=EXP(-(U0)*(SX(I)-(X(I)*.5))*P)
900 G1(I)=EXP(-(U1)*(SX(I)-(X(I)*.5))*P)
910 Q1(0)=0 : G1(0)=0
920 REM--Q1&G1 ARE THE TRANSMISSION OF THE X-RAY THROUGH THE SAMPLE
930 REM---LOG10(X)=.434294*LN(X)---(TO TRANSFER LN TO LOG OF BASE 10)
940 REM ** REUTERS CROSS-SECTION CALCULATIONS **
950 Y3=(LOG((EN(I)*1000)/(1836.118*BE)))*.434294
960 Y1=(.1923*(Y3)↑4)-(.07459*(Y3)↑5)-(.05084*(Y3)↑6)-(.005949*(Y3)↑7)
970 Y2=-19.04+(.03028*Y3)-(1.11*(Y3)↑2)+(.3771*(Y3)↑3)+Y1
980 Y4=EXP(Y2*2.302585)
990 OA(I)=((Y4*Z↑2)/((BE)↑2))
1000 Y(I)=.877886*OA(I)
1010 W(I)=.1221139*OA(I)
1020 REM ** OA(I)=THE PRODUCTION CROSS-SECTION,Y(I) IS KX CROSS-SECTION **
1030 REM ** W(I) IS THE KB CROSS-SECTION **
1040 F(I)=ND*(CA(S)/AA)*P*W1*Y(I)*Q1(I)*X(I)
1050 L(I)=ND*(CA(S)/AA)*P*W1*W(I)*G1(I)*X(I)
1060 REM ** SIMILAR CALCULATION FOR ELEMENT (B) **
1070 Q2(I)=EXP(-(U2)*(SX(I)-(X(I)*.5))*P)
1080 G2(I)=EXP(-(U3)*(SX(I)-(X(I)*.5))*P)
1090 YB=(LOG((EN(I)*1000)/(1836.118*BB)))*.434294
1100 Y5=(.1923*(YB)↑4)-(.07459*(YB)↑5)-(.05084*(YB)↑6)-(.005949*(YB)↑7)
1110 Y6=-19.04+(.03028*YB)-(1.11*(YB)↑2)+(.3771*(YB)↑3)+Y5
1120 Y7=EXP(Y6*2.302585)
1130 OB(I)=((Y7*Z↑2)/((BB)↑2))
1140 Y8(I)=.877116*OB(I)
1150 WB(I)=.1228839*OB(I)
1160 REM---OB(I)=IS TOT.X-SEC.-- & Y8&WB=ARE KX&KB X-SEC. OF ELEMENT B
1170 F2(I)=ND*(CB(S)/AB)*P*W2*Y8(I)*X(I)
1180 L2(I)=ND*(CB(S)/AB)*P*W2*WB(I)*X(I)
1190 F3(I)=ND*(CB(S)/AB)*P*W2*Y8(I)*Q2(I)*X(I)
1200 D=.5*.88*W1*((CA(S)*UP)/U2)
1210 REM---R-1/P=.88 IS AFRACTION OF THE INTENSITY WHICH ABSORBED BY K-SHELL
1220 REM ** IONIZATION WITH SUBSEQUENT EMISSION OF KX PHOTON OF ELEM. A **
1230 NEXT I
1240 R3=0
```

```
1250 R4=0
1260 R5=0
1270 FOR I = 1 TO N
1280 R3=R3+F(I)
1290 R4=R4+F3(I)
1300 REM ** R3,R4 ARE THE TOTAL X-RAY YIELD PRODUCTION OF ELEM. A & B RES. **
1310 NEXT I
1320 PRINT#1,SPC(6)"C"SPC(9)"ENERGY"SPC(5)"ST.POWER";
1330 PRINT#1,SPC(2)"   THICKNESS OF EACH SLAB"
1340 PRINT#1,SPC(5)"---"SPC(8)"------"SPC(5)"-------";
1350 PRINT#1,SPC(2)"   ------------------"
1360 FOR I=1 TO N
1370 Z4=I:Z2=2:GOSUB 2850:PRINT#1,Z4$SPC(3);
1380 Z4=EN(I):Z2=3:GOSUB 2850:PRINT#1,Z4$SPC(3);
1390 Z4=SS(I):Z2=3:GOSUB 2850:PRINT#1,Z4$SPC(6);
1400 PRINT#1,SPC(2)X(I)
1410 NEXT I
1420 PRINT#1,"-------------------------------------------------------------------"
1430 PRINT#1,SPC(6)"C"SPC(9)"X-RAY PATH"SPC(8)" KX-CORR"SPC(9)" KB-CORR."
1440 PRINT#1,SPC(5)"----"SPC(7)"-----------"SPC(7)"--------"SPC(8)"---------"
1450 FOR I=1 TO N
1460 Z4=I:Z2=2:GOSUB 2850:PRINT#1,Z4$SPC(5);
1470 PRINT#1,SPC(1)SX(I);
1480 Z4=G1(I):Z2=4:GOSUB 2850:PRINT#1,Z4$SPC(6);
1490 Z4=G1(I):Z2=4:GOSUB 2850:PRINT#1,Z4$
1500 NEXT I
1510 PRINT#1,"-------------------------------------------------------------------"
1520 PRINT#1,SPC(6)"C"SPC(9)"TOT.X-SEC."SPC(9)"KX.AX-SEC."SPC(7)"KB.AX-SEC"
1530 PRINT#1,SPC(5)"---"SPC(8)"----------"SPC(8)"-------"SPC(8)"----------"
1540 FOR I=1 TO N
1550 Z4=I:Z2=2:GOSUB 2850:PRINT#1,Z4$SPC(5);
1560 PRINT#1,SPC(1)OA(I);
1570 PRINT#1,SPC(1)Y(I);
1580 PRINT#1,SPC(1)W(I)
1590 NEXT I
1600 PRINT#1,"-------------------------------------------------------------------"
1610 PRINT#1,SPC(6)"C"SPC(9)"TOT.X-SEC"SPC(9)"KX.BX-SEC."SPC(7)"KB.BX-SEC."
1620 PRINT#1,SPC(5)"---"SPC(8)"----------"SPC(8)"-------"SPC(8)"----------"
1630 FOR I= 1 TO N
1640 Z4=I:Z2=2:GOSUB 2850:PRINT#1,Z4$SPC(5);
1650 PRINT#1,SPC(1)OB(I);
1660 PRINT#1,SPC(1)YB(I);
1670 PRINT#1,SPC(1)WB(I)
1680 NEXT I
1690 PRINT#1,"-------------------------------------------------------------------"
1700 PRINT#1,SPC(6)"C"SPC(8)"KX.YIELD OF(A)"SPC(6)"KB.YIELD OF (A)"
1710 PRINT#1,SPC(5)"---"SPC(6)"-------------"SPC(5)"--------------"
1720 FOR I = 1 TO N
1730 Z4=I:Z2=2:GOSUB 2850:PRINT#1,Z4$SPC(5);
1740 PRINT#1,SPC(1)F(I);
1750 PRINT#1,SPC(1)L(I)
1760 NEXT I
1770 PRINT#1,"-------------------------------------------------------------------"
1780 PRINT#1,SPC(6)"C"SPC(9)"KX.YIELD(B)"SPC(8)"KB.YIELD(B)"SPC(9)"CORR.KX(B)"
1790 PRINT#1,SPC(5)"---"SPC(8)"------------"SPC(8)"------------"SPC(7)"--------"
1800 FOR I =1TO N
1810 Z4=I:Z2=2:GOSUB 2850:PRINT#1,Z4$SPC(3);
1820 PRINT#1,SPC(1)F2(I);
```

```
1830 PRINT#1,SPC(1,L2(I);
1840 PRINT#1,SPC(1)F1(I)
1850 NEXT I
1860 PRINT#1,"-------------------------------------------------------------------------------"
1870 PRINT#1," R3=" R3;"  R4=" R4
1880 PRINT#1,"-------------------------"
1890 FOR I=1TO N
1900 FF(I)=F2(I):U4=U0:U5=U2
1910 NEXT I
1920 GOSUB 2440
1930 SY=0
1940 FOR J=1 TO N
1950 FOR I=1 TO N
1960 SY=SY+YY(J,I)
1970 NEXT I
1980 NEXT J
1990 PRINT#1,"   SUM OF SEC.YIELD OF (A)"
2000 PRINT#1,"  SY="SY
2010 FOR J=1 TO N
2020 FF(J)=L2(J):U4=U0:U5=U3
2030 NEXT J
2040 GOSUB 2440
2050 SZ=0
2060 FOR J=1 TO N
2070 FOR I=1 TO N
2080 SZ=SZ+YY(J,I)
2090 NEXT I
2100 NEXT J
2110 PRINT#1,"SUM OF SEC.YIELD OF (A) BY KB OF ELEM.(B)"
2120 PRINT#1,"  SZ="SZ
2130 PRINT#1,"-----------------------"
2140 NS=SY+SZ
2150 NT=R3+NS
2160 NZ=SY/R3
2170 NB=SZ/R3
2180 NY=NS/R3
2190 DF=(NT*.63)/(R4*.737)
2200 REM---.6300 = IS THE CORR. FACTOR FOR FE & THE .737  FOR NI
2210 PRINT#1,"TOT.SUM OF SEC.YIELD BY KX&KB OF ELEM. B   "
2220 PRINT#1," NS=" NS
2230 PRINT#1,"-----------------------"
2240 PRINT#1,"TOT. KX YIELD OF ELEM. A + SEC. EFF.OF(KX&KB OF B) "
2250 PRINT#1," NT="  NT
2260 PRINT#1,"-----------------------"
2270 PRINT#1,"ENEHANCEMENT OF (A) BY KX OF (B) IS "
2280 PRINT#1," NZ="  NZ
2290 PRINT#1,"-------------------------"
2300 PRINT#1,"ENEHANCEMENT OF (A) BY KB OF (B) IS "
2310 PRINT#1," NB="  NB
2320 PRINT#1,"ENEHANCEMENT  FACTOR (NY)IS"
2330 PRINT#1,"NY="  NY
2340 PRINT#1,"TOT. KX-YIELD + THE SEC.(OF ELEM. A)/TOT KX-YIELD OF ELEM. B"
2350 PRINT#1,"DF="  DF
2360 PRINT#1,"-----------------------"
2370 NEXT S
2380 CLOSE 1,4
2390 END
2400 STOP
```

```
2410 REM *** THIS SUBROUTINE IS USE TO CALCULATE THE SECONDARY X-RAY YIELD OF
2420 REM *   ELEMENT A DUE TO THE SECONDARY EXITATION FROM THE X-RADIATON OF
2430 REM * ELEMENT B IN THE TARGET
2440 FOR J=1 TO N
2450 FOR I=1 TO N
2460 IF I=J THEN 2770
2470 C1=(U4*P)
2480 R1=0
2490 L=1
2500 IF I < J THEN L = -1
2510 FOR K = J TO I STEP L
2520 R1=R1+X(K)
2530 NEXT K
2540 R1=R1-.5*X(J)-X(I)
2550 T=U5*P*ABS(R1)
2560 SH=((1/T)-.422784+LOG(T))
2570 M = 2
2580 X5=-.5*T
2590 SH=SH+X5
2600 IF ABS(X5/SH)< .0001 THEN 2640
2610 M=M+1
2620 X5=-X5*T*((M-2)/((M-1)*M))
2630 GO TO 1990
2640 TS=T*SH
2650 T=T+X(J)*U5*P
2660 SH=((1/T)-.422784+LOG(T))
2670 M = 2
2680 X5=-.5*T
2690 SH=SH+X5
2700 IF ABS(X5/SH)< .0001 THEN 2740
2710 M=M+1
2720 X5=-X5*T*((M-2)/((M-1)*M))
2730 GO TO 2045
2740 SH=T*SH
2750 YY(J,I)=FF(J)*(TS-SH)
2760 GO TO 2080
2770 T=U5*P*X(J)*.5
2780 YY(J,I)=FF(J)*T*2*(-LOG(T)+(.5*T)+.422784-(T*T/12)+((T↑3)/72)-(T↑4)/480)
2790 R1=SX(I)-X(I)*.5
2800 YY(J,I)=D*YY(J,I)*EXP(-R1*C1)
2810 NEXT I
2820 NEXT J
2830 RETURN
2840 REM *** SUBROUTINE TO SET THE DECIMAL POINTS LIMIT ***
2850 Z4=INT(Z4*10↑Z2+0.5)/10↑Z2
2860 IF Z4<.01THEN2880
2870 Z4$=LEFT$(RIGHT$("           "+STR$(Z4+.5/10↑Z2*SGN(Z4)),10),9):GOTO2890
2880 Z4$=LEFT$(RIGHT$("           "+STR$(Z4+.5/10↑Z2*SGN(Z4)),10),10)
2890 IFVAL(Z4$)=0 THEN Z4$="      0.00"
2900 RETURN
2910 END
2920 REM *** SUBROUTINE TO CAL.THE ST.POWER FOR FE&NI FOR E(I)>=1MEV ***
2930 H=(A6/(.00213*E(I)))
2940 G=LOG((A7*.00213*E(I))/(1-(.00213*E(I))))
2950 K=A8+A9*LOG(EE(I))+A0*(LOG(EE(I)))↑2+A1*(LOG(EE(I)))↑3+AF*(LOG(EE(I)))↑4
2960 SA=(H*(G-(.00213*E(I))-K))*((ND*PA)/AA)
2970 SP=(H*(G-(.00213*E(I))-K))
2980 H1=(B6/(.00213*E(I)))
```

```
2990 G1=LOG(1-B7*.00213*E(I))/(1-(.00213*E(I)))
3000 K1=B8+B9*LOG(EE(I))+B0*(LOG(EE(I)))↑2+B1*(LOG(EE(I)))↑3+BF*(LOG(EE(I)))↑4
3010 S8=(H1*(G1-(.00213*E(I))-K1))*((ND*PB)/AB)
3020 SR=(H1*(G1-(.00213*E(I))-K1))
3030 S(I)=(SA*CA(S)+SR*CB(S))
3040 S5(I)=(SF*CA(S)+SA*CB(S))
3050 RETURN
3060 END
3070 REM ***  SUBROUTINE TO CAL.THE ST.POWER FOR FE&NI FOR E(I)< 1MEV ***
3080 S1=A2*(EE(I))↑.45
3090 S2=(A3/EE(I))*LOG(1+(A4/EE(I))+(A5*EE(I)))
3100 S3=((S1*S2)/(S1+S2))*((ND*PA)/AA)
3110 S7=((S1*S2)/(S1+S2))
3120 S4=B2*(EE(I))↑.45
3130 S5=(B3/EE(I))*LOG(1+(B4/EE(I))+(B5*EE(I)))
3140 S6=((S4*S5)/(S4+S5))*((ND*PB)/AB)
3150 S8=((S4*S5)/(S4+S5))
3160 S(I)=S3*CA(S)+S6*CB(S)
3170 S5(I)=S7*CA(S)+S8*CB(S)
3180 RETURN
3190 END
3200 DATA.05,2.0,.05,7.111,8.331,3.963,6065,1243,.007782,.01326,3650,-9.809
3210 DATA 3.763,-.5164,.0385,-.00066,4.004,6205,555.1,.008763,.01428,3297
3220 DATA -10.53,4.019,-.549,.03229,-.0006957
3230 DATA 70.07,90.5,53.69,69.22,364.4,59.24,280.8,44.92,26,28
3240 DATA 7.874,8.902,.347,.414,6.02E23,58.71,55.85,1
3250 DATA .0002,.9998,.0005,.9995,.001,.999,.005,.995,.01,.99,.05,.95,.1,.9
3260 DATA.2,.8,.4,.6,.8,.2
```

REFERENCES

Ahlberg, M. S., Akselsson, R., Brune, D. and Lorenzen, J.
Nuclear Instruments and Methods, 123, (1975), pp. 385-393.

Ahlberg, M. S. and Akselsson, R.
International Journal of Applied Radiation and Isotopes, Vol. 27, (1976), pp. 279-290.

Ahlberg, M. S.,
Nuclear Instruments and Methods, 142, (1977), pp. 61-65.

Akselsson, R. and Johansson, T. B.,
Z. Physik, 266, (1974), pp.245-255.

Alder, K., Bohr, A., Huss, T., Mottleson, B. and Winther, A.
Review Modern Physics, 28, (1956), pp.432-542.

Anderson, H. H.
2, Pergamon Press, New York, (1977).

Anderson, H. H. and Ziegler, J. F.
3, Pergamon Press, New York, (1977).

Armaghani, M. A. S. and Crumpton, D.
M.Sc. Report, University of Aston in Birmingham (1980).

Bambynek, W., Crasemann, B., Fink, R. W., Freund, H. U., Mark, H., Swift, C. D., Price, R. E. and Venugopala, R.
Reviews of Modern Physics, Vol. 44, No. 4, (1972), pp. 716-813.

Bang, J. and Hansteen, J. M.
Mat. Fys. Medd. Dan. Selsk, 31, (1959), No. 13.

Basbas, G., Brandt, W. and Laubert, R.
Physical Review A: Vol. 7, No. 3, (1973), pp. 983-1001.

Basbas, G., Brandt, W. and Laubert, R.
Physical Review A: Vol. 17, No. 5, (1978), pp. 1655-1674.

Bauer, K. G., Fazly, Q., Mayer, K. T., Mommsen, H. and Schürkes, P.
Nuclear Instruments and Methods, 148, (1978), pp. 407-413.

Bearse, R. C., Close, D. A., Malanify, J. J. and Umberger, C. J.
Physical Review, A7, (1973), pp. 1269-1272.

Benka, O. and Geretschläger, M.
Journal of Physics B: Atomic and Molecular Physics, 13, (1980), pp. 3223-3233.

Bertin, E. P.
"Introduction to X-Ray Spectromatic Analysis", Plenum Press, (1978).

Bewers, J. M. and Flack, F. C.
Nuclear Instruments and Methods, 59, (1968), pp. 337-338.

Blondiaux, G., Valladon, M., Ishii, K. and Debrun, J. L.
Transactions of the American Nuclear Society, 32, (1979), pp. 199-200.

Birks, L. S., Seebold, R. E. and Batt, A. P.
Journal of Applied Physics, 35 (1964), pp. 2579-2581.

Brandt, W. and Lapicki, G.
Physical Review A: Vol. 20, No. 2, (1979), pp. 465-480.

Brandt, W. and Lapicki, G.
Physical Review A: Vol. 23, No. 4, (1981), pp. 1717-1729.

Brice, D. K., Ion Implantation and Energy deposition. Distributions, Plenum Press (1975).

Burhop, E. H. S. and Asaad, W. N.
Advance in Atomic and Molecular Physics, 8, (1972), pp. 163-287.

Burnett, W. C. and Mitchum, G. T.
Nuclear Instruments and Methods, 181, (1981), pp. 231-138.

Cahill, T. A.
"New Use of Ion Accelerators" Ed. J. F. Ziegler, Plenum Press, New York, (1975), pp. 1-71.

Cahill, T. A.
Nuclear Instruments and Methods, 181, (1981), pp. 473-480.

Campbell, J. L.
Nuclear Instruments and Methods, 142, (1977), pp. 263-273.

Campbell, J. L., Russell, S. B., Faiz, S. and Schulte, C. W.
Nuclear Instruments and Methods, 181, (1981), pp. 97-98.

Carlson, T. A.,
"Photoelectron and Auger Spectroscopy", Plenum Press, London (1975).

Chattarji, D., "The Theory of Auger Transition", Academic Press, London (1976).

Chen, M. H., Crasemann, B. and Kostroun, V. O.
Physical Review A: Vol. 4., No. 1, (1971), pp. 1-6.

Chen, M. H., Crasemann, B. and Mark, H.
Atomic Data and Nuclear Data Tables, 24, (1979), pp.13-37.

Chen, M. H., Crasemann, B. and Mark, H.
Physical Review A: Vol. 24, No. 1, (1981), pp. 177-182.

Chu, W. K., Mayer, J. W. and Nicolet, M. A.
"Backscattering Spectrometry", Academic Press, London, (1978).

Chu, T. C., Ishii, K., Yamadera, A., Sebata, M. and Morita, S.
Nuclear Instruments and Methods, 190, (1981), pp. 395-399.

Clayton, E.
Nuclear Instruments and Methods, 191, (1981), pp. 567-572.

Cookson, J. A. and Campbell, J. L.
Nuclear Instruments and Methods, 216, (1983), pp. 489-495.

Cohen, D. D., Duerden, P., Clayton, E. and Wall, T.
Nuclear Instruments and Methods, 168, (1980), pp. 523-528.

Davis, L. E., MacDonald, N. C., Palmberg, P. W., Riach, G. E. and Weber, R. E.
"Hand Book of Auger Electron Spectroscopy", 2nd Edition, Physical Electronics, Ind., Inc., Eden Pravie, Minnesota, (1976).

Deconninck, G., Demortier, G. and Bodart, F.
Atomic Energy Review, Vol. 13, No. 2, (1975), pp. 367-412.

Deconninck, G.
Nuclear Instruments and Methods, 142, (1977), pp. 275-284.

Dias, M. S. and Renner, C.
Nuclear Instruments and Methods, 193, (1982), pp. 91-93.

Duffin, W. J.
"Electricity and Magnatism", McGraw-Hill Book Co., U.K., (1980).

Dyson, N. A.
X-Ray in Atomic and Nuclear Physics, Longman Group Limited, London (1973).

Dyson, N. A.
"An Introduction to Nuclear Physics with Applications in Medicine and Biology", Ellis Horwood Limited, England, (1981).

Enge, H. A.,
"International to Nuclear Physics", Reading, Massachusette: Addison-Wesley Publishing Co. Inc., (1966), pp. 181-188.

Feng, J. S. Y., Chu, W. K. and Nicolet, M. A.
Thin Solid Films, 19, (1973), pp. 227-238.

Fink, R. W., Jopson, R. C., Mark, H. and Swift, C. D.
Reviews of Modern Physics, 38, (1966), pp. 513-540.

Folkmann, F., Gaarde, C., Huss, T. and Kemp, K.
Nuclear Instruments and Methods, 116, (1974a), pp. 487-499.

Folkmann, F., Braggren, J. and Kjeldgaard, A.
Nuclear Instruments and Methods, 119, (1974b), pp. 117-123.

Folkmann, F.
Journal of Physics E: 8, (1975), pp. 429-444.

Folkmann, F.
"Ion Beam Surface Layer Analysis II", Plenum Press, New York, (1976), pp. 695-718.

Garcia, J. D.
Physical Review A1, (1970a), pp. 280-285.

Garcia, J. D.
Physical Review A1, (1970b), pp. 1402-1403.

Garcia, J. D., Fortner, R. J. and Kavanagh, T. M.
Review of Modern Physics, Vol. 45, No. 2., Part 1, (1973), pp. 111-177.

Gardner R. K. and Gray, T. J.
Data and Nuclear Data Tables, 21, (1978), pp. 515-536.

Gedcke, D. A., Elad, E. and Dyer, G. R.
Proceeding Sixth National Conference on Electron Probe Analysis, Pittsburgh, 1971, pp. 5A-5C.

Gedcke, D. A.
X-ray Spectrometry, 1, (1972), pp. 129-141.

Goodfellow Metals Limited, U.K., (1982).

Grant, J. T.
Applied Surface Science, 13, (1982), pp. 35.

Gray, T. J., Lear, R., Dexter, R. J., Schwettmann, F. N. and Wiemer, K. C.
Thin Solid Films, 19, (1973), pp. 103-119.

Hansteen, J. M. and Mosebekk, O. P.
Nuclear Physics A: 201, (1973), pp. 541-560.

Hansteen, J. M., Johansen, O. M. and Kocbach, L.
Atomic Data Nuclear Data Tables, 15, (1975), pp. 305-317.

Hardt, T. L. and Watson, R. L.
Atomic Data Nuclear Data Tables, 17, (1976), pp. 107-125.

Hansen, J. S.
Physical Review A: Vol. 8, No. 2, (1973), pp. 822-839.

Hubbell, J. H.
NBS-29, Washington, (1969).

Huda, W.
Nuclear Instruments and Methods, 158, (1979), pp. 587-594.

Holloway, P. H.
Advance in Electronics and Electron Physics, 34, (1980), pp. 241-298.

Ishii, K., Kamiya, M., Sera, K., Morita, S. and Tawara, H.
Physical Review A: Vol. 15, No. 5, (1977), pp. 2126-2129.

Ishii, K., Valladon, M. and Debrun, J. L.
Nuclear Instruments and Methods, 150, (1978), pp. 213-219.

Jaklevic, J. M., Goulding, F. S. and Landis, D. A.
IEEE Transactions on Nuclear Science, NS-18, (1972), pp. 392-395.

Janni, J. F.
Technical Report No. AFWL-TR-65-150, Air Force Weapons Laboratory Research and Technology, (1966).

Jenkins, R., Gould, R. W. and Gedcke, D.
"Quantitative X-Ray Spectrometry", Marcel Dekker Inc., (1981).

Johansson, T. B., Akselsson, R. K. and Johansson, S. A. E.
Nuclear Instruments and Methods, 84, (1970), pp. 141-143.

Johansson, S. A. E. and Johansson, T. B.
Nuclear Instruments and Methods, 137, (1976), pp. 473-516.

Johansson, S. A. E.
Proceedings of the 1st International Conference on PIXE and its Applications, Lund, Sweden, August 1976.
Published in Nuclear Instruments and Methods, 142, (1977).

Johansson, S. A. E.
Proceedings of the 2nd International Conference on the PIXE and its Applications, Lund, Sweden, June 1980.
Published in Nuclear Instruments and Methods, 181, (1981).

Johnson, G. A., Manson, E. L. and O'Foghludha, J. R.
Nuclear Instruments and Methods, 151, (1978), pp. 217-220.

Khaliquzzaman, M., Zaman, M. B. and Khan, A. H.
Nuclear Instruments and Methods, 181, (1981), pp. 209-215.

Khaliquzzaman, M., Lam, S. T., Sheppard, D. M. and Stephens-Newsham, L. G.
Nuclear Instruments and Methods, 216, (1983), pp. 481-488.

Khan, R.
Ph.D. Thesis, Aston University in Birmingham, (1975).

Khan, Md. R., Crumpton, D. and Francois, P. E.
Journal of Physics B: Atomic Molecular Physics, Vol. 9, No. 3, (1976), pp. 455-460.

Khan, Md. R., Hopkins, A. G. and Crumpton, D.
Proceedings of the 8th International Conference on X-Ray Optics and Microanalysis, Boston, (1977), pp. 287-290.

Khan, Md. R., and Crumpton, D.
CRC Critical Reviews in Analytical Chemistry, (1981), Part I pp. 103-155, Part II pp. 166-193.

Kivits, H.
"Particle Induced X-ray Emission for Quantiative Trace-Element Analysis using the Eindhoven Cyclotron", (1980).

Krause, M. O.
Journal of Physical and Reference Data, 8, (1979), pp. 307-322.

Laegsgaard, E., Andersen, J. U. and Lund, M.
10th International Conference on the Physics of Electronic and Atomic Collision", (1978), pp. 353.

Laegsgaard, E., Andersen, J. U. and Høgedal, F.
Nuclear Instruments and Methods, 169, (1980), pp. 293-300.

Lander, J. J.
Physical Review, Vol. 91, No. 6, (1953), pp. 1382-1387.

Land, D. J., Brown, M. D., Simons, D. G. and Brennan, J. G.
Nuclear Instruments and Methods, 192, (1982), pp. 53-62.

Lindhard, J., Scharff, M., and Schiøtt. H. E.
Kgl. Danske Videnskab. Selskab., Mat. Fys. Medd., 33, No. 14, (1963).

Lin, T. L., Luo, C. S. and Chou, J. C.
Nuclear Instruments and Methods, 159, (1979), pp. 387-393.

Loef, J. J. Van, Brekoo, H. P. J., Swift, D. W. and Verheyke, M. L.
Philips Research Lab. Report, Nr. 133/62.

Lopes, J. S., Jesus, A. P. and Ramos, S. C.
Nuclear Instruments and Methods, 169, (1980), pp. 311-317.

Mogami, A., Sekine, T., Nagasawa, Y., Kudoh, M., Sakai, Y., Parkes, A. S., Geller, J. D. and Hirota, H.
Handbook of Auger Electron Spectroscopy, (JEOL Inc., Tokyo, 1982).

MacDonald, J. R., Feldman and Silverman, P. J.
Nuclear Instruments and Methods, 218, (1983), pp. 765-770.

Madison, D. H. and Merzbacher, E.
"Atomic Inner-Shell Processes", Vol. 1, Ed. by Crasemann, B., London, Academic Press, (1975), pp. 1.

Mahrok, M. F.
Ph.D. Thesis, University of Aston in Birmingham.

Malmqvist, K. G., Karlsson, E. and Akselsson, K. R.
Nuclear Instruments and Methods, 192, (1982), pp. 523-532.

Mangelson, N. F., Hill, M. W., Nielson, K. K. and Ryder, J. F.
Nuclear Instruments and Methods, 142, (1977), pp. 133-142.

M.B.H. Analytical Limited, U.K., (1983).

McGuire, E. J.
Physical Review, Vol. 2, No. 2, (1970a), pp. 273-278.

McGuire, E. J.
Physical Review A:, Vol. 3, No. 6, 587, (1971), pp. 1801-1810.

McMaster, W. H., Grande, N. K. D., Mallett, J. H. and Hubbell, J. H.
UCRL-5-174 Secs. 1, 2, 3, (1969).

Merzbacher, E. and Lewis, H. W.
Encyclopedia of Physics, Edited by Flugge, S., Springer Verlag, Berlin, Vol. 34, (1958), pp. 166-192.

Millar, R. H. and Greening, J. R.
Journal of Physics B: Atomic and Molecular Physics, Vol. 7, No. 17, (1974), pp. 2332-2344.

Mingay, D. W., Jonker, W. D. and Smith, B. J.
Atomic Energy Board, Pel-259, Pretoria, Republic of South Africa, (1978).

Mitchell, L. V., Barfoot, K. M. and Eschback, H. L.
Nuclear Instruments and Methods, 168, (1980), pp. 233-240.

Mommsen, H., Sarkar, M., Sarter, W. and Schmittinger, T.
Nuclear Instrumetns and Methods, 166, (1979), pp. 361-365.

Montenegro, E. C., Baptista, G. B. and Duarte, W. E. P.
Atomic Data and Nuclear Data Tables, 22 (1978), pp. 131-177.

Morgan, A. E.
Nuclear Instruments and Methods, 218 (1983), pp. 401-408.

Mukoyama, T. and Sarkadi, L.
Nuclear Instruments and Methods, 205, (1983), pp. 341-346.

Newell, J. E.
Nuclear Engineering International, Vol. 16, (1972), pp. 637-639.

Northcliffe, L. C. and Schilling, R. F.
Nuclear Data Tables, A7, (1970), pp. 233-251.

Patnaik, B. K. and Dhere, N. G.
Nuclear Instruments and Methods, 131, (1975), pp. 503-509.

Paul, H.
Nuclear Instruments and Methods, 169, (1980), pp. 249-258.

Phull, J.
Private Communications, (1982), University of Aston in Birmingham.

Plouns, M. A.
"Applied Electromagnatics", McGraw-Hill Kogakusha Ltd., (1978).

Powers, D., Lodhi, A. S., Lin, W. K. and Cox, H. L. Jr.
Thin Solid Films, 19, (1973), pp. 205-215.

Raith, B., Roth, M., Göllner, K., Gonsior, B., Ostermann, H. and Uhlhorn, C. D.
Nuclear Instruments and Methods, 142, (1977), pp. 39.

Riath, B., Stratmann, A., Wilde, H. R., Gonsior, B., Brüggerhoff, S. and Jackwerth, E.
Nuclear Instruments and Methods, 181, (1981), pp. 199-204.

Reed, S. J. B.
British Journal of Applied Physics, Vol. 16, (1965), pp. 913-926.

Renan, M. J.
X-Ray Spectrometry, Vol. 9, No. 2, (1980), pp. 90-94.

Reuter, W., Lurio, A., Gardone, F. and Ziegler, J. F.
Journal of Applied Physics, Vol. 46, No. 7, (1975), pp. 3194-3202.

Rice, R., Basbas, G. and McDaniel, F. D.
Atomic Data and Nuclear Data Tables, 20, (1977), pp. 503-511.

Richter, F. W. and Wätjen, U.
Nuclear Instruments and Methods, 181, (1981), pp. 189-194.

Roy, D. and Garette, J. D.
"Design of Electron Spectrometers for Surface Anlaysis", in Topics in Current Physics, Vol. 4, Ibach. H., Ed. Springer-Verlag, Berlin, (1977), pp. 13.

Rutledge, C. H. and Watson, R. L.
Atomic Data and Nuclear Data Tables, 12 (1973), pp. 195-216.

Saied, S. O.
Ph.D. Thesis (1981), University of Aston in Birmingham.

Schmidt, W. and Saemann, I.
Nuclear Instruments and Methods, 218, (1983), pp. 757-763.

Shabason, L., Cohen, B. L., Wedberg, G. H. and Chan, K. C.
Journal of Applied Physics, Vol. 44, No. 10, (1973), pp. 4749-4752.

Shiraiwa, T. and Fujino, N.
Japanese Journal of Applied Physics, Vol. 5, No. 10, (1966), pp. 886-899.

Sokhi, R. S. and Crumpton, D.
Atomic Data and Nuclear Data Tables, 30, (1984), pp. 49-124.

Sokhi, R. S.
Ph.D. Thesis, (1984), University of Aston in Birmingham.

Statham, P. J. and Long, J. V. P.
X-Ray Spectrometry, Vol. 3, (1974), pp. 153-158.

Storm, E. and Israel, H. I.
Nuclear Data Tables, A7, (1970), pp. 565-681.

Sullivan, J. L. and Granville, N. W.
Tribology International, Vol. 17, No. 2, (1984), pp. 63-73.

Tan, M., Braga, R. A. and Fink, R. W.
Physica Scripta, Vol. 25, (1982), pp. 536-542.

Taulbjerg, K.
Proceeding 2nd International Conference on Inner Shell Ionization, Eds. Mehlhorn, W. and Brenn, R., Freiburg, West Germany, (1976).

Taulbjerg, K.
Jouranl of Physics B: Atomic Molecular Physics, Vol. 10, No. 9, (1977), pp. L341-L346.

Tawara, H., Ishii, K. and Marita, S.
Nuclear Instruments and Methods, 132, (1976), pp. 503-505.

Valkovic, V.
"Trace Element Analysis" Taylor and Francis Ltd., London, (1975).

Valkovic, V., Rendic, D. and Phillips, G. C.
Environmental Science and Technology, 9, (1975), pp. 1150-1152.

Van der Kam, P. M. A., Vis, R. D. and Verheul, H.
Nuclear Instruments and Methods, 142, (1977), pp. 55-60.

Varelas, C. and Biersack J. P.
Nuclear Instruments and Methods, 79, (1970), p. 213-218.
(see also Biersack, J. P. and Fink, D. in S. Datz, B. R. Appleton and Moak, C. D. (Eds)., Atomic Collisions in Solids, Plenum Press, New York, (1975), pp. 737.

Veigele, W. J.
Atomic Data, 5, (1973), pp. 51-111.

Walter, D. L. and Bhalla, C. P.
Physical Review A3, (1971), pp. 519-520.

Walter, R. L., Willis, R. D., Gutknecht, W. F. and Joyce, J. M.
Analytical Chemistry, Vol. 46, No. 7, (1974), pp. 843-855.

Wentzel, G.
Zeitschrift fuer Physik, 43, (1927), pp. 524.

Williamson, C. F., Boujot, J. P. and Picard, J.
Report No., CEA-R3042, C.E.A., Saclay, France, (1967).

Willis, R. D., Walter, R. L., Shaw, R. W. and Gutknecht, W. F.
Nuclear Instruments and Methods, 142, (1977), pp. 67-77.

Woldseth, R.
"X-Ray Energy Spectrometry", Published by Kevex Corporation, Burlington, California, (1973).

Young, F. C., Roush, M. L. and Bergman, P. G.
International Journal of Applied Radiation and Isotopes, 24, (1973), pp. 153-163.

Ziegler, J. F.
New Use of Ion Accelerators, Plenum Press, London, (1975), pp. 75.

Ziegler, J. F., Chu, W. K. and Feng, J. S. Y.
Applied Physics Letter, Vol. 27, (1975), pp. 387-390.